

Stochastic Characterization and Reconstruction of Porous Media

by

Lalit Mohan Pant

A thesis submitted in partial fulfillment of the requirements for the degree of

Doctor of Philosophy

Department of Mechanical Engineering

University of Alberta

©Lalit Mohan Pant, 2016

Abstract

Heterogeneous materials are omnipresent in several critical engineering applications such as polymer electrolyte fuel cells (PEFCs), coal bio-conversion process, geological storage of CO₂ and membrane water filtration. These applications rely on physical processes such as transport (e.g., mass, momentum, or energy) and chemical reactions for their functioning. The physical processes in the porous media are strongly dependent on morphology of the porous media structure. A detailed understanding of the porous media is therefore necessary for understanding and improving the physical processes in the porous media. A detailed understanding of microstructure can be utilized to find the physical properties, and then to estimate and improve the performance.

This work is focused on using statistical correlation functions for characterization and reconstruction of porous media structure. The statistical method is chosen due to its ability to capture stochastic nature of porous media in practical amount of cost and time. A simulated annealing based reconstruction method is used to reconstruct porous media structures with different statistical properties. A new unified pixel swapping method is presented, which can implement all available pixel swapping techniques in literature. The new pixel swapping method results in time reduction by a factor of 3-4 compared to conventional random swapping. Furthermore, compared to available biased pixel swapping methods, current method does not cause unrealistic structures to be reconstructed. A new different phase neighbor based multigrid hierarchical method has been developed, which reduces reconstruction time by one to two orders of magnitude, while improving reconstruction accuracy.

Multiple statistical correlation functions are used to reconstruct porous media structures which can closely match the original structure in terms of statistical and physical properties. Effect of different correlation functions on transport properties is studied in order to find a set of statistical correlation functions which can accurately characterize transport properties of a porous media. The effective molecular diffusivity was found to strongly depend on the two-point correlation function of porous media.

Overall, this work provides a novel method for fast and accurate characterization of porous media structures and transport properties by statistical correlation functions. This provides an ideal framework for reconstructing random porous media structures, and understanding the relationship between correlation functions and their transport properties. With the relationship between correlation functions and properties known, this work paves way for designing porous media structures with desired transport properties.

Keywords: Porous media, stochastic reconstruction, correlation functions, diffusion

Preface

Parts of chapter 2, chapter 3, and chapter 4 of this thesis have been published as L. M. Pant, S. K. Mitra and M. Secanell. “Stochastic Reconstruction Using Multiple Correlation Functions with Different-Phase-Neighbor-Based Pixel Selection”. *Physical Review E*, 2014, Volume 90, Issue 2, pp. 023306. I was responsible for review, programming, analysis, data processing and manuscript writing. S. K. Mitra was the supervisory author and contributed to manuscript composition and editing. M. Secanell was supervisory author, and contributed with concept formation, manuscript composition, and editing.

Parts of chapter 3 and 4 have been published as L. M. Pant, S. K. Mitra and M. Secanell. “Multigrid Hierarchical Simulated Annealing Method for Reconstructing Heterogeneous Media”. *Physical Review E*, 2015, Volume 92, Issue 6, pp. 063303. I was responsible for review, programming, analysis, data processing and manuscript writing. S. K. Mitra was the supervisory author and contributed to manuscript composition and editing. M. Secanell was supervisory author, and contributed with concept formation, manuscript composition, and editing.

Dedicated to my Mother

Acknowledgements

First and foremost, I would like to thank my parents for their blessings and constant support. Even with all the hardships they faced in their life, they have always supported my quest for education. Without their calm words and encouragement for learning, I could have never reached this far. My father has been a teacher for me who not only taught me mathematics in my childhood, but also the valuable lessons of life. My mother, who has been a source of constant emotional support for me, without which it would be impossible to stay away from home so long. I would like to thank all my family members for their love and encouragement over all these years. The help and encouragement from my family has been the driving force in my life. I would specially like to thank my eldest brother, who has been like another father figure in the family. Without his constant push and encouragement, I may have never gotten a good basis for education.

I would like to thank my supervisors Dr. Marc Secanell and Dr. Sushanta Mitra for awarding me the opportunity to pursue research under their guidance and for their support and encouragement. I would like to thank Dr. Marc Secanell for he has been a great source of inspiration and learning for me. Over the course of my graduate studies, I have had a great opportunity to learn from him about all the facets of life. His zeal for learning and exploring are something I hope to acquire myself. His help in all my works has been invaluable. Be it the problems in modelling, experimentation or reviews of my writings, he has always been very helpful and understanding. Our discussions over beer on technical subjects and on life in general will be always cherished in life.

I would like to thank Dr. Sushanta Mitra for bringing me here at University of Alberta. His encouragement and confidence during the tough times of research has been very helpful. He has always been very brisk and generous in resolving the problems. He has always involved me in group projects and networks, which has been very valuable for forming network collaborations and contacts. His work management skills and ambitious perspective of life are something I try to apprentice in my life.

I would like to thank Dr. Shawn Litster and Pratiti Mandal at Mechanical Engineering, Carnegie Mellon University for providing me with the nano-CT image of PEFC catalyst layer. I would also like to thank Dr. Murray Gingras, at Earth and Atmospheric Sciences, University of Alberta for providing micro-CT images of Ti foam for my work. Finally, I would like to thank Dr. Kirill Gerke at CSIRO, Land and Water Division, Australia for providing the X-ray microtomography image of the ceramic material.

This research work would not have been possible without the financial assistance of several grant agencies, and scholarships. I would like to thank Carbon Management Canada (CMC), Natural Sciences and Engineering Research Council of Canada (NSERC), Canada Foundation for Innovation (CFI), University of Alberta doctoral recruitment scholarship, and Alberta Innovates Technology Futures (AITF) Graduate Student Scholarship for financial assistance.

Finally, I would like to thank my friends without whom life here in Edmonton would be very difficult to live. Thank you Madhur, Malyaj, Ishwar, Shantanu, and Prashant for your constant support and companionship. I would also like to thank all my lab-mates at energy system design laboratory (ESDL) for sharing their enthusiasm and ideas of research. A special thanks to Mayank for his help in setting up openFCST simulations for me. Last, but not least, thank you Chad for setting up my CMake scripts, and all the cakes and ice-creams, they shall be missed.

Table of Contents

| | | |
|----------|---|-----------|
| 1 | Introduction | 1 |
| 1.1 | Motivation | 1 |
| 1.2 | Literature Review | 3 |
| 1.2.1 | Imaging Techniques | 3 |
| 1.2.2 | Statistical Characterization | 4 |
| 1.2.3 | Fabrication based Reconstruction | 8 |
| 1.2.4 | Stochastic Reconstruction | 10 |
| 1.3 | Contributions of This Work | 22 |
| 1.4 | Structure of the Thesis | 23 |
| 2 | Theory of Stochastic Analysis | 24 |
| 2.1 | Porous Media as a Stochastic Process | 24 |
| 2.1.1 | Indicator Functions | 25 |
| 2.2 | Statistical Correlation Functions | 26 |
| 2.2.1 | n-point Correlation Function | 26 |
| 2.2.2 | Homogeneous and Isotropic Porous Media | 27 |
| 2.2.3 | One-point Correlation Function | 28 |
| 2.2.4 | Two-point Correlation Function | 28 |
| 2.2.5 | Lineal Path Function | 32 |
| 2.2.6 | Chord Length Function | 32 |
| 2.2.7 | Two-point Cluster Function | 35 |
| 2.3 | Correlation Function Computation for Digital Images | 37 |
| 2.3.1 | One-point correlation function | 37 |
| 2.3.2 | Two-point Correlation Function | 38 |
| 2.3.3 | Lineal Path Function | 39 |
| 2.3.4 | Chord Length Function | 39 |
| 2.3.5 | Two-point Cluster Function | 40 |
| 2.3.6 | Dealing with Boundaries in Correlation Functions Computing | 41 |
| 2.4 | Validation of the Correlation Function Computing Algorithms | 42 |

| | | |
|----------|---|-----------|
| 2.4.1 | Two-point Correlation Function | 44 |
| 2.4.2 | Lineal path function | 44 |
| 2.4.3 | Chord Length Function | 46 |
| 2.4.4 | Two-point Cluster Function | 46 |
| 3 | Stochastic Reconstruction of Random Media | 50 |
| 3.1 | Simulated Annealing | 50 |
| 3.2 | Energy Minimization Method | 53 |
| 3.2.1 | Probability based Energy Minimization (Metropolis Method) | 53 |
| 3.2.2 | Threshold Energy based Energy Minimization | 54 |
| 3.2.3 | Termination of Energy Minimization | 56 |
| 3.3 | Cooling Mechanisms | 57 |
| 3.4 | Pixel Swapping Methods | 59 |
| 3.4.1 | Random Pixel Swapping | 59 |
| 3.4.2 | Surface Pixel Swapping | 59 |
| 3.4.3 | Different Phase Neighbor (DPN) based Pixel Swapping | 60 |
| 3.5 | Multigrid Hierarchical Annealing | 63 |
| 3.6 | Computational Implementation | 67 |
| 3.6.1 | Reference Image Scaling | 68 |
| 3.6.2 | Reference Image Generation for Coarse Scales | 68 |
| 3.6.3 | DPN Computation | 68 |
| 3.6.4 | Accounting for Anisotropy | 71 |
| 3.6.5 | Updating Correlation Functions | 72 |
| 4 | Stochastic Analysis and Reconstruction of Porous Media | 73 |
| 4.1 | Materials and Methods | 73 |
| 4.1.1 | Materials | 73 |
| 4.1.2 | Imaging and Image Processing | 74 |
| 4.2 | Stochastic Analysis | 80 |
| 4.2.1 | Analysis of 2D PEFC Catalyst Layer Image | 81 |
| 4.2.2 | Analysis of 2D Ceramic Image | 83 |
| 4.2.3 | Analysis of 3D PEFC Catalyst Layer Images | 85 |
| 4.2.4 | Analysis of 3D Titanium Foam Images | 85 |
| 4.3 | Stochastic Reconstruction | 88 |
| 4.3.1 | Effect of Energy Minimization Method | 88 |
| 4.3.2 | Effect of Cooling Schedule | 93 |
| 4.3.3 | Effect of Pixel Swapping | 95 |

| | | |
|----------|---|------------|
| 4.3.4 | Effect of Multigrid Method | 103 |
| 4.3.5 | Effect of Correlation Functions on Structure | 110 |
| 4.4 | Reconstruction of 3D Structures of Different Porous Media | 113 |
| 4.5 | Summary of the Reconstruction Method | 120 |
| 5 | Mass Transport Analysis in Porous Media | 124 |
| 5.1 | Mass Transport in Porous Media | 124 |
| 5.1.1 | Molecular Diffusion | 126 |
| 5.1.2 | Knudsen Diffusion | 127 |
| 5.1.3 | Transport in Transition Region | 128 |
| 5.2 | Simulation Methodology | 129 |
| 5.2.1 | Governing Equation | 129 |
| 5.2.2 | Domain Generation | 129 |
| 5.2.3 | Simulation | 130 |
| 5.3 | Representative Size Estimation | 131 |
| 5.4 | Transport Studies in Ti Foam | 132 |
| 5.4.1 | Transport Analysis in Reference Images | 134 |
| 5.4.2 | Transport Analysis in Reconstructed Images | 136 |
| 5.5 | Summary | 147 |
| 6 | Conclusions and Future Work | 149 |
| 6.1 | Conclusions | 149 |
| 6.2 | Future Work | 151 |
| | References | 153 |
| A | Computational Algorithms for Correlation Function Estimation | 170 |
| A.1 | Algorithm for Computing Volume Fraction | 170 |
| A.2 | Algorithm for Computing Two-point Correlation Function | 170 |
| A.3 | Algorithm for Computing Lineal Path Function | 172 |
| A.4 | Algorithm of computing Chord Length Function | 172 |
| A.5 | Algorithm for Computing Two-point Cluster Function | 173 |
| A.5.1 | Cluster Identification | 173 |
| A.5.2 | Cluster Function Computation | 174 |
| B | Computational Algorithms for Stochastic Reconstruction | 177 |
| B.1 | Reference Image Synthesis | 177 |
| B.2 | Image Resizing Method | 177 |

| | | |
|-------|---|-----|
| B.3 | DPN Computation Methods | 177 |
| B.3.1 | DPN Value Computation Algorithm | 177 |
| B.4 | DPN Set Assembling Algorithm | 179 |
| B.5 | DPN Set Updating | 179 |

List of Tables

| | | |
|-----|---|-----|
| 1.1 | A summary of reconstruction literature related to study of physical properties of reconstructions | 21 |
| 4.1 | Parameters used for reconstruction of square grid pattern. | 89 |
| 4.2 | Explanation of different DPN parameters used in DPN based pixel swapping | 99 |
| 4.3 | General simulated annealing parameters used for multigrid reconstruction. | 105 |
| 4.4 | Comparison of average reconstruction times for different multigrid reconstructions (final image size 600×600). The margins of error are based on 10 trials and represent a 95% confidence interval | 106 |
| 4.5 | Comparison of speedup factor using Freeze ₂ based multigrid method for different image sizes. The margins of error are based on 10 trials and represent a 95% confidence interval | 110 |
| 4.6 | Reconstruction time for different final reconstructed image sizes. All reconstructions are performed using Freeze ₂ with 4 grid levels. The margins of error are based on 10 trials and represent a 95% confidence interval | 110 |
| 4.7 | Comparison of discrepancy in different correlation functions for 2D PEFC CL reconstructions of size 200×200 pixels using different correlation function combinations. Blue color indicates the function which is being optimized. Green color indicates a function which is not included in optimization but still gets optimized. The margins of error are estimated based on 10 trials and reflect a 95% confidence interval | 112 |
| 4.8 | Comparison of discrepancy in different correlation functions for 3D reconstructions using different correlation function combinations. Blue color indicates the function which is being optimized. Green color indicates a function which is not included in optimization but still gets optimized. The margins of error are based on 5 trials and represent a 95% confidence interval. | 119 |
| 4.9 | Comparison of simulated annealing based reconstruction times in the literature to the proposed method | 123 |

| | | |
|-----|--|-----|
| 5.1 | Applicability of different flow models in different flow regimes based on Knudsen number | 128 |
| 5.2 | Effect of tolerance on z direction effective bulk diffusivity for two-point correlation function based reconstructions. The margins of error are estimated based on 5 samples and reflect a 95% confidence interval | 137 |
| 5.3 | Effect of tolerance on effective bulk diffusivity for void phase lineal path function based reconstructions. The margins of error are estimated based on 5 samples and reflect a 95% confidence interval | 141 |
| 5.4 | Effect of tolerance on effective bulk diffusivity for void phase chord length function based reconstructions. The margins of error are estimated based on 5 samples and reflect a 95% confidence interval | 144 |
| 5.5 | Comparison of discrepancy in different correlation functions for 3D Ti foam reconstructions with different correlation functions. Blue color indicates the function which is being optimized. Green color indicates a function which is not included in optimization but still gets optimized. The margins of error are estimated based on 5 samples and reflect a 95% confidence interval . . . | 145 |
| 5.6 | Comparison of transport properties of reference and reconstructed Ti foam structure. The margins of error are estimated based on 5 samples and reflect a 95% confidence interval | 146 |
| 5.7 | Tortuosity estimations for reference and reconstructed images from pore scale simulations, and their comparison with Bruggeman estimation | 147 |

List of Figures

| | | |
|------|---|----|
| 1.1 | Effect of microstructure on performance of porous media applications | 2 |
| 1.2 | Summary of different microstructure characterization and reconstruction methods | 3 |
| 1.3 | Schematic for finding the optimum set of correlation functions for porous media transport property characterization | 11 |
| 2.1 | A schematic depicting different instances of same phase and inter-phase two-point correlation function estimation (White is phase 1 and gray is phase 2) | 29 |
| 2.2 | A schematic depicting instances of lineal path functions for different phases (White is phase 1 and gray is phase 2) | 33 |
| 2.3 | An illustration of chords in a two phase medium (White is void phase and gray is solid) | 34 |
| 2.4 | A schematic depicting instances of two-point cluster function estimation. Also shown is an example of $D_2^{(i)}(r)$ (White is phase 1 and gray is phase 2) | 36 |
| 2.5 | An illustration of normal and periodic sampling in a digital image | 42 |
| 2.6 | 3D image of packing of penetrable spheres (Red shows the solid spheres, and void phase is white) | 43 |
| 2.7 | Comparison of analytical and estimated two-point correlation function for penetrable sphere packing | 45 |
| 2.8 | Comparison of analytical and estimated lineal path function for penetrable sphere packing | 45 |
| 2.9 | Comparison of analytical and estimated chord length function for penetrable sphere packing | 47 |
| 2.10 | Comparison of analytical and average estimated chord length function for penetrable sphere packing. The estimation is averaged over 27 instances of random sphere packing | 47 |
| 2.11 | Comparison of analytical and estimated two-point cluster function for penetrable sphere packing | 48 |

| | | |
|------|--|----|
| 2.12 | An illustration of the cluster identification in a random media. The clusters are identified only for void phase (white). | 49 |
| 3.1 | A general schematic of simulated annealing based reconstruction process | 52 |
| 3.2 | An illustration of different phase neighbors in image and their selection priority | 61 |
| 3.3 | Schematic depicting the reference image synthesis for smaller scales | 64 |
| 3.4 | Schematic depicting the reconstructed image refinement and pixel freezing using method 1. DPN values are calculated using periodic boundaries on the images. Gray is only used for depiction and does not represent a new phase | 66 |
| 3.5 | An illustration of DPN sets stored using maps | 70 |
| 4.1 | Evolution of 2D SEM image of a PEFC catalyst layer from raw image to final binary image | 75 |
| 4.2 | Binary 2D image of ceramic obtained using X-ray microtomography (white is void, and black is solid) | 76 |
| 4.3 | Evolution a 2D slice of PEFC CL nano-CT image during different stages of image pre-processing | 77 |
| 4.4 | A 3D binary image of one of the nano-CT samples for PEFC CL (white is void, and black is solid) | 78 |
| 4.5 | Evolution a 2D slice of Ti foam micro-CT image during different stages of image pre-processing | 79 |
| 4.6 | 3D binary images of the Ti foam (white is void, and black is solid) | 80 |
| 4.7 | Correlation functions in x and y directions for the 2D PEFC CL image | 82 |
| 4.8 | Correlation functions in x and y directions for the 2D ceramic image | 84 |
| 4.9 | Correlation functions in x , y and z directions for the 3D PEFC CL images. Solid line shows the average, and shaded region shows the 95% margin of error. | 86 |
| 4.10 | Correlation functions in x , y and z directions for the 3D Ti foam images. Solid line shows the average, and shaded region shows the 95% margin of error. | 87 |
| 4.11 | An illustration of reference and reconstructed square grid pattern | 90 |
| 4.12 | Comparison of energy convergence for probability based and threshold based algorithms for a square grid geometry (solid line represents average and shaded region represents 95% confidence interval) | 91 |
| 4.13 | Reconstructions of 2D PEFC catalyst layer image using probability and threshold based method | 92 |
| 4.14 | Comparison of energy convergence for probability based and threshold based algorithms for a PEFC catalyst layer image (solid line represents average and shaded region represents 95% confidence interval. The margin is not visible, as the error margin is negligible) | 92 |

| | | |
|------|--|-----|
| 4.15 | Comparison of threshold energy change during reconstruction for static and dynamic methods | 94 |
| 4.16 | A coarse reconstruction of PEFC catalyst layer using random swapping, used as starting point with $E= 4.99 \times 10^{-3}$ | 96 |
| 4.17 | Reconstructed images of PEFC catalyst layer using different swapping methods | 97 |
| 4.18 | Comparison of energy convergence for random, interfacial and DPN based pixel swapping (Solid line represents average and shaded region represents 95% confidence interval. Error margin is not visible, as it is negligible) . . . | 98 |
| 4.19 | DPN based reconstructions of size 600^2 using maximum set probability $m = 0.4100$ | |
| 4.20 | DPN based reconstructions of size 600^2 using no maximum set probability . | 102 |
| 4.21 | PEFC CL reconstructions of size 200^2 using different DPN implementations and without any maximum set probability | 103 |
| 4.22 | Effect of image size on computation time for different correlation functions. The time is normalized by computation time of chord length function for a size of 100 pixels | 104 |
| 4.23 | Fraction of non frozen (permutating) pixels at each refinement level for multi-grid methods (Values show average over 10 trials. Margins of error are less than 1% and therefore not plotted) | 106 |
| 4.24 | Comparison of energy evolution (convergence) for different grid level | 107 |
| 4.25 | Reconstructed images at different scales using the multigrid method. Images are to scale | 109 |
| 4.26 | Comparison of correlation functions for reference and reconstructed 2D PEFC catalyst layer image. The reconstruction was performed using $S_2^{(v)}(r)$ only . | 114 |
| 4.27 | Comparison of correlation functions for reference and reconstructed 2D PEFC catalyst layer image. The reconstruction was performed using $S_2^{(v)}(r)$, $L^{(s)}(r)$ and $L^{(v)}(r)$ | 115 |
| 4.28 | 3D reconstructions of porous media using only $S_2^{(v)}(r)$ (Blue shows solid phase and red shows void phase) | 116 |
| 4.29 | Comparison of reference correlation functions between CL and ceramic . . . | 117 |
| 4.30 | 3D reconstructions using $S_2^{(v)}(r)$, $L^{(v)}(r)$ and $L^{(s)}(r)$. Blue shows solid phase and red shows void phase | 120 |
| 5.1 | Effect of image size on normalized structural and transport properties of Ti foam micro-CT image. All the properties are normalized by their value at size 200 pixels | 133 |
| 5.2 | The discretized void phase of different sub-samples of Ti foam 3D image . . | 135 |
| 5.3 | Oxygen profile for diffusion along z direction in the discretized domain . . . | 136 |

| | | |
|-----|--|-----|
| 5.4 | Concentration profile on the discretized geometries of two-point correlation function based reconstructions with different tolerances | 138 |
| 5.5 | Variation of error in effective diffusivity with change in energy tolerance for two-point correlation function based reconstructions | 139 |
| 5.6 | Concentration profiles on the discretized geometries of void phase lineal path function based reconstructions with different tolerances | 140 |
| 5.7 | Variation of error in effective diffusivity with change in energy tolerance for void phase lineal path function based reconstructions | 141 |
| 5.8 | Concentration profiles on the discretized geometries of void phase chord length function based reconstructions with different tolerances | 143 |
| 5.9 | Variation of error in effective diffusivity with change in energy tolerance for void phase chord length function based reconstructions | 144 |
| A.1 | An illustration of the cluster equivalence array | 174 |

Chapter 1

Introduction

1.1 Motivation

Heterogeneous materials are omnipresent in natural and artificial objects, such as porous media, biological and artificial membranes, and textiles [1]. Heterogeneous media are critical to several major engineering applications, such as polymer electrolyte fuel cells (PEFCs), coal gasification and bio-conversion process, geological storage of CO₂, and membrane water filtration. Some of these applications, such as PEFCs and CO₂ sequestration, are evolving technologies with a potential for becoming major future applications in sustainable energy. For example, PEFCs have emerged as promising energy conversion devices for power electronics, backup power units, domestic co-generation of electricity and hot water, and as a replacement for the internal combustion engine in automobiles [2]. Even though promising, these applications are still not efficient and economic enough for significant market presence [3]. Performance, cost, and durability of these applications needs to be improved before they can become consumer oriented applications.

The aforementioned engineering applications rely on physical processes, such as transport (e.g., mass, momentum, or energy) and chemical reactions inside the porous media for their functioning. For example, PEFCs depend on transport of gaseous reactants, and gaseous and liquid products through the void phase of porous electrodes, and transport of electrons through the solid phase of the electrodes [4, 5]. Utility of these engineering applications is dependent on the outcome of these physical processes, i.e., the physical processes must run in an efficient manner for optimized performance of the engineering application. Reduced reactant transport due to blockage of pores by ionomer electrolyte or liquid water results

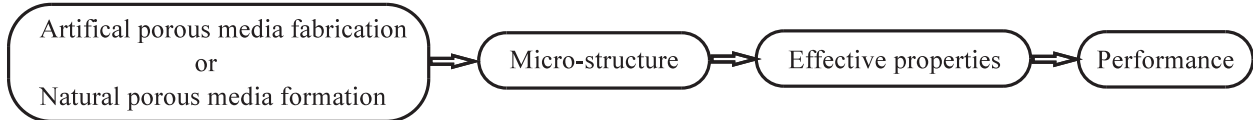


Figure 1.1 – Effect of microstructure on performance of porous media applications

in decreased fuel cell performance [6, 7]. The physical processes are strongly dependent on morphology of the porous media structure, e.g., mass transport is dependent on the porosity, tortuosity, pore connectivity, and pore size distribution, electron transport is dependent on the solid phase connectivity, and chemical reactions are dependent on the surface area [8–12]. A detailed understanding of the porous media is therefore necessary for understanding and improving these physical processes. Due to the importance of mass transport in our application of interest (PEFC), and in other applications, this study is focused on understanding and enhancing mass transport in porous media.

The effect of porous media structure on physical processes, such as mass transport is summarized in Figure 1.1. The easiest and most direct way to understand the performance is by knowing effective properties, such as permeability and diffusivity from experimental measurements. Several experimental measurements of transport properties have been presented in literature for PEMFCs [9, 13–17] as well as other porous media [18–23]. Even though these techniques are able to accurately determine the transport properties, they are not able to provide sufficient insight on how the microstructural parameters can affect them. Since the underlying factors are not well understood, any manipulation therefore becomes challenging. A better way to understand and optimize the transport processes is by increasing our understanding of the porous media microstructure. Microstructure parametrization can be utilized to find effective properties, and then using appropriate simulation tools to estimate performance. Using appropriate microstructure parametrization, the effect of manipulating the microstructure on effective properties can be analyzed, and used to optimize transport properties in the structure.

The motivation of this study is to develop a reliable and effective methodology to understand and characterize the microstructure of the porous media. The characterization methodology should be able to encompass all the features of porous media which are im-

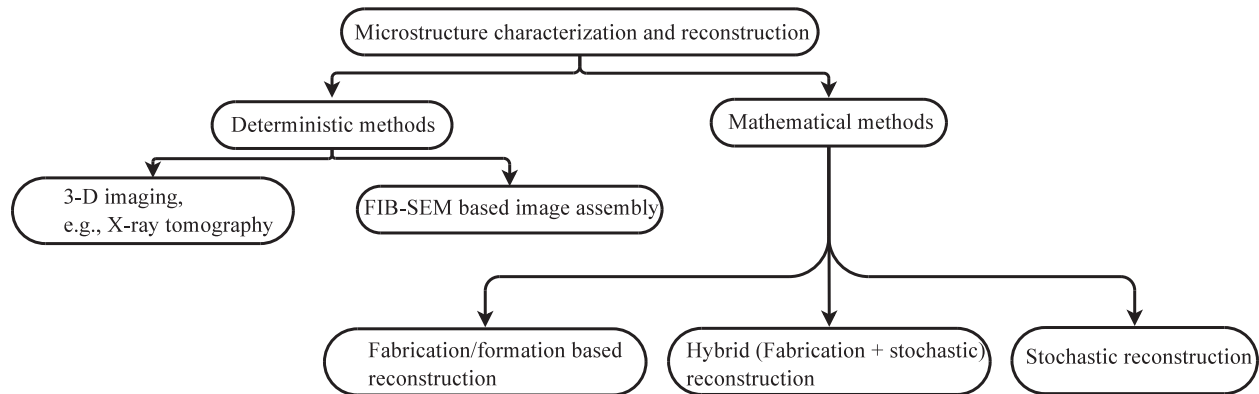


Figure 1.2 – Summary of different microstructure characterization and reconstruction methods

portant for mass transport. Furthermore, the characterization method should be able to parametrize the microstructure in order to facilitate structure manipulation and transport optimization. A methodology to generate microstructures with desired parametrization functions is also necessary for transport simulations. By performing transport simulations on the generated microstructures, the structural parameters can be correlated to the effective transport properties, which provides a way for designing porous media with desired transport performance.

1.2 Literature Review

An understanding of microstructure can be utilized to estimate effective properties, and ultimately to estimate material performance. For a complete understanding of the microstructure, i.e. phase distribution, connectivity, interfacial features and pore sizes, several methods can be used. Figure 1.2 shows different possible ways of characterizing and reconstructing the porous media structure. The following sections discuss these methodologies and their advantages and drawbacks.

1.2.1 Imaging Techniques

The heuristic method of deterministic characterization and reconstruction of porous media involves imaging techniques, such as X-ray computed tomography (CT) [24–31], or focused ion beam scanning electron microscopy (FIB-SEM) [32–39]. X-ray computed tomography (CT) has recently shown good prospects for analyzing geological and porous structures due to its ability to differentiate between different phases [29, 30, 40–46]. It is a non-invasive and

non-destructive imaging technique which can provide details of internal structure of porous media. The porous media is imaged from different directions, thereby generating projections of the structure in different planes. These projections are combined using a computational tomographic reconstruction algorithm to generate sequential 2D cross-sections of the porous media. The different cross sections can be combined together to obtain a 3-D realization of the imaged structure. Depending on the desired image resolution (minimum resolved feature size), either a micro-CT (pixel resolution 1–5 μm), or a nano-CT (pixel resolution 10–20 nm) can be used.

An alternative technique to the CT is the focused ion beam scanning electron microscopy. FIB-SEM has been extensively used for determination of microstructure of various materials in past decade [32–39, 47, 48]. FIB-SEM uses a focused ion beam for milling the porous media, while a scanning electron microscope takes images of newly exposed sections. The consecutive cross sections are then merged into a three-dimensional structure. FIB-SEM is a destructive technique, which can offer image resolutions of upto 2nm in each image slice, and around 10–20 nm in slicing direction.

The deterministic techniques provide a good way of obtaining insight of the internal structure of the porous media. Furthermore, they provide accurate and realistic reconstruction of the structure. These techniques however, are extremely time and cost intensive, and therefore, can not be used for performing extensive parametric studies [49]. These methods are also not well suited to capture the stochastic behavior exhibited by the majority of porous media structures, as they provide only a single realization of the material. Finally, these methods do not provide a way to mathematically parametrize the structure, and therefore, combined with the time and cost issues, make it difficult to characterize, manipulate, and optimize the structure.

1.2.2 Statistical Characterization

The technique of stochastic characterization relies on different statistical functions to characterize the porous media structure. The statistical correlation functions describe the probabilities of different phase encounters and other geometric features, and aim to encompass all the details of the porous media structure [50]. The statistical correlation functions can

be used to retrieve the microstructure via the process of stochastic reconstruction.

One of the most common correlation function used to characterize porous media is the phase volume fraction (e.g., porosity for void phase). Based on the volume fraction, effective medium approximations such as Bruggeman equation [51], or Maxwell-Garnett equation [52, 53] have been used to approximate the effective properties of a porous medium. These effective medium estimates however, are only useful for geometries like packed bed of spheres with distributed range of diameters, and are not valid for generic porous media structures [14, 54].

For better characterization of the porous media structure, a more detailed accounting of the phases is required. Brown Jr. [55] first defined n -point matrix functions for characterizing heterogeneous domains. The n -point functions were defined as the probability of finding n random points in a given phase. Frisch [56] extended this theory by considering the random porous media structure as a collection of stochastic processes. Consideration of the random porous media as a collection of stochastic processes is a critical step, which paved the way for statistical analysis of the random porous media structures. Frisch [56] also defined the generic n -point correlation functions for two-phase media and derived their unique properties. Torquato and Stell [50, 57] expanded on the previous work [56] by explaining the geometric interpretations of the n -point correlation functions, and estimating these functions for a system of impenetrable and penetrable spheres. Lower order n -point correlation functions, such as two-point correlation functions and three-point correlation functions were also explicitly computed for the system of spheres. Smith and Torquato [58] computed two-point correlation functions for a system of spheres using computer simulation and found the results in agreement with theoretical estimates. Berryman [59], and Coker and Torquato [60] presented computational methodologies to estimate two-point and three-point correlation functions from digitized images of random media. These lower order functions, especially the two-point correlation function have since been used extensively for characterization and reconstruction of random media structures [61–70].

One of the most common correlation functions, the two-point correlation function is defined as the probability of finding two points separated by a given distance in the same

phase [63]. The two-point correlation function has been extensively used, and provides a much better characterization compared to volume fractions alone; however, it has several limitations for detailed characterization of porous media structure. The two-point correlation function does not contain any long range information [57] and is therefore not able to characterize long range features such as domain wide phase connectivity [71]. Using higher order n -point correlation function such as three-point correlation function or four-point correlation function comes at a considerably higher computational complexity, but with little improvement in long range characterization [72]. Lu and Torquato [73] proposed a new correlation function named lineal path function, which is the probability of finding two points and the line connecting them in a given phase. Later, Torquato and Lu [74] proposed another correlation function named chord length function, which is the probability of finding a chord (line between phase boundaries) of certain length in a given phase. Coker and Torquato [60] presented a computational methodology to compute lineal path function and chord length function for a digitized image of porous medium. Manwart et al. [75] proposed a pore size distribution function, which is the probability that a randomly chosen point in the pore space lies at a given distance from the nearest surface. Unlike the chord length function or lineal path function, which only trace connectivity in one direction, the pore size distribution function estimates the connectivity in all directions at once. A combination of lineal path function, chord length function, and pore size distribution function with two-point correlation function has been used for reconstructing random media structures [63, 71, 75–78]. The studies show that adding either lineal path function, or chord length function, or pore size distribution function to the two-point correlation function improves the overall characterization of the porous media [66, 71, 75].

Torquato et al. [79] proposed a two-point cluster function, which is the probability of finding two points in the same phase and in the same cluster. The cluster is defined as the volume of porous media which is connected and percolating. The two-point cluster function can be thought as a two-point correlation function with additional restrictions. It was shown that the two-point cluster function provides a better characterization of the porous media compared to the two-point correlation function. In a later study, Jiao et al. [72] showed that the two-point cluster function is able to reconstruct porous media with better long range connectivity than all other correlation functions aforementioned. With all its benefits

however, the two-point cluster function is difficult to implement in a computer program for reconstruction. While computation of all the other correlation functions requires a simple scan of the digital image, computation of two-point cluster function requires identification of different clusters [72]. This process is extremely time consuming, and becomes extremely cumbersome when the cluster identification has to be repeated millions of times for reconstruction. Due to this very reason, only a few studies actively employ two-point cluster functions for reconstruction purposes.

Apart from the volume phase based correlation functions, interface correlation functions are also defined. Torquato [80] defined the surface-surface correlation function, which is the probability of finding interfaces at both ends of a line of given length. Even though combining surface correlation function with other functions can result in improved characterization, the chord length function already contains the information about interface separation. Either chord length function, or surface-surface function should therefore provide the desired improvement in characterization.

Recently, a new class of statistical descriptors known as multiple point statistics have been used for characterization and reconstruction of porous media structures [81–85]. The multiple point statistics are obtained by sampling the image with several templates. A template is a set of query points placed at predefined intervals. While scanning the image with the templates, occurrence of different patterns is recorded. All the occurrences are finally normalized to obtain a probability distribution. The probability distribution characterizes the structure as a collection of different pattern occurrences with certain probabilities [83]. The reconstructions based on multiple-point statistics have shown to improve long range connectivity and provide better characterization. This descriptor however, suffers from the same problem as of two-point cluster function. For obtaining a detailed characterization, which can reproduce long range features, the templates need to be large and detailed. This increases the computational complexity considerably, and makes this method slower compared to the one with normal correlation functions [83].

Among all the characterization methods, the use of correlation functions has several advantages. First, most of the correlation functions have a geometric meaning, and are there-

fore able to characterize some particular aspect of porous media structure. For example, the two-point correlation function is related to the interface area [63], the lineal path and chord length functions characterize the phase cluster sizes, and the cluster function characterizes long range phase connectivity. Second, using correlation functions enables the use of as many statistical descriptors as needed. For example, if only interface area is of importance, then only two-point correlation function needs to be used, while if other properties also need characterization, more correlation functions can be added sequentially in order to keep computational costs in check. Due to their relationship with structural properties, volume fraction, two-point correlation function, lineal path function, and chord length function are used in this work. The two-point cluster function, and multi-point statistics are not used because of the computational burden associated with them.

In spite of all the advantages of the statistical correlation functions for characterization and reconstruction, most of the literature on stochastic methods consists of theoretical exercises on reconstruction methods [61, 63, 65, 66, 71, 72, 76, 78, 83, 83, 86–92]. The variants mostly include ways of improving the structural accuracy (in terms of correlation functions), and improving the computational speed. Very few studies however, have attempted to study the physical properties of the reconstructions and compare them to the reference structure [75, 93–100]. The ability of the correlation functions to characterize physical properties has therefore not been well understood. To optimally utilize the correlation functions for accurate characterization of porous media structure, it is necessary to understand the ability of each correlation function for characterizing the physical properties.

1.2.3 Fabrication based Reconstruction

To understand the physical properties of porous media, its porous structure must be digitally reconstructed for use in simulations. An ideal way to obtain the porous media microstructure is by simulating its formation process. This provides a way to account for each step in the fabrication/formation process, which will result in a realistic structure. The fabrication/formation parameters will provide a way to manipulate the structure, and in turn for optimizing the structure for desired transport properties. For simulating fabrication process of artificial porous media, such as PEFC electrodes, an agglomerate growth model is often used. In PEFC electrode reconstructions for example, random seeds are distributed in

the domain and the carbon particles grow around them in a stochastic manner [101–103]. Platinum and Nafion[®] are deposited on the grown structure using heuristic rules. Volume fractions of different phases are used as optimization variables. These methods even though promising, lack the inclusion of porous media formation physics, e.g., colloidal interactions and aggregation mechanics, and rely on heuristic rules to distribute each phase. Furthermore, the spherical agglomerates used are an idealization of what is observed in reality [104].

Latest methods use the information of porous structure features combined with statistical correlation functions for reconstruction. For example, in PEFCs, the structure is assumed to consist of ideal building blocks such as spherical agglomerates, and uniform fibres [37, 105–110]. The distribution of the building blocks is defined by some statistical function, which becomes the characterizing parameter of the porous media. The assumption of a predefined building block makes the reconstruction easier, as there are less variables to model (basic blocks of the porous media are already assumed, only the distribution needs to be adjusted). These ideal building blocks however do not usually accurately represent the real porous media structure. In these studies, only a limited number of statistical functions have been used for reconstruction, which limits its accuracy. Most of the methods use one-point correlation function (porosity), or autocorrelation function for characterizing the distribution, neither of which contains information on phase connectivity in the porous medium. Using this method on natural porous media, such as carbonates, coal, and sandstones is extremely challenging because of the lack of well defined microstructural features, which can be used as a building block.

The prospects of formation/fabrication based simulations may be promising; however, it is extremely difficult to account for all the processes of fabrication/formation. For example, the PEFC catalyst layers are made by applying an ink composed of platinum supported on carbon, Nafion[®], and solvents on a polymer electrolyte membrane [111]. The final porous structure of the catalyst layer depends on several parameters including: colloidal interactions between carbon particles, Nafion[®], and solvents; drying temperature; application technique; and ink-substrate interactions [112]. The physics for several of these processes are either not well known, or are extremely complicated to model accurately, making the prediction of final porous structure a daunting task. For natural porous media such as sandstone

and carbonates, modeling is even more difficult due to the involvement of several geological processes over the time scale of millions of years.

1.2.4 Stochastic Reconstruction

As discussed in section 1.2.2, statistical correlation functions provide an ideal way of characterizing random porous media. The accuracy and effectiveness of statistical characterization however, depends on finding a set of correlation functions, which can characterize physical and transport properties of the porous media. To understand the ability of correlation functions to characterize physical properties (transport properties for this work), one must first obtain porous media structures with the appropriate correlation functions. Figure 1.3 shows a schematic for finding the optimum set of correlation functions to characterize a transport property of the porous media. A reference structure is needed for comparison and benchmarking of the different correlation functions, as well as for possible experimental testing. Usually a physical image is used as a reference structure, from which its transport properties and statistical correlation functions are obtained. To see the ability of a single or a set of correlation functions to characterize a particular transport property, virtual structures need to be generated, which have the same correlation functions. Transport properties of these virtual structures are then obtained and compared against the simulation results of the reference structure. If a particular correlation function, or a combination thereof can characterize a particular property, then that property should be similar in reference and reconstructed structure.

It is evident from the aforementioned discussion, that a reconstruction method which can generate virtual structures with desired correlation function functions is a necessity for evaluating the effectiveness of different correlation functions. A good reconstruction method should be able to provide a virtual structure with desired correlation functions in a practical amount of time. Several reconstruction methods are available in literature; however, since this work explores correlation functions for characterization, only the reconstruction methods which use correlation functions have been explored.

The initial approach towards stochastic reconstruction involved use of filtered Gaussian fields [61, 62, 86, 87, 89, 93, 113–115]. One of the approaches proposed by Joshi [86] in-

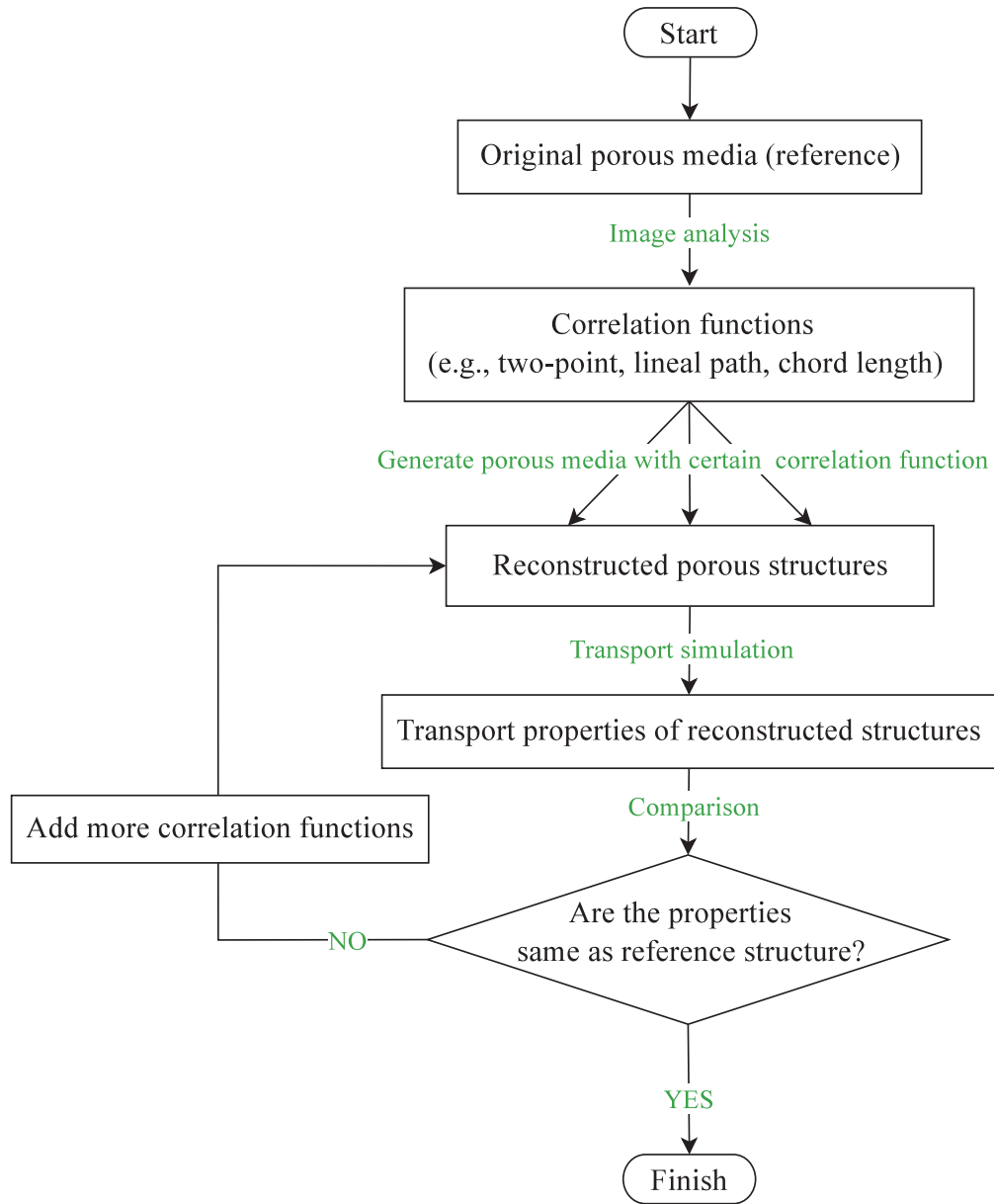


Figure 1.3 – Schematic for finding the optimum set of correlation functions for porous media transport property characterization

volves the use of two filters: one linear, and other non-linear. A random and continuous Gaussian field is passed through a linear filter, which results in a correlated Gaussian field. This correlated Gaussian field is then passed through a non-linear filter to obtain a discrete field representing phases of the porous media. The non-linear filter also ensures that the statistical correlation functions of final field are as desired. Overall, the problem reduces into solving a system of non-linear equations in order to find coefficients of the linear filter [62, 63]. This approach was enhanced by Quiblier [61] for generating 3D reconstructions, and by Adler et al. [62] for using periodic boundary conditions. Another approach proposed by Cahn [113] uses an improved linear filter, and is able to reconstruct structures such as glass and membranes. Ioannidis et al. [116] proposed use of discrete Fourier transform (DFT), instead of linear filters for obtaining the correlated set. Even though the method is computationally superior to the linear filter, it has high resident memory requirements [117], and therefore could not be used for large 3D images. Ioannidis et al. [116] proposed use of hybrid method, combining both DFT and linear filters to avoid the memory issues, while obtaining the speed advantages. The DFT method is used to generate correlated data sets for each 2D slice, then the z-direction correlations are imposed by the linear filter.

Gaussian random field based method reduces to a set of non-linear equations, which can be easily solved with minimal computational expense on modern computers. This method however, can only use correlation functions which can be analytically expressed and incorporated into the filtering process. Unfortunately, among the several correlation functions discussed earlier, only volume fractions and two-point correlation function satisfy these criteria. Due to the limited amount of information contained in the two-point correlation function, this method is not very successful in most types of porous media (e.g., multiphase, anisotropic and particulate media) [115] .

Recently, signal processing methods involving fast Fourier transforms (FFT) and phase separation algorithms have also been used to reconstruct porous media structures [67, 118, 119]. In these methods, a fast Fourier transform (FFT) is used to compute the autocorrelation function (normalized two-point correlation function). The reconstruction is either performed using Gaussian random fields, simulated annealing, or phase recovery methods. The phase recovery method is an iterative process where a trial structure is consecutively

modified until it has a desired autocorrelation function. FFT based methods have the same disadvantage as of the Gaussian random field methods, since the FFT transforms can only be used with autocorrelation function.

Ouenes et al. [88] first proposed a new method of simulated annealing to reconstruct porous media structures, which was first used by Rintoul and Torquato [90] to reconstruct dispersion of particles. The simulated annealing technique is based on the physical phenomena of annealing, in which a high energy system (a random structure) is slowly cooled down to a low energy state (structured media) through a well defined temperature schedule [95]. A random image is used as the starting structure. The structure is perturbed by exchanging (swapping) pixels from two different phases, and the success or failure of the perturbation is judged by analyzing system energy. The system energy is defined as the L_2 -norm of the difference between the correlation function(s) of reference image and current image. In this way, the problem of reconstruction becomes an energy minimization problem, where the aim is to obtain a structure with zero energy, or as close to zero as practically possible. The structure evolution is guided in such a way that, primarily energy decreasing perturbations are accepted over energy increasing perturbations. While energy decreasing moves are always accepted for energy minimization, energy increasing moves are only accepted with a certain probability. Acceptance of energy increasing moves is done in order to avoid the entrapment of the minimization process in a local minima [63]. The probability of selecting energy increasing moves is controlled by the system temperature. The temperature is decreased slowly throughout the reconstruction procedure in such a way, that at the beginning, almost half the energy increasing moves are allowed, and by the end of reconstruction, almost none of the energy increasing moves are allowed. An ideal temperature cooling schedule allows the reconstruction to be performed with minimum steps, while not getting trapped in a local minima.

The overall mechanism of simulated annealing is mathematically easy to implement. The crucial advantage of the simulated annealing method is in its ability to include as many statistical correlation functions as practically possible. L_2 -norms of differences of all correlation functions can be combined together to obtain overall optimization of multiple correlation functions. Weights can also be added to increase the importance of one corre-

lation function over another. This facilitates the creation of structures with multiple statistical characteristics, which may be desired to emulate different physical properties. Due to these advantages, this technique has been extensively used recently [1, 64–66, 71, 75–78, 90, 91, 96, 98, 99, 102, 119–126] for reconstructing porous media structures as well particulate suspensions. Two-dimensional as well as three dimensional reconstructions of Fontainebleau stone were presented with great resemblance to actual porous media. Manwart et al. [75] used the same technique to reconstruct Fontainebleau and Berea sandstones with considerable accuracy. Talukdar et al. [64, 76], Talukdar and Torsaeter [77], Talukdar et al. [96, 121] used the simulated annealing method to reconstruct pore networks in chalk and in particulate media. Pant et al. [66] used the simulated annealing method to reconstruct 2D images of PEFC catalyst layers using multiple correlation functions.

Even though the simulated annealing method is easy to implement, and has immense potential for characterization and reconstruction of porous media structures, most of the studies have not focused on the applications of the method. Furthermore, there are several shortcomings in the conventional simulated annealing which prevent it from being extensively used in practical porous media studies. The various issues and shortcomings of conventional simulated annealing method are discussed as follows.

One of the major issues with conventional simulated annealing method is the excessive computational time and presence of noise (segregated unphysical pixels) in the final reconstruction [98]. The most common variant of the simulated annealing algorithm discussed in the literature is based on random pixel swapping, i.e., the pixels to be swapped at each step are selected at random. The random selection does not take into account the current state of the structure, and therefore a particular swap has an equal probability of improving or deteriorating the structure. During the later stages of reconstruction, most of the energy increasing moves are rejected, causing significant number of rejected swaps, and thereby significantly increasing the reconstruction time. The random selection also results in several segregated pixels being left in the final structure, as the probability of getting these particular pixels picked is extremely low. To overcome this problem, biased pixel selection algorithms such as interfacial pixel swapping [91] and different phase neighbor (DPN) based swapping [78, 98] have recently been proposed. The DPN method [98] gives priority to pixels

which have the higher number of different phase neighbors, thereby quickly eliminating stray pixels. The interfacial pixel selection method swaps pixels which are at an interface, i.e., all pixels with non zero different phase neighbors have equal probability of getting picked. The studies show that the DPN based method is able to obtain a reconstruction with minimum number of swaps [66, 98].

The DPN based method, even though promising, has not been studied in detail. Using two point correlation function with DPN based pixel swapping, Tang et al. [98] have shown that the DPN method outperforms all other pixel selection methods in terms of speed and accuracy of the final reconstruction. However, the effect of the biased pixel selection on the structure has not been analyzed. Furthermore, the application of DPN with multiple correlation functions has not been explored. Given that the ability to use multiple correlation functions for enhanced accuracy is a crucial aspect of simulated annealing, it is imperative that the use of DPN based technique with multiple correlation functions be assessed. The DPN computation method also needs to be computationally improved. Even though the DPN based method reduces the number of swaps required to achieve a target energy, each step is more time consuming. One reason for the additional time is due to the calculations of probabilities for different DPN numbers; however, the majority of time is consumed by updating the DPN information after each pixel swap. Computing DPN information for the whole image after each swap can exacerbate the computational cost, especially for large image sizes. Faster updating algorithms therefore need to be developed for DPN information management.

Another issue with the conventional simulated annealing method has been the lack of studies using multiple correlation functions. Even with the potential of using multiple correlation functions, only a few articles in the literature use multiple correlation functions [63, 66, 71, 75, 76, 99, 125]. As discussed in the last section, several correlation functions may be needed to reproduce pore sizes, surface area, and pore connectivity of the porous media. Several studies have shown that addition of multiple correlation functions is critical for better characterization of porous media structure [63, 66, 71, 75]. A few studies on transport properties of reconstructions by Yeong and Torquato [95] and Capek et al. [99] show that inclusion of multiple correlation function is needed for reconstructions with transport

properties similar to reference structures. The major impediment in using multiple correlation functions is the increase in computational cost with each correlation function. Increase in correlation functions increases reconstruction time due to two reasons: 1) additional time required to compute and update additional correlation functions, and 2) the optimization objective becomes more complex with increased correlation functions [125].

Due to the aforementioned reasons, reconstructing large images is extremely challenging with the conventional simulated annealing method. Most of the reconstruction studies therefore have focused on 2D images [63, 65, 76], which are less computationally exhaustive for reconstruction. Most of the 3D reconstructions with conventional methods have been of sizes between 100^3 to 150^3 voxels. Capek et al. [71] performed a 3D reconstruction of size 320^3 voxels, which took around 160 – 400 hours for reconstruction.

The conventional random swapping, and use of multiple correlation functions results in computationally expensive reconstruction process; however, even with better algorithms, such as surface, or DPN swapping, reconstructing large images is challenging. Two additional issues in reconstructing large images are as follows:

1. *High reconstruction time:* In simulated annealing method, the correlation functions need to be recomputed after each swap, as the structure of porous media changes, thereby changing the correlation functions. The time to compute the updated correlation functions after swap is directly dependent on the image size, i.e., the larger the image size, the more time it takes to compute the function. This causes the reconstruction method to become impractical for large image sizes, as the method can take several weeks to obtain a single structure.
2. *Reduced long range connectivity:* Due to random swapping, final reconstructed images with simulated annealing have many isolated pixels left. These stray pixels contribute to dead volume (non-connectivity) and reduce the long range connectivity of the reconstructed image compared to the reference image [98]. The inability to reproduce long range connectivity is inherent to the simulated annealing technique, and it is exacerbated for large image sizes, even with newer pixel selection methods. The simulated annealing method works by performing multiple pixel swaps on the initial structure.

Each pixel swap can be thought of as a local perturbation or a local interaction on the structure, as it will mostly change the structural features in its immediate neighborhood. Apart from the local features, most of the porous media exhibit some kind of large scale behavior, e.g., percolating volume, which is essential to the performance of the porous media. Being a Markov chain process, each step of the simulated annealing process is only dependent on previous step. It is therefore difficult to reconstruct large-scale features by accumulating multiple continuous local interactions [127].

To mitigate the issues related to image size and long range feature reproduction, multigrid hierarchical methods have recently been presented [49, 127–129]. In the multigrid hierarchical methods, the reconstructions are started at small scale (coarse scales). Once a coarse scale reconstruction is obtained, it is successively refined and annealed to obtain large scale refined structures. Reconstruction at each scale is treated as an independent simulated annealing problem, where a reference image of corresponding scale is used. The reference image for coarse scales is obtained by coarsening and thresholding the refined reference image. Initial attempts by Campaigne et al. [128] and Alexander et al. [127] used a simple hierarchical annealing, where the reconstruction is started at a coarse scale. Then, after achieving convergence at the coarse scale, the image is refined and used as the initial structure for simulated annealing at the next scale. Even though this method is faster than conventional single grid methods, it is not able to improve the reconstruction speed significantly for two reasons:

1. Since each step is treated as an independent simulated annealing problem, the structural features generated at the coarse scale can be completely undone at the beginning of next scale simulated annealing, when the temperature is favorable for energy increasing moves. Precise control of temperature is required to reduce the structural deterioration at refined scales.
2. The random swapping procedure in simulated annealing still permutes among all the pixels at each image scale, i.e., all the pixels of the image at refined scales are available for swapping. The computational cost is therefore similar to the conventional single grid method.

The limitations of the simple multigrid methods were resolved by the frozen state meth-

ods presented by Campaigne and Fieguth [49] and Chen et al. [129]. The overall process of multigrid reconstruction remains the same as in simple hierarchy; however, a concept of freezing is introduced to avoid the issues related to simple hierarchy. While generating reference images for coarser scales, a gray phase is introduced to indicate a pixel whose phase is not certain at the given scale. The reconstruction is started at coarsest scale with all three phases (black, white, and gray), and successively refined. At each refinement step, the pixels with black or white color have a certainty of placement. These pixels are therefore frozen for subsequent refinement levels. Some of the gray pixels are converted back to black and white pixels at each refinement step, in order to keep volume fractions consistent with the reference image at the corresponding scale. These pixels are not frozen, and are moved during the simulated annealing procedure. At the finest scale, no gray pixel remain, and all the phases of image are recovered. This method mitigates both problems associated with the simple hierarchy. Since certain pixels at the coarse scale are frozen at refined scales, the structure can not be destroyed at later refinements. Also, since most of the pixels are frozen at refined scales, the number of possible pixel permutations is significantly reduced, thereby reducing the reconstruction time. The overall process can be thought of as a two step process: 1) generating a skeleton at coarse scales, which will dominate the large scale structure in the final reconstruction, and 2) adding local fine-resolution features at refined scales. These method has shown significant speed advantages compared to conventional methods [49].

Even though the frozen state hierarchical simulated annealing method provides many advantages, only a few studies in the literature have explored it. Campaigne and Fieguth [49] used the grayscale hierarchical simulated annealing method with neighborhood matching instead of correlation function . It is therefore difficult to separate the reported time advantage between the use of hierarchical simulated annealing method, and the use of neighborhood matching. To the best of author’s knowledge, only Chen et al. [129] have used hierarchical annealing for 3D image reconstruction with correlation function; however, they did not present any comparison with other methods in literature. Although the multigrid method shows high potential for improving the simulated annealing methods, several improvements need to be made. The gray pixel based hierarchical simulated annealing is difficult to implement due to the presence of an extra phase. The presence of an extra phase requires additional correlation functions to be introduced in the optimization function, making the

process more complex. DPN information could possibly be used instead of the gray pixels for freezing; however, the use of multigrid methods with DPN has not been explored in literature. The DPN based method may also be able to further improve the accuracy of the hierarchical simulated annealing method. A frozen state multigrid hierarchical annealing method using DPN will be explored in this work.

Most of the reconstruction studies in the literature have focused on improving reconstruction speed, accuracy, or the overall optimization of the reconstructed structure (in terms of correlation functions). It should be noted that, in general, the objective of a reconstruction procedure is not necessarily to find the set of correlation functions that give the quickest turn-around time, or best matching of correlation functions. Instead, it is to develop a reconstruction for the most complex class of microstructures that can provide a good estimate of the physical properties of interest, such as effective diffusivity or Knudsen diffusivity, with a minimum set of statistical descriptors, in a manageable amount of computational time.

Only a few studies in the literature have attempted to study the physical properties of the reconstructed structures in order to assess the ability of the reconstructions to estimate physical properties [75, 93–100]. The earliest attempts were made by comparing the Gaussian filters and variogram based reconstructions to reference porous structures [93, 94]. The Gaussian filter based reconstructions were found to underpredict solid and void phase properties compared to reference structures and experimental values. Since the Gaussian filter based methods can only use two-point correlation functions, it is not possible to improve the reconstruction methodology. Simulated annealing based reconstructions can include multiple correlation functions, and therefore have a better chance at characterizing the porous media. Effect of including multiple correlation functions on the transport properties have been studied using random walk simulation [75, 95, 99, 100]. It is found that inclusion of a lineal path function, or a pore size function improves the predictions for mean survival time, effective diffusion coefficient, and permeability. Politis et al. [97] showed that, a hybrid reconstruction method combining simulated annealing with fabrication process parameters, results in reconstructions that can better predict transport properties. Recently, Tang et al. [98] showed that simulated annealing with a DPN based pixel swapping method results in reconstructions with better transport properties than reconstructions performed using ran-

dom pixel swapping.

Table 1.1 shows a comprehensive list of all the literature that presents analysis of physical properties on the reconstructed structures. Most of the literature has either used empirical relations like Kozeny–Carman formula, or have used simple random walk simulations. Even though these methods provide an easy way of understanding the transport in porous media, they do not fully account for the complex nature of the porous media and its effects on the physical processes. Some earlier studies have used techniques of finite difference method [93], and Lattice Boltzmann method [94]; however, due to computational limitations the domain size was kept at a minimum, thereby compromising accuracy of the simulations. To the best of author’s knowledge, only Capek et al. [99] have recently used finite difference method to simulate Stokes flow and obtain permeability in a reconstructed sample. So far no studies have used finite element method to simulate the mass transport in reconstructed geometries. With the advancement in computing resources and simulation tools, large scale simulations can be performed in detail, and accurate transport properties can be obtained. These simulations can be used to study the effect of different correlation functions on transport properties and to find out the relationship between correlation functions and transport properties.

Due to the lack of understanding between correlation functions and transport properties, the impact of correlation functions on structures is not well understood. The effect of changing a particular correlation function in the reconstructed structure on its transport properties has not been studied. Since the impact of correlation functions is not well understood, the correlations functions can not be used as design parameters for obtaining structures with desired properties. Yeong and Torquato [63] presented some preliminary work on reconstructing structures with hypothetical correlation functions; however, no analysis of physical properties was presented. To the best of author’s knowledge, there are no studies in literature using correlation functions as design parameters for fabricating porous materials with desired properties.

Stochastic reconstruction using simulated annealing is a versatile and accurate methodology for generating virtual structures with desired statistical properties. This technique has

Table 1.1 – A summary of reconstruction literature related to study of physical properties of reconstructions. The correlation functions described are: ϕ - one-point correlation function, $S_2^{(v)}(r)$ -void phase two-point correlation function, $L^{(v)}(r)$ - void phase lineal path function, $L^{(s)}(r)$ - solid phase lineal path function, $P^{(v)}(r)$ - void phase pore size function. The transport properties described are: K_0 - compressibility modulus, E - Young’s modulus, κ - permeability, τ - mean survival time, \bar{r}_p - mean pore size, P_c - capillary pressure, D - effective diffusion coefficient, D_K - Knudsen diffusion coefficient.

| Ref. | Reconstruction details | Transport properties simulated | Simulation method | Remarks |
|-------|--|--------------------------------|---|--|
| [93] | Gaussian, $S_2^{(v)}(r), \phi$ | K_0, E | Finite difference method | Reconstructions overpredict, poor agreement with experiments |
| [94] | SA, variogram | κ | Lattice Boltzmann method | Reconstructions underpredict, poor agreement |
| [95] | SA, $S_2^{(v)}(r), (S_2^{(v)}(r) + L^{(v)}(r))$ | τ, κ | Random walk for τ , empirical for κ | Reconstructions underpredict, combination of $S_2^{(v)}(r) + L^{(v)}(r)$ improves properties |
| [75] | SA, $(S_2^{(v)}(r) + P^{(v)}(r)), (S_2^{(v)}(r) + L^{(v)}(r))$ | τ, \bar{r}_p | Random walk | τ underpredicted, reasonable agreement |
| [96] | SA, SA+Gaussian, $S_2^{(v)}(r)$ | P_c, κ | Pore network model with fractal decoration | Reconstructions overpredict, reasonable agreement |
| [97] | Process+SA, $S_2^{(v)}(r)$ | κ | Finite difference method | Reconstructions underpredict, hybrid method shows better results (within 5-6% of reference) than pure SA |
| [98] | SA with DPN swapping, $S_2^{(v)}(r)$ | κ | Kozeny–Carman formula | Reconstructions underpredict, DPN based reconstructions better than random |
| [99] | SA, $(S_2^{(v)}(r) + L^{(v)}(r) + L^{(s)}(r))$ | κ, D, D_K | Random walk for D and D_K , finite difference method for κ | Combination of the correlation functions increases transport properties, no comparison with reference |
| [100] | SA, $(S_2^{(v)}(r) + L^{(v)}(r) + L^{(s)}(r))$ | κ | Random walk | Reconstructions overpredict but show reasonable match with reference |

immense potential for accurate characterization and reconstruction of porous media structures, which can be used for detailed studies of porous media physical processes. For the technique to become reliable and practically useful, several improvements in the technique are necessary. Two areas where further research is critical are: 1) improvements of accuracy and computational speed in stochastic reconstruction method, and 2) understanding the effect of correlation functions on transport properties. Based on these objectives, and by analyzing the information in the available literature, the following topics were identified for this work:

1. Development and implementation of an improved pixel selection algorithm and detailed comparison with other methods.
2. Development and implementation of an easy to implement multigrid hierarchical simulated annealing method.
3. Use of multiple correlation functions for reconstruction, and study the effect of correlation functions on transport properties.

1.3 Contributions of This Work

The main contributions of this work are in the area of developing accurate and efficient stochastic reconstruction methodologies, and using them for characterizing porous media transport properties. This work contributes to the field by:

- Developing a simple and efficient multigrid hierarchical annealing method based on different phase neighbors (DPN), which can improve reconstruction time and accuracy, and that can use multiple correlation functions.
- Studying the sensitivity of molecular diffusion towards the correlation functions used during reconstructions

In the area of stochastic characterization and design, this work presents one of the first attempts at trying to characterize and design the transport properties of porous media by its statistical correlation functions. As such, this work presents for the first time in literature:

- Use of DPN based pixel swapping method for reconstructing porous media with multiple correlation functions

- A DPN based frozen state multigrid hierarchical simulated annealing method which does not require extra gray phases
- Characterization of porous media transport properties by its correlation functions

Characterization of the porous material by its statistical correlation functions is, in the author's opinion, the key to design porous media with desired physical properties by manipulating its statistical descriptors.

1.4 Structure of the Thesis

This thesis is organized in six chapters. The first chapter presents the motivation for this work, and a literature review of earlier work on porous media characterization; stochastic analysis of random media; stochastic reconstruction methods and variants; and physical characterization of stochastic reconstructions. Chapter 2 presents the stochastic characterization approach for random porous media, definitions of different correlation functions, and the computational methods to compute them. Chapter 3 presents the simulated annealing based reconstruction methodology, with detailed descriptions of each of its aspects and their variants. Chapter 4 presents the results of stochastic analysis and reconstruction of several porous media structures. This chapter also studies the effect of different reconstruction parameters on the accuracy and speed of the reconstructions. Chapter 5 presents a preliminary study of mass transport in the porous media structures. Effect of correlation function on transport properties is determined. Finally, chapter 6 summarizes the contributions of this work and proposes possible applications and extensions of this work.

Chapter 2

Theory of Stochastic Analysis[†]

This chapter describes the different stochastic correlation functions used in this study. As discussed in Chapter 1, this work uses two-point correlation function, lineal path function, chord length function, and two-point cluster function for the stochastic analysis and reconstruction studies. Section 2.1 presents the idea of considering a porous media as an outcome of a stochastic process, thereby enabling the use of stochastic tools for its analysis. Section 2.2 provides the theoretical definitions of the aforementioned correlation functions, with their unique properties and their relevance in characterizing physical properties of the porous media. Section 2.3 discusses the methods of computing the correlation functions from digital images of the porous media. The detailed algorithms corresponding to this section are presented in Appendix A. Finally, section 2.4 presents some validation studies to test the accuracies of the computational algorithms which have been developed and implemented for estimating the correlation functions.

2.1 Porous Media as a Stochastic Process

Random media presents itself in several instances, e.g., geological rock formations, biological membranes, ceramics, suspensions, and artificial porous media. All of these random media can be hypothesized as a collection of multiple geometric points, which can be continuous or discrete [56]. Furthermore, each point can be thought of as an outcome of a stochastic process, which assigns a material to the point. For example, in a two phase porous media, the stochastic process may assign solid or void phase to a point. In this way, the entire

[†]A part of this chapter has been published. L. M. Pant, S. K. Mitra, and M. Secanell, *Physical Review E*. 90(2):023306, 2014

random media becomes a particular outcome of multiple stochastic processes. A collection of all possible realizations will contain all the possible random media structures in the given physical domain. This collection is also known as an ensemble [130]. Thinking of a random media as an outcome of stochastic process allows us to use probability theories combined with geometric descriptors for characterization of the stochastic process, and in turn of the random media.

2.1.1 Indicator Functions

The indicator function is used to represent the outcome of the stochastic process at each geometric point in a particular realization. Assume that Ω is the sample space of the stochastic process and ω is a particular realization. Furthermore, assume that $\omega \in \Omega$ is a particular realization occupying the volumetric space \mathcal{V} in a space of dimension $d \in \{1, 2, 3\}$, i.e., $\mathcal{V} \in \mathbb{R}^d$. The location of a geometric point in this realization is defined as $\mathbf{r} \in \mathcal{V}$. A random media can have multiple phases $i = 1, 2, 3, \dots, n$. Assume that each phase i occupies a volume subset \mathcal{V}_i of the total volume \mathcal{V} . The existence of the phase i at any geometric location \mathbf{r} in the random media realization ω is given by an indicator function, which can be given as follows [130] :

$$I^{(i)}(\mathbf{r}; \omega) = \begin{cases} 1, & \text{if } \mathbf{r} \in \mathcal{V}_i(\omega), \\ 0, & \text{otherwise.} \end{cases} \quad (2.1)$$

Summing Eq. (2.1) over all phases, the following equation is obtained:

$$\sum_i I^{(i)}(\mathbf{r}; \omega) = 1. \quad (2.2)$$

Equation (2.2) simply states that each geometric point in any realization space $\mathcal{V}(\omega)$ has certain phase associated with it. The probability of finding a particular phase at a given location is the same as finding the probability of having a certain value of the indicator function at that place, which can be given as follows:

$$P\{I^{(i)}(\mathbf{r}; \omega) = 1\} = 1 - P\{I^{(i)}(\mathbf{r}; \omega) = 0\}. \quad (2.3)$$

A complete knowledge of indicator functions at each location of the random media is equivalent to knowing the exact structure of the random media. Once the indicator functions for the phases are defined, indicator functions for interfaces can be defined. An interface can exist at a location only if there is change of phase at that location. Hence, the interface

indicator function is given as follows [130]:

$$\mathcal{M}(\mathbf{r}; \omega) = |\nabla I^{(i)}(\mathbf{r}; \omega)|. \quad (2.4)$$

When working with a single realization of the stochastic process, the realization indicator can be dropped. In this case the phase indicator and surface indicator functions can be expressed as $I^{(i)}(\mathbf{r})$ and $\mathcal{M}(\mathbf{r})$, respectively.

2.2 Statistical Correlation Functions

A particular realization of the random media can be characterized by using statistics of its formation. The statistical functions can provide information on the probabilities of formation of different geometric features of the realization. These probabilities are known as correlation functions. One mathematical concept which will be used repeatedly for obtaining the correlation functions is the expectation of a statistical function, or the ensemble average. Before defining the expectation, let us assume that these estimations are being done on a single realization, and therefore, $I^{(i)}(\mathbf{r})$ will suffice for indicator function. The expectation of a function $f[I^{(i)}(\mathbf{r})]$ is the average of the function over the entire geometric space \mathcal{V} in all realizations ω . It is represented by angled brackets, and can be given as follows [130]:

$$\langle f[I^{(i)}(\mathbf{r})] \rangle = P\{I^{(i)}(\mathbf{r}) = 1\}f[1] + P\{I^{(i)}(\mathbf{r}) = 0\}f[0]. \quad (2.5)$$

If $f[I^{(i)}(\mathbf{r})] = I^{(i)}(\mathbf{r})$, then due to the $\{0, 1\}$ nature of indicator function:

$$\langle I^{(i)}(\mathbf{r}) \rangle = P\{I^{(i)}(\mathbf{r}) = 1\}. \quad (2.6)$$

If a single realization is used, the expectation is simply the average of function over the physical domain \mathcal{V} .

2.2.1 n-point Correlation Function

One of the most generic classes of correlation functions is known as the n -point correlation functions. To know the exact random media structure $\mathcal{V}(\omega)$, one must know the indicator function at each point. The complete probability description of the realization can be given by knowing the probabilities of the indicator functions at each location. The probability of finding a given set of points in given phases can be expressed as follows:

$$P\{I^{(i)}(\mathbf{r}_1) = j_1, I^{(i)}(\mathbf{r}_2) = j_2, \dots, I^{(i)}(\mathbf{r}_n) = j_n\} \quad \forall j_i \in \{0, 1\}. \quad (2.7)$$

A collection of all the probability functions for each phase can statistically describe the complete random media. The n -point correlation function is a generalized correlation function giving the probability that n given points with given locations will be in the same phase i , i.e.

$$S_n^{(i)}(\mathbf{r}_1, \mathbf{r}_2, \dots, \mathbf{r}_n) = P\{I^{(i)}(\mathbf{r}_1) = 1, I^{(i)}(\mathbf{r}_2) = 1, \dots, I^{(i)}(\mathbf{r}_n) = 1\}. \quad (2.8)$$

It can be shown that, the n -point correlation function is the expectation of the multiplication of indicator functions at the n locations.

$$\begin{aligned} S_n^{(i)}(\mathbf{r}_1, \mathbf{r}_2, \dots, \mathbf{r}_n) &= P\{I^{(i)}(\mathbf{r}_1) = 1, I^{(i)}(\mathbf{r}_2) = 1, \dots, I^{(i)}(\mathbf{r}_n) = 1\} \\ &= \langle I^{(i)}(\mathbf{r}_1)I^{(i)}(\mathbf{r}_2) \dots I^{(i)}(\mathbf{r}_n) \rangle. \end{aligned} \quad (2.9)$$

Geometrically, the n -point correlation function can be interpreted as the probability of having all corners of a n -sided polygon in phase i . Using the laws of probability, the n -point correlation function of a phase in two-phase random media can be given as function of correlations functions of another phases [130]:

$$\begin{aligned} S_n^{(2)}(\mathbf{r}_1, \mathbf{r}_2, \dots, \mathbf{r}_n) &= \left\langle \prod_{i=1}^n I^{(2)}(\mathbf{r}_j) \right\rangle \\ &= \left\langle \prod_{i=1}^n [1 - I^{(1)}(\mathbf{r}_j)] \right\rangle \\ &= 1 - \sum_{j=1}^n S_1^{(1)}(\mathbf{r}_j) + \sum_{j<k}^n S_2^{(1)}(\mathbf{r}_j, \mathbf{r}_k) \\ &\quad - \sum_{j<k<l}^n S_3^{(1)}(\mathbf{r}_j, \mathbf{r}_k, \mathbf{r}_l) + \dots + (-1)^n S_n^{(1)}(\mathbf{r}_1, \mathbf{r}_2, \dots, \mathbf{r}_n). \end{aligned} \quad (2.10)$$

By varying the value of n , one can define several specific correlation functions such as one-point correlation function, two-point correlation function, and three-point correlation function.

2.2.2 Homogeneous and Isotropic Porous Media

A porous media can be described as statistically homogeneous, if its probability distribution functions are the same for a transverse shift (shift of the origin) [130], i.e:

$$\begin{aligned} P\{I^{(i)}(\mathbf{r}_1) = j_1, I^{(i)}(\mathbf{r}_2) = j_2, \dots, I^{(i)}(\mathbf{r}_n) = j_n\} \\ = P\{I^{(i)}(\mathbf{r}_1 + \mathbf{y}) = j_1, I^{(i)}(\mathbf{r}_2 + \mathbf{y}) = j_2, \dots, I^{(i)}(\mathbf{r}_n + \mathbf{y}) = j_n\}, \end{aligned} \quad (2.11)$$

or for the n -point correlation function:

$$S_n^{(i)}(\mathbf{r}_1, \mathbf{r}_2, \dots, \mathbf{r}_n) = S_n^{(i)}(\mathbf{r}_1 + \mathbf{y}, \mathbf{r}_2 + \mathbf{y}, \dots, \mathbf{r}_n + \mathbf{y}). \quad (2.12)$$

Hence, for a homogeneous media, it is not the absolute position of the points which matters, but the relative positions between points.

In most random media, true homogeneity is extremely rare, as it requires the structure to be periodic at all possible shifts. For practical purposes, a porous media can be considered homogeneous, if the expected values (averaged values) of probability functions are similar in all sub-samples $\Delta\mathcal{V}$ ($\Delta\mathcal{V} \in \mathcal{V}$) of the physical space. As the physical size of sub-sample is increased, the homogeneity condition will be more easily satisfied. The minimum sub-sample size at which the realization shows homogeneity is known as the representative elementary size (representative elementary volume or REV for a 3D space). For any statistical analysis or averaging over the physical space, the size of the realization must be at least equal to the representative elementary size. If the correlation function $S_n^{(i)}$ is independent of the magnitude of shift vector \mathbf{y} , but dependent on direction, then the porous media is known as anisotropic.

2.2.3 One-point Correlation Function

The one point correlation function is the probability of finding a given phase at any given location in a realization. Using the definition of n -point correlation function from Eq. (2.9), the one-point correlation function can be defined as follows [130]:

$$S_1^{(i)}(\mathbf{r}) = \langle I^{(i)}(\mathbf{r}) \rangle = P\{I^{(i)}(\mathbf{r}) = 1\} \quad (2.13)$$

From a physical perspective, the 1-point correlation function is the probability that a randomly thrown point in the media will land in the given phase \mathcal{V}_i . This is the same as the volume fraction of phase i , given by ϕ_i . For a porous media, the one-point correlation function of the pore space is the void volume fraction, which is also known as porosity.

2.2.4 Two-point Correlation Function

Another specific case of the n -point correlation function is the two-point correlation function, also known as auto correlation function. The two point correlation function is the probability

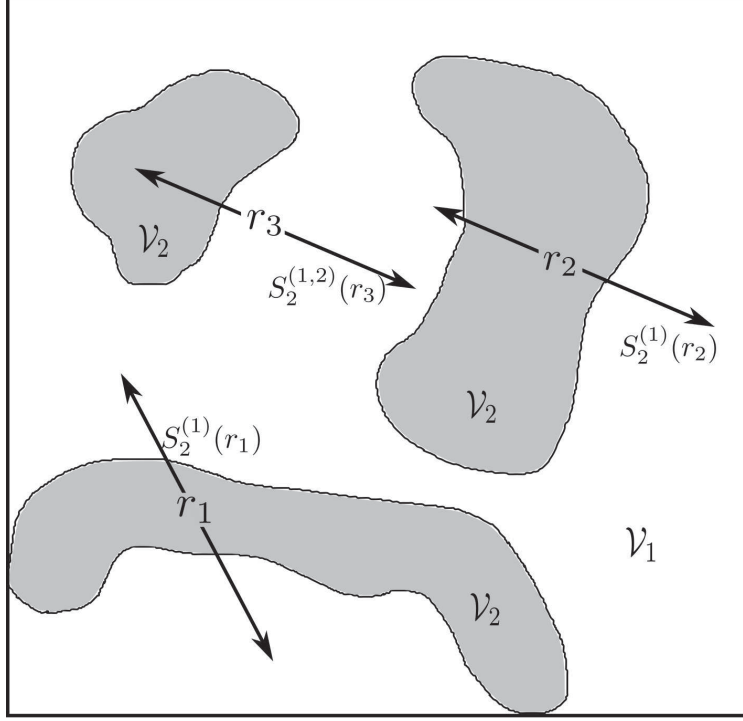


Figure 2.1 – A schematic depicting different instances of same phase and inter-phase two-point correlation function estimation (White is phase 1 and gray is phase 2)

of finding any two points \mathbf{r}_1 and \mathbf{r}_2 in the same phase i . Using the definition of n -point correlation function from Eq. (2.9), the two-point correlation function can be defined as follows [130]:

$$S_2^{(i)}(\mathbf{r}_1, \mathbf{r}_2) = P\{I^{(i)}(\mathbf{r}_1) = 1, I^{(i)}(\mathbf{r}_2) = 1\} \quad (2.14)$$

For a homogeneous media, the two points \mathbf{r}_1 and \mathbf{r}_2 can also be represented by a vector between these two points, i.e, $\mathbf{r} = \mathbf{r}_2 - \mathbf{r}_1$. In that case, the two-point correlation function is expressed as $S_2^{(i)}(\mathbf{r})$.

$$S_2^{(i)}(\mathbf{r}_1, \mathbf{r}_2) = S_2^{(i)}(\mathbf{r}_2 - \mathbf{r}_1) = S_2^{(i)}(\mathbf{r}). \quad (2.15)$$

If the random media is isotropic, the direction of vector \mathbf{r} is inconsequential, and the two-point correlation function only depends on its magnitude r . The two-point correlation function for an isotropic and homogeneous random media can be simply expressed as $S_2^{(i)}(r)$, which is the probability of finding two points r distance apart in any orientation and at any location.

Figure 2.1 depicts different instances of obtaining the two-point correlation function. Each color in the image represents a different phase. It can be seen that the normal two

point correlation function is the probability of finding the end points of a given vector in the same phase. Inter-phase two-point correlation functions can also be defined to analyze phase segregation in random media [124]. An inter-phase two-point correlation function $S^{(i,j)}(r)$ is the probability of finding a line of length r with one end in phase i , and other end in phase j .

The two point correlation function is linked to several geometric properties of the random media. For an isotropic random media without long range order, the following limiting values are obtained for $S_2^{(i)}(r)$ [63] :

$$\begin{aligned} S_2^{(i)}(0) &= \phi_i, \\ \lim_{r \rightarrow \infty} S_2^{(i)}(r) &= \phi_i^2. \end{aligned} \tag{2.16}$$

For a two-phase random media with phase values 1 and 2, the different two-point correlation functions of the two phases hold the following relations :

$$\begin{aligned} S_2^{(1,1)}(r) + S_2^{(1,2)}(r) &= \phi_1 \\ S_2^{(2,1)}(r) + S_2^{(2,2)}(r) &= \phi_2 \\ S_2^{(1,2)}(r) &= S_2^{(2,1)}(r) \\ \phi_1 + \phi_2 &= 1, \end{aligned} \tag{2.17}$$

where $S_2^{(i,i)}(r)$ is the same as $S_2^{(i)}(r)$. Solving these equations yields the following relationships between the different two-point correlation functions :

$$\begin{aligned} S_2^{(2)}(r) &= S_2^{(1)}(r) + 2\phi_2 - 1 \\ S_2^{(1,2)}(r) &= \phi_1 - S_2^{(1)}(r) \\ S_2^{(2,1)}(r) &= \phi_1 - S_2^{(1)}(r). \end{aligned} \tag{2.18}$$

It can be seen that if one of the correlation functions is known, the others can be found out easily due to the relationships in Eq. (2.18). It is due to these relationships that, for a two phase media, the two-point correlation function does not distinguish between phases. In other words, using more than a single two-point correlation function will not augment the information content.

The specific surface area (area per unit volume) for a two phase medium is an important characteristic inverse length scale of the porous medium. The specific surface area of a two phase medium can be obtained as a function of its two-point correlation function as follows:

$$s = - \beta \frac{d}{dr} S_2^{(1)}(r) \Big|_{r=0}, \tag{2.19}$$

where $\beta = 2 \times \text{dim}$ for discrete media, and dim is the space dimension [60]. The specific surface area can also be used to approximate permeability of porous media using the Kozeny-Carman relations [131].

A normalized version of the two-point correlation function, known as autocorrelation function is often used in image characterization, random media characterization and reconstruction. The autocorrelation function for a phase i is defined as follows [121, 131, 132]:

$$R_z^{(i)}(r) = \frac{S_2^{(i)}(r) - \phi_i^2}{\phi_i - \phi_i^2} \quad (2.20)$$

The autocorrelation function for a random media has been obtained by image processing, as well by analyzing its scattering properties from experiments such as small angle X-ray scattering [133–135]. The autocorrelation function has been used to estimate a characteristic length scale for the random media. Ioannidis et al. [132] proposed the following expression for the correlation length of the random media, which can be used as a characteristic length scale.

$$\bar{\lambda} = \int_0^\infty R_z^{(i)}(r) dr \quad (2.21)$$

The correlation length is a measure of the range of autocorrelation function. It may be used for estimating sample sizes and representative elementary sizes. Ioannidis et al. [132] used the correlation length as an estimation parameter for permeability calculations. An empirical equation of the following form was fitted to experimental data for permeability:

$$\kappa = a + b \ln \phi_v + c \ln \bar{\lambda}, \quad (2.22)$$

where κ is the permeability, ϕ_v is the volume fraction of void phase, and a, b, c are fitting parameters. The empirical model did not show strong agreement; however, it can be used for coarse approximations. Another two-point correlation function based characteristic length appears in upper bounds of random media permeability as follows [136, 137] :

$$\kappa \leq \frac{2\lambda_B^2}{3(1 - \phi_v)^2}, \quad (2.23)$$

where κ is the permeability, ϕ_v is the volume fraction of void phase and λ_B is the characteristic length. The relationship between λ_B and two-point correlation function is given as [137] :

$$\lambda_B = \left\{ \int_0^\infty [S_2^{(v)}(r) - \phi_v^2] r dr \right\}^{1/2}. \quad (2.24)$$

It is evident that the two-point correlation function is an important statistical correlation function. Due to its strong correlations with several geometric properties, and some weak correlations with physical properties, it plays an important role in the characterization of a random media. It is therefore critical to include it in any characterization or reconstruction methodology.

2.2.5 Lineal Path Function

The lineal path function $L^{(i)}(\mathbf{r}_1, \mathbf{r}_2)$ is the probability of finding all points of the line connecting \mathbf{r}_1 and \mathbf{r}_2 in phase i [73]. Mathematically, it can be represented as:

$$L^{(i)}(\mathbf{r}_1, \mathbf{r}_2) = P \left\{ I^{(i)}(\mathbf{r}_1) = 1, I^{(i)}(\mathbf{r}_1 + d\mathbf{r}) = 1, I^{(i)}(\mathbf{r}_1 + 2d\mathbf{r}) = 1, \dots, I^{(i)}(\mathbf{r}_2) = 1 \right\} \\ = \left\langle \prod_{\mathbf{r}_1}^{\mathbf{r}_2} I^{(i)}(r)^{dr} \right\rangle. \quad (2.25)$$

For a homogeneous and isotropic media, the location and orientation of the line between \mathbf{r}_1 and \mathbf{r}_2 is inconsequential. In this case, the lineal path function can be simply expressed as $L^{(i)}(r)$, where r is the distance between \mathbf{r}_1 and \mathbf{r}_2 [63]. For an isotropic random media, the following limiting values are obtained for $L^{(i)}(r)$ [60]:

$$L^{(i)}(0) = \phi_i, \\ \lim_{r \rightarrow \infty} L^{(i)}(r) = 0. \quad (2.26)$$

Figure 2.2 shows instances of obtaining lineal path functions for different phases. Each color in the image represents a different phase. For an isotropic and homogeneous media, $L^{(i)}(r)$ is the probability of finding any line of length r completely in phase i . The lineal path function not only contains the phase information at the specific points, but also in between them, thereby enabling it to capture information on phase connectivity. The lineal path functions of different phases are not linearly dependent, making it a phase distinguishing property compared to the two point correlation function [63]. The lineal path functions for all phases can therefore be incorporated in the characterization and reconstruction process.

2.2.6 Chord Length Function

The chord length function is the probability of finding a chord of given size in phase i [60, 74]. $C(\mathbf{r}_1, \mathbf{r}_2)d\mathbf{r}$ is the probability of finding a chord between $\lim_{\mathbf{r} \rightarrow \mathbf{r}_1^-} \mathbf{r}$ and $\lim_{\mathbf{r} \rightarrow \mathbf{r}_2^+} \mathbf{r}$. For a

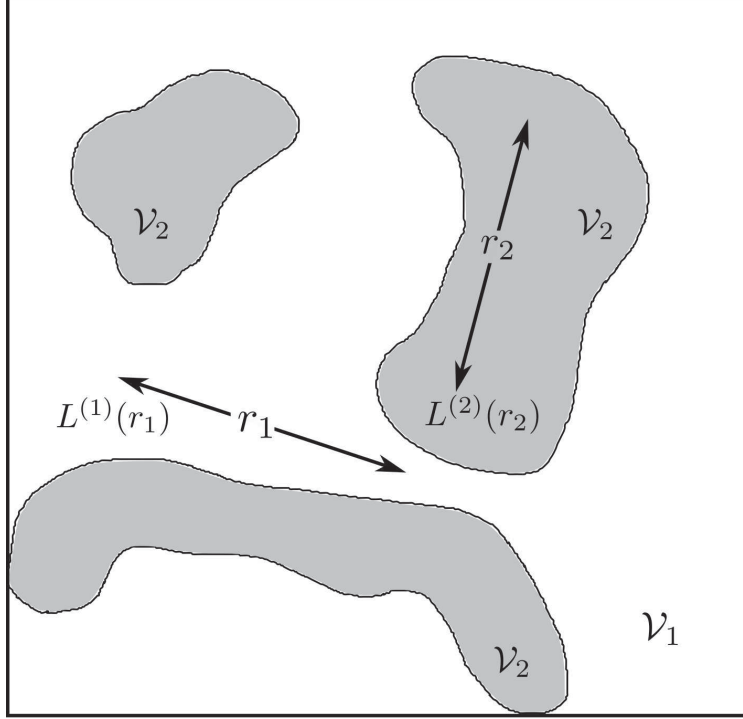


Figure 2.2 – A schematic depicting instances of lineal path functions for different phases (White is phase 1 and gray is phase 2)

homogeneous and isotropic media, the location and orientation of the line between \mathbf{r}_1 and \mathbf{r}_2 is inconsequential, and the chord length function can be simply expressed as $C^{(i)}(r)$, where r is the distance between \mathbf{r}_1 and \mathbf{r}_2 . $C^{(i)}(r)dr$ can be defined as the probability of finding a chord of length between r and $r + dr$ in phase i . A chord is essentially the line segment between immediate inter-phase boundaries. Figure 2.3 shows an illustration of solid and void phase chords in a two phase media.

The chord length and lineal path functions are related as follows [74]:

$$C^{(i)}(r) = \frac{\langle l \rangle}{\phi_i} \frac{d^2 L^{(i)}(r)}{dr^2}, \quad (2.27)$$

where ϕ_i is the void fraction of phase i , and $\langle l \rangle$ is the mean chord length given as [60]:

$$\langle l \rangle = \int_0^\infty r C(r) dr. \quad (2.28)$$

It may therefore not be necessary to incorporate both lineal path and chord length functions for same phase, as it will only add marginal additional information about the random media.

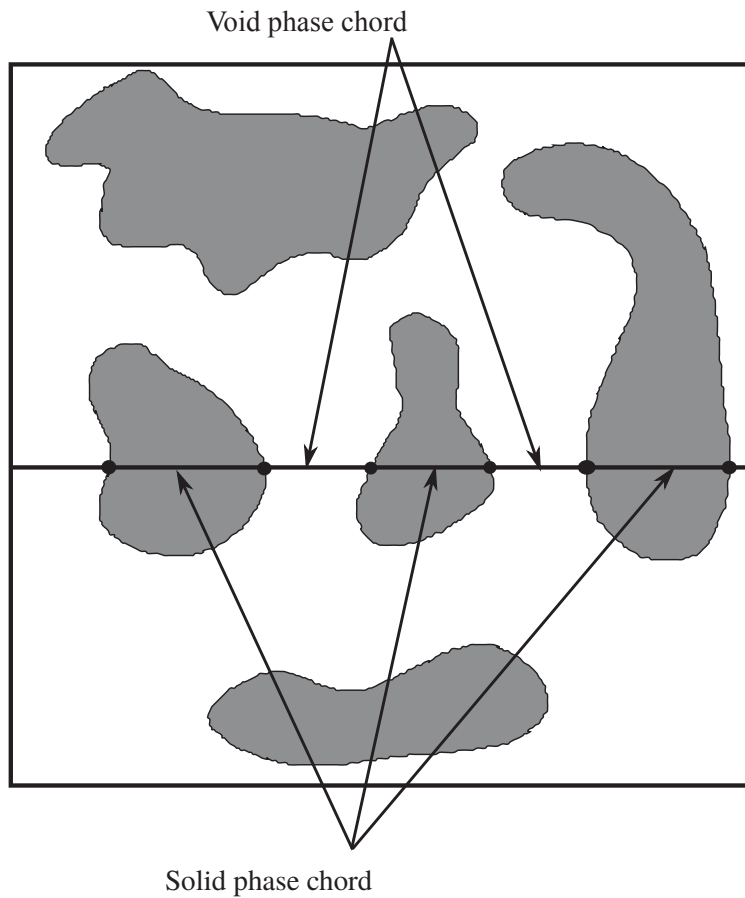


Figure 2.3 – An illustration of chords in a two phase medium (White is void phase and gray is solid)

The chord length function contains information about the cluster sizes in the image and is similar to the pore size distribution function. Due to this, the chord length function can be used to characterize Knudsen diffusion and related transport properties. In pure Knudsen diffusion (i.e., molecule-wall interactions only), the paths of molecules between wall collisions are similar to the chords [138, 139]. The mean distance between wall collisions can be therefore related to the mean chord length $\langle l \rangle$ [139]. By comparing the definition of Knudsen diffusion with the Derjaguin formulation, Berson et al. [139] obtained the following relationship between mean distance between collisions and mean chord length:

$$d = \left(\frac{\langle l^2 \rangle}{2\langle l \rangle^2} - \beta \right) \langle l \rangle, \quad (2.29)$$

where $\beta = - \sum_{m=2}^{\infty} \langle \cos \gamma_m \rangle$, and γ_m is the angle between particle trajectories separated by m wall collisions [139]. The Knudsen diffusivity in terms of mean chord length is given as [139]:

$$D_k = \frac{1}{3} \langle l \rangle \langle v_T \rangle \left(\frac{\langle l^2 \rangle}{2\langle l \rangle^2} - \beta \right), \quad (2.30)$$

where $\langle v_T \rangle$ is the mean velocity of the particles given as follows [140]:

$$\langle v_T \rangle = \sqrt{\frac{8RT}{\pi M}}, \quad (2.31)$$

R is the universal gas constant, and M is the molecular weight of the species.

Based on its effects on pore sizes and Knudsen diffusion, it can be hypothesized that the chord length function may also be related to permeability. Although no direct relationships are available between chord length function and permeability, inclusion of chord length function, or its integral (lineal path function) appear to improve the permeability of the reconstructed structures [99, 100]. It is therefore necessary to include either chord length, or lineal path function for characterization and reconstruction of random media, where Knudsen diffusion or permeability are of importance.

2.2.7 Two-point Cluster Function

The two point cluster function $C_2^{(i)}(\mathbf{r}_1, \mathbf{r}_2)$ is the probability of finding any two points \mathbf{r}_1 and \mathbf{r}_2 in the same phase i and also in the same cluster [79]. Two points are said to be in the same cluster if they can be connected within the same phase. The two-point cluster function is related to the two-point correlation function as follows [79]:

$$S_2^{(i)}(\mathbf{r}_1, \mathbf{r}_2) = C_2^{(i)}(\mathbf{r}_1, \mathbf{r}_2) + D_2^{(i)}(\mathbf{r}_1, \mathbf{r}_2), \quad (2.32)$$

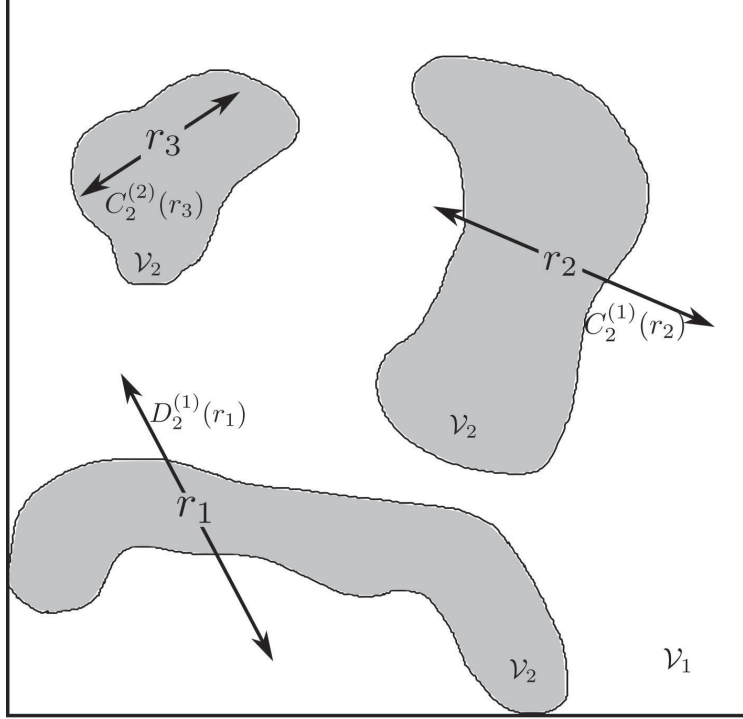


Figure 2.4 – A schematic depicting instances of two-point cluster function estimation. Also shown is an example of $D_2^{(i)}(r)$ (White is phase 1 and gray is phase 2)

where $D_2^{(i)}(\mathbf{r}_1, \mathbf{r}_2)$ is the probability of finding \mathbf{r}_1 and \mathbf{r}_2 in different clusters, but still in phase i .

For a homogeneous and isotropic porous media, the location of \mathbf{r}_1 and \mathbf{r}_2 is inconsequential, and the two-point cluster function can be simply expressed as $C_2^{(i)}(r)$, where r is the distance between \mathbf{r}_1 and \mathbf{r}_2 . Figure 2.4 shows a schematic of estimating two-point cluster function for the two phases of a binary random media. As discussed earlier, the two points must be in the same cluster (i.e., connected through same phase). The figure also shows an instance of $D_2^{(1)}(r_1)$, where the two end points are in different clusters, albeit in the same phase.

The two-point cluster function is a critical parameter to pinpoint the connectivity of a porous medium. It is linked to the percolation threshold of the random media [79]. The two-point cluster function inherently contains the connectivity information in three dimensions. Jiao et al. [72] showed that the two-point cluster function contains the most information

among all the discussed correlation functions, and can capture the information content of other correlation functions as well. It is however computationally expensive to calculate, as the clusters have to be identified before computing the function. This creates challenges especially during reconstruction, as the cluster identification may have to be done after each pixel swap.

2.3 Correlation Function Computation for Digital Images

All the definitions of correlation functions so far have considered the random media as continuous. In most of the situations however, one must analyze the digital images of porous media to obtain its correlation functions. The definitions of the correlations functions must therefore be adjusted to suit the discrete nature of the digital images. The primary changes are due to the fact that the correlation functions can now be computed only for certain discrete distances. This section presents the definitions of the correlation functions for discrete random media, with a special emphasis on computational methods.

2.3.1 One-point correlation function

The one-point correlation function for a digital image can be defined as the probability of finding a pixel of desired color (phase). The one-point correlation function from an image can be obtained by taking the ratio of total pixels of the desired color to the total pixels. The volume fraction of phase i for a digitized image can be given as [59]:

$$\phi_i = \frac{1}{WHD} \sum_{abc} I_{a,b,c}^{(i)} \quad : \forall a \in [1, W], \forall b \in [1, H], \forall c \in [1, D], \quad (2.33)$$

where W , H , and D are the digital dimensions (number of pixels) of the image in x , y and z directions respectively. $I_{a,b,c}^{(i)}$ is the indicator function stating the phase at the location $\{x, y, z\} \equiv \{a, b, c\}$ with the following definition:

$$I_{a,b,c}^{(i)} = \begin{cases} 1, & \text{if pixel}\{a, b, c\} \text{ is in phase } i \\ 0, & \text{otherwise.} \end{cases} \quad (2.34)$$

Algorithm A.1 presents a computational algorithm for estimating the volume fraction of phase i .

2.3.2 Two-point Correlation Function

The two-point correlation function for a digital image can be defined as the probability of finding two pixels of the same color at a given distance r , where r is always an integer due to the discrete nature of the image. The two point correlation function $S_2^{(i)}(r)$ can be obtained by translating a line of length r successively pixel by pixel across the whole image and noting down the number of times both ends fall in the phase i [59, 63]. This is then normalized by the total number of trials, which is the sampling space. For a complete characterization, the line must be translated across the whole domain at all possible orientations; however, for a porous media with no exclusive directional features, sampling in only the orthogonal directions will suffice. Orthogonal sampling has two advantages: 1) the computation time is less, because of the limited number of directions used; and 2) during reconstruction, when a pixel is updated, only the corresponding row and columns need to be sampled again, thereby resulting in additional time advantage.

The two-point correlation function is calculated separately in x , y , and z directions for each pixel row and column. For example, the two point correlation function for a pixel row in x direction for an image of size ($W \times H \times D$) can be given as follows:

$$S_2^{(i)}(r) = \frac{1}{a_{max}} \sum_{a=1}^{a_{max}} I_{a,b,c}^{(i)} I_{a+r,b,c}^{(i)} \quad \text{for a pixel row with } y = b, \text{ and } z = c, \quad (2.35)$$

where $a_{max} = W - r$ is the number of points sampled in the row. For any length r , the sampling is stopped r pixels away from the edge, as the other end of the line will go over the image. This can be avoided by using a periodic boundary condition, where the line loops back to the beginning of image. In this way, all the pixels in the image can be sampled. The two-point correlation function does not contain any long range information, and becomes periodic for an estimation length of more than half the length of image. Therefore, to avoid redundant computations, the two-point correlation function should only be computed until half the length of image in any direction. The details of computational algorithm for computing two-point correlation functions in any row/column are presented in section A.2. Once the two-point correlation functions for all the rows and columns are obtained, they are averaged separately in each direction to obtain reference correlation functions.

2.3.3 Lineal Path Function

The lineal path function for a digital image $L^{(i)}(r)$ is the probability of finding a line spanning r pixels which are all of the same color corresponding to phase i . To avoid computational complexity, the sampling can be limited to the orthogonal directions. For estimating the lineal path function along any direction, chords in the phase of interest must be searched. To find a chord in phase i , the image is scanned along the given direction (\mathbf{x} , \mathbf{y} , or \mathbf{z}) until an interfacial pixel is encountered in the phase of interest. This pixel is marked as 0 and scanning continues until another interfacial pixel is encountered signifying the end of chord. Once a chord of length l is found in phase i , the lineal-path function of the phase can be calculated as follows [63]:

$$L^{(i)}(r) = \begin{cases} (l - r)/N, & \text{when } 0 \leq r \leq l \\ 0, & \text{otherwise,} \end{cases} \quad (2.36)$$

where N is the maximum number of lines of length r that can be placed in the sample. For example, along x direction, a maximum of $W - r$ lines of length r can be found, where W is the width of the image. For each additional chord in the same line, the lineal path functions are superimposed. The lineal path function can be computed for any r less than image length; however, after certain $r = r_{max}$ it reaches zero, as no lines of such length can be found in a single phase. To save computational time, the lineal path function can be computed only up to r_{max} . Section A.3 presents the details of a computational algorithm to estimate lineal path function in a pixel row/column for digital images. Once the lineal path functions for all the rows and columns are obtained, they are averaged separately in each direction.

2.3.4 Chord Length Function

The chord length function $C^{(i)}(r)$ for a digital image can be defined as the probability of finding a chord of length r pixels in phase i . The process of estimating chord length function is similar to the one used for estimating lineal path function. For estimating chord length function along any direction, all the chords must be searched and recorded. The recorded chord lengths are then binned by their occurrence frequency, and then normalized by total number of chords. The chord length function can be computed for any r less than image length; however, it will be zero for any length bigger than the largest chord present in the

media. To save computational time, the chord length length function can be computed only up to the maximum chord length r_{max} . Section A.4 presents the details of a computational algorithm to estimate chord length function in a pixel row/column for digital images. Once the chord length functions for all the rows and columns are obtained, they are averaged separately in each direction.

2.3.5 Two-point Cluster Function

The two-point cluster function for a digital image can be defined as the probability of finding two pixels of same color and in the same cluster at a distance of r pixels. The two point cluster function $C_2^{(i)}(r)$ can be obtained by translating a line of length r successively pixel by pixel across the whole image, and noting down the number of times both ends fall in the phase i and in the same cluster. To estimate two-point cluster function, the different clusters have to be identified.

Cluster Identification

Cluster identification is a connected component labeling problem which has been a topic of thorough research in percolation modeling and image processing. Rosenfeld and Pfaltz [141] have presented one of the first attempts to identify clusters over an entire image for percolation determination. The cluster identification algorithm consists of a two pass algorithm. In the first pass, each pixel in the targeted phase is assigned a cluster label. Each pixel is assigned the minimum label among its neighbors. If no labeled neighbors are found, a new label is given to the site. When a site joins two sub-clusters and therefore has two or more different neighbor labels, the minimum label is assigned to the site. To keep track of the connectivity between labels, an equivalence table is used. The equivalence table is handled using a disjoint set data-structure such as a union-find algorithm [142], which helps in finding the minimum equivalent label.

In the second pass, all the labels are replaced by the equivalent minimum labels from the equivalence table. A variation of this algorithm is well known as the Hoshen and Kopelman [143] algorithm. It consists of a single scan algorithm, where the first pass is similar to the one presented by Rosenfeld and Pfaltz [141]. The only difference is that when an equivalence of labels is found, the number of sites belonging to the higher cluster number

are added to the number of sites belonging to the smaller cluster. This algorithm, however does not assign new labels to the sites with higher cluster numbers. A second pass has to be used for the cluster identification, if desired. The Hoshen and Kopelman [143] method is the most widely used algorithm for cluster labeling in percolation physics. Other methods, such as the well known recursive algorithm by Wolff [144] for Monte Carlo simulations also exist. These methods however, are known to have stack memory issues due to high number of consecutive recursive calls [145].

Due to its simple implementation, less memory intensive operations, and a potential for parallel operations, the Hoshen and Kopelman [143] algorithm was used in conjunction with the union-find algorithm. Section A.5.1 presents the details and the algorithm for the method to identify cluster labels in an image. Once the clusters are identified, the two-point cluster function for a pixel row/column is computed using the algorithm presented in section A.5.2.

It can be seen that the computation of the cluster function is similar to the two-point correlation function, except for the requirements of cluster identification. The requirement of cluster identification indeed makes this method computationally much more expensive, especially during the reconstruction process. Unlike other correlation functions, where changing a pixel only changes the correlation functions of corresponding row or column, changing a pixel can change cluster connectivity over a wide range. This in turn means that, the two-point cluster functions of several rows and columns will change. During reconstruction, this additional burden of computing new cluster information, and new correlation functions can make the use of two-point cluster function computationally expensive. In this study therefore, the two-point cluster function is only used as an independent verification function to access the effectiveness of the reconstruction method. Furthermore, it must be kept in mind that the two-point cluster function essentially represents three-dimensional connectivity of porous media, and it is not applicable to the 2D cases.

2.3.6 Dealing with Boundaries in Correlation Functions Computing

There are two methods for computing the correlation functions for an image. The simplest method is to start at the beginning of the image and sample until the end of the image.

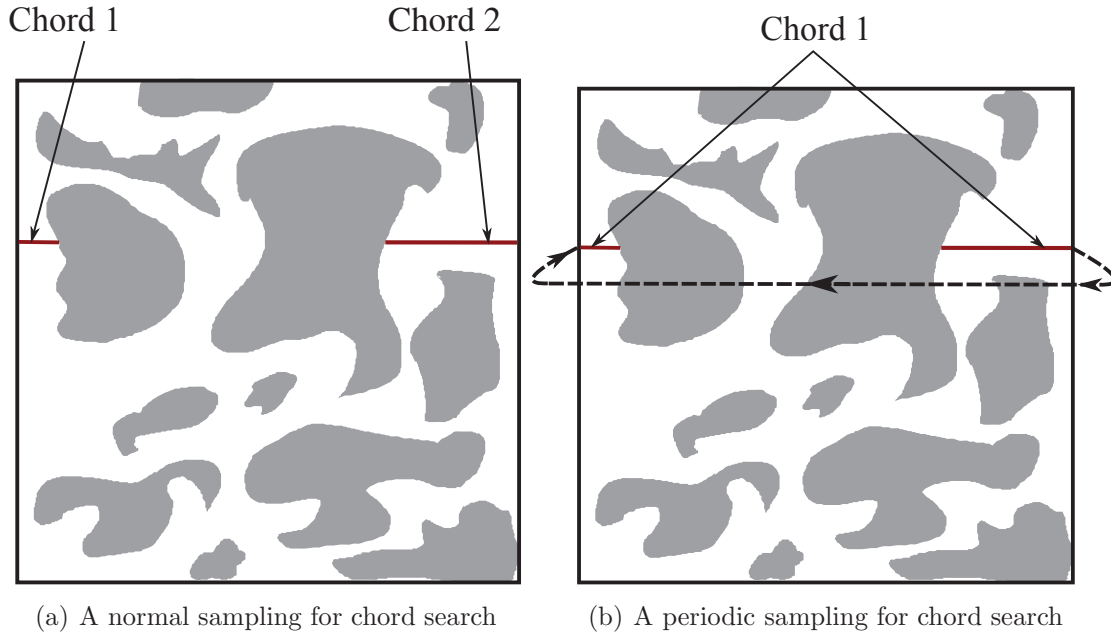


Figure 2.5 – An illustration of normal and periodic sampling in a digital image

Another method is to use a periodic boundary condition. Using the normal sampling to measure the chord length function, the sampling is stopped whenever the end of line \mathbf{r} falls out of the image (see Fig. 2.5(a)). In a periodic boundary condition however, the end of the line is wrapped back to the beginning of the image and sampling is done until the beginning of segment \mathbf{r} reaches the end of the image (see Fig. 2.5(b)). Since a stochastic reconstruction process works on the assumption that the reconstruction instance is a representative element of the entire system, the periodic boundary condition is more appropriate for reconstruction purposes [66]. In this work, normal sampling is used to analyze reference images obtained from imaging techniques, as these images do not show periodicity at the edges. During reconstruction however, the correlation functions for the reconstructed structure are estimated periodically.

2.4 Validation of the Correlation Function Computing Algorithms

To test the accuracy of the developed algorithms and the computer program based on them, the correlation function estimations were compared to available analytical results. Berryman [59], and Coker and Torquato [60] have presented analytical results for void phase two-point correlation function, lineal path function and chord length function for a random packing of

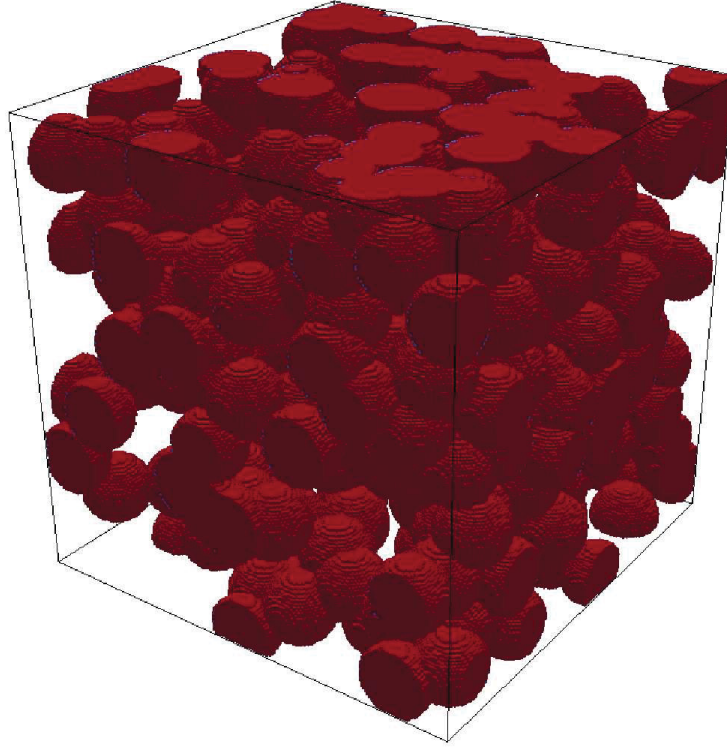


Figure 2.6 – 3D image of packing of penetrable spheres (Red shows the solid spheres, and void phase is white)

penetrable spheres. All the programs developed in this study are made phase independent, i.e., the same routines are used to compute the correlation functions for all phases by changing the phase index. Therefore, if the algorithms and programs are verified for one phase, they should accurately compute correlation functions for other phases as well.

For the validation, a 3D image of fully penetrable sphere packing with each side of length 200 pixels was chosen. The spheres have a radius of 15 pixels and the porosity of the system is fixed at 0.5. Once the sphere radius and the porosity are decided, the following equation is used to determine the sphere packing density [59]:

$$\phi = \exp\left(-\rho \frac{4\pi}{3} R^3\right), \quad (2.37)$$

where ϕ is the desired porosity, ρ is the sphere packing density, and R is the sphere radius. Using the aforementioned parameters, the required sphere number density is obtained as 4.9×10^{-5} spheres/pixel³. This translates to roughly 392 spheres in the domain of size $200 \times 200 \times 200$ pixels. A MATLAB code was used to generate the 3D image. Figure 2.6 shows the image of penetrable sphere packing.

2.4.1 Two-point Correlation Function

Berryman [59] derived the following analytical expression for two-point correlation function of void phase in a packing of fully penetrable spheres:

$$S_2^{(v)}(r) = \exp\{-\rho v_2(r)\}, \quad (2.38)$$

where ρ is the number density of spheres, and $v_2(r)$ is the normalized union volume of 2 spheres which are separated by a distance r , which is given as follows:

$$v_2(r) = \frac{V_2(r)}{V_{\text{domain}}}. \quad (2.39)$$

V_{domain} is the volume of the domain, and $V_2(r)$ is the total union volume of 2 spheres separated by distance r , which is given as:

$$\frac{V_2(r)}{R^3} = \begin{cases} \frac{4\pi}{3} \left(1 + \frac{3}{4}x - \frac{x^3}{16}\right) & \text{for } x \leq 2 \\ \frac{8\pi}{3} & \text{for } x > 2, \end{cases} \quad (2.40)$$

where $x = r/R$ and R is the sphere radius.

Figure 2.7 shows the comparison of analytical and estimated two point correlation function of the void phase for the penetrable sphere packing. The estimation was done using only the orthogonal sampling in x , y , and z directions. The correlation function in all the directions and in all pixels rows are averaged together to obtain an estimate of isotropic two-point correlation function. It can be seen that despite using only orthogonal sampling, the algorithm is able to estimate the two-point correlation function with good accuracy. It can also be observed that $S_2^{(v)}(r)|_{r=0} = \phi_v \equiv 0.5$, and $S_2^{(v)}(r)|_{r>30} = \phi_v^2 \equiv 0.25$, thereby satisfying two requirements of a two-point correlation function.

2.4.2 Lineal path function

Lu and Torquato [73] derived the following analytical expression for the lineal path function of void phase in a packing of fully penetrable spheres:

$$L^{(v)}(r) = \phi_v^{1+(3r/4R)}, \quad (2.41)$$

where ϕ_v is the void volume fraction. Figure 2.8 shows the comparison of analytical and estimated lineal path function for the void phase of penetrable sphere packing. It can

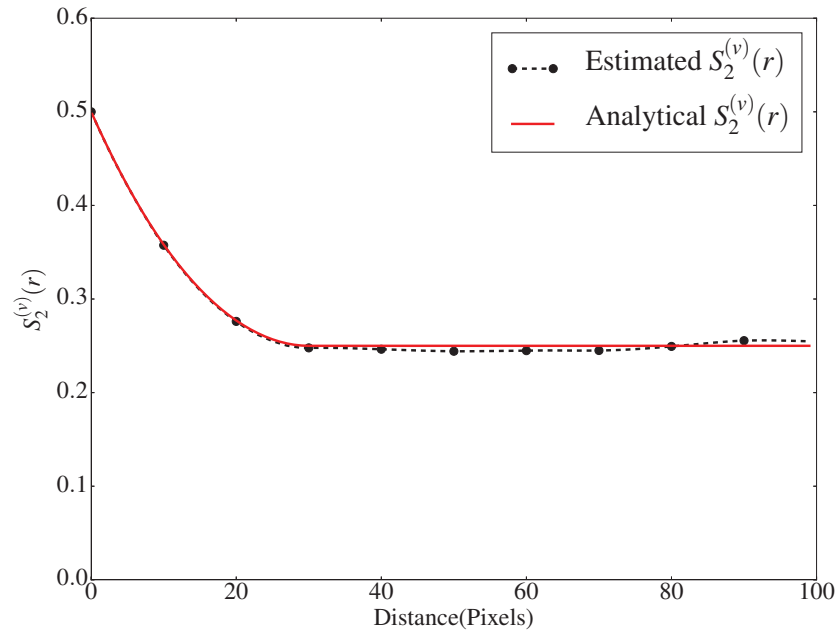


Figure 2.7 – Comparison of analytical and estimated two-point correlation function for penetrable sphere packing

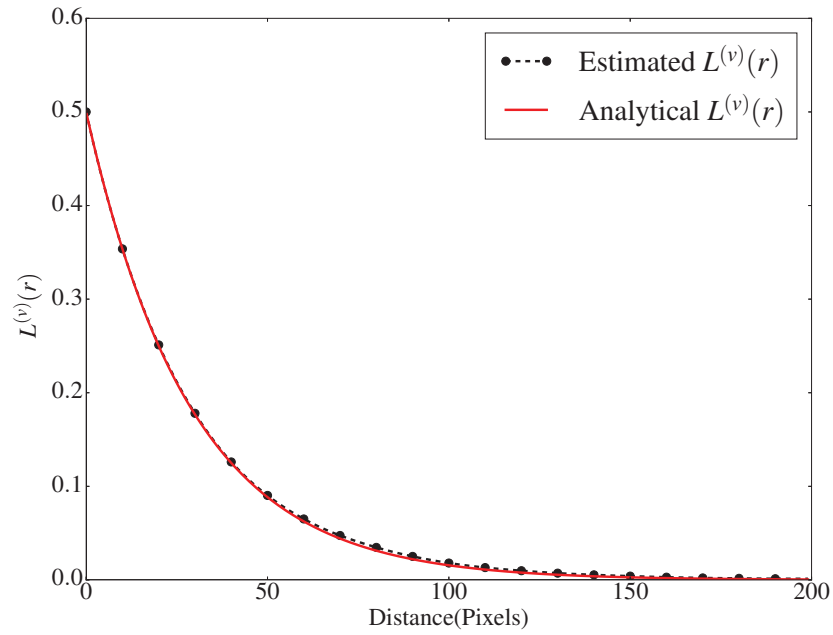


Figure 2.8 – Comparison of analytical and estimated lineal path function for penetrable sphere packing

be observed that orthogonal sampling results in a good accuracy estimation of lineal path function as well. Furthermore, it can also be observed that $L^{(v)}(r)|_{r=0} = \phi_v \equiv 0.5$, and $L^{(v)}(r)|_{r>150} = 0$, thereby satisfying two requirements of a lineal path function.

2.4.3 Chord Length Function

Torquato and Lu [74] derived the following expression for the chord length function of the void phase for a packing of penetrable spheres:

$$C^{(v)}(r) = -\frac{3}{4R} \ln(\phi_v) \phi_v^{3r/4R}. \quad (2.42)$$

Figure 2.9 shows the comparison of analytical and estimated chord length function for the void phase of penetrable sphere packing. Even though the algorithm provides a good estimate, the accuracy is lower than other correlation functions. The major reason for this higher inaccuracy is the discrete nature of the image being analyzed. While the algorithm can only account for discrete chord lengths, the analytical expression is obtained assuming a non-discrete structure. Using multiple instances of randomly packed spheres for estimation, and averaging over them, the chord length becomes smoother and closer to the analytical expression. Figure 2.10 shows the comparison of analytical chord length function with the estimated chord length function averaged over 27 instances of random sphere packing. With high number of instances, sufficient chords of each length are encountered, resulting in better statistics and closer match with analytical function.

2.4.4 Two-point Cluster Function

No analytical expressions for two-point cluster function are available in literature; however, the fact that for a media with completely percolating void phase, the two-point cluster function is the same as two-point correlation function can be utilized for verification. By performing percolation analysis on the 3D image shown in Fig. 2.6, 99.999% of the void phase was found to be in a single percolating cluster. This image can be therefore used to estimate two-point cluster function and verification. Figure 2.11 shows the comparison of analytical and estimated two-point cluster function for the void phase of penetrable sphere packing. The accuracy of estimation is the same as two-point correlation function.

To ensure that the cluster functions are computed accurately in images with more than one clusters, the cluster identification algorithm was tested in a random media image. For

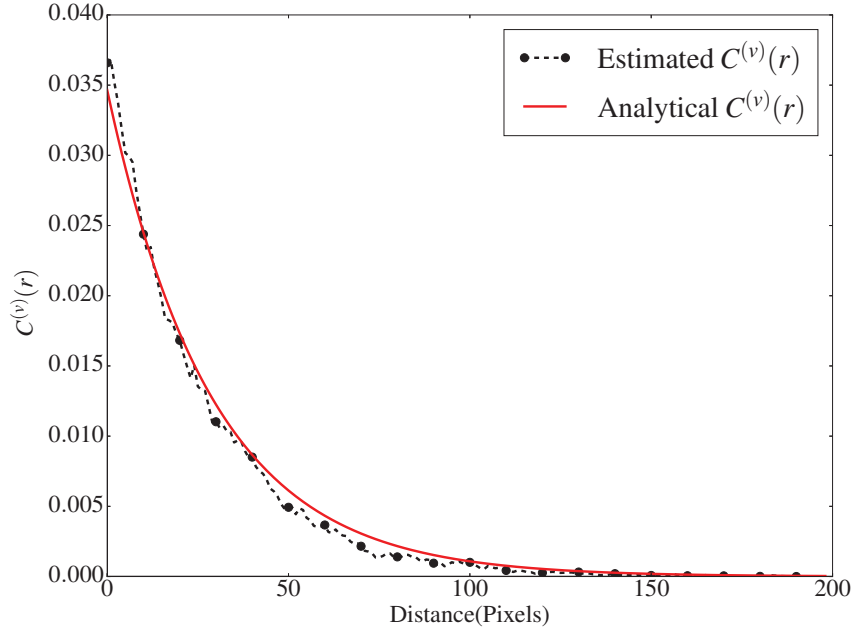


Figure 2.9 – Comparison of analytical and estimated chord length function for penetrable sphere packing

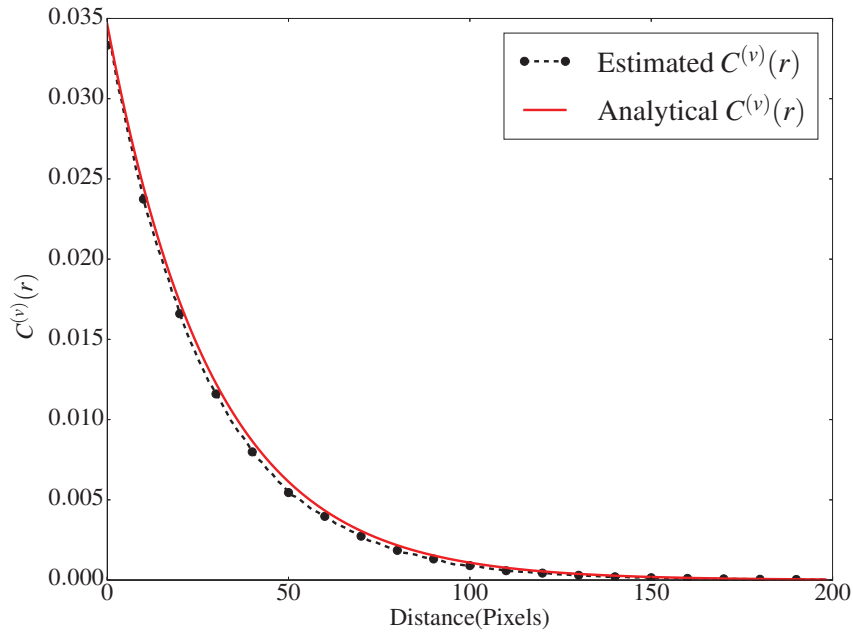


Figure 2.10 – Comparison of analytical and average estimated chord length function for penetrable sphere packing. The estimation is averaged over 27 instances of random sphere packing

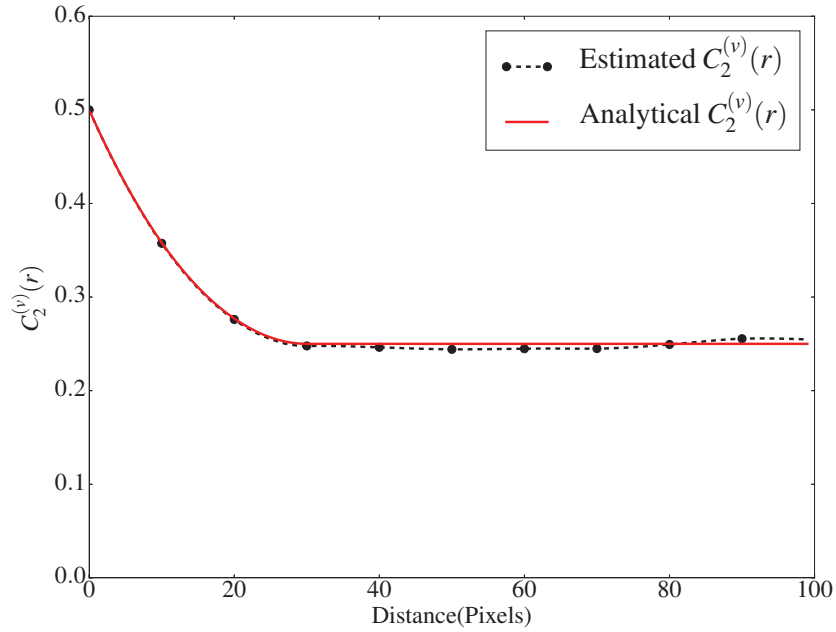
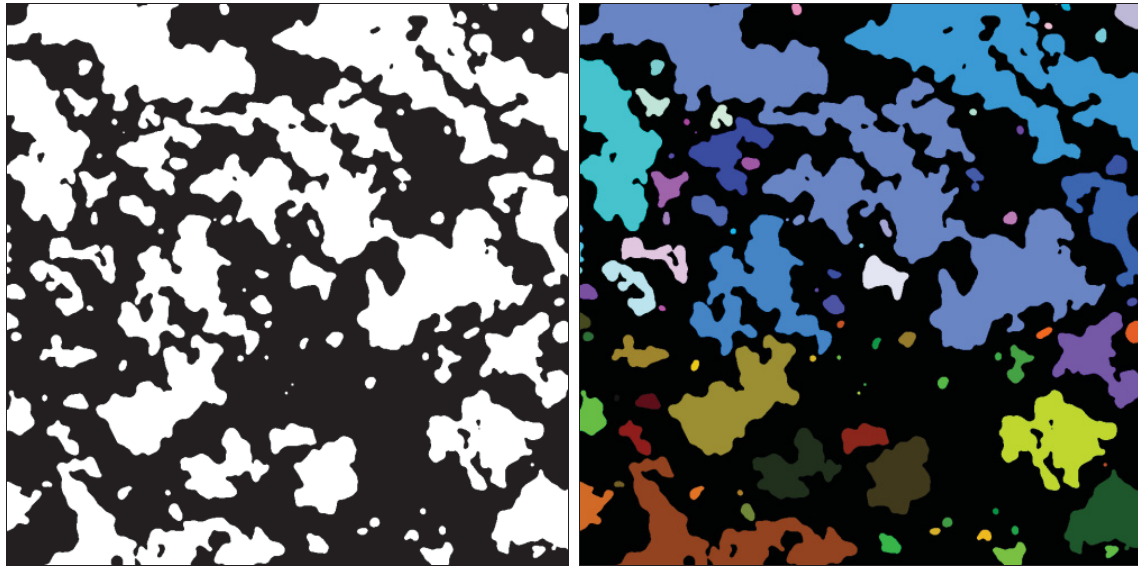


Figure 2.11 – Comparison of analytical and estimated two-point cluster function for penetrable sphere packing

ease in visualization, an analysis on 2D image is presented here. Figure 2.12(a) shows the random media image used for testing the cluster identification. The void phase is represented by white color. Once the clusters are identified and labeled using the computational program, a unique color is assigned corresponding to each cluster label. Figure 2.12(b) shows the image with different clusters, where each different color represents a different cluster. It can be observed that the program can identify each cluster accurately.



(a) Test image for cluster identification (White is the void phase) (b) The test image with different clusters (Each color represents different cluster)

Figure 2.12 – An illustration of the cluster identification in a random media. The clusters are identified only for void phase (white).

Chapter 3

Stochastic Reconstruction of Random Media[†]

This chapter describes the simulated annealing based stochastic reconstruction method used in this work. As discussed in Chapter 1, several variations have been proposed to the method in terms of pixel swapping, energy minimization and hierarchical annealing. This chapter discusses the details of all the methods and variations explored in this work. Section 3.1 provides an overview of the general simulated annealing method, followed by Section 3.2, which discusses the two energy minimization methods: probability, and threshold based minimization. Section 3.3 provides the details of temperature reduction in simulated annealing. Section 3.4 describes the different pixel swapping methods used in this work. Section 3.5 provides the details of a new multigrid hierarchical annealing method. Finally, Section 3.6 provides the details of computational implementation of the simulated annealing method. Detailed algorithms for the important parts of the reconstruction process are presented in Appendix B.

3.1 Simulated Annealing

The simulated annealing method presented by Ouenes et al. [88] is used in this work for generating stochastic reconstructions of porous media. As discussed in Chapter 1, simulated annealing is a Monte-Carlo process based optimization method, with a primary advantage of being able to use multiple correlation functions for reconstructions. Figure 3.1 shows the schematic of a typical simulated annealing based reconstruction process. The aim of the

[†]Parts of this chapter have been published. (1) L. M. Pant, S. K. Mitra, and M. Secanell, *Physical Review E*. 90(2):023306, 2014. (2) L. M. Pant, S. K. Mitra, and M. Secanell, *Physical Review E*. 92(6):063303, 2015.

stochastic reconstruction process is to generate a structure with desired statistical properties, i.e., statistical correlation functions. These reference correlation functions can be obtained from reference images of the porous media acquired through imaging techniques, or they can be specified manually. The reconstruction process starts with an initial guess of the structure, which is mostly obtained by randomly generating a black and white pixel distribution with the desired volume fractions.

The initial structure is perturbed and annealed to a structure with the desired correlation functions through the process of simulated annealing. Consider the two phases of porous media as i and j . A known statistical correlation function for phase i in the reference configuration is expressed as $f_0^{(i)}(r)$. The same statistical correlation function in the reconstructed structure is given by $f_{r,t}^{(i)}(r)$ at some step t of the reconstruction process. The aim of the reconstruction procedure is to evolve the reconstructed structure towards a reference structure from the initial guess, i.e., converge $f_{r,t}^{(i)}(r)$ towards $f_0^{(i)}(r)$. The discrepancy in the reconstruction compared to the target at any given step t can be expressed as the L₂-norm of the difference of reference and reconstructed correlation functions. This difference is expressed as follows [63, 64]:

$$E_t = \sum_k \left[f_0^{(i)}(r_k) - f_{r,t}^{(i)}(r_k) \right]^2, \quad (3.1)$$

where r_k represents the length scale at which the correlation function is evaluated. E_t plays the role of energy in simulated annealing, where the target is to minimize it. At every step of the reconstruction, two pixels in phase i and j are swapped. Due to the change in structure, its statistical correlation functions will change, which in turn will change the energy of the system. Taking the new energy of the system as E_{t+1} , the change in energy can be given as $\Delta E_t = E_{t+1} - E_t$. Depending on the change in energy, the swap is either accepted or rejected, which depends upon the adopted minimization procedure. This process is repeated until the energy has reached a value close to zero, i.e., the correlation function of the structure is the same as the reference correlation function.

The primary advantage of the simulated annealing process is its ability to incorporate as many statistical correlation functions for as many phases as desired. The energy for a porous media with m phases (e.g., i, j, k) and n correlation functions for each phase can be

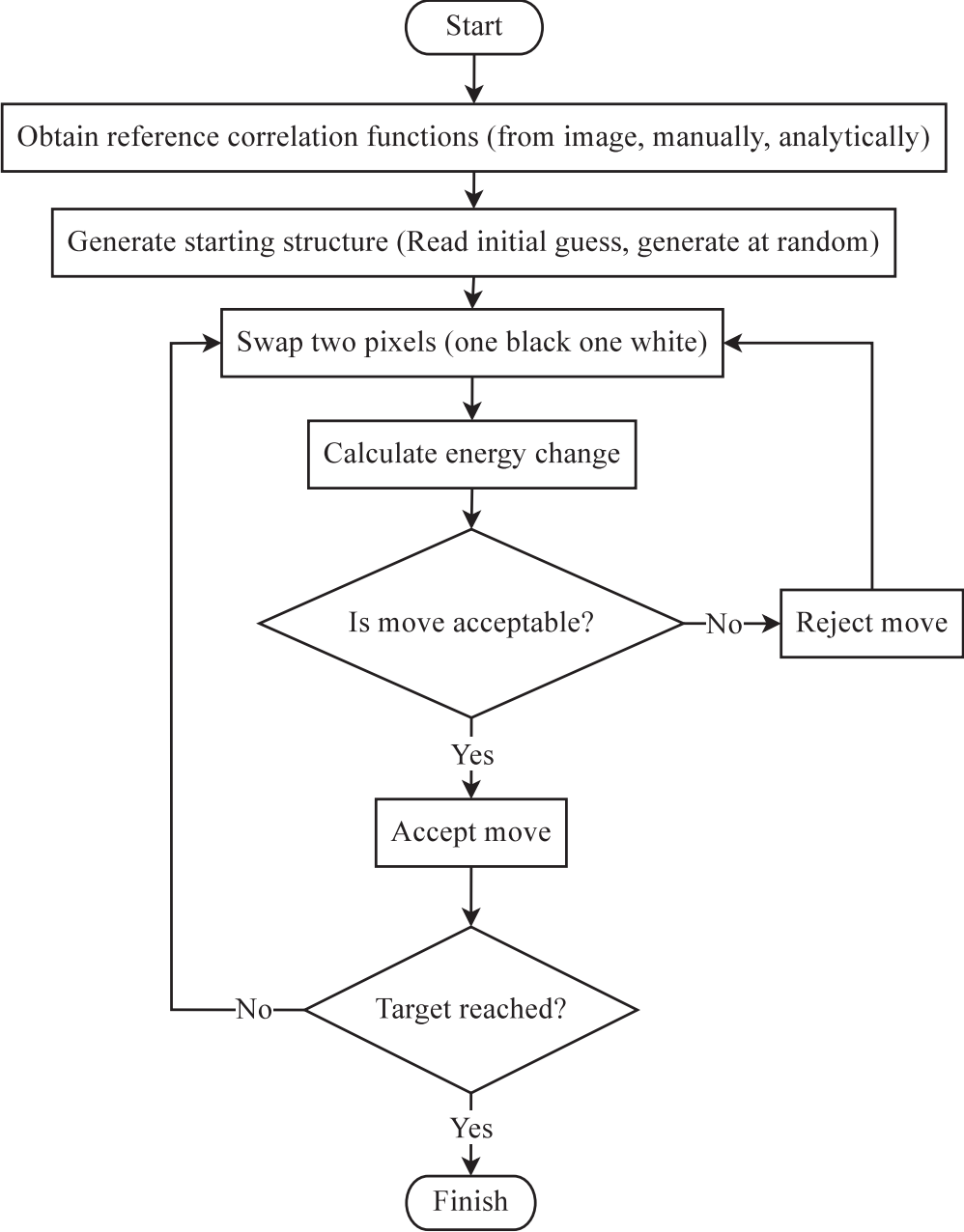


Figure 3.1 – A general schematic of simulated annealing based reconstruction process

defined as follows [63]:

$$E_t = \sum_{i=1}^m \sum_{q=1}^n \sum_{r_k=0}^{r_{max}} \alpha_{i,q} \left[f_0^{(i,q)}(r_k) - f_{r,t}^{(i,q)}(r_k) \right]^2, \quad (3.2)$$

where r_k is the length scale at which the statistical correlation function is evaluated, r_{max} is the maximum length scale at which the correlation function is evaluated, $\alpha_{i,q}$ is the weight assigned to the energy of phase i using the correlation function q , and $f^{i,q}(r_k)$ is q^{th} correlation function for phase i evaluated at length scale r_k . The weight $\alpha_{i,q}$ is used to control the contribution of each correlation function and can be changed during reconstruction. For example, initially a single suitable correlation function can be chosen for quick convergence to a rough estimate, and then more functions can be added to improve the accuracy of the reconstruction.

3.2 Energy Minimization Method

The energy minimization method is at the center of a simulated annealing process. The energy minimization method is used to determine whether to accept or reject a pixel swap based on the amount of energy change it causes. One of the simplest energy minimization method is known as the Deluge algorithm [146]. This algorithm simply accepts all energy decreasing moves and rejects all energy increasing moves. This algorithm is simple in implementation, and results in fast convergence for simple optimization problems; however, for complex optimization problems with multiple local minima, this algorithm can result in locally optimal structures. Since no energy increasing moves are allowed, the optimization may not recover from a local minimum, and therefore it might result in a sub-optimal solution. To avoid these issues, enhanced algorithms are presented in the literature, which are discussed in the following sections.

3.2.1 Probability based Energy Minimization (Metropolis Method)

One of the most common algorithms used for energy minimization in simulated annealing is the probability based acceptance criteria proposed by Metropolis et al. [147]. The probability of accepting a swap is given as follows:

$$p(\Delta E_t) = \begin{cases} 1, & \Delta E_t \leq 0 \\ \exp(-\Delta E_t/T_t), & \Delta E_t > 0, \end{cases} \quad (3.3)$$

where $p(\Delta E_t)$ is the probability of accepting a swap with energy change ΔE_t , and T_t is known as the annealing temperature. It is used to control the reconstructed structure evolution. A higher temperature indicates higher entropy of the system, and allows more energy increasing moves, whereas a lower temperature indicates a cooling structure with lower entropy, where fewer energy increasing moves are permitted.

Similar to the thermal annealing, the simulated annealing method also starts at high temperatures, so that all the possible structure states are sampled. During reconstruction, the temperature is slowly reduced in steps, and the structure is allowed to stabilize before another reduction in temperature. Each level of the temperature reduction is referred to as a Markov chain. By the end of the reconstruction, the temperature is reduced sufficiently to freeze the structure, and the probability of accepting energy increasing moves is almost zero.

The initial temperature of the reconstruction process is decided by knowing the fraction of energy increasing moves to allow at the start. The temperature is selected in such a way that, at the beginning, some fraction p_0 of energy increasing moves are accepted. To estimate the temperature, the energy changes are observed for the first N energy increasing swaps. From these observations, the average energy change is obtained as follows:

$$\overline{\Delta E_{in}} = \frac{1}{N} \sum_{i=1}^N \Delta E_i. \quad (3.4)$$

Once the average energy change is known, the following equation is used to obtain the initial temperature [88].

$$p_0 = \exp(-\overline{\Delta E_{in}}/T_0), \quad (3.5)$$

where p_0 is the probability of accepting energy increasing moves at the beginning of reconstruction (usually 0.5), and T_0 is the initial temperature.

3.2.2 Threshold Energy based Energy Minimization

Dueck [148] has proposed an optimization algorithm known as threshold based simulated annealing method. This method has been used in mathematical optimization problems such as the traveling salesman problem; however, it has been rarely used in the simulated

annealing literature [119]. From the studies in the literature [148], this method shows reduced computational time compared to Metropolis method discussed in Section 3.2.1. Using this method, a pixel swap at a step t is accepted with the following probability [148]:

$$p(\Delta E_t) = \begin{cases} 1, & \Delta E_t \leq E_{th} \\ 0, & \text{Otherwise,} \end{cases} \quad (3.6)$$

where ΔE_t is the energy change after pixel swap, and E_{th} is known as the threshold energy for acceptance. The threshold energy E_{th} is always greater than zero. This ensures that all the energy decreasing moves are accepted, while the extent of accepting energy increasing moves is determined by the magnitude of E_{th} .

The threshold energy plays the same role as the temperature in the Metropolis method. The major difference between these methods is that, while the Metropolis method will always assign a certain non-zero probability to all energy increasing moves, the threshold method does not allow energy increasing moves above a certain magnitude. This reduces the chances of accepting moves which cause high energy increase, and thereby can result in reduced reconstruction time. The threshold method however is not ergodic [119], as certain states of the structure become inaccessible due to the threshold energy. The reconstruction procedure starts with a high threshold energy to allow all possible moves that can result in a reconstruction. The threshold energy is then slowly reduced, so that by the end of the reconstruction no energy increasing moves are accepted. Similar to the temperature, the threshold energy is reduced between Markov chains. The Markov chain length has to be sufficiently high to achieve equilibrium at the given threshold energy.

To obtain the initial threshold energy, a procedure similar to the one used for estimating initial temperature is used. The average energy change for the initial N swaps is obtained using Eq. (3.4). From this, the initial threshold energy is estimated as:

$$E_{th,0} = p_0 \overline{\Delta E_{in}}, \quad (3.7)$$

where p_0 is the probability of accepting an energy increasing swap at the beginning of reconstruction. The choice of p_0 is problem dependent and needs to be optimized for each study.

3.2.3 Termination of Energy Minimization

The aim of the simulated annealing method is to minimize energy. If the structure is realizable with given correlation functions, i.e., in the case the functions are obtained from an existing image, the energy should be minimized to a value of zero, where the statistical correlation functions of the structure are exactly the same as the reference correlation functions. Practically however, a tolerance close to zero is specified. For most of the simulated annealing problems, the annealing is terminated when a threshold/tolerance energy is reached; however, in many situations the tolerance may not be reached due to a sub optimal solution. In these situations, the algorithm may get trapped at a local minima, and may not terminate; therefore, alternative exit conditions must be specified as well. In this work, the following three termination conditions are used to terminate a simulated annealing minimization:

1. *Energy tolerance:* This is the most relevant termination condition. The simulation is terminated when the structure has reached a desired tolerance level, which usually close to zero. In this work, a tolerance of 10^{-6} is used unless specified otherwise. The tolerance is not imposed on the total energy, instead it is imposed on L_2 -norm of each correlation function separately.
2. *Number of failed swaps:* This condition is used when the simulated annealing method is not able to produce any more energy decreasing moves. The simulation is therefore terminated after certain number of consecutive energy increasing moves. For example, the simulation may be terminated when no move has resulted in an energy decrease for X number of Markov chains. In this work, a value of 20 is used for X , unless otherwise specified.
3. *Relative slope of energy:* This condition is used to terminate the minimization procedure, when the rate of energy decrease is lower than a threshold. This is useful, when either very few energy decreasing moves occur, or moves with negligible energy decrease occur. These conditions will not be caught by termination condition 2, and therefore the slope of the energy curve has to be analyzed. In this condition, the simulated annealing is terminated if the relative slope of the energy curve has been below a certain threshold for X number of Markov chains. The slope is defined relative to

the desired energy tolerance. The relative slope across a Markov chain k is defined as:

$$E_{\text{slope},k} = \frac{\Delta E_k}{\text{Iter}_{\text{Markov}} E_{\text{tol}}}, \quad (3.8)$$

where ΔE_k is the energy change in Markov chain k , $\text{Iter}_{\text{Markov}}$ is the size of Markov chain (number of swaps in a Markov chain), and E_{tol} is the desired energy tolerance. In this work, the reconstruction is terminated if the relative slope has been less than 10^{-7} for 20 Markov chains, unless otherwise specified.

3.3 Cooling Mechanisms

The energy minimization process in simulated annealing is based on the annealing of molten metals. In metal annealing, the temperature is slowly reduced in steps, and at each step the structure is allowed to achieve thermal equilibrium. In simulated annealing, a similar ideology is used, where multiple permutations are allowed at each step in order to achieve an organized state. Depending on the energy minimization method, either the temperature or the threshold energy is reduced after each step. A collection of swaps at any step is known as the Markov chain, where each swap is a Markov process.

The temperature reduction method has a significant impact on the success and speed of the reconstruction process. If the temperature is reduced slowly, significant energy increasing swaps will be accepted, which will increase the time required to reach target energy tolerance. On the other hand, if the temperature is reduced too quickly, it might lead to the process getting trapped at a local minima where the temperature is not sufficient to jump over the barrier. An ideal cooling schedule allows the reconstruction to converge quickly to the reference structure, while attaining the global minimum energy [63].

Geman and Geman [149] have shown that a logarithmic temperature schedule given by the following equation is ideal for obtaining a global optimum.

$$T_k = \frac{T_0}{\log(1+k)}, \quad (3.9)$$

where T_k is the temperature of the k^{th} Markov chain. This schedule however, reduces the temperature extremely slowly, and therefore results in excessive reconstruction time [88].

The most common temperature reduction scheme is the power law schedule, given as follows [150] :

$$T_k = \lambda T_{k-1} = \lambda^k T_0, \quad (3.10)$$

where λ is the temperature reduction parameter, which can be adjusted in order to ensure both: convergence and speed.

Most of the reconstruction literature using the power law method use a static value of λ during reconstruction. While it is easy to implement, it may cause reduced convergence. During the reconstruction process for complex geometries, the energy landscape maybe different at different stages. This causes rapid fluctuations in the energy of system. A static schedule does not take these fluctuations into account, and therefore may result in an un-optimized solution or in a high computational time. Siarry et al. [151] have proposed the following ad-hoc formula for a dynamic temperature schedule, which can take into account the evolution of energy:

$$\lambda_k = \max \left[\lambda_{min}, \min \left(\lambda_{max}, \frac{E_{min}}{\bar{E}_{k-1}} \right) \right], \quad (3.11)$$

where λ_k is the temperature reduction factor for k^{th} Markov chain, λ_{min} and λ_{max} are specified by the user, E_{min} is the minimum energy reached, and \bar{E}_{k-1} is the average energy during the $k - 1^{th}$ Markov chain. Using λ_k , the temperature of the k^{th} Markov chain is calculated as follows:

$$T_k = \lambda_k T_{k-1} \quad (3.12)$$

Using the dynamic temperature schedule, it must be kept in mind that $T_k \neq \lambda_k^k T_0$, as the parameter λ_k is most likely different for each Markov chain.

For the threshold energy based method, the threshold energy is also reduced using a power law schedule. Either using a static λ , or with a dynamic λ_k , the threshold energy for Markov chain k is calculated as follows:

$$E_{th,k} = \lambda_k E_{th,k-1}, \quad (3.13)$$

where λ_k is obtained using Eq. (3.11). Even though some researchers have used the dynamic temperature schedule for reconstruction [64, 76, 96], no proper comparisons have been done

to the static schedules in order to see the exact amount of time saving which can result from the dynamic schedule.

3.4 Pixel Swapping Methods

In the simulated annealing based structure optimization, the structure perturbation is performed by swapping pixels of two different phases. Swapping pixels from different phases ensures that the volume fraction of each phase is preserved. Several methods are available in the literature to select the pixels for swapping. The following sections describe the different pixel selection methods which have been used in this work.

3.4.1 Random Pixel Swapping

In random pixel swapping, two pixels in different phases are chosen completely at random. The probability of a particular pixel getting selected is the same for all pixels in a single phase. The initial convergence is good for random pixel swapping, as a significant number of swaps minimize the energy of the system; however, convergence becomes very slow in the later stages of reconstruction once the random initial structure is partially clustered and only a few isolated pixels remain disconnected from the primary clusters. The probability of selecting the isolated pixels in both phases together is very low, and hence they tend to remain in the final reconstruction. Energy minimization is only possible by temporarily moving a pixel out of the already formed clusters. This however, increases the energy of the reconstruction and therefore is not acceptable at later stages of reconstruction due to low temperatures [152]. This results in a very slow convergence towards the final structure, and a final reconstruction with several non-physical segregated pixels.

3.4.2 Surface Pixel Swapping

Interfacial pixel swapping was proposed by Torquato [130] and was later implemented by Capek et al. [71], Rozman and Utz [91], and Tang et al. [98]. In this technique, one needs to select pixels which are at interfaces in order to avoid disturbing any clusters which are already formed. It has shown improvements over random swapping by removing the segregated pixels, and by reducing reconstruction time [98]. Usually, the pixel selection has been done by moving along a random direction from a random starting location until an interface

is encountered [71]. This method can be time consuming. In this work, the interface pixels are identified by their neighborhood. If pixels of other phase are present in immediate neighborhood, the pixel is identified as an interfacial pixel. More details about the neighborhood identification are presented in the next section.

3.4.3 Different Phase Neighbor (DPN) based Pixel Swapping

To avoid the issues related to the random pixel swapping, a biased pixel selection algorithm known as different phase neighbor (DPN) based pixel selection was proposed by Tang et al. [98]. A similar algorithm was earlier proposed by Zhao et al. [78]. The DPN based method preferably selects pixels with more number of different phase neighbors for swapping. Figure 3.2 shows the concept of the pixel neighbors, and shows the biased selection of higher DPN pixels. The neighbors of a pixel are defined as the pixels which are a unit pixel distance away either along axes or along diagonals. A different phase neighbor (DPN) is a neighbor with a different phase than the center pixel. It can be seen in Fig. 3.2(a) that the maximum possible number of DPNs are 8 and 26 in 2-D and 3-D geometries, respectively.

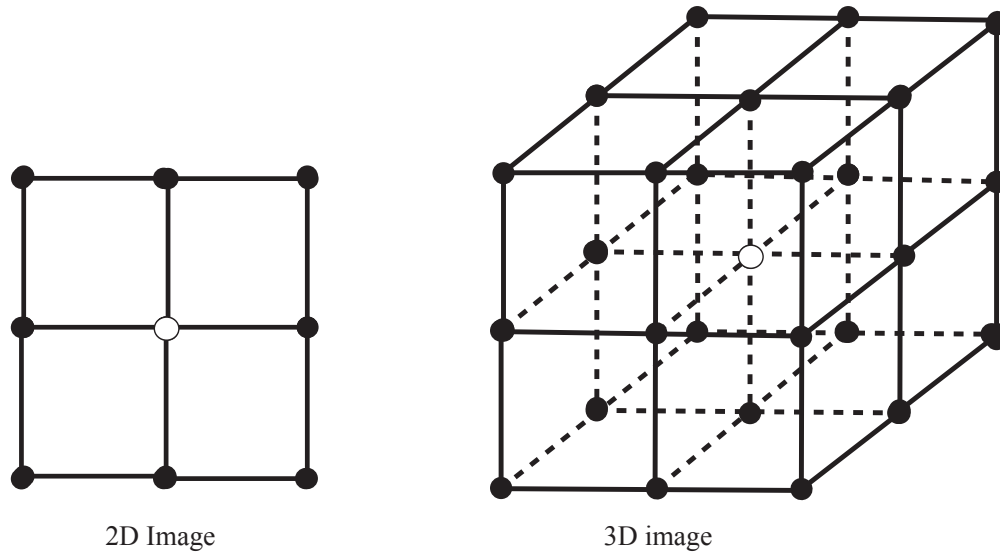
The first step of the DPN method is grouping the pixels in each phase with the same number of DPNs. Define S_i as the set of pixels with $DPN = i$, and $n(S_i)$ as the number of pixels in this set. Further, define the probability of selecting a pixel from this set as $p(S_i)$. Even though the maximum number of DPNs are 8 and 26 in 2-D and 3-D geometries respectively, it is not necessary that all the DPNs will be present in an image. The maximum DPN present in the system is defined as M , where $M = \max(i) : n(S_i) \neq 0$. Since this is the set with highest DPN, it is usually assigned the highest probability m which is manually defined. Tang et al. [98] have used a value of m in the range of 0.4 – 0.6. For the remaining sets, Tang et al. [98] have proposed the following formulation for estimating probability of selection:

$$p(S_i) = \omega n(S_i)(i + 1)^2 \quad i = 0, 1, \dots, M - 1, \quad (3.14)$$

where ω is a weighting factor. Since the probabilities for all sets should add up to unity, the following equation is obtained by summing Eq. (3.14) over all DPNs:

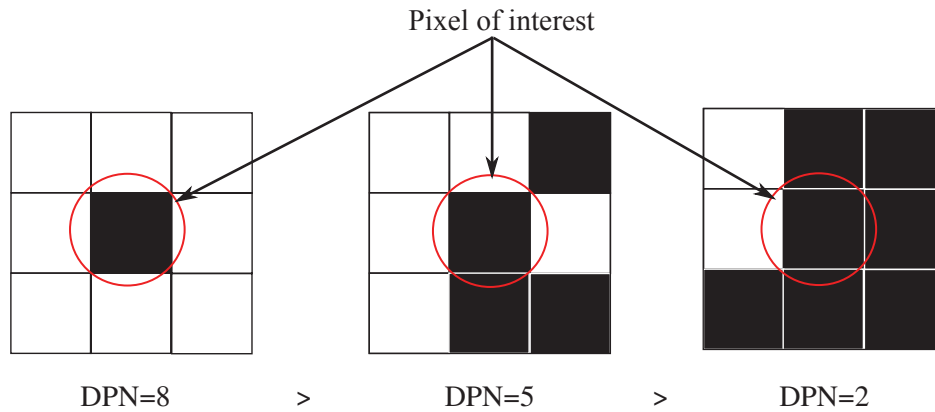
$$\sum_{i=0}^M p(S_i) = \sum_{i=0}^{M-1} \omega n(S_i)(i + 1)^2 + m = 1. \quad (3.15)$$

Since m , i and $n(S_i)$ are known, ω can be obtained using (3.15). Then, the probabilities



- Pixel of interest
- Neighbor pixel

(a) Illustration of neighborhood of a pixel in a 2D and 3D image



(b) Demonstration of biased pixel selection based on DPN. Geometries in decreasing order of priority for pixel of interest.

Figure 3.2 – An illustration of different phase neighbors in image and their selection priority

for all DPN sets can be found. Using these probabilities, a DPN set is selected, and then a random pixel is picked from the selected DPN set. The same procedure is used to select a pixel from another phase. The two selected pixels are then swapped.

Even though the DPN based method has shown to remove pixel noise and reduce reconstruction time, the effects of biased pixel selection on the final structure have not been studied. Since the highest DPN values are preferably selected for swapping, the algorithm essentially tries to minimize the maximum DPN values present in the image. This may cause changes to the structure of the reconstructions. To explore the effects of the DPN method on the reconstructed structure, the following general formula is used for estimating the probability of picking a pixel from set S_i ,

$$p(S_i) = \omega n(S_i)(i + a)^b, \quad (3.16)$$

where a is a parameter to decide whether pixels with zero DPN are allowed to be swapped, and b controls the amount of bias given to the DPN value. The effect of specifying the maximum probability m was also studied by performing two sets of reconstructions: 1) with the biggest set M_i being assigned a probability m ; and 2) with the biggest set getting its probability from Eq. (3.16) as well. For the second case, the normalization factor ω is calculated using the following equation, instead of Eq. (3.15).

$$\sum_{i=0}^M p(S_i) = \sum_{i=0}^M \omega n(S_i)(i + a)^b = 1 \quad (3.17)$$

By varying the values of a and b , and using Eq.(3.17), all possible variations of the pixel swapping methods can be implemented through DPN method. For $a = 1$, and $b = 0$, the probability of each set is proportional to the number of pixels belonging to it. This is the same as random pixel swapping, where the probability of picking a particular type of pixel is proportional to its fraction in the image. For $a = 0$, and $b = \epsilon$ ($0 < \epsilon \ll 1$), the probability of each set is proportional to the number of pixels belonging to it, except for the set with zero DPN, which has a selection probability of zero. This case represents surface swapping. Equation (3.16) therefore provides a way to unify all the swapping methods, and to study the effect of bias on the reconstructed structure. The value of ϵ should be kept quite low, in

order to ensure that, i^ϵ is approximately equal to one for all values of i . A value less than 10^{-4} should be sufficient to satisfy this criteria.

3.5 Multigrid Hierarchical Annealing

To solve the problems of slow convergence in large images, multigrid hierarchical methods have been presented in the literature [49, 127]. These methods employ either a simple hierarchy, which is not able to significantly reduce computational time, or gray-scale methods, where additional phase is introduced for freezing the structure during refinement. The gray-scale methods even though time saving, are complex to implement. To get the best of both methods, i.e., ease of implementation, and the benefits of pixels freezing, a DPN based multigrid hierarchical annealing method is proposed. The multigrid method is initiated by reconstructing a small scale coarse image, which is then continuously refined until the desired size has been achieved. At each scale, the reconstruction is performed as an independent simulated annealing problem. Two critical parts of the multigrid method are the reference image synthesis and the reconstructed image refinement.

To perform a reconstruction at coarser scales (smaller image size), a reference image is required at the corresponding scale. Figure 3.3 shows the schematic of the process for synthesizing coarse reference images from the original high resolution image. Let Ω^s represent a binary image at refinement scale s , where increasing s represents a coarser image. The binary image is represented as a collection of pixel values Ω_{ij}^s . The pixel values at a coarser scale s are obtained by averaging the values of its parent pixels at finer scale $s - 1$, where the average is represented as $\bar{\Omega}_{ij}^{s-1}$

$$\Omega_{ij}^s = \begin{cases} 0 & \text{if } \bar{\Omega}_{ij}^{s-1} < 126.5, \\ 255 & \text{if } \bar{\Omega}_{ij}^{s-1} > 126.5, \\ 0 \text{ or } 255 & \text{Otherwise (i.e. } \bar{\Omega}_{ij}^{s-1} = 126.5). \end{cases} \quad (3.18)$$

For the third case, the pixel values are randomly assigned in such a way that the volume fraction of each phase is conserved; however, due to the digitized nature of the image, the volume fractions may not stay exactly the same at each scale. The reference image synthesis can be thought of as a two step process, which involves linear image coarsening followed by static image thresholding.

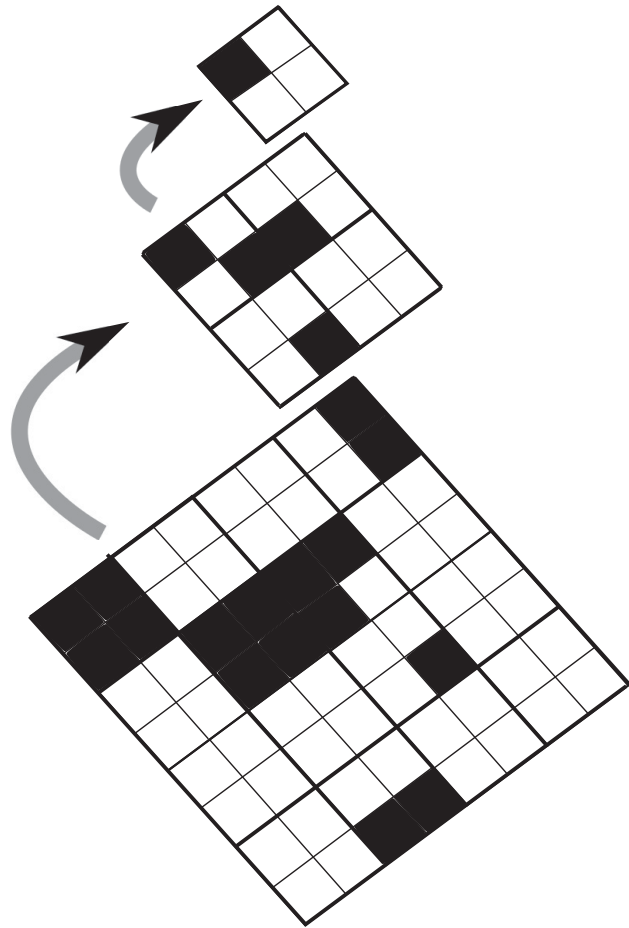


Figure 3.3 – Schematic depicting the reference image synthesis for smaller scales

During the coarsening of images, the pixels belonging to the interior of pixel clusters in the parent image will retain their color after coarsening, as they are surrounded by same color pixels. Many of the pixels at the interfaces of the parent image however, will be in the neighborhood of opposite color pixels. This will result in many of these pixels being assigned a color at random in the coarse scale. It is evident that all the uncertain pixels during coarsening will always end up at the interfaces of coarser images. This fact must be remembered during the opposite process, i.e., refinement during reconstruction.

The second part of the multigrid process is the refinement of images during reconstruction. The reconstruction starts at the coarsest scale, where the reconstruction is performed using simulated annealing with the reference image of corresponding scale. Once a final solution is obtained at this scale, the image is refined by breaking each pixel into four new pixels (children pixels), which are then assigned a phase and a freezing status. The color of the children pixels is kept the same as the parent pixels, in order to keep the volume fractions constant. In order to account for the volume fraction change between scales due to digitization, some pixels are randomly assigned a different phase. This is done in order to match the phase volume fractions of the refined reconstructed structure to the reference image at the corresponding scale. The freezing status is used to decide which pixels will not be allowed to move in the next stage. Since all the uncertain pixels are at the interfaces, they must be allowed to permutate and readjust at refined scales; however, moving the interior pixels will erode the formed clusters, and nullify the reconstruction process which has been performed at smaller scales.

To avoid deterioration of the coarse scale structures, all the internal pixels are frozen in the refined image and all the pixels at the interfaces are non-frozen. In this work, the interface pixels have been handled using one of two separate methods: 1) all the children of interfacial pixels at the coarse scale are allowed to be swapped at the next refined scale, or 2) only the interfacial pixels in the refined structure are allowed to be swapped. When an interfacial pixel at the coarse scale is refined, not all of its children will necessarily be at the interface in the refined image. Since the second method does not allow the non-interfacial children to be swapped, it will reduce the number of pixels to be swapped.

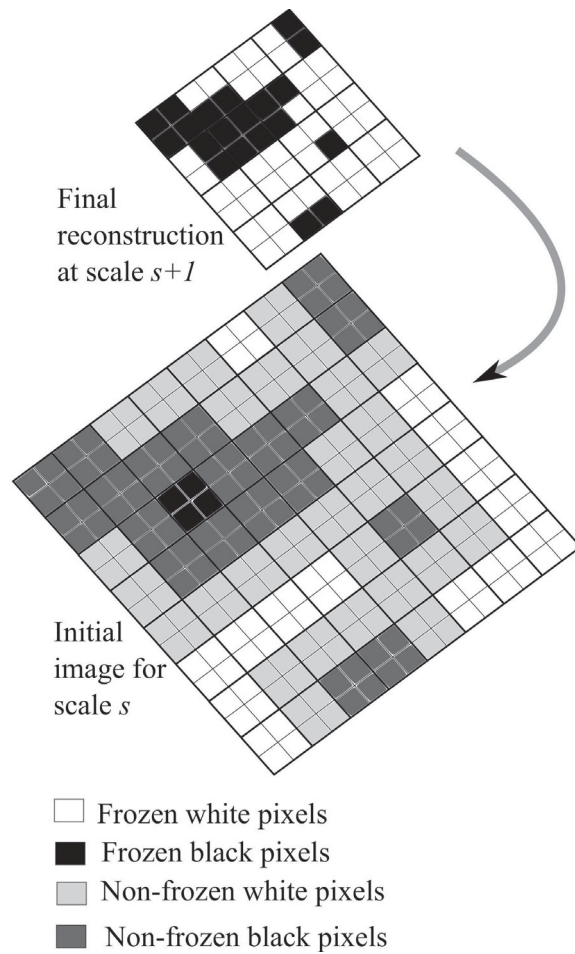


Figure 3.4 – Schematic depicting the reconstructed image refinement and pixel freezing using method 1. DPN values are calculated using periodic boundaries on the images. Gray is only used for depiction and does not represent a new phase

Figure 3.4 shows the schematic of image synthesis and pixel freezing for method 1. The frozen status of a pixel in the refined image is decided based on its parent's DPN value. Children of all the pixels with non zero DPN ($\text{DPN} > 0$, i.e., interfacial pixel) at the coarse scale are not frozen, while the rest of the pixels are frozen. If the parent of a pixel Ω_{ij}^s at a refined scale s is Ω_{ij}^{s+1} at a coarse scale $s + 1$, then, the refined image will be synthesized as:

$$\begin{aligned} \text{Color}(\Omega_{ij}^s) &= \text{Color}(\Omega_{ij}^{s+1}), \\ \text{Status}(\Omega_{ij}^s) &= \begin{cases} \text{Frozen} & \text{if } \text{DPN}_{ij}^{s+1} = 0 \\ \text{Not frozen} & \text{otherwise,} \end{cases} \end{aligned} \quad (3.19)$$

where DPN_{ij}^{s+1} is the number of different phase neighbors for the parent pixel at coarse scale.

For method 2, the frozen status is defined after refinement, and it is based on the DPN of the refined image itself. For this method, the image is synthesized as:

$$\begin{aligned} \text{Color}(\Omega_{ij}^s) &= \text{Color}(\Omega_{ij}^{s+1}), \\ \text{Status}(\Omega_{ij}^s) &= \begin{cases} \text{Frozen} & \text{if } \text{DPN}_{ij}^s = 0 \\ \text{Not frozen} & \text{otherwise,} \end{cases} \end{aligned} \quad (3.20)$$

Not only is the freezing status determined using the DPN information of the image, it is enforced using the DPN methodology as well. While assembling the pixels in different DPN sets, all the pixels with a frozen status are not included in the sets. This ensures that the frozen pixels are not included in swapping process, and are therefore not moved. In summary, the DPN assisted multigrid hierarchical annealing method uses DPN values to freeze the interior pixels of clusters at refined scales. This ensures that the structure does not erode at refined scales, irrespective of the threshold energy/temperature schedule. The swapping of interfacial pixels allows the small scales features to develop at refined scales while keeping the majority of the structure intact. This method also reduces the number of visited pixels at refined stages without needing to introduce gray scale values.

3.6 Computational Implementation

An in-house code has been developed in C++ using object oriented programming for the reconstruction process. Algorithm 3.1 shows the overall procedure of the multigrid hierarchical simulated annealing method using DPN based pixel swapping and threshold based

energy minimization. The following sections present the computational details of some of the important sub-components of the overall reconstruction process in order to enhance the understanding.

3.6.1 Reference Image Scaling

In many cases, the provided reference image may not match the desired reconstruction size. To preserve statistical accuracy, the provided image should always be equal to or larger than the desired reconstruction size. In case the desired reconstruction size is smaller than the provided reference image size, two methods are used for size equalization: a) reference function resizing, and b) image resizing. For function resizing, the reference correlation functions are computed on the large reference image. The correlation information is then removed for lengths which are bigger than desired reconstruction size. The trimmed correlation functions are then used for reconstruction purpose. This technique preserves the physical resolution of the image in reconstructions.

For image resizing, the reference image is rescaled to the desired reconstruction size. The reference correlation functions are then computed on the resized image. Image resizing changes the physical resolution of the image. In this work, a nearest neighbor interpolation method is used for scaling binary images. Section B.2 presents the computational details of the resizing method.

3.6.2 Reference Image Generation for Coarse Scales

The reference images for coarse scales (small lengths) are generated by coarsening the original high resolution reference image. At each scale s , the corresponding reference image is generated by coarsening the reference image at scale $s - 1$, i.e., one refinement scale higher. Section B.1 describes the details of the computational algorithm to obtain the reference images.

3.6.3 DPN Computation

The DPN computations are necessary for pixel swapping and freezing process. This section describes the procedures for computing DPN values, assembling DPN sets, and updating the information after pixel swaps.

Algorithm 3.1 Algorithm for DPN assisted multigrid hierarchical simulated annealing

```
Read original reference image  $\Omega_{\text{ref}}^0$ ;  
Define number of multigrid stages as  $n$ ;  
for  $i = 1$  to  $n-1$  do  
  | Generate coarse image  $\Omega_{\text{ref}}^i$  from  $\Omega_{\text{ref}}^{i-1}$  using Eq. (3.18) ;  
end for  
for  $i = n-1$  to  $0$  do  
  | procedure OBTAIN THE STARTING IMAGE FOR STAGE  $i$   
  |   | if ( $i == (n-1)$ ) then ▷ First (coarsest) stage  
  |   |   | Generate random pixel distribution;  
  |   |   | Set all pixels as not frozen;  
  |   | else ▷ Some refinement stage  
  |   |   | Get reconstructed image at scale  $i + 1$ ;  
  |   |   | Get DPN information at scale  $i + 1$ ;  
  |   |   | Generate pixel color values using Eq. (3.19) or (3.20);  
  |   |   | Generate pixel status using Eq. (3.19) or (3.20);  
  |   | end if  
  | end procedure  
  | procedure OBTAIN RECONSTRUCTION FOR STAGE  $i$   
  |   | Get reference correlation functions from image  $\Omega_i^{\text{ref}}$ ;  
  |   | Read starting image ( $\Omega_{\text{rec}}^i$ );  
  |   | while None of termination condition reached do  
  |   |   | Swap two pixels among not frozen set using DPN method;  
  |   |   | Compute update correlation functions;  
  |   |   | Compute new energy and  $\Delta E$ ;  
  |   |   | Compute applicable threshold energy  $E_{\text{th}}$ ;  
  |   |   | if  $\Delta E \leq E_{\text{th}}$  then  
  |   |   |   | Accept pixel swap;  
  |   |   |   | Update image information;  
  |   |   |   | Reset  $\text{Iter}_{\text{failed}}$ ;  
  |   |   | else  
  |   |   |   | Reset image information;  
  |   |   |   | Increment  $\text{Iter}_{\text{failed}}$ ;  
  |   |   | end if  
  |   |   | Increment total iterations;  
  |   | end while  
  |   | Save the final image  $\Omega_{\text{rec}}^i$ ;  
  | end procedure  
end for
```

| Key | Pixel array |
|----------|---|
| 0 | $(a_1, b_1, c_1), (a_2, b_2, c_2), \dots$ |
| 1 | $(i_1, j_1, k_1), (i_2, j_2, k_2), \dots$ |
| 2 | $(l_1, m_1, n_1), (l_2, m_2, n_2), \dots$ |
| \vdots | \vdots |
| M | $(x_1, y_1, z_1), (x_2, y_2, z_2), \dots$ |

Figure 3.5 – An illustration of DPN sets stored using maps

DPN Value Computation

The DPN value for each pixel is calculated by scanning its neighbors and reading their phase values. Two arrays, DPN_w and DPN_b , are used to store the DPN information for white and black pixels, respectively. Whenever a pixel of different phase is found in the neighborhood, the DPN count is increased. The final DPN count is assigned to the pixel. To avoid edge effects, periodic boundary condition is always used for DPN calculations. Section B.3.1 describes the computational details of the DPN computation method.

DPN Set Computation

The DPN sets are necessary to know the number of pixels with certain DPN value. The simplest way of knowing the number of pixels belonging to each DPN is by moving through the image and based on the DPN value, incrementing its corresponding count. This method however, requires that the DPN sets be re-computed after each pixel swap. The work by Tang et al. [98] does not provide any details to overcome these issues.

In this work, C++ maps are used to store all the pixels belonging to a certain DPN. Two maps, Set_w and Set_b , are created for white and black pixels respectively. An illustration of a DPN set using the maps is shown in Fig. 3.5. Each map contains a key index, which is the DPN value, and an array of pixels corresponding to the key. The array contains the coordinates of all the pixels in given phase with a DPN value equal to the key. The array is assembled by scanning through the image, and assigning each pixel to its corresponding DPN set based on its phase and DPN value. The algorithmic details for assembling the DPN

sets are given in section B.4. The number of pixels belonging to a set can be easily found out using the array size, and can be then used for probability calculations.

DPN Information Updating

After each pixel swap, the phases of the two pixels change. Furthermore, the pixel swap changes the neighborhood for the pixels which are neighbor to the swapped pixels. The DPN information for the swapped pixels and their neighbors must be therefore updated after each swap. Since the DPN values of all the pixels are stored individually, only the changed DPN values need to be calculated. The DPN values for the swapped pixels and their neighbors are computed using the Algorithm B.3. Once the DPN arrays, DPN_w and DPN_b , are updated, the DPN sets need to be updated. Before updating the DPN arrays, the swapped pixels and their neighbors are removed from their corresponding sets. Once the new DPN values for the pixels are calculated, they are inserted in the sets corresponding to their new DPN values. Section B.5 presents the computational details of the method.

3.6.4 Accounting for Anisotropy

Even though most of the statistical analysis is done assuming a isotropic random media assumption, the anisotropy can be partially accounted for in this work. As discussed in section 2.3, the correlation function for each row and column are individually calculated. In order to facilitate partial accounting for anisotropy, the correlation functions for each direction are averaged separately. The net energy due to some q^{th} correlation function for phase i at reconstruction step t is then given as:

$$E_{q,t}^{(i)} = \sum_{x_k=0}^{x_{max}} \left[f_0^{(i,q)}(x_k) - f_{r,t}^{(i,q)}(x_k) \right]^2 + \sum_{y_k=0}^{y_{max}} \left[f_0^{(i,q)}(y_k) - f_{r,t}^{(i,q)}(y_k) \right]^2 + \sum_{z_k=0}^{z_{max}} \left[f_0^{(i,q)}(z_k) - f_{r,t}^{(i,q)}(z_k) \right]^2, \quad (3.21)$$

where x_k , y_k , and z_k are the correlation function evaluation distances in x , y and z directions respectively. By accounting for separate correlation functions in the three orthogonal directions, some of the anisotropy can be taken into account. It would however require sampling in multiple directions to completely account for the anisotropy. Keeping the x , y , and z directions separate also makes it easy to reconstruct porous media with different lengths in different directions.

3.6.5 Updating Correlation Functions

As discussed in Section 2.3, the correlation functions are individually computed for each row and column of the image. They are then summed over all rows and averaged to get the overall correlation function for the image. In this work, the correlation functions for each row and column are stored separately in order to facilitate quick updating after a pixel swap. Due to the orthogonal sampling in correlation function computing, only the correlation functions for corresponding rows and columns will change after a pixel swap. The correlation functions for changed rows and column are re-computed and stored. To avoid summing all the rows/columns after each swap, the sum of all the rows or columns is also saved. After updating the functions, the new sum and new average can be easily calculated as:

$$\begin{aligned} \text{New sum} &= \text{old sum} - \text{old function} + \text{new function} \\ \text{New average function} &= \frac{\text{New sum}}{\text{Number of rows/columns}}. \end{aligned} \tag{3.22}$$

Using the new average function, the corresponding system energy can be calculated using Eq. (3.21).

Chapter 4

Stochastic Analysis and Reconstruction of Porous Media[†]

This chapter describes the analysis and reconstruction studies carried out using the different methodologies described in Chapter 3. All the different methods are compared against each other in terms of the reconstruction accuracy and computational time. Section 4.1 describes the different random materials studied in this work, their imaging methodologies, and image processing methods for obtaining binary images. Section 4.2 discusses the results of stochastic analysis on different materials, and the structural properties obtained using statistical analysis. Section 4.3 provides a detailed study of the different reconstructions performed using different methods. The effects of energy minimization method, annealing method, pixel swapping method, multigrid method, and number of correlation functions are studied. Section 4.4 demonstrates the ability of performing reconstructions of large 3D images using the best methods obtained from Section 4.3. Finally, Section 4.5 summarizes the findings, and shows a comparison of current method against methods available in literature.

4.1 Materials and Methods

4.1.1 Materials

Three porous materials: a) an inkjet printed catalyst layer (CL) of polymer electrolyte fuel cell (PEFC) [111], b) a titanium (Ti) foam mesh used as a gas diffusion layer in electrolyzers, and c) a ceramic are analyzed. These porous media were selected in order to be able to analyze three porous media with different porosity, pore network and pore morphology.

[†]Parts of this chapter have been published. (1) L. M. Pant, S. K. Mitra, and M. Secanell, *Physical Review E*. 90(2):023306, 2014. (2) L. M. Pant, S. K. Mitra, and M. Secanell, *Physical Review E*. 92(6):063303, 2015.

While the PEFC CL is a low porosity porous media with nanometer size pores, the Ti foam is a high porosity media with pores in micrometer range. The ceramic is a medium porosity media with a different porous structure than the CL or Ti foam.

4.1.2 Imaging and Image Processing

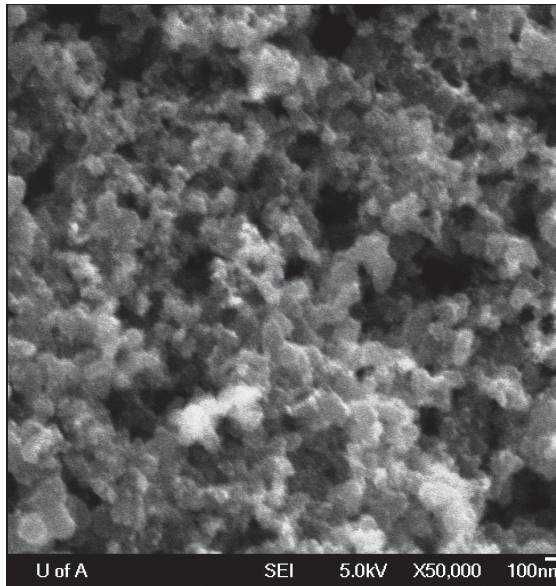
Several imaging techniques were used to obtain two-dimensional and three-dimensional images of the porous media. The imaging techniques were selected based on requirements, and availability of equipment. While the 2D images are used for reconstruction method assessments, comparisons and parametric studies, the 3D images are primarily used for transport studies.

2D Image of PEFC Catalyst Layer

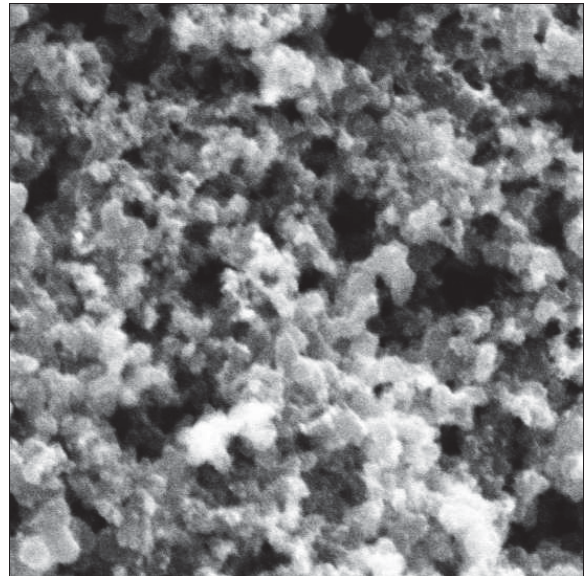
For initial studies on the different reconstruction methods, a 2D image of a PEFC CL was used. Two-dimensional images are less time consuming to reconstruct and therefore multiple instances can be reconstructed for better statistical analysis. Furthermore, the 2D reconstructions are easy for visualization and qualitative comparison. A scanning electron microscope (SEM) at University of Alberta was used for obtaining an in-plane 2D image of PEFC CL. Figure 4.1(a) shows the raw SEM image of PEFC catalyst layer with a size of 960×960 pixels. The image resolution is approximately $2nm/\text{pixel}$. First, a histogram equalization of the image is performed. The image is then passed through a Gaussian filter, followed by a smoothing operation using a 3×3 Kernel. Finally, the image is binarized using a manual thresholding. Any remaining noise is removed using a median filter. Figure 4.1 shows the SEM image in different stages of pre-processing, which culminates in the final binary image as shown in Fig. 4.1(d).

2D Images of Ceramic

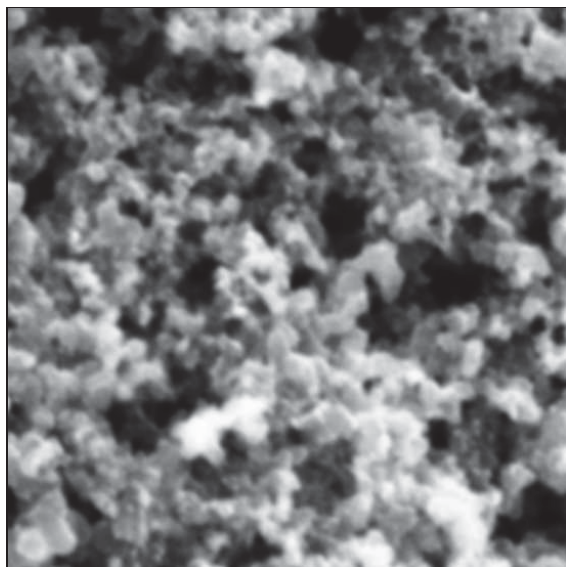
The 2D image of the ceramic was received from collaborators at Commonwealth Scientific and Industrial Research Organisation (CSIRO), Land and water division, Australia. The image was obtained using X-ray microtomography. More details about the imaging method are not available. Figure 4.2 shows the provided binary 2D image of the ceramic structure with a size of 500×500 pixels. It can be observed that the porous structure and morphology of the ceramic is different than the PEFC catalyst layer sample.



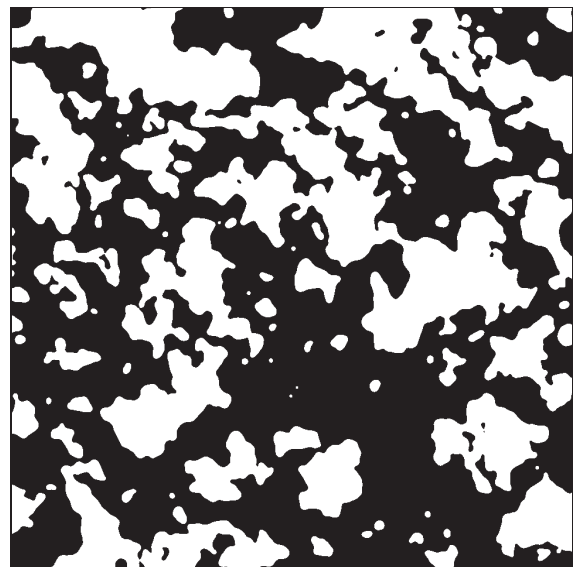
(a) A raw 2D SEM image of PEFC CL



(b) Image after cropping and histogram equalization



(c) Image after Gaussian filtering and smoothing



(d) The binary 2D SEM image of PEFC CL after thresholding (white is void, and black is solid)

Figure 4.1 – Evolution of 2D SEM image of a PEFC catalyst layer from raw image to final binary image

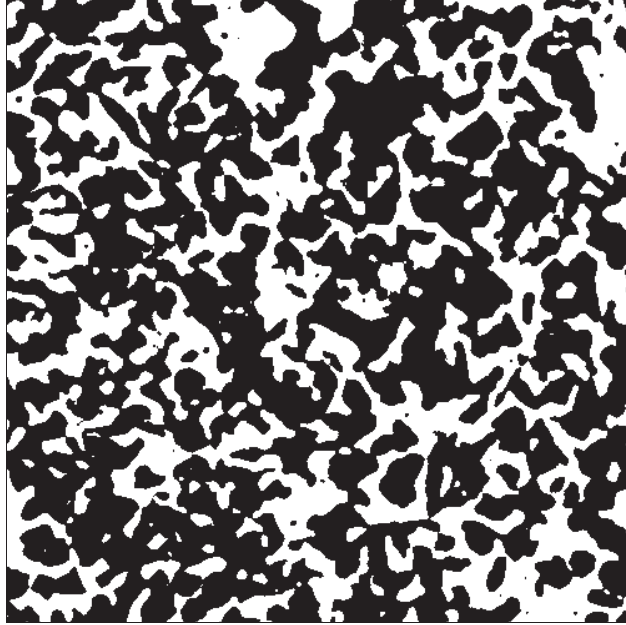
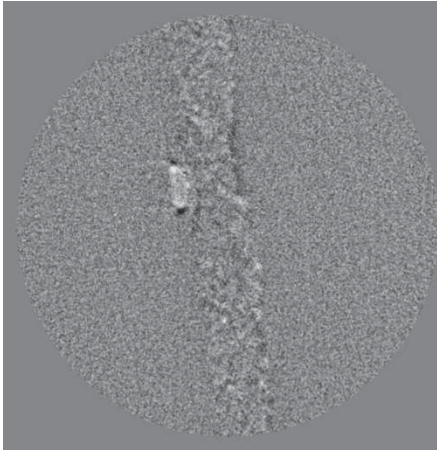


Figure 4.2 – Binary 2D image of ceramic obtained using X-ray microtomography (white is void, and black is solid)

3D Images of PEFC Catalyst Layer

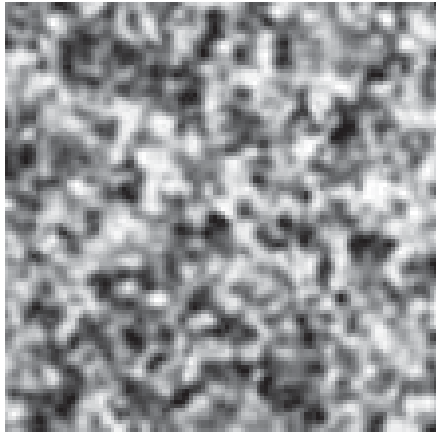
While the 2D images are easy to obtain, reconstruct and visualize, they are not useful for simulating transport processes. A three-dimensional structure is required as physical domain for transport simulation. The 3D structures can be used for estimating transport properties of reference structures, which provide benchmarks for the reconstructed geometries. For accurate estimation of transport properties in a reference structure, the 3D image should resolve structural features in all three directions accurately. The 3D image of catalyst layer was obtained using a nano-CT system (UltraXRM-L200, Xradia Inc., Pleasanton, CA, USA) at Carnegie Mellon University [29]. The pixel resolution of the nano-CT images is 16nm/pixel in each direction. Figure 4.3(a) shows a 2D slice of the reconstructed structure. Each of the slices were rotated to align them in orthogonal directions. The catalyst layer area from each slice is then extracted by cropping the image. Figure 4.3(b) shows a cropped and rotated 2D slice of the PEFC nano-CT. Due to the small thickness of PEFC CL, only 100 pixels were obtained in x direction. To keep the dimensions similar in all three directions, subsections of 100×100 pixels were selected from each slice. The histogram of all the slices were equalized for contrast adjustment. The slices were then passed through a Gaussian filter for noise reduction. Finally, Sauvola and Pietikainen [153] algorithm is used for determining the



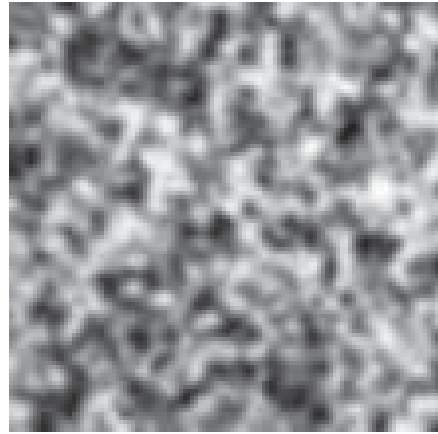
(a) A raw 2D slice generated from nano-CT tomographic reconstruction algorithm



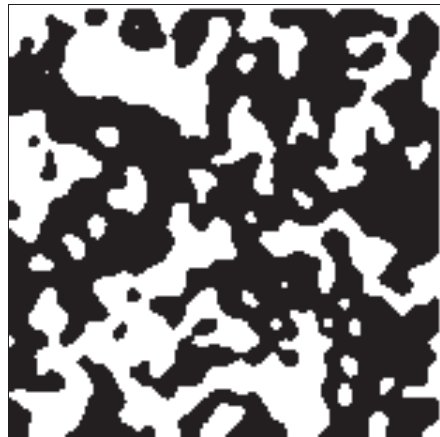
(b) The image after rotating and cropping. Red box shows the sub-sample area



(c) The sub-sample of the 2D slice after histogram equalization



(d) The 2D section after Gaussian filtering



(e) Final binary 2D slice of a the nano-CT image

Figure 4.3 – Evolution a 2D slice of PEFC CL nano-CT image during different stages of image pre-processing

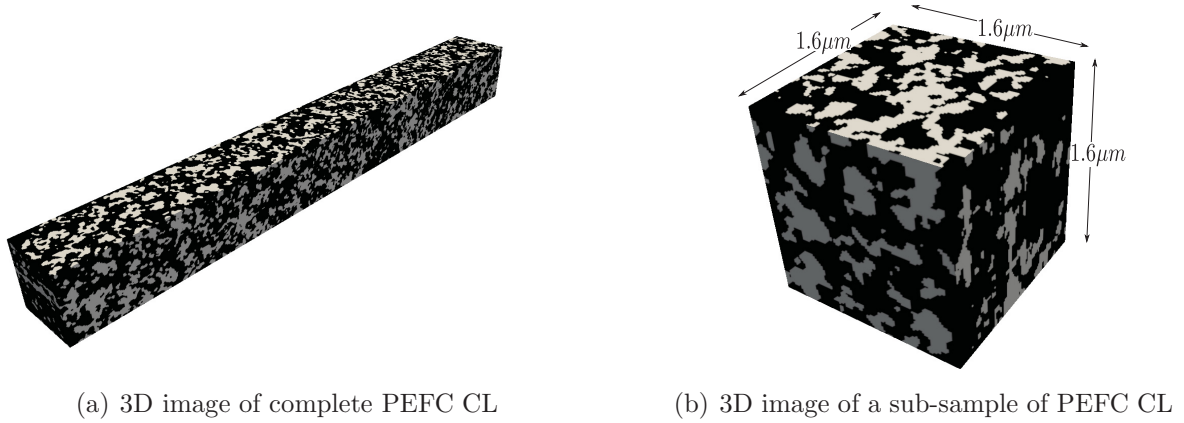
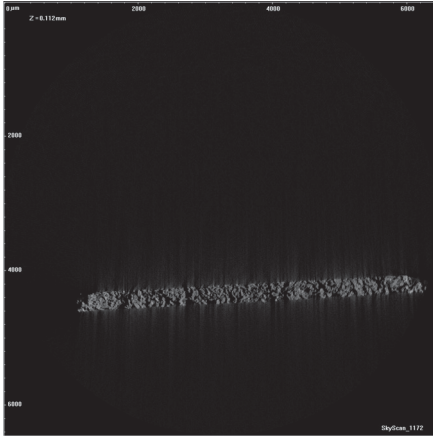


Figure 4.4 – A 3D binary image of one of the nano-CT samples for PEFC CL (white is void, and black is solid)

image threshold for binarization of each slice. The Sauvola and Pietikainen [153] algorithm is used instead of manual thresholding, because manual thresholding is error prone and time consuming for multiple slices. Figure 4.3 shows a 2D slice of the nano CT at different stages of pre-processing. From the large nano-CT image, nine 3D sub-samples of dimension $100 \times 100 \times 100$ pixels were extracted. Figure 4.4 shows a 3D binary image of the entire sample, and of one of the nine sub-samples.

3D images of Ti Foam

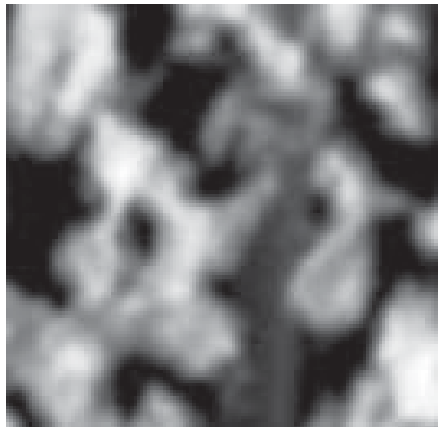
The Ti foam is a high porosity media with pore feature sizes in the range of $5\text{-}10 \mu\text{m}$. A micro-CT is therefore sufficient for resolving the features of this media. A micro-CT system (SkyScan 1172, Bruker microCT, Kartuizersweg, Kontich, Belgium) at University of Alberta [154] was used for imaging the Ti foam. The pixel resolution of the micro-CT images is $1.6\mu\text{m}/\text{pixel}$ in each direction. Figure 4.5(a) shows a 2D slice of the reconstructed structure. Each of the slices were rotated to align them in orthogonal directions. The Ti foam image from each slice is then extracted by cropping the image. Figure 4.5(b) shows a cropped and rotated 2D slice of the Ti foam image. Only 100 pixels are available along the thickness of the Ti foam (y – direction). To keep the dimensions similar in all three directions, sub-sections of 100×100 pixels were selected from each of the slices. The histogram of all the slices were equalized for contrast adjustment. The slices were then passed through a Gaussian filter for noise reduction. Finally, Sauvola and Pietikainen [153] algorithm is used for determining the image threshold for binarization of each slice. Figure 4.5 shows a 2D slice of the micro-CT



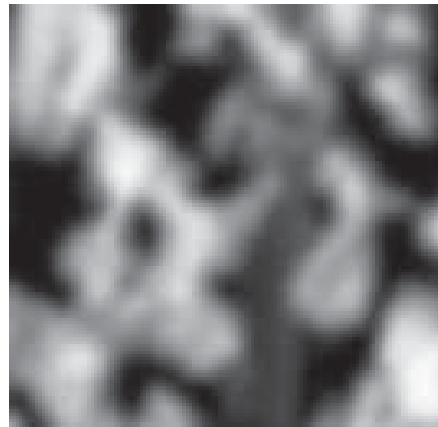
(a) A raw 2D slice of Ti foam generated from micro-CT tomographic reconstruction algorithm



(b) The image after rotating and cropping. Red box shows the sub-sample area



(c) The sub-sample of the 2D slice after histogram equalization



(d) The 2D section after Gaussian filtering



(e) Final binary 2D slice of a the micro-CT image

Figure 4.5 – Evolution a 2D slice of Ti foam micro-CT image during different stages of image pre-processing

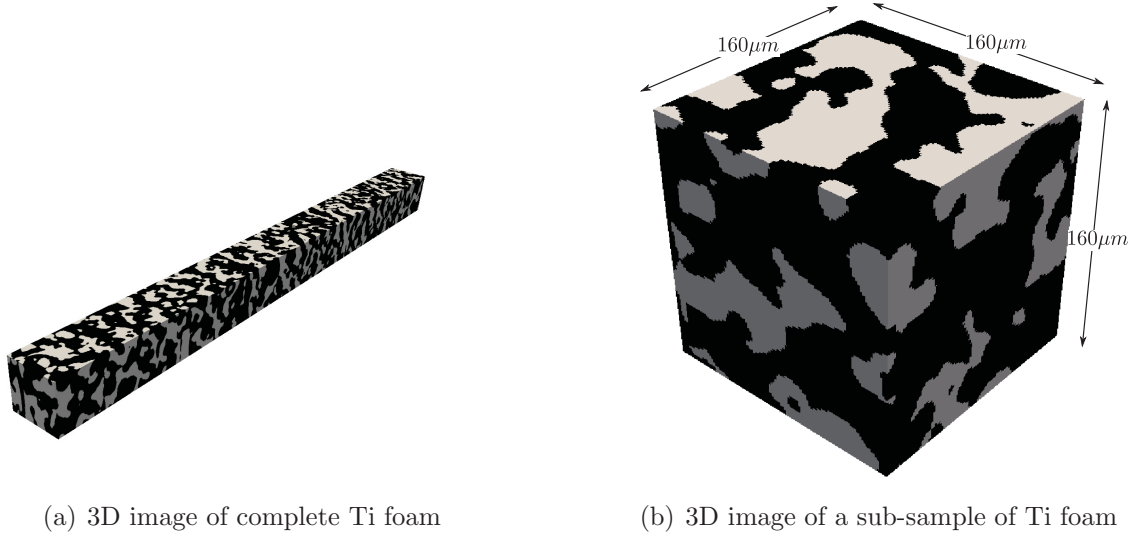


Figure 4.6 – 3D binary images of the Ti foam (white is void, and black is solid)

image at different stages of pre-processing. From the large micro-CT image, thirteen 3D sub-samples of dimension $100 \times 100 \times 100$ pixels were extracted. Figure 4.6 shows a 3D image of the entire micro-CT sample, and a sub-sample after binarization.

4.2 Stochastic Analysis

Statistical analysis is used for characterizing the different porous media used in this study. Comparison of correlation functions in each direction is done to assess the isotropy in each porous media. The two-point correlation function is used to estimate the interface area, and the characteristic length of the porous media. Cluster functions are analyzed to study the percolating volume fraction. The lineal path function and chord length function are used to analyze the maximum cluster sizes in orthogonal directions.

The characteristic length is obtained by integrating the autocorrelation function. Equation (2.21) can be rearranged to obtain the following expression for characteristic length [77]:

$$\bar{\lambda} = \int_0^\infty (\phi_i - \phi_i^2) S_2^{(i)}(r) dr. \quad (4.1)$$

The interface area can be calculated by finding the slope of the two-point correlation function at $r = 0$. Using a linear expression for slope estimation, the specific surface area is obtained

as follows:

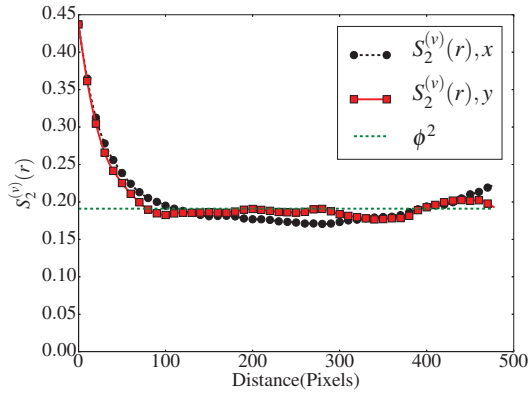
$$s = \beta[S_2(0) - S_2(1)], \quad (4.2)$$

where the value of β is 4 and 6 for 2D and 3D images, respectively [63]. Since the statistical area calculations rely on large sample sizes, finite sample size results in slight discrepancies; therefore, the actual surface area was also calculated by counting the interfaces in the image. The percolating volume is analyzed by finding clusters percolating from one face to the opposing phase. The total volume of the percolating clusters is then identified as the percolating volume. The percolating volume analysis is only performed for the 3D images, as it is a transport parameter relevant only to 3D structures.

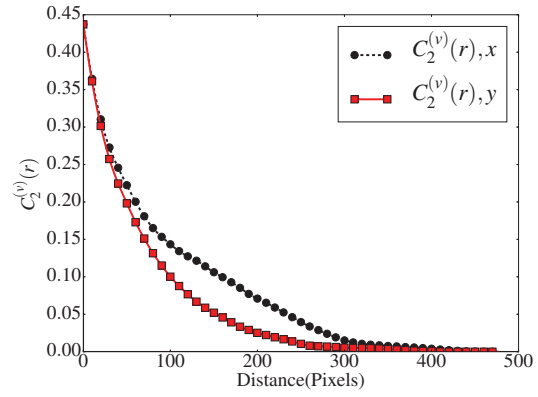
4.2.1 Analysis of 2D PEFC Catalyst Layer Image

The PEFC CL 2D image shown in Fig. 4.1(d) with a size of 960×960 pixels was analyzed to obtain different correlation functions and properties. Based on image analysis, the void volume fraction was found to be 0.437. Figure 4.7 shows different correlation functions in x and y directions for the 2D PEFC CL image. Using the two-point correlation function shown in Fig. 4.7(a) with Eq. (4.1), the characteristic length of the image was found to be approximately 24 pixels. Any reconstructions or analysis on the 2D image must be therefore performed at a size significantly larger than this. Another characteristic length can be obtained by observing the length at which the two-point correlation function reaches ϕ^2 [60]. This is the length after which the long-range pixel interactions are insignificant. The length is around 100 pixels. Any reconstructions or analysis therefore must be performed for sizes larger than 100 pixels. Looking at the lineal path and chord length functions in Figs. 4.7(d) and 4.7(e), it is seen that the maximum feature size in the image is around 300 pixels. In order to account for all the features therefore, the reconstructions should be either performed at a size larger than 300 pixels, or in a smaller resized image with lower resolution.

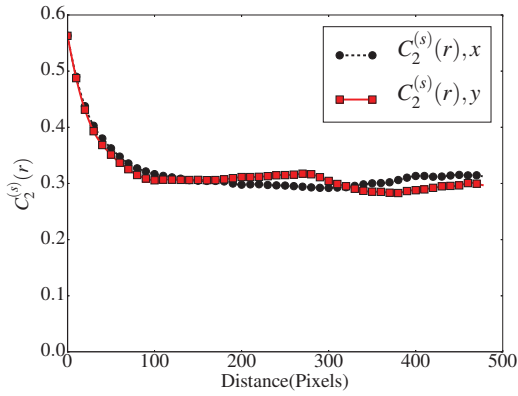
The statistical estimate of specific interface area (surface area per unit volume) using Eq. (4.2) is 0.0314/pixel, while the actual specific interface area is 0.03147/pixel. It shows that the two-point correlation function can accurately estimate the interface area. Looking at the different correlation functions, it can be observed that the correlation functions in x and y direction are different, signifying that the media is not isotropic. Analysis of the void phase



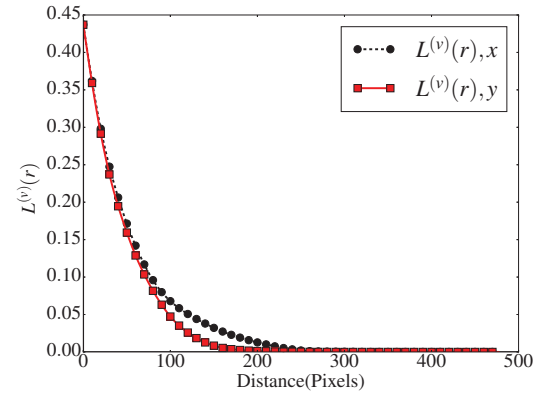
(a) Void two-point correlation function



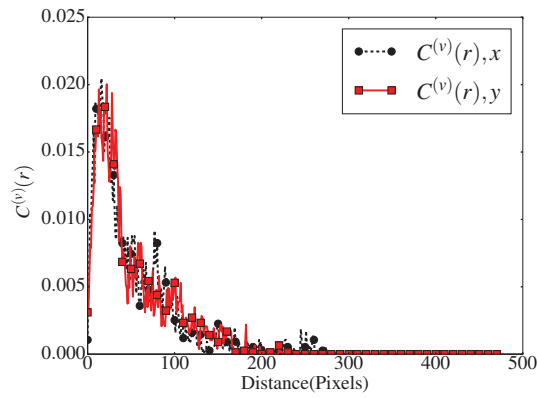
(b) Void two-point cluster function



(c) Solid two-point cluster function



(d) Void lineal path function



(e) Void chord length function

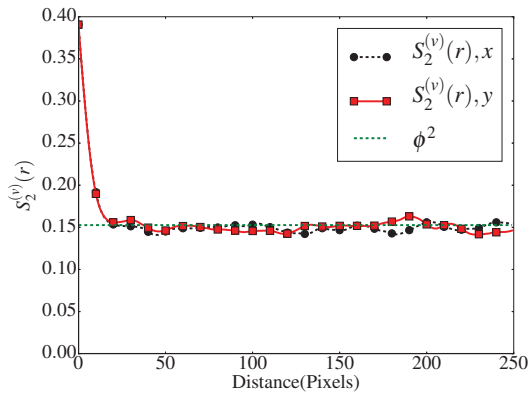
Figure 4.7 – Correlation functions in x and y directions for the 2D PEFC CL image

two-point cluster function in Fig. 4.7(b) shows that the void phase does not percolate across the entire image length, as the cluster function reaches zero at around 300 pixels. The non percolating void phase can also be observed in the image. On the other hand, analysis of solid phase two-point cluster function in Fig. 4.7(c) shows that the solid phase percolates across the domain, which is also evident from the actual image.

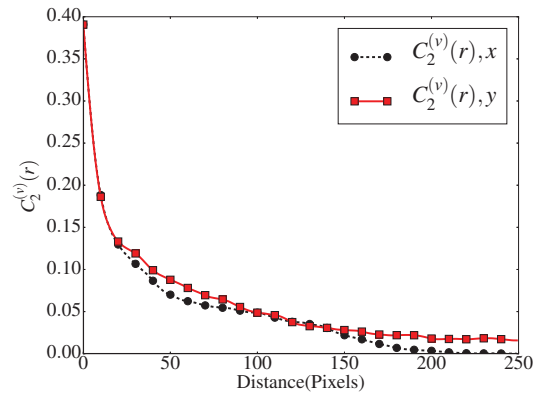
4.2.2 Analysis of 2D Ceramic Image

The ceramic 2D image shown in Fig. 4.2 is of size 500×500 pixels. The ceramic has a void volume fraction of 0.391. Figure 4.8 shows different correlation functions in x and y directions for the ceramic image. Integrating the two-point correlation function shown in Fig. 4.8(a) with Eq. (4.1), the characteristic length of the ceramic is found to be approximately 9 pixels. Comparing with the 2D PEFC CL image, this length is much smaller, as the features in the ceramic image are smaller compared to the PEFC image. The length at which the two-point correlation function reaches its final value of ϕ^2 is around 25 pixels, which is also smaller than the PEFC image. The representative size of the ceramic must be therefore smaller than PEFC CL. Looking at the lineal path and chord length functions in Figs. 4.8(d) and 4.8(e), it is seen that the maximum feature size in the ceramic image is around 100 pixels. The reconstructions must be therefore performed at a size larger than 100 pixels

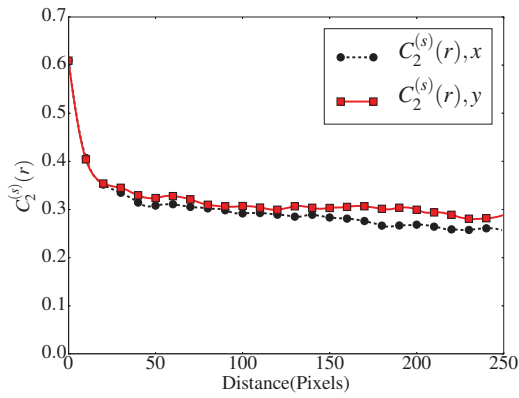
The statistical estimate of specific surface area for ceramic is obtained as 0.107/pixel, while the actual specific interface area is 0.1067/pixel. The specific surface area of the ceramic is much higher compared to the PEFC, as the ceramic contains higher number of smaller features in the same image size thereby increasing its interface area. Comparing the x and y direction correlation functions for the ceramic in Fig. 4.8, it is seen that the difference between x and y directions is quite small, making the ceramic an almost isotropic media. Analyzing the void and solid phase two-point cluster functions shown in Figs. 4.8(b), and 4.8(c) respectively, it can be seen that while the void phase is not percolating across the domain, the solid phase percolates. These observations can also be verified by analyzing the actual image.



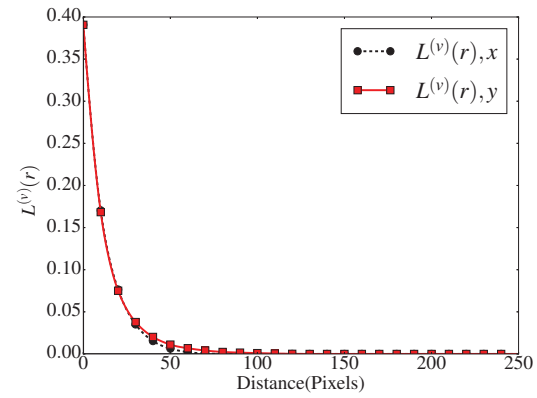
(a) Void two-point correlation function



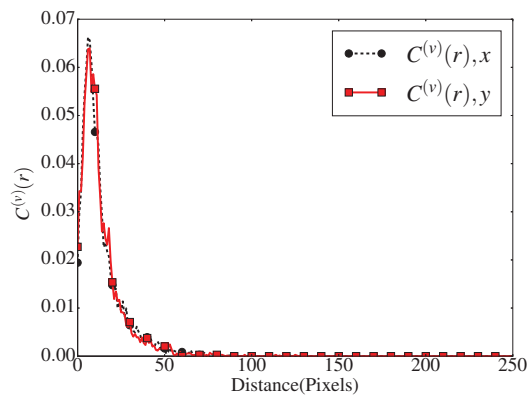
(b) Void two-point cluster function



(c) Solid two-point cluster function



(d) Void lineal path function



(e) Void chord length function

Figure 4.8 – Correlation functions in x and y directions for the 2D ceramic image

4.2.3 Analysis of 3D PEFC Catalyst Layer Images

As discussed earlier, nine sub-samples were extracted from the nano-CT image. All the sub-samples are of size $100 \times 100 \times 100$ pixels. All the images were analyzed and their properties measured. The average void volume fraction among the nine samples is 0.32 ± 0.005 . Figure 4.9 shows the correlation functions for all the images. Since the 3D images are also used for physical analysis, the correlation functions are also plotted against physical distance. Integrating the two-point correlation function shown in Fig. 4.9(a), the characteristic length for the nine samples was found to be 1.24 ± 0.05 pixels. This is much smaller than the length obtained using 2D SEM image. The main reason for that is the loss of resolution between the SEM image and nano CT image, which results in nanoCT accounting for fewer features compared to the SEM image. The length at which the two-point correlation function reaches its asymptotic value is around 10 pixels. Analysis of lineal path and chord length functions in Figs. 4.9(d), and 4.9(e) shows that the maximum feature size in the PEFC CL 3D image is around 30 pixels.

The statistical estimate for specific surface area was obtained as $0.291 \pm 0.001/\text{pixel}$, while the actual specific interface area was obtained as $0.29 \pm 0.002/\text{pixel}$. Looking at the shaded regions in Fig. 4.9, it can be seen that the margin of error between samples is negligible, which shows that the catalyst layer and the resulting nanoCT image is homogeneous. Furthermore, the correlation functions in all the three directions are close to each other, leading to the conclusion that the images are almost isotropic. The percolating volume fractions for the void and solid phase were found to be 0.99 ± 0.001 , and 0.999 ± 0.0001 respectively. This shows that almost the entire void and solid phase is connected and percolating. This can also be observed by analyzing the void and solid phase two-point cluster functions shown in Figs. 4.9(b), and 4.9(c) respectively. The functions reach a plateau and do not decrease to zero, signifying a domain wide connectivity.

4.2.4 Analysis of 3D Titanium Foam Images

All the thirteen sub-sample of the Ti foam microCT images were analyzed. All the sub-samples are of size $100 \times 100 \times 100$ pixels. The average void volume fraction among the thirteen samples is 0.36 ± 0.009 . Figure 4.10 shows the correlation functions for all the images. Integrating the two-point correlation function shown in Fig. 4.10(a), the characteristic

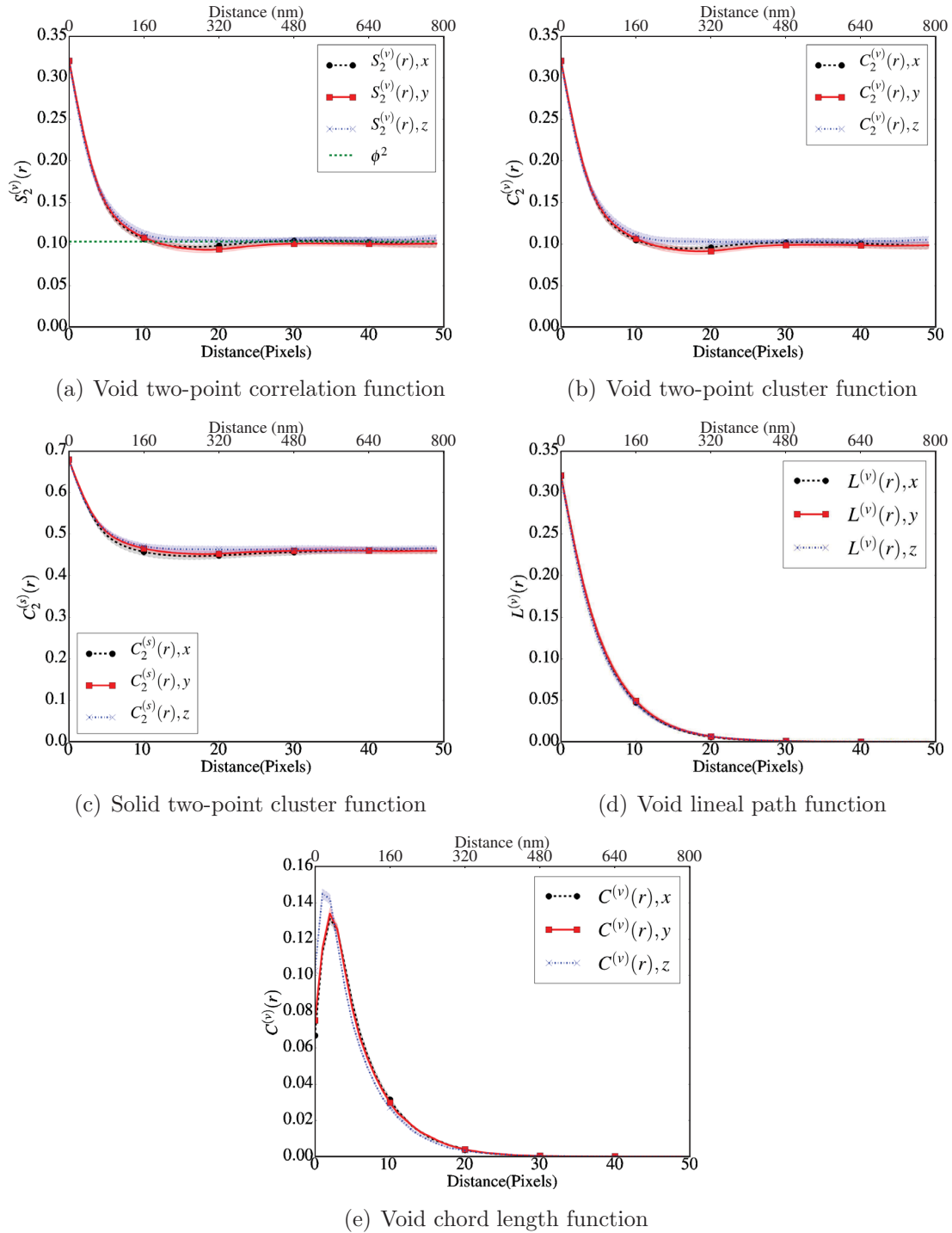


Figure 4.9 – Correlation functions in x , y and z directions for the 3D PEFC CL images. Solid line shows the average, and shaded region shows the 95% margin of error.

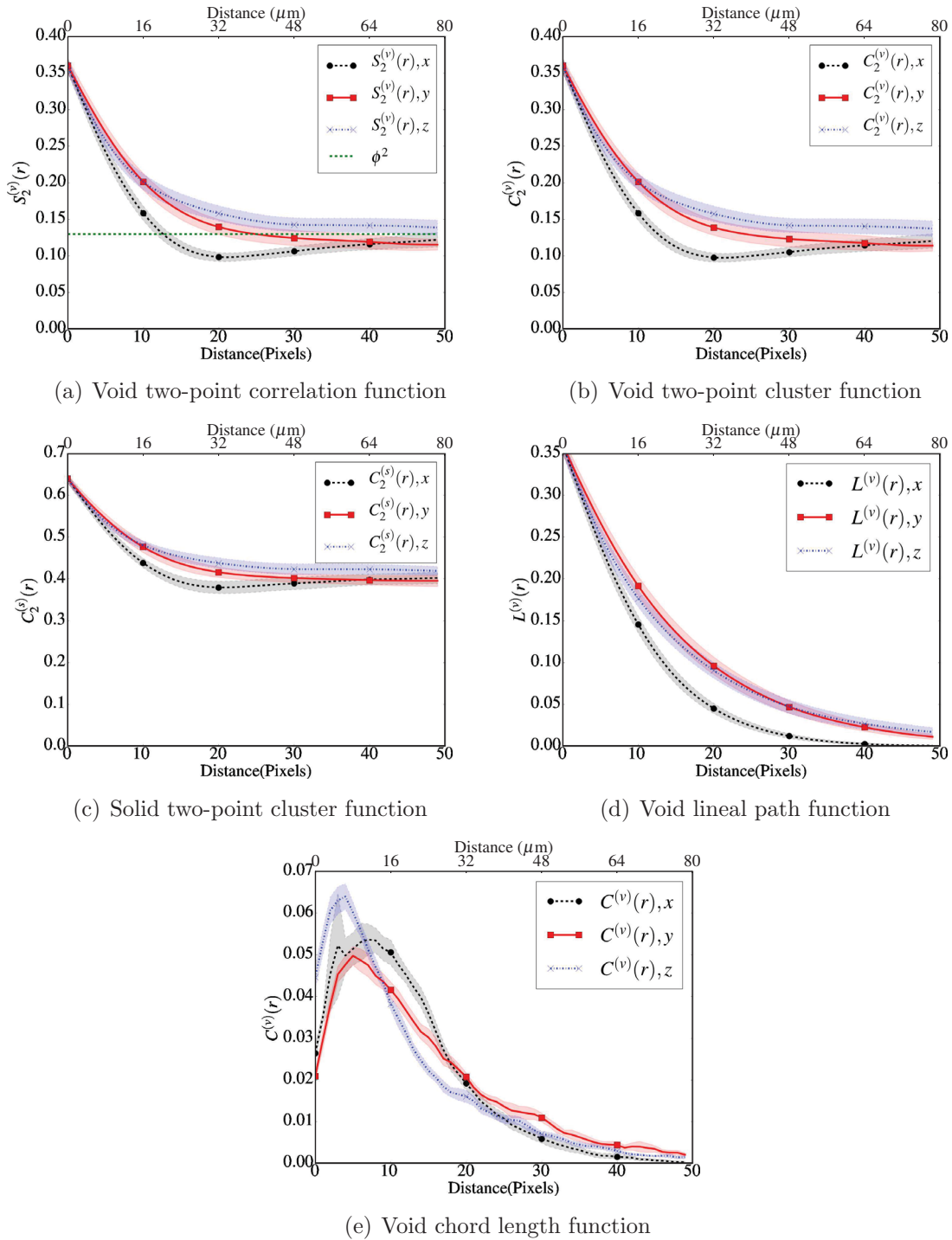


Figure 4.10 – Correlation functions in x , y and z directions for the 3D Ti foam images. Solid line shows the average, and shaded region shows the 95% margin of error.

length for the thirteen samples was found to be 1.81 ± 0.11 pixels. The asymptotic convergence length of the two-point correlation function value is around 50 pixels. Analyzing lineal path and chord length functions in Figs. 4.10(d), and 4.10(e), it can be seen that the maximum feature size is also approximately 50 pixels. The reconstructions must be therefore larger than 50 pixels.

The statistical estimate for specific surface area was obtained as 0.135 ± 0.003 , while the actual specific interface area was obtained as $0.136 \pm 0.003/\text{pixel}$. Looking at the shaded regions in Fig. 4.10, it can be seen that the margin of error between samples is small, but not negligible, which shows that the Ti foam may have minor inhomogeneity. The correlation functions in all the directions are not the same, with the x -direction correlation functions being significantly different than other two directions. This signifies a strong anisotropy in x -direction, which also indicates that the transport properties in x -direction should be different from the other two directions. The percolating volume fractions for the void and solid phase were found to be 0.994 ± 0.009 , and 0.999 ± 0.0001 respectively. This shows that almost the entire void and solid phase is connected and percolating. This can also be observed by analyzing the void and solid phase two-point cluster functions shown in Figs. 4.10(b), and 4.10(c) respectively. The functions reach a plateau and do not decrease to zero, signifying a domain wide connectivity.

4.3 Stochastic Reconstruction

Stochastic reconstruction of the different media described in the previous section is performed. The aim of the reconstruction studies is to assess the accuracy and effectiveness of the reconstruction algorithm and resulting computer program. Furthermore, the studies analyze the effect of different reconstruction methods and parameters on the accuracy and speed of the reconstruction process.

4.3.1 Effect of Energy Minimization Method

To understand the effect of the energy minimization method, i.e. the effect of probability or threshold based acceptance, a square grid pattern of size 60×60 pixels, as shown in Fig. 4.11(a) was chosen as the reference geometry. The square grid is easy to reconstruct and

Table 4.1 – Parameters used for reconstruction of square grid pattern.

| Parameter | Value |
|---|----------------|
| Maximum number of allowed failed Markov chains (X) | 20 |
| Minimum relative slope of energy curve required before termination | 10^{-7} |
| Markov chain size | 5000 |
| Fixed temperature update factor for probability based method (λ) | 0.9 |
| Fixed energy threshold update factor for threshold based method (λ) | 0.9 |
| Pixel swapping method | random |
| Boundary condition for reference function computing | periodic |
| Boundary condition for reconstructed function computing | periodic |
| Initial probability for probability based acceptance method (p_0) | 0.5 |
| Initial factor for threshold based acceptance method(p_0) | 0.5 |
| Initial iterations N | 2000 |
| Number of multigrid levels | 1 |
| Correlation function used | $S_2^{(v)}(r)$ |
| Number of processors | 2 |

provides a qualitative validation of the accuracy of the reconstruction program. The parameters used for reconstruction are given in Table 4.1. The aim is to study the effect of the minimization method; therefore, conventional random swapping with only void phase two point correlation function is used. A static annealing schedule is used in both cases. Even though the reference correlation functions are usually calculated without a periodic boundary condition, for this specific case they were computed using periodic boundaries, as the reference geometry is periodic. Figures 4.11(b) and 4.11(c) show the reconstructed images of size 60×60 pixels using probability based and threshold based algorithms respectively. It can be seen that, apart from a few pixels, the square grid pattern is reconstructed accurately by both methods. The periodic nature of the reconstruction process can also be observed in the reconstructed structure. Being a simple geometry, it can be completely characterized by its two point correlation function [119].

To gain further understanding of both methods, 20 reconstructions were obtained using both algorithms on a computer with an Intel(R) Core(TM) i7-2600 CPU with a clock speed of 3.40 GHz. The reconstructions were terminated when either of the three termination conditions discussed in Section 3.2.3 was reached. The average value of energy at the end of the simulation was $(1.26 \pm 0.29) \times 10^{-5}$ for threshold based, and $(2.05 \pm 0.44) \times 10^{-5}$ for

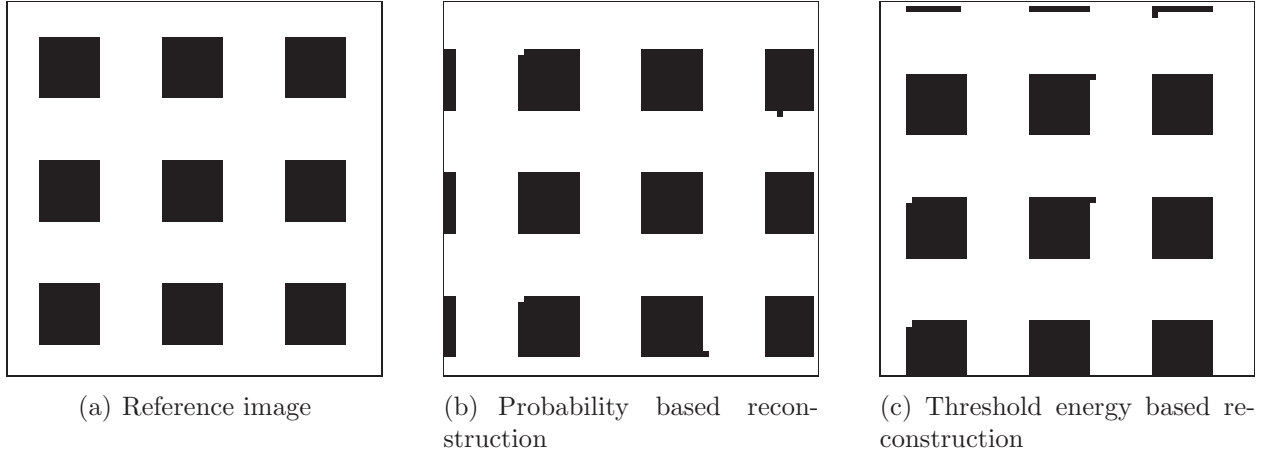


Figure 4.11 – An illustration of reference and reconstructed square grid pattern

probability based algorithm. The margins of error are with a 95% confidence interval. It was observed that the accuracy of reconstruction is marginally higher for the threshold based method. The average number of iterations for final convergence were $(7.73 \pm 0.61) \times 10^5$ for threshold based method, and $(7.51 \pm 0.70) \times 10^5$ for probability based method. The reconstruction time was (67.29 ± 5.13) s for threshold energy based method, and (65.50 ± 5.89) s for probability based method. It can be seen that both minimization methods require similar time, and number of iterations; however, the threshold based method results in lower energy, which shows a minor speed advantage of threshold based method. Figure 4.12 shows the evolution of energy during reconstruction for both algorithms. It is observed that the threshold based algorithm is slower in the beginning, but becomes faster at the later stages of reconstruction. It may be therefore marginally faster for low tolerance reconstructions.

The grid of squares is a simple reconstruction geometry with a simple energy landscape [119]; therefore, it can not provide definite information about the effectiveness of the threshold energy based algorithm. For more extensive testing of the threshold energy based algorithm, a complex energy landscape is required. A random porous media is quite complex and contains stochastic information at several length scales. The 2D PEFC CL image shown in Fig. 4.1(d) is therefore used as reference. To reduce computational time while remaining statistically representative, the image is resized to a size of 200×200 pixels using nearest neighbor interpolation as described in Section 3.6.1. This size is still significantly higher than the characteristic length of 24 pixels, and the asymptotic convergence length of 100

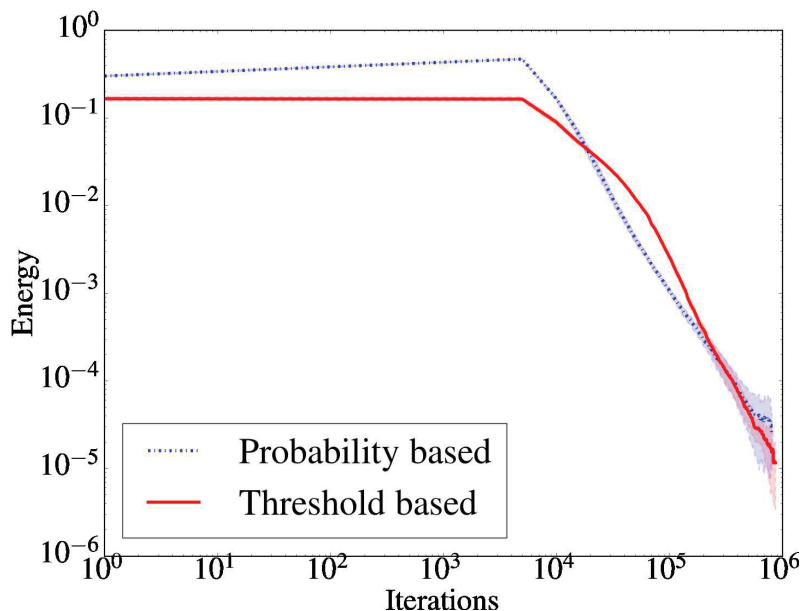
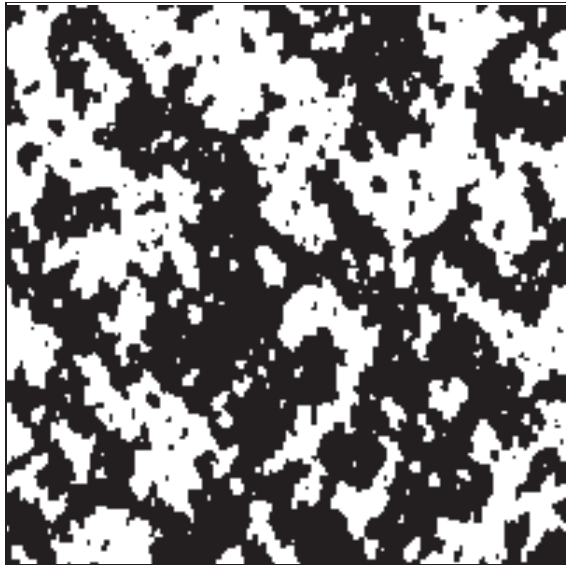


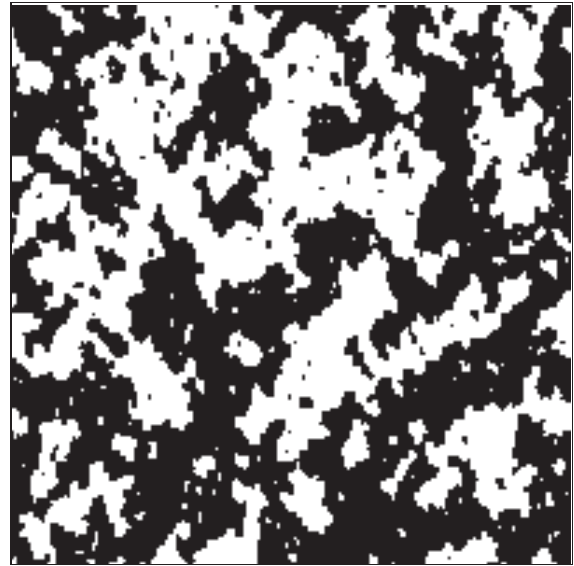
Figure 4.12 – Comparison of energy convergence for probability based and threshold based algorithms for a square grid geometry (solid line represents average and shaded region represents 95% confidence interval)

pixels. The reconstructed image size was fixed at 200×200 pixels², fixed annealing factor λ was changed to 0.95 for both probability and threshold based methods, initial iterations N were changed to 5000, and reference functions were computed using non-periodic boundary condition. The rest of the reconstruction parameters are the same as in Table 4.1.

Figures 4.13(a) and 4.13(b) show the reconstructions using probability based and threshold energy based algorithms respectively. Qualitatively, the images look similar, with significant noise due to random pixel swapping. A computer with an Intel(R) Core(TM) i7-2600 CPU with a clock speed of 3.40 GHz was used to perform 20 simulations using both methods. The average value of final energy was found to be $(1.61 \pm 0.19) \times 10^{-6}$ for probability based, and $(1.51 \pm 0.14) \times 10^{-6}$ for threshold based algorithm, therefore providing minor advantage with threshold energy based method. The average number of iterations was $(1.93 \pm 0.18) \times 10^6$ for probability based and $(2.17 \pm 0.19) \times 10^6$ for threshold based method, showing a minor advantage for the probability based method. The reconstruction time was (1865.3 ± 169.3) s for the threshold energy based method, and (1665.7 ± 155.3) s for the probability based method. Overall, for similar target energy, it can be concluded that both methods will provide similar reconstruction speed. Figure 4.14 shows the convergence profile for both algorithms in the



(a) Reconstruction using probability based method



(b) Reconstruction using threshold based method

Figure 4.13 – Reconstructions of 2D PEFC catalyst layer image using probability and threshold based method

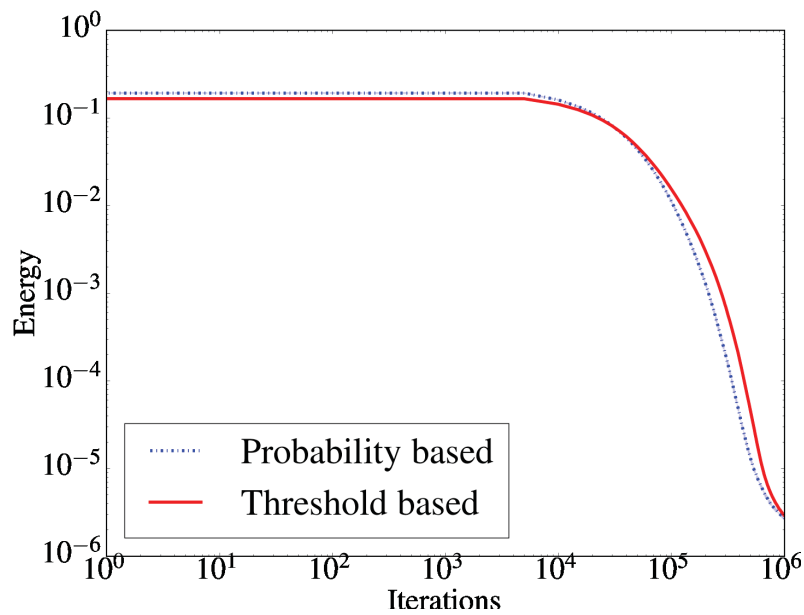


Figure 4.14 – Comparison of energy convergence for probability based and threshold based algorithms for a PEFC catalyst layer image (solid line represents average and shaded region represents 95% confidence interval. The margin is not visible, as the error margin is negligible)

reconstruction of 2D PEFC catalyst layer. Again, it can be observed that the threshold based algorithm is slower than the probability based method at the beginning, but catches up to it in the later stages. Since both the algorithms show similar reconstruction speed, one of them was chosen for further studies. Due to its ease of implementation, and potential of speed up for lower energy tolerances, threshold based method will be used in all the studies in upcoming sections.

4.3.2 Effect of Cooling Schedule

Most of the reconstruction studies in literature use a static annealing schedule. The static schedule uses a constant reduction factor λ for updating temperature or threshold energy after each Markov chain. The static schedule does not take into account rapid changes in energy, and may therefore result in the algorithm getting trapped at a local minimum (in case the static annealing is too fast for problem), or high reconstruction time (in case the static annealing is too slow for the problem). A dynamic schedule changes the reduction factor λ between Markov chains to account for the slope of the energy landscape. Since a direct comparison between static and dynamic methods is not available in literature, a detailed comparison between the two methods is carried out. The 2D PEFC image shown in Fig. 4.1(d) was resized to a size of 200×200 pixels, and was used as the reference image. The static annealing factor λ was fixed at 0.95, while for the dynamic annealing factors λ_{min} and λ_{max} were fixed at 0.4 and 0.95 respectively. A threshold energy based minimization method is used. The number of initial iterations are 5000, and the rest of the parameters are the same as in Table 4.1.

For a quantitative comparison between these methods, a computer with an Intel(R) Core(TM) i7-2600 CPU with a clock speed of 3.40 GHz was used to perform 20 simulations using both methods. The average final energy of the reconstructions was $(1.51 \pm 0.14) \times 10^{-6}$ for static annealing, and $(1.58 \pm 0.08) \times 10^{-6}$ for dynamic annealing, showing a marginal change in the accuracy between the methods. The average number of iterations were $(2.17 \pm 0.19) \times 10^6$ for static annealing, and $(1.91 \pm 0.13) \times 10^6$ for dynamic annealing, showing around 10% reduction in iterations. Overall, the dynamic method seems to improve the reconstruction speed by only a small margin.

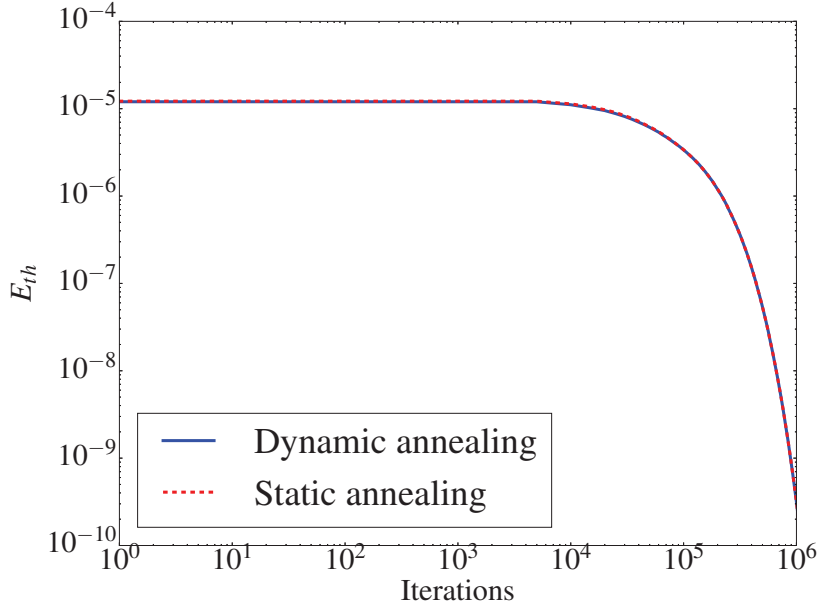


Figure 4.15 – Comparison of threshold energy change during reconstruction for static and dynamic methods

To understand the effect of static and dynamic annealing, the threshold energy at each Markov chain was observed. Figure 4.15 shows the comparison of threshold energy change during one of the reconstructions for static and dynamic methods. It can be seen that the threshold energy for both method changes at virtually the same rate, suggesting that the adaptive λ is mostly close to λ_{max} , which is also the same as the λ for static annealing. During analysis of the adaptive method, it was observed that the predicted λ using Eq. (3.11) is mostly the same as λ_{max} , and never the same as λ_{min} . The reason for the calculated λ being close to λ_{max} is the slow reduction of energy. For a slow reduction in energy, E_{min} , and \bar{E} for a Markov chain are similar in Eq. (3.11), thereby resulting in a value of λ close to λ_{max} . The adaptive method may result in better time savings for an annealing problem with simple energy landscape and fast cooling, which is rarely the case with random porous media. Also, in the beginning of biased pixel selection methods the cooling rate is high, and therefore, a lower λ can be observed for first few Markov chains. Overall, it can be concluded that the adaptive annealing schedule results only in small improvements over the static method due the slow annealing nature of most of the porous media. The adaptive method is not used for any comparison studies, as it may change the reconstruction time differently for different methods, making it difficult to perform a direct comparison.

4.3.3 Effect of Pixel Swapping

The last sections showed that the reconstructions of PEFC catalyst layers using random swapping produce significant noise in the image. Due to random selection of pixels, removing this noise is not possible during late stages of reconstruction [98]. To reduce the noise, and speedup the reconstructions, biased pixel selection algorithms, e.g., DPN and interface pixel swapping methods are studied. The primary purpose of biased pixel selection methods is to refine the reconstructed image. Since each swap in the biased methods takes more time than random swap due to additional computations, a coarsely reconstructed image using random swapping is used as starting point, which is then refined using random, interfacial and DPN based pixel swapping algorithms to save time. To compare the swapping methods, the PEFC catalyst layer 2D image given in Fig. 4.1(d) is resized to 200×200 pixels, and chosen as the reference structure. The coarse reconstruction shown in Fig. 4.16 is used as the starting structure, which corresponds to an energy value of $E = 5 \times 10^{-3}$. The initial structure is generated by random pixel swapping, which is terminated when most of the pixels have formed the clusters, as can be seen in the image. These initial clusters form the backbone of the image for further refinement and clustering of remaining pixels. All the parameters are similar to the ones used in the previous section for the PEFC catalyst layer (Table 4.3), and the threshold based method is used for energy minimization. The initial factor p_0 was reduced to 0.25 in order to reduce the initial energy threshold, which in turn prevents unraveling (melting) of the initial structure. A static annealing schedule was used, as a dynamic schedule can cause the reconstruction time to vary between reconstructions. The reconstructions were terminated when either of the three termination conditions discussed in Section 3.2.3 was reached. The parameters for termination are given in Table 4.1.

Initially, a comparison between conventional random swapping, conventional interface swapping, and conventional DPN swapping is done. The surface swapping is done by searching for interfacial pixels at random. The DPN swapping implements the formulation proposed by Tang et al. [98], as given in Eq. (3.14). Ten reconstructions were performed from the initial image given in Fig. 4.16 with each method on a computer with an Intel(R) Core(TM) i7-2600 CPU with a clock speed of 3.40 GHz. Figures 4.17(a) 4.17(b) and 4.17(c) shows the reconstructions using random interfacial and DPN swapping, respectively. It can be observed that surface and DPN method have significantly improved the reconstructed

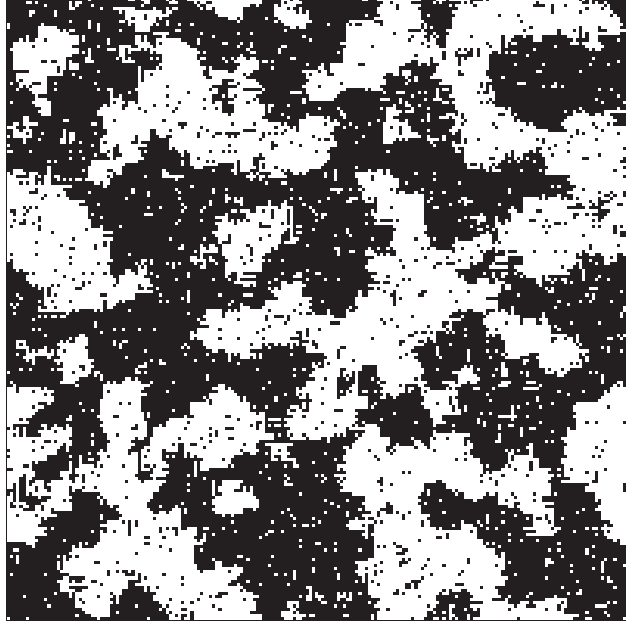
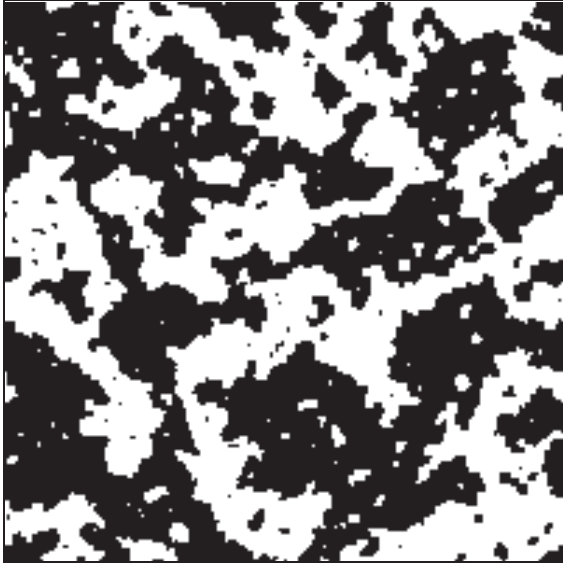


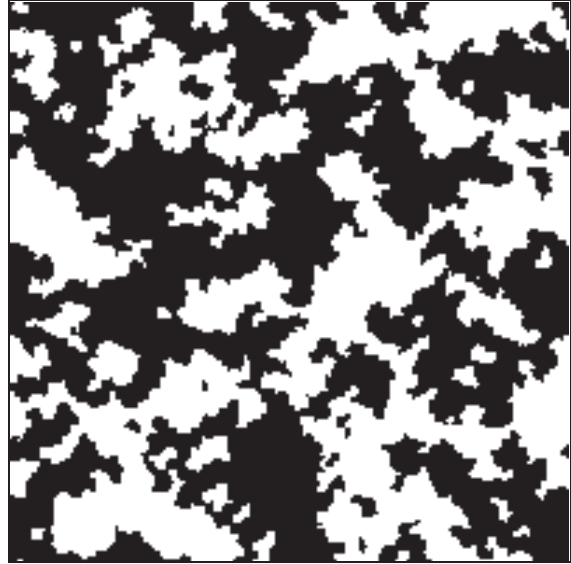
Figure 4.16 – A coarse reconstruction of PEFC catalyst layer using random swapping, used as starting point with $E= 4.99 \times 10^{-3}$.

structure compared to random swapping. Among the two biased methods, the reconstructions using interface and DPN based swapping have no noise. The improvements in the reconstructions are also evident from their final energy. While the average final energy using random swapping is $(2.12 \pm 0.25) \times 10^{-6}$, which indicates that the structure did not converge to the desired tolerance of 10^{-6} , the average energy using interfacial and DPN swapping reached the tolerance of 10^{-6} . The average iterations (swaps) used to reach the final energy were $(2.13 \pm 0.31) \times 10^6$, $(7.14 \pm 0.34) \times 10^5$, and $(3.91 \pm 0.08) \times 10^5$ for random, interfacial, and DPN based reconstructions, respectively. On average, the interfacial swapping reduced the number of required swaps by a factor of three, while the DPN based swapping reduced them by a factor of five.

The energy evolution of the reconstructed structures was studied for each of the swapping methods. Figure 4.18 shows the comparison of average energy evolution for the three pixel swapping methods. It can be observed from Fig. 4.18, that the DPN based method eliminates the noise at the beginning, as evident by the sharp decline in energy. Similarly, the interfacial pixel swapping also reduces the energy faster than random swapping; however, it is slower than the DPN based swapping. Due to the higher rate of energy convergence,



(a) Reconstruction using random swapping



(b) Reconstruction using interfacial swapping



(c) Reconstruction using DPN base swapping

Figure 4.17 – Reconstructed images of PEFC catalyst layer using different swapping methods

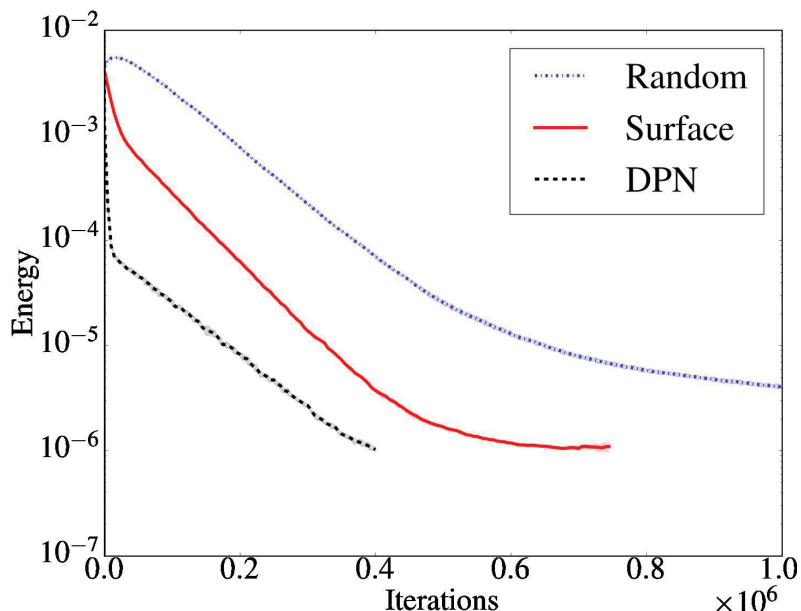


Figure 4.18 – Comparison of energy convergence for random, interfacial and DPN based pixel swapping (Solid line represents average and shaded region represents 95% confidence interval. Error margin is not visible, as it is negligible)

the DPN based method reaches the tolerance target in the least number of swaps followed by the interfacial method. Actual reconstruction time for all the three cases was also analyzed. The average reconstruction time was 32.56 ± 4.15 minutes, 10.40 ± 0.48 minutes, and 5.76 ± 0.20 minutes for random, interfacial, and DPN based swapping respectively. It can be seen that compared to conventional random swapping, the interfacial swapping method reduced reconstruction time by a factor of approximately three, while the DPN based swapping reduced it by a factor of six. The time reduction should be even higher for larger image sizes.

The DPN based method proposed by Tang et al. [98] improves the reconstruction accuracy, and reduces the reconstruction time significantly; however, the bias in the pixel selection may cause the reconstructed structure to become unrealistic. Even though the reconstructed image using DPN based swapping in Fig. 4.17(c) looks similar to the reference structure, the behavior may be different for larger images. A detailed study on the effect of DPN parameters on the reconstructed structure was carried out. The PEFC catalyst layer 2D image given in Fig. 4.1(d) is resized to 600×600 pixels using nearest neighbor interpolation as described in Section 3.6.1. The large image size should make it easy to visually identify any abnormalities in the reconstructions. The DPN set probabilities were calculated using

Table 4.2 – Explanation of different DPN parameters used in DPN based pixel swapping

| Parameter value | Explanation |
|-----------------|---|
| $m = 0.4$ | The probability of highest DPN set getting selected for swap is 0.4 |
| m not used | The probability of all sets including the highest DPN are obtained using Eq. (3.16) |
| $a = 0$ | The pixels with zero DPN are not included in swapping |
| $a = 1$ | The pixels with zero DPN are included in swapping |
| $b = 0$ | The value of DPN has no bias |
| $b = 0.5$ to 2 | The value of DPN has bias dependent on the value of b |

the general formula given by Eq. (3.16). Since the images are large, they are reconstructed using multigrid method. Due to the use of multigrid method, all the images have negligible noise, even when a random swapping equivalent is implemented. More details about the multigrid method will be discussed in upcoming section.

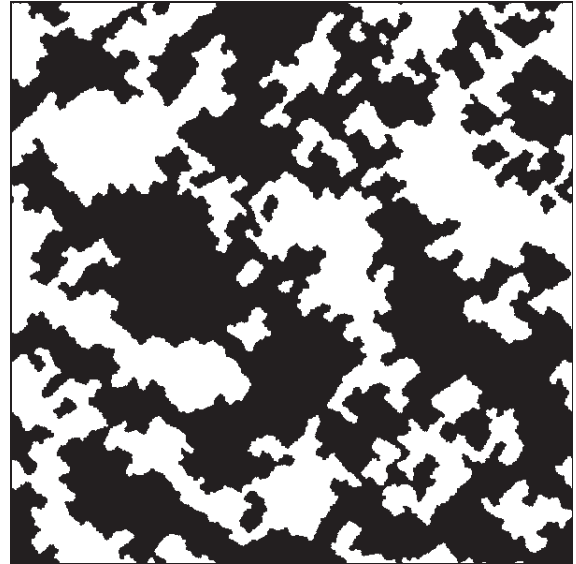
Three parameters are of critical importance in pixel selection using DPN based swapping: 1) the value of probability assigned to the maximum DPN set m , 2) the value of parameter a in Eq. (3.16), which decides whether or not to include the set with zero DPN in pixel swapping, and 3) the value of parameter b in Eq. (3.16), which increases or decreases the bias given to the DPN value. Several variations of these parameters are used to study their effect. The different used parameters and their explanation is given in Table 4.2.

Figure 4.19 shows some of the reconstructed 2D PEFC structures using different DPN parameters. All the reconstructions use a maximum DPN set probability (m) of 0.4. It can be seen that all the reconstructed structures bear no similarity to the reference image. Due to excessive DPN minimization, all the surfaces have been flattened, resulting in unrealistic images. Varying the parameters a and b has minimal affect on improving the structure. Similar observations were made for a value of $m = 0.2$. For a reconstructed image to have all the contours present in the reference image, some high DPN values must remain. Forcing a value of m causes the algorithm to consecutively pick the highest DPN, regardless of the set size, thereby minimizing the highest DPN in the image, and resulting in unrealistic images.

In the next study, no probability for the highest DPN set was specified. The probabilities



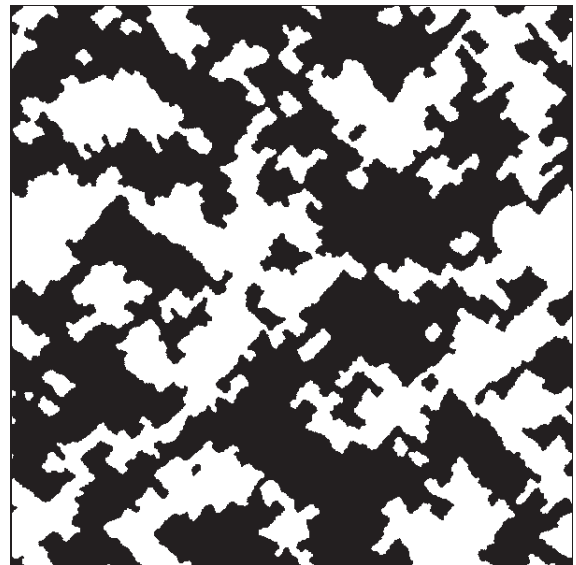
(a) $a = 0, b = 1$



(b) $a = 0, b = 10^{-5}$



(c) $a = 1, b = 1$



(d) $a = 1, b = 2$

Figure 4.19 – DPN based reconstructions of size 600^2 using maximum set probability $m = 0.4$

for all the sets were calculated using Eqs. (3.16) and (3.17). Figure 4.20 shows few of the relevant reconstructed 2D PEFC structures using different DPN parameters. It can be observed that all the reconstructions shows significant improvement compared to Fig. 4.19. The reconstruction using conventional DPN parameters of $a = 1$, and $b = 2$ shown in Fig. 4.20(d) still shows some surface flattening. The best reconstructions were obtained using DPN equivalent of random swapping, surface swapping, and DPN swapping with minor DPN bias ($a=0$, $b=0.5$). The noise removal in random swapping is due to the multigrid method, which is explained later in the thesis.

The three methods resulting in best case reconstructions were compared in terms of accuracy and speed using the 200×200 pixel size image of PEFC CL. Ten reconstructions were performed from the initial image given in Fig. 4.16 using each method on a computer with an Intel(R) Core(TM) i7-2600 CPU with a clock speed of 3.40 GHz. Since the images are small, conventional single grid method is used. Figure 4.21 shows the reconstructed images using random swapping implementation, and new DPN swapping. The images are similar to the conventional implementation of the methods. The average energy of the final structure is $(2.01 \pm 0.29) \times 10^{-6}$ for the random equivalent ($a = 1$, $b = 0$), and the desired tolerance (10^{-6}) for surface equivalent ($a = 0$, $b = 10^{-5}$), and new DPN method ($a = 0$, $b = 0.5$). These values are similar to the ones observed in earlier comparison studies of conventional random, surface and DPN methods. Average amount of time taken is 30.93 ± 3.67 minutes, 11.2 ± 0.59 minutes, and 9.90 ± 1.06 minutes for random equivalent, surface equivalent, and new DPN method respectively. The reconstruction time for random and surface equivalent methods is almost similar to their conventional implementation discussed earlier, thereby providing a unified way of implementing all the swapping methods without significant changes in computational performance. The reconstruction time using new DPN parameters ($a=0$, $b=0.5$, no maximum probability) is almost two times higher than the conventional DPN swapping proposed by Tang et al. [98]. The time increase is due to the reduced bias to high DPN values, which results in lower DPN pixel getting swapped more frequently. The DPN method with new parameters however is more accurate, results in realistic reconstructions, and is still around 3-4 times faster than conventional random swapping.



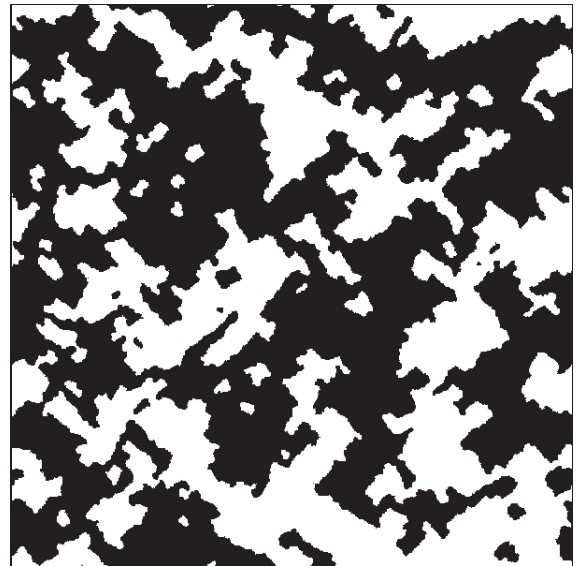
(a) $a = 0, b = 10^{-5}$. Equivalent to surface swapping



(b) $a = 1, b = 0$. Equivalent to random swapping

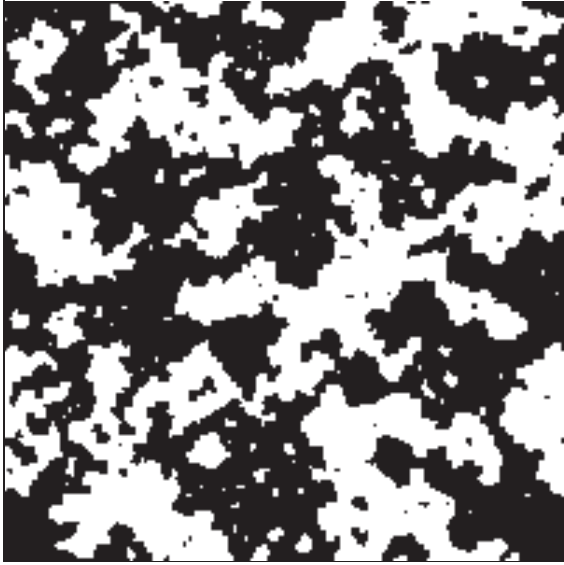


(c) $a = 0, b = 0.5$

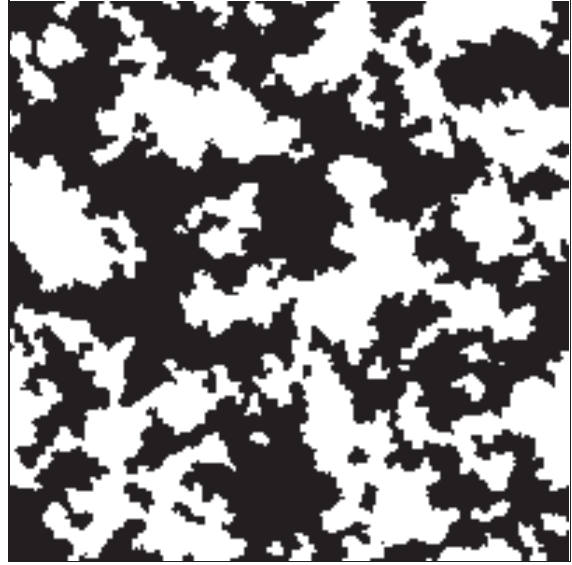


(d) $a = 1, b = 2$

Figure 4.20 – DPN based reconstructions of size 600^2 using no maximum set probability



(a) $a = 1, b = 0$. Equivalent to random swapping



(b) $a = 0, b = 0.5$

Figure 4.21 – PEFC CL reconstructions of size 200^2 using different DPN implementations and without any maximum set probability

4.3.4 Effect of Multigrid Method

The reconstructions so far have focused on small size 2D images; however, the speed advantages gained by DPN based method are not sufficient for reconstructing large 2D or 3D images in practical time. The multigrid hierarchical annealing method is therefore implemented to aim at achieving increased reconstruction speed. The 2D SEM image of a PEFC CL shown in Fig. 4.1(d) was taken as the reference image for 2D reconstructions. The image was resized to a size of 600×600 pixels using nearest neighbor interpolation method described in Section 3.6.1. This large size was chosen in order to clearly demonstrate the advantages of multigrid method.

As discussed earlier, one of the major factors deciding the reconstruction time is the time required to compute correlation functions. To understand the effect of image size on correlation function computing time, a study on the computation time for different correlation functions was performed using different image sizes. The maximum span (r_{max}) of the correlation functions was kept fixed. Figure 4.22 shows the increase in computation time as the image size increases. For a given span size, the computation time increases linearly with image size for all correlation functions. The increment factor was found to be higher

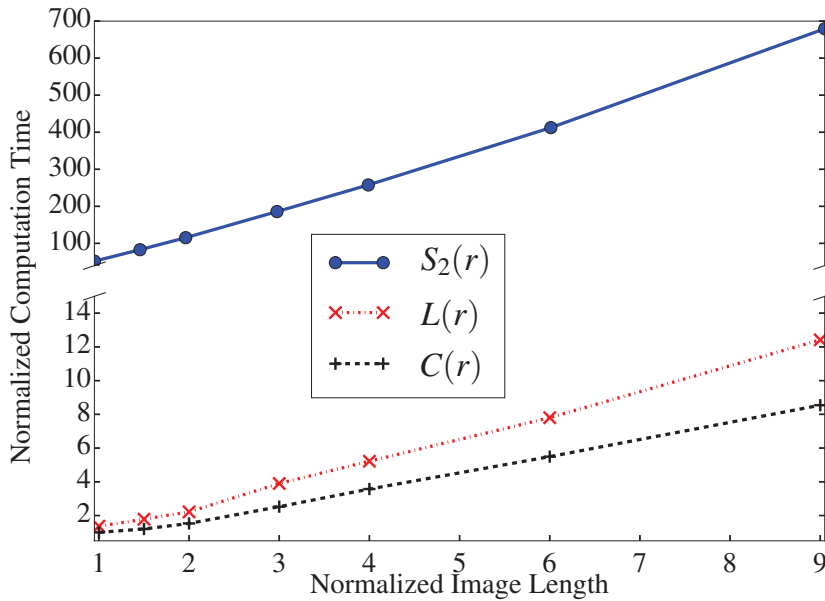


Figure 4.22 – Effect of image size on computation time for different correlation functions. The time is normalized by computation time of chord length function for a size of 100 pixels

for two-point correlation function compared to lineal path and chord length functions. For n times increase in image size, the computation time increased by $1.5n$, $1.02n$ and $0.96n$ times for $S_2(r)$, $L(r)$ and $C(r)$ respectively. It was also found that the absolute time taken by $S_2(r)$ is higher than the time taken by $L(r)$ and $C(r)$ by a factor of the span (in this study 50). During reconstruction, the computational time increment factor is expected to be slightly higher, as the spans of the correlation functions also increase with image sizes.

It is evident that image size plays a critical role in reconstruction time. In the multigrid method, the reconstruction sizes are decreased by introducing additional coarse grid levels. The effect of grid levels was studied by performing reconstructions using different grid levels. The general simulated annealing parameters are shown in Table 4.3. Again, a static annealing schedule was used, as a dynamic schedule can cause the reconstruction time to vary between reconstructions. All the reconstructions were performed using the new DPN based pixel swapping ($a = 0$, $b = 0.5$, and no maximum probability). All the reconstructions converged to the desired tolerance of 10^{-6} . Table 4.4 shows the average reconstruction time

Table 4.3 – General simulated annealing parameters used for multigrid reconstruction.

| Parameter | Value |
|--|--------------------|
| Number of multigrid levels | varies (1-4) |
| Maximum number of allowed failed Markov chains (X) | 20 |
| Minimum relative slope of energy curve required before termination | 10^{-7} |
| Target energy tolerance | 10^{-6} |
| Markov chain size | 5000 |
| Fixed energy threshold update factor (λ) | 0.95 |
| Boundary condition for reference function computing | normal |
| Boundary condition for reconstructed function computing | periodic |
| Initial energy factor (p_0) | 0.5 |
| Initial iterations (N) | 5000 |
| Correlation functions used | $S_2^{(v)}(r)$ |
| Cutoff energy for switching to DPN | 5×10^{-3} |
| Initial energy factor (p_0) after starting DPN | 0.25 |
| Number of processors | 2 |

for different multigrid levels. The margins of error are reported for 10 samples with a 95% confidence interval. The levels refer to the number of grid levels used for reconstruction, e.g., single grid means reconstruction on original size, two levels means reconstruction at a coarse scale (300×300) followed by reconstruction at the final scale (600×600). Freeze₁ refers to instances where freezing was done using method 1, i.e, Eq. (3.19), whereas Freeze₂ refers to instances where freezing was done using method 2, i.e., Eq. (3.20).

The results in Table 4.4 clearly show that increasing grid levels reduces the reconstruction time; however, the incremental reduction in time is reduced with each additional grid level. It is therefore expected that coarsening below a certain size by adding more grid levels will not result in additional time savings. By introducing four grid levels, the reconstruction time reduced by a factor of 15.6 for a Freeze₂ based method. The reduction factor will be dependent on the final reconstruction size, i.e., time advantages will be more prominent for larger images than the smaller ones.

There are two primary reasons for the observed reduction in the reconstruction time with more grid levels: a) The reduction in image size for coarser grid levels, and b) the smaller number of pixels to permutate at higher sizes. As all the interior pixels are frozen at coarse

Table 4.4 – Comparison of average reconstruction times for different multigrid reconstructions (final image size 600×600). The margins of error are based on 10 trials and represent a 95% confidence interval

| Type of reconstruction | Reconstruction time (Minutes) | Average advantage ($\bar{t}_{\text{single}}/\bar{t}$) |
|-------------------------------------|-------------------------------|---|
| Single level | 448.34 ± 1.8 | 1 |
| Two levels (Freeze ₁) | 45.46 ± 0.56 | 9.86 |
| Three levels (Freeze ₁) | 38.09 ± 1.55 | 11.77 |
| Four levels (Freeze ₁) | 35.38 ± 0.43 | 12.67 |
| Two levels (Freeze ₂) | 42.38 ± 0.39 | 10.57 |
| Three levels (Freeze ₂) | 30.53 ± 0.35 | 14.66 |
| Four levels (Freeze ₂) | 28.69 ± 0.24 | 15.62 |

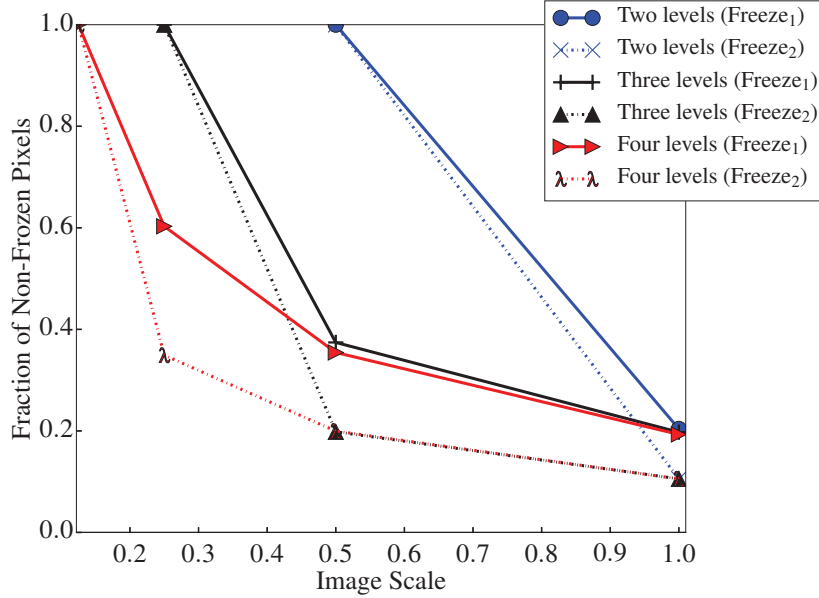


Figure 4.23 – Fraction of non frozen (permutating) pixels at each refinement level for multigrid methods (Values show average over 10 trials. Margins of error are less than 1% and therefore not plotted)

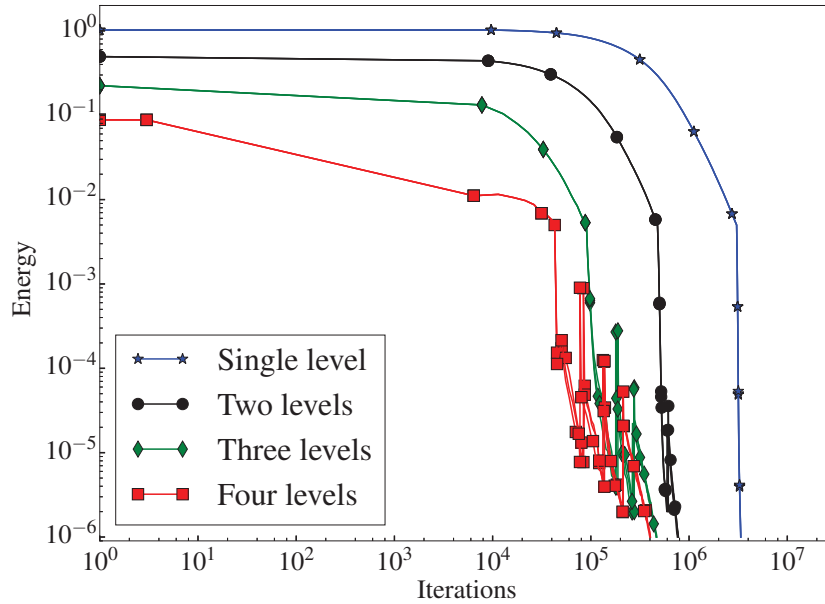


Figure 4.24 – Comparison of energy evolution (convergence) for different grid level

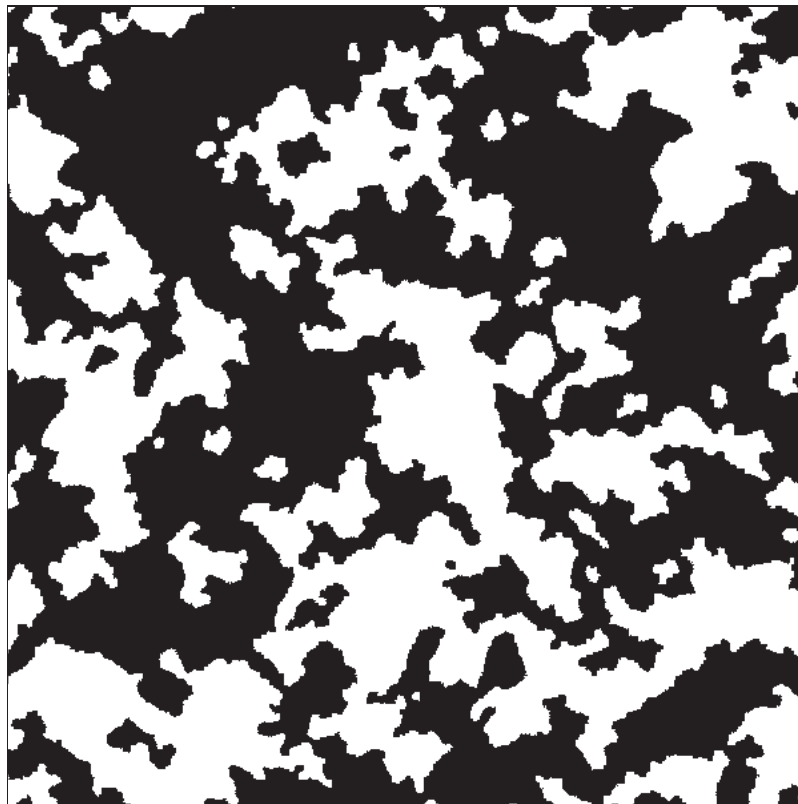
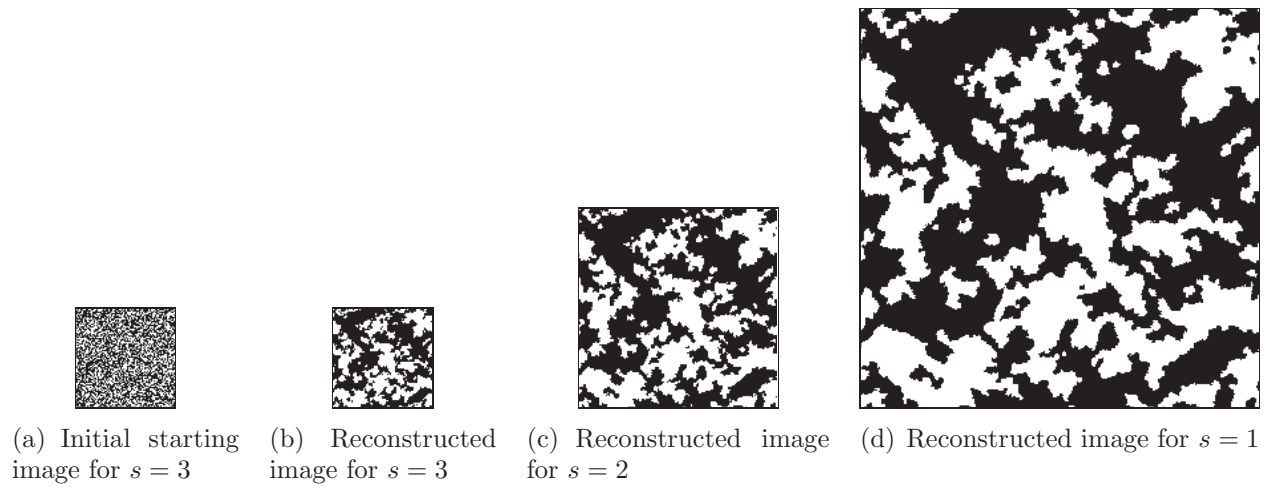
scales, very few of the pixels need to be visited by the swapper at refined scales. This reduces the total number of required swaps and hence the reconstruction time. Figure 4.23 shows the fraction of non frozen pixels at each grid scale (ratio of image size at current scale to the image size at finest scale). The fraction of permuting pixels at the finest scale is around 0.1 – 0.2, thereby reducing the number of swaps required at the finest scale by a significant amount compared to a conventional method, where all the pixels are permuting at the finest scale. As expected, Freeze_2 freezes more pixels at each stage compared to Freeze_1 , which results in Freeze_2 providing more time advantage compared to Freeze_1 .

The energy evolution for Freeze_2 based method was also studied for different grid levels. Figure 4.24 shows multiple energy evolutions during reconstruction for different number of multigrid levels. The starting energy is lower when more coarse levels are introduced, as it reduces the starting image size. Since the starting energy is lower, less iterations will be required to converge to a given final tolerance. The number of iterations at the finest level (towards the end of the reconstruction) become smaller with increasing grid levels due to the pixel freezing. Since image size is one of the main contributing factors towards computational time, lesser iterations at higher sizes will result in significant time reduction.

Figure 4.25 shows the evolution of the reconstructed image through all the grid levels (indicated by s). The overall structure does not change significantly after the first grid level. After each refinement, most of the changes occur at the interfaces, where more refinements to the structure are added. It can be seen that no isolated pixels remain in the final reconstruction, which is due to the use of DPN method, as well as due to multigrid method. Using multigrid method, reconstructions using random swapping also result in noise free images, as seen in Fig. 4.20(b). During multigrid annealing, all the segregated pixels at coarse scale are not frozen at refined scales. Since the swapping is only done among non-frozen pixels, the chances of a segregated pixel getting picked significantly increase.

As discussed earlier, the advantage of multigrid method is expected to be higher for larger images. Table 4.5 shows the time advantage of a Freeze₂ based multigrid method for different reconstruction sizes. The speedup factor increases non-linearly with increase in image size. The time advantage of multigrid methods therefore should be significant for large 2D images (1000^2 or bigger), or for 3D images. On the other end, it is seen that, for an image size of 80×80 pixels, the multigrid method requires more time than a single grid. The multigrid method is therefore not advantageous for very small image sizes, as the cost of intermediate operations (e.g., coarsening and refinement) will become comparable to reconstruction time. It can also be noticed that, for a single grid method, increasing image size by a factor of 7.5 increases the reconstruction time by almost a factor of 400, while in multigrid method, the same size increment increases reconstruction time by only a factor of 20. This is due to pixel freezing in multigrid method, which results in small number of pixel swaps getting performed at large sizes. On the other hand, in a single grid method, all the swaps are performed at the largest size.

The overall effect of image size on total reconstruction time was also studied. Table 4.6 shows the average computational time for reconstructing 2D CL images of different sizes using $S_2^{(v)}(r)$. Freeze₂ method with four grid levels was used for all image sizes. The overall time for reconstruction increases non-linearly with increase in image size. The increase in time can be divided into two parts: 1) Time increase due to additional cost of computing $S_2^{(v)}(r)$, which increases by a factor of approximately 1.5 with image size, and 2) time increase due



(e) Final reconstructed image ($s = 0$)

Figure 4.25 – Reconstructed images at different scales using the multigrid method. Images are to scale

Table 4.5 – Comparison of speedup factor using Freeze₂ based multigrid method for different image sizes. The margins of error are based on 10 trials and represent a 95% confidence interval

| Image size | Image size increment factor (L/80) | Time for single grid (minutes) | Time for 4 pass multigrid (minutes) | Speedup factor ($\bar{t}_{\text{single}}/\bar{t}$) |
|------------|------------------------------------|--------------------------------|-------------------------------------|--|
| 80 × 80 | 1 | 1.26 ± 0.29 | 1.45 ± 0.25 | 0.87 |
| 160 × 160 | 2 | 4.96 ± 0.35 | 3.36 ± 0.25 | 1.47 |
| 320 × 320 | 4 | 34.61 ± 0.48 | 7.19 ± 0.2 | 4.81 |
| 600 × 600 | 7.5 | 448.34 ± 1.8 | 28.69 ± 0.24 | 15.62 |

Table 4.6 – Reconstruction time for different final reconstructed image sizes. All reconstructions are performed using Freeze₂ with 4 grid levels. The margins of error are based on 10 trials and represent a 95% confidence interval

| Image size | Image size increment factor (L/80) | Reconstruction time (Minutes) | Average time increment (\bar{t}/\bar{t}_{80}) |
|------------|------------------------------------|-------------------------------|---|
| 80 × 80 | 1 | 1.45 ± 0.25 | 1 |
| 160 × 160 | 2 | 3.36 ± 0.25 | 2.31 |
| 240 × 240 | 3 | 4.85 ± 0.20 | 3.34 |
| 320 × 320 | 4 | 7.19 ± 0.20 | 4.95 |
| 400 × 400 | 5 | 13.02 ± 0.41 | 8.79 |
| 600 × 600 | 7.5 | 28.69 ± 0.24 | 19.78 |

to more pixel swaps (i.e., more iterations) at larger image sizes. It can be observed that the time increment due to increase in swaps is higher than the time increment due to increase in correlation function computing time. Due to the non-linear increase in reconstruction time, reconstructing very large images (2000² pixels or bigger) may become impractical.

4.3.5 Effect of Correlation Functions on Structure

So far, it has been concluded that a combination of DPN swapping, and multigrid hierarchy based method results in a fast and low tolerance energy minimization; however, the minimization only optimized the two-point correlation function (i.e., only surface area) and therefore, can not guarantee a good representation of the actual porous media structure. Each correlation function contains specific stochastic information regarding the microstructure of the porous media. It is therefore imperative to assume that inclusion of additional functions will improve the reconstructed structure. The time savings offered by the combination of DPN, and multigrid methods provide a feasible way to investigate multiple correlation

functions in a practical amount of time. To enhance the structural accuracy of the reconstructions, several combinations of correlation functions were used for reconstruction. When using multiple correlation functions, the same weight is given to each correlation function. A threshold energy based acceptance method, DPN based swapping (a=0, b=0.5, no maximum probability), and multigrid hierarchy with three grid levels is used to reconstruct multiple 2D images of PEFC CL with a size of 200×200 pixels. A tolerance of 10^{-6} is specified for each correlation function. The rest of the parameters are the same as in Table 4.3. Using the DPN based pixel swapping, all the reconstructions provide a noise free image, which are qualitatively similar; therefore, a quantitative analysis of the different methods is necessary for comparison.

For quantitative analysis of the accuracy, a comparison of correlation functions for reference and reconstructed geometries is done. Table 4.7 shows the L_2 norm of the difference of the different correlation functions (i.e., energy equivalent of that correlation function) for the reconstructed image compared to reference correlation functions. The cells highlighted in blue color indicate the function which is the optimization target, and green color indicates a function which is not included in optimization but still improves. It can be observed that the optimization algorithm is capable of minimizing the error associated with desired correlation functions. Among all the correlation functions, it is seen that $L^{(s)}(r)$, $C^{(s)}(r)$ and $C^{(v)}(r)$ do not optimize to the specified tolerance of 10^{-6} , while $S_2^{(v)}(r)$, and $L^{(v)}(r)$ are able to optimize. Since two-point cluster function is only valid for 3D images, it does not get optimized using any combination. Optimizing both: solid, and void phase constrains the optimization to a limited space, which makes reaching global optimum difficult, and may result in sub-optimal solutions. The chord length function is less smooth compared to the lineal path function and changes suddenly between different length scales. This may result in a complex energy landscape which is difficult and more time consuming to solve compared to lineal path functions. It was also observed that a few combinations resulted in added advantage of error reduction for non-target functions, i.e., functions which were not included in the optimization function. Among all the combinations, it can be seen that a combination of $S_2^{(v)}(r)$, $L^{(s)}(r)$ and $L^{(v)}(r)$ results in the best optimization results. On the other hand, adding chord length functions to two-point correlation function improves the optimization of chord length functions; however, the two-point correlation function does not get optimized

Table 4.7 – Comparison of discrepancy in different correlation functions for 2D PEFC CL reconstructions of size 200×200 pixels using different correlation function combinations. Blue color indicates the function which is being optimized. Green color indicates a function which is not included in optimization but still gets optimized. The margins of error are estimated based on 10 trials and reflect a 95% confidence interval

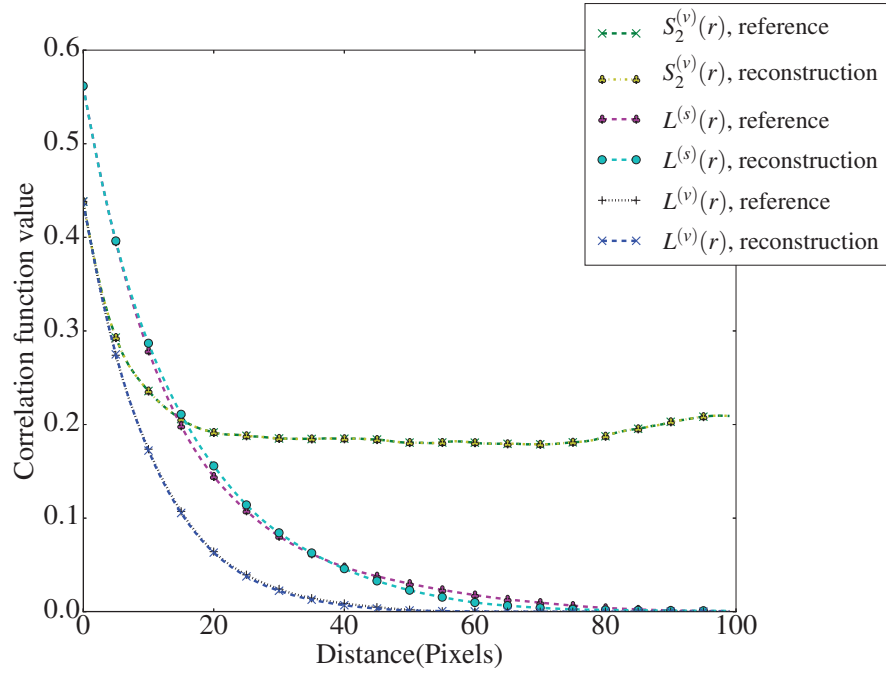
| Functions used | L2 norms of error for the function | | | | | |
|--|------------------------------------|----------------------------------|----------------------------------|----------------------------------|----------------------------------|----------------------------------|
| | $S_2^{(v)}(r)$ | $C_2^{(v)}(r)$ | $L^{(s)}(z)$ | $L^{(v)}(z)$ | $C^{(s)}(z)$ | $C^{(v)}(z)$ |
| $S_2^{(v)}(r)$ | $(9.91 \pm 0.05) \times 10^{-7}$ | $(1.26 \pm 0.78) \times 10^{-1}$ | $(1.20 \pm 0.21) \times 10^{-2}$ | $(4.63 \pm 1.63) \times 10^{-3}$ | $(3.78 \pm 0.35) \times 10^{-3}$ | $(3.36 \pm 0.34) \times 10^{-3}$ |
| $S_2^{(v)}(r), L^{(s)}(r)$ | $(6.22 \pm 0.36) \times 10^{-7}$ | $(2.00 \pm 1.20) \times 10^{-1}$ | $(3.56 \pm 1.59) \times 10^{-6}$ | $(4.14 \pm 1.17) \times 10^{-3}$ | $(9.95 \pm 0.72) \times 10^{-4}$ | $(3.02 \pm 0.23) \times 10^{-3}$ |
| $S_2^{(v)}(r), L^{(v)}(r)$ | $(9.91 \pm 0.03) \times 10^{-7}$ | $(2.41 \pm 1.19) \times 10^{-1}$ | $(1.51 \pm 0.35) \times 10^{-2}$ | $(8.04 \pm 0.77) \times 10^{-7}$ | $(3.44 \pm 0.37) \times 10^{-3}$ | $(9.46 \pm 0.77) \times 10^{-4}$ |
| $S_2^{(v)}(r), C^{(s)}(r)$ | $(2.48 \pm 0.12) \times 10^{-5}$ | $(7.00 \pm 3.51) \times 10^{-2}$ | $(2.24 \pm 0.21) \times 10^{-2}$ | $(8.47 \pm 1.76) \times 10^{-3}$ | $(1.64 \pm 0.12) \times 10^{-5}$ | $(2.87 \pm 0.17) \times 10^{-2}$ |
| $S_2^{(v)}(r), C^{(v)}(r)$ | $(1.50 \pm 0.13) \times 10^{-5}$ | $(5.95 \pm 3.04) \times 10^{-1}$ | $(1.51 \pm 0.28) \times 10^{-2}$ | $(4.65 \pm 0.62) \times 10^{-3}$ | $(1.88 \pm 0.10) \times 10^{-2}$ | $(8.88 \pm 0.76) \times 10^{-6}$ |
| $S_2^{(v)}(r), L^{(s)}(r), L^{(v)}(r)$ | $(8.50 \pm 0.69) \times 10^{-7}$ | $(1.60 \pm 1.11) \times 10^{-1}$ | $(3.08 \pm 0.45) \times 10^{-6}$ | $(7.07 \pm 0.95) \times 10^{-7}$ | $(1.05 \pm 0.04) \times 10^{-3}$ | $(1.05 \pm 0.07) \times 10^{-3}$ |
| $S_2^{(v)}(r), C^{(s)}(r), C^{(v)}(r)$ | $(4.98 \pm 0.43) \times 10^{-5}$ | $(1.73 \pm 1.23) \times 10^{-1}$ | $(1.51 \pm 0.32) \times 10^{-3}$ | $(6.83 \pm 1.96) \times 10^{-4}$ | $(6.15 \pm 0.40) \times 10^{-5}$ | $(3.51 \pm 0.23) \times 10^{-5}$ |

to its tolerance. This suggests additional complexity associated with chord length functions. These results however only indicate better statistical representation in a 2D geometry. The results may be different for 3D geometries, and for transport properties.

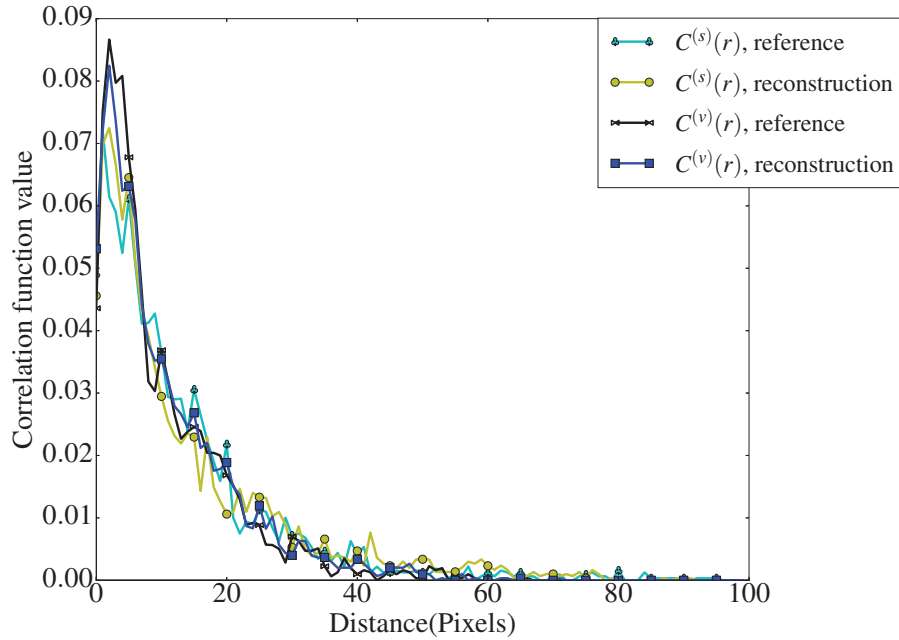
The effect of using multiple correlation functions can also be visualized by comparing the correlation functions for the reference and the reconstructed image. Figure 4.26 shows the comparison of the correlation functions for a particular reconstruction using only the void phase two point correlation function. It can be seen that $S_2^{(v)}(r)$ for the reconstructed image, the optimized function, matches quite well with the reference image. However, all other functions except $L^{(v)}(r)$ do not match, indicating an incomplete representation of the porous media by the reconstructed image. Using a combination of $S_2^{(v)}(r)$, $L^{(s)}(r)$ and $L^{(v)}(r)$, it can be seen in Fig. 4.27 that all the functions are properly matched. This indicates a better representation of the original porous media structure, and therefore should be able to provide more accurate physical characteristics. Even though adding more correlation functions improves the reconstruction accuracy, it increases computational time. For example, the average total time consumed for a $S_2^{(v)}(r)$ based reconstruction is 4.05 ± 0.26 minutes, whereas the average total time for the $S_2^{(v)}(r)$, $L^{(s)}(r)$ and $L^{(v)}(r)$ based reconstruction is 22.96 ± 3.61 minutes. The increased time with small 2D images is not a significant issue; however, for large images, especially large 3D images, using multiple correlation functions becomes cumbersome. Due to this enhanced computational requirements, conventional random swapping, and single grid based methods are not able to use multiple correlation functions. Therefore, the time savings offered by DPN swapping, and multigrid hierarchy based method are critical for developing an advance reconstruction algorithm capable of reconstructing porous media with multiple correlation functions in practical amount of time.

4.4 Reconstruction of 3D Structures of Different Porous Media

Once the two-dimensional reconstructions were completed and an optimal set of parameters obtained, three-dimensional reconstruction of porous media was studied. Since the primary aim of the reconstruction process is to provide a physical domain for studying physical processes in the porous media, 3D reconstructions are critical to assess the performance of any

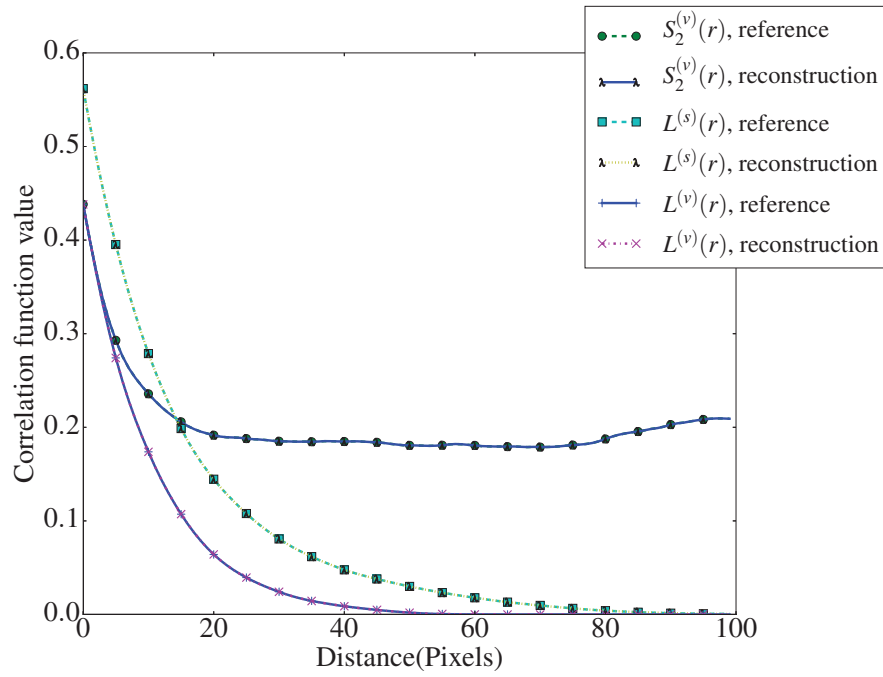


(a) Comparison of $S_2^{(v)}(r)$, $L^{(s)}(r)$ and $L^{(v)}(r)$

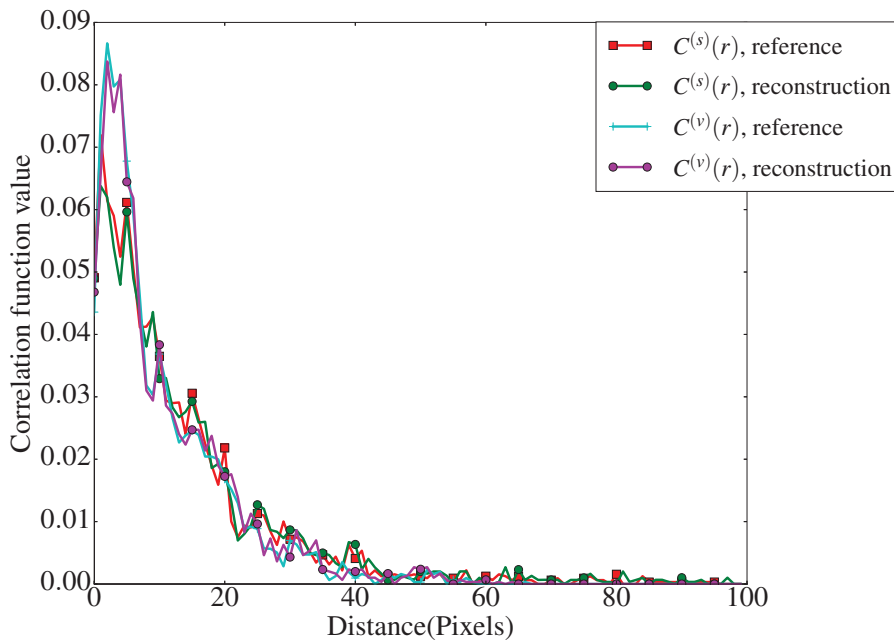


(b) Comparison of $C^{(s)}(r)$ and $C^{(v)}(r)$

Figure 4.26 – Comparison of correlation functions for reference and reconstructed 2D PEFC catalyst layer image. The reconstruction was performed using $S_2^{(v)}(r)$ only

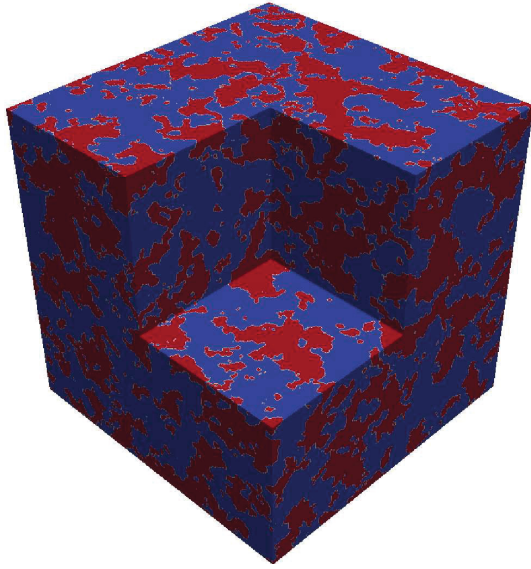


(a) Comparison of $S_2^{(v)}(r)$, $L^{(s)}(r)$ and $L^{(v)}(r)$

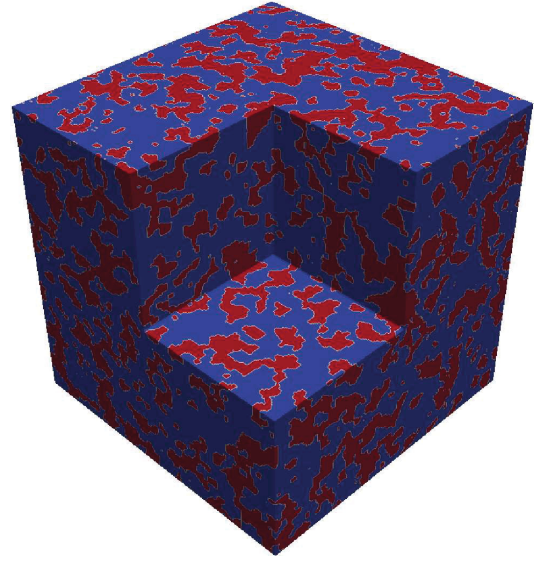


(b) Comparison of $C^{(s)}(r)$ and $C^{(v)}(r)$

Figure 4.27 – Comparison of correlation functions for reference and reconstructed 2D PEFC catalyst layer image. The reconstruction was performed using $S_2^{(v)}(r)$, $L^{(s)}(r)$ and $L^{(v)}(r)$



(a) 3D reconstruction of catalyst layer

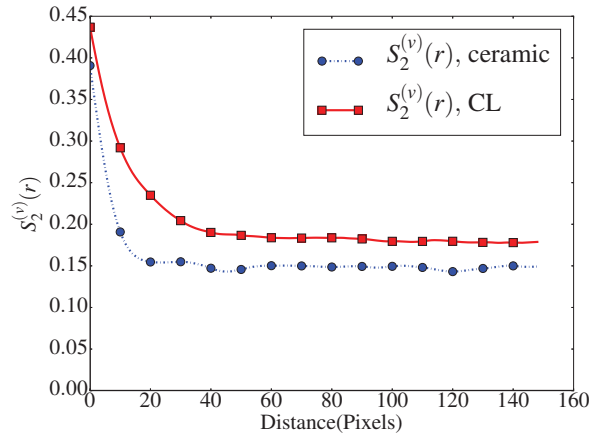


(b) 3D reconstruction of ceramic

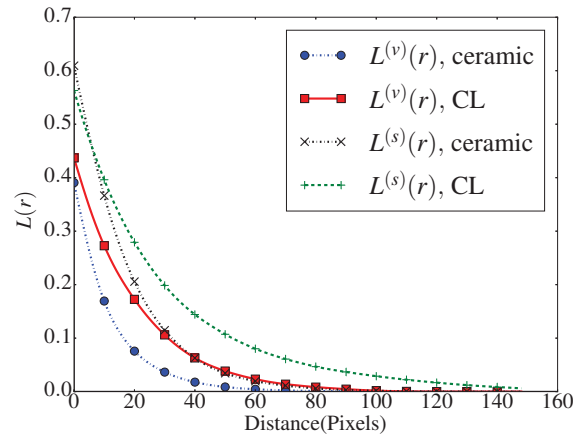
Figure 4.28 – 3D reconstructions of porous media using only $S_2^{(v)}(r)$ (Blue shows solid phase and red shows void phase)

reconstruction methodology. For this study, 3D reconstructions of two porous media: 1) a fuel cell CL, and 2) a ceramic were performed. For the CL, the SEM image shown in Fig. 4.1(d) is used for 3D reconstructions as well. For 3D reconstructions of ceramic, the reference image shown in Fig. 4.2 is used. The reason for using the 2D images instead of the available 3D reference images is that, the 2D images are larger than the 3D images, and provide a way to understand the feasibility of reconstructing large 3D images with the new methodology. Since the information in the third direction is not available, the reference correlation functions in the z direction are obtained by averaging the x and y direction correlation functions of the 2D reference images. Three grid levels are used for reconstructing a CL of size 300^3 voxels, and a ceramic of size 300^3 voxels. The new DPN method is used for swapping with $a = 0$, and $b = 0.5$. Tolerance for the all the correlation functions used in the reconstruction is specified as 10^{-6} . Freeze₂ is used for pixel freezing and all the reconstructions are done on a PC with Intel E5-2690 CPU with clock speed of 3.00 GHz. Three processor cores are used for all the 3D reconstructions. The rest of the parameters are the same as shown in Table 4.3.

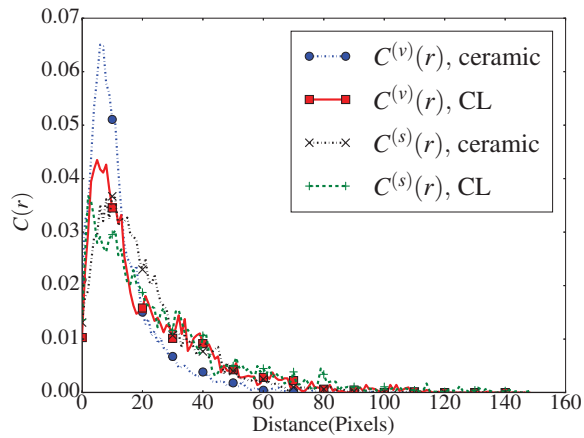
First, 3D reconstructions were created by using only two-point correlation function. Figure 4.28(a) shows the reconstructed 3D image of CL and Fig. 4.28(b) shows reconstructed 3D image of the ceramic. The interior cross sections of the 3D structures are also shown to



(a) Comparison of two-point correlation function



(b) Comparison of lineal path function



(c) Comparison of chord length function

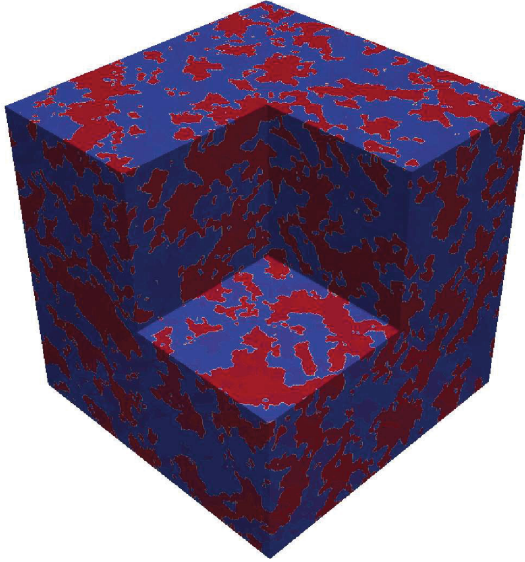
Figure 4.29 – Comparison of reference correlation functions between CL and ceramic

analyze the pore connectivity and internal features. Qualitatively, the reconstructed images show similar features to their reference images with good connectivity of the pore and solid phases. Five reconstructions of each media were performed using $S_2^{(v)}(r)$. The average time taken for the reconstructions to converge to an energy of 10^{-6} was 22.67 ± 0.11 hours for CL and 27.39 ± 0.03 hours for ceramic. The reason for difference in reconstruction times is likely due to the difference between the correlation functions of the CL and ceramic as shown in Fig. 4.29. This may result in more complex energy landscape for ceramic, and therefore a higher computational time. Even though these reconstruction times may appear large in absolute terms, it must be noted that single grid instances of these reconstructions using conventional random swapping did not converge even after one and a half months. For example, the energy for the ceramic went from 0.2 to approximately 3×10^{-4} in 35 days. Given that the energy reduction is slower at later stages, it can be expected that a final convergence to 10^{-6} would have taken at-least 30-40 additional days. Based on this, it can be concluded that the DPN and multigrid method provided at least around 70–90 times speedup.

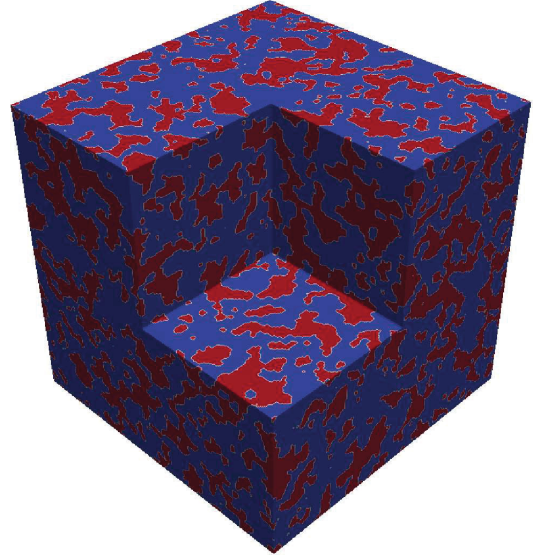
After obtaining 3D reconstructions based on only two-point correlation functions, reconstructions were performed using several correlation function combinations. Similar to the 2D images, the combination of $S_2^{(v)}(r)$, $L^{(v)}(r)$ and $L^{(s)}(r)$ was found to result in the best overall optimization of the structure. Figure 4.30(a) shows the reconstructed 3D image of the CL, and Fig. 4.30(b) shows a reconstructed 3D image of the ceramic using this combination. Qualitatively, the images are similar to the reference images and also to the two-point correlation function based reconstructions shown in Fig. 4.28. Looking at the internal cross sections of the reconstructed images, the phase connectivity seems to have improved compared to only $S_2^{(v)}(r)$ based reconstructions. For quantitative comparison, the discrepancy in all the correlation functions is computed and compared between the different reconstructions. Table 4.8 shows the average discrepancy in all correlation functions for the different reconstructions. It can be observed that, the addition of $L^{(v)}(r)$ and $L^{(s)}(r)$ not only decreases the discrepancy of $L^{(v)}(r)$ and $L^{(s)}(r)$ as expected, but also decreases the discrepancy of $C^{(v)}(r)$ and $C^{(s)}(r)$. Since a 2D reference image is used, the cluster functions are still not properly characterized, resulting in high discrepancy of $C_2^{(v)}(r)$ and $C_2^{(s)}(r)$.

Table 4.8 – Comparison of discrepancy in different correlation functions for 3D reconstructions using different correlation function combinations. Blue color indicates the function which is being optimized. Green color indicates a function which is not included in optimization but still gets optimized. The margins of error are based on 5 trials and represent a 95% confidence interval.

| Porous Media | Functions used | Average L2 norms of error for the function | | | | | | |
|--------------|--|--|-------------------|----------------------------------|----------------------------------|----------------------------------|----------------------------------|----------------------------------|
| | | $S_2^{(v)}(r)$ | $C_2^{(v)}(r)$ | $C_2^{(s)}(r)$ | $L^{(s)}(z)$ | $L^{(v)}(z)$ | $C^{(s)}(z)$ | $C^{(v)}(z)$ |
| CL | $S_2^{(v)}(r)$ | $(1.00 \pm 0.00) \times 10^{-6}$ | (9.24 ± 0.03) | $(6.76 \pm 0.06) \times 10^{-2}$ | $2.96 \pm 0.25 \times 10^{-2}$ | $(2.89 \pm 0.22) \times 10^{-3}$ | $(5.52 \pm 0.06) \times 10^{-3}$ | $6.61 \pm 0.04 \times 10^{-3}$ |
| | $S_2^{(v)}(r), L^{(v)}(r), L^{(s)}(r)$ | $(5.71 \pm 0.17) \times 10^{-7}$ | (9.18 ± 0.01) | $(6.77 \pm 0.02) \times 10^{-2}$ | $(1.00 \pm 0.00) \times 10^{-6}$ | $(5.36 \pm 0.11) \times 10^{-7}$ | $(2.61 \pm 0.07) \times 10^{-3}$ | $(2.86 \pm 0.07) \times 10^{-3}$ |
| Ceramic | $S_2^{(v)}(r)$ | $(1.00 \pm 0.00) \times 10^{-6}$ | (3.11 ± 0.00) | (1.37 ± 0.00) | $(2.67 \pm 0.51) \times 10^{-2}$ | $(9.80 \pm 1.01) \times 10^{-3}$ | $(9.46 \pm 0.07) \times 10^{-3}$ | $(1.19 \pm 0.00) \times 10^{-2}$ |
| | $S_2^{(v)}(r), L^{(v)}(r), L^{(s)}(r)$ | $(6.57 \pm 0.11) \times 10^{-7}$ | (3.08 ± 0.01) | (1.37 ± 0.00) | $(1.00 \pm 0.00) \times 10^{-6}$ | $(8.68 \pm 0.44) \times 10^{-7}$ | $(6.49 \pm 0.16) \times 10^{-3}$ | $(7.52 \pm 0.12) \times 10^{-3}$ |



(a) 3D reconstruction of catalyst layer



(b) 3D reconstruction of ceramic

Figure 4.30 – 3D reconstructions using $S_2^{(v)}(r)$, $L^{(v)}(r)$ and $L^{(s)}(r)$. Blue shows solid phase and red shows void phase

Similar to the 2D images, the improvement in the reconstruction comes at the cost of reconstruction time. While the $S_2^{(v)}(r)$ based reconstruction times for CL and ceramic were 22.67 ± 0.11 hours, and 27.39 ± 0.03 hours respectively, $S_2^{(v)}(r)$, $L^{(v)}(r)$ and $L^{(s)}(r)$ based reconstruction times were 36.85 ± 0.41 hours for CL, and 47.19 ± 0.41 hours for ceramic. As with the $S_2^{(v)}(r)$ based reconstructions, ceramic reconstructions take longer to perform than CL. The addition of correlation functions increases the reconstruction time. There are two primary reasons for the time increase. First, addition of extra correlation functions requires extra computations after each swap, thereby increasing the total reconstruction time. Second, the energy landscape with multiple correlation function may be more complex than with a single correlation function, thereby requiring more time to exit local minima.

4.5 Summary of the Reconstruction Method

A detailed study of different reconstruction method variants have been performed. The comparison studies between different methods result in the following conclusions:

- Probability based and threshold energy based energy minimization methods are similar in accuracy and computational time.
- An adaptive annealing schedule marginally reduces the computational time compared

to the static annealing schedule.

- The proposed unified pixel swapping method provides a generic method for pixel swapping. The method reduces to random, surface or conventional DPN swapping by changing the parameters.
- The conventional DPN method proposed by Tang et al. [98] significantly improves reconstruction time; however, the high amount of bias to DPN values causes unrealistic structures to be reconstructed
- The new proposed DPN based method results in significant improvements in both, reconstruction time and accuracy when compared to the conventional random swapping.
- DPN based method provides flexibility of implementation, and a way for freezing pixels during multigrid refinements.
- The proposed multigrid hierarchical method results in significant computational time reduction compared to the conventional method, which is dependent on the image size.
- Overall, the combination of DPN and multigrid method reduces reconstruction time by a factor of around 100 compared to conventional single, and random swapping based method.
- Addition of multiple correlation functions improves the statistical accuracy of the reconstructions, making them a better representation of the reference media.

It is evident from the studies presented in this chapter that the use of the proposed multigrid method results in significant amount of time savings compared to the conventional single grid method. Table 4.9 shows a comparison of reconstruction times between the current work and the limited information available in literature (Unfortunately very few articles in the reconstruction literature report the computing specifications and times). It can be seen that the proposed method outperforms all single grid methods [65, 66, 71, 76]. Among the single grid methods, the one by Capek et al. [71] shows the most promising results due to fine tuned simulated annealing parameters and an adaptive temperature schedule; however, the proposed method outperforms it even when using all three correlation functions for reconstruction.

The multigrid methods by Alexander et al. [127] and Campaigne and Fieguth [49] seem to outperform the proposed method in terms of reconstruction time. These methods however use either neighborhood matching [49] (instead of correlation function optimization), or a higher energy tolerance [127]. The final energy in references [49, 127] is three orders of magnitude higher, i.e. $\geq 10^{-3}$, than current results. A higher tolerance in our method results in a dramatic decrease in computational time. For example, the average reconstruction time ($S_2^{(v)}(r)$ based) for reconstructing a 2D image of size 600×600 with a final energy of 1×10^{-3} was 0.1 ± 0.006 hours, which is less than half of the time reported by Alexander et al. [127] for a similar sized 2D image. When comparing to Campaigne and Fieguth [49], it must be noted that the total time saving is due to the grayscale method, as well as neighborhood matching. Comparing the reported time (0.1 ± 0.006 hours) to the one for a similarly sized image using the grayscale method by Campaigne and Fieguth [49], it can be seen that the combination of grayscale method and neighborhood matching results in a speed advantage of around two times. Based on this result, it appears that the major time advantage of Campaigne and Fieguth [49]’s method over the proposed method is due to the use of neighborhood matching, and not due to the use of the gray-scale based pixel freezing.

In summary, the proposed method based on multigrid hierarchical annealing with DPN based pixel selection outperforms all conventional single grid methods, and the multigrid method by Alexander et al. [127]. The grayscale method by Campaigne and Fieguth [49] is faster than the proposed method due to the use of neighborhood matching; however, the correlation function of the reconstruction does not match the reference image statistical correlation functions very well (the L_2 norm is approximately $\sim \mathcal{O}(10^{-3})$). Even though the proposed method is able to perform medium size (200-600 pixel length) reconstructions in practical amounts of time, it may still not be well suited for very large scale image reconstructions (600^3 and above). In most of the physical phenomena studies however, the required sizes are in the medium range, as a large 3D mesh also causes computational issues in simulating the physical phenomena. The current method therefore should be able to reconstruct 3D simulation domains for most of the physical phenomena studies.

Table 4.9 – Comparison of simulated annealing based reconstruction times in the literature to the proposed method. Acronyms used are as follows, SG-single grid, MG-multigrid, PA-probability based selection, TA- threshold based selection, RND-random swapping, INT-interfacial swapping, DPN-DPN based swapping, GSM-gray scale methods (multigrid) using extra phase for freezing, E_f - final energy of the reconstructed structure. Neighborhood refers to the cases where local neighborhood matching is carried out instead of correlation function optimization. * represents the cases where E_f is not known from the reference article. Approximate value is estimated from the available comparison of reference and reconstructed correlation functions

| Ref. | System Specs. | Correlation Functions | Size | Reconstruction Time(Hours) | Remarks |
|--------------|---------------------------|---|--------------------|----------------------------|--|
| Current work | Intel E5-2690 3.00 GHz | $S_2^{(v)}(r)$ | 600×600 | 0.5 | Unified DPN (a=0, b=0.5), MG, TA, $E_f = 10^{-6}$ |
| | | $S_2^{(v)}(r) + L^{(v)}(r) + L^{(s)}(r)$ | | 5 | |
| | | $S_2^{(v)}(r)$ | 300^3 | 22-28 | |
| | | $S_2^{(v)}(r) + L^{(v)}(r) + L^{(s)}(r)$ | | 36-47 | |
| [76] | IBM RS/6000 | $S_2^{(v)}(r) + C^{(s)}(r)$ | 500×500 | 220 | RND, SG, PA, $E_f = 10^{-4}$ |
| | | $C^{(v)}(r) + C^{(s)}(r)$ | 500×500 | 55 | |
| [71] | SGI Altix 350 1.5 GHz | $S_2^{(v)}(r) + L^{(v)}(r)$ or $S_2^{(v)}(r) + L^{(s)}(r)$ | 320^3 | 160-400 | INT, SG, PA, $E_f \sim \mathcal{O}(10^{-7})$, Adaptive temperature |
| [65] | Chebyshev super-computer | $S_2^{(v)}(r)$ | 200×200 | 48-72 | RND, SG, PA, $E_f = 10^{-7}$ |
| [66] | Intel E5-2690 3.00 GHz | $S_2^{(v)}(r)$ | 200×200 | 1.5 | DPN, SG, TA, $E_f = 10^{-6}$ |
| | | $S_2^{(v)}(r) + L^{(v)}(r) + L^{(s)}(r)$ | 200×200 | 15 | |
| [127] | N/A | $S_2^{(v)}(r) + C^{(v)}(r)$ | 512×512 | 0.25 | RND, MG, PA, $E_f = 0.483$ |
| | | Neighborhood | 8192×8192 | 96 | RND, MG, PA, $E_f \sim \mathcal{O}(10^{-3})^*$ |
| [49] | N/A | Neighborhood | 512×512 | 0.04 | RND, GSM, PA, $E_f \sim \mathcal{O}(10^{-3})^*$ |
| | | | 8192×8192 | 2-14 | |

Chapter 5

Mass Transport Analysis in Porous Media

This chapter presents a preliminary study on applications of the developed reconstruction methodology for real porous media reconstruction, transport estimation, and characterization. It primarily analyzes mass transport in reconstructed and reference 3D structures, and compares their properties. The aim of these studies is to find the effect of different correlation functions on the transport properties of reconstructions. The analysis should identify the required correlation functions for characterizing diffusion in the reconstructed structures. Section 5.1 presents a theoretical overview of mass transport in porous media structures, and provides the mathematical models for mass transport. Section 5.2 presents the details of the simulation method used for transport analysis in reference and reconstructed images. Section 5.3 presents a representative elementary volume study for estimating required reconstruction size for Ti foam media studied in this work. Section 5.4 presents the results of the transport study on the porous media, and analyzes the effects of correlation functions on transport estimations. Finally, Section 5.5 provides the summary of the transport analysis.

5.1 Mass Transport in Porous Media

Mass transport is of critical importance in several porous media applications. For example, the performance of the polymer electrolyte fuel cells is primarily restricted by mass transport limitations [8]. To improve mass transport, a detailed understanding of the relationship between transport properties and porous media structure is required. Statistical correlation functions provide an ideal way of characterizing and parametrizing the porous media struc-

ture; however, the relationship between the correlation functions and transport properties is not well understood. Apart from developing a fast and accurate reconstruction methodology, another aim of this work is to explore the relationships between different correlation functions and the transport properties of a random porous media. In particular, this preliminary study is focused on finding the diffusion characterization abilities of different correlation functions, i.e., how well can the correlation functions capture the diffusion coefficients.

To understand the transport characterization abilities of different correlation functions, the transport properties of reconstructed images must be compared against reference image properties. This process can be usually done in four steps: 1) Obtain a 3D reference image, 2) obtain reference correlation functions, and reference transport properties, 3) obtain stochastic reconstructions from the reference correlation functions, and 4) obtain transport properties of the reconstructions and compare against reference properties. To understand the effect of each correlation function on the transport properties, sensitivity of transport properties must be analyzed against each relevant correlation function. Since only void phase properties are analyzed, the effect of two-point correlation function, void phase lineal path function, and void phase chord length function on the transport properties needs to be analyzed. For sensitivity studies, reconstructions can be performed using each correlation function with different final tolerances. The effect of tolerance increase on transport properties can be then studied.

The sensitivity analysis is able to reveal the correlation function which has most impact on transport property prediction. The best correlation function can be combined with other correlation functions for reconstruction in order to improve statistical characterization, which should also improve the transport characterization. Using these studies, once a correlation function or a set of correlation functions has been found, which can describe the transport properties of a media with high accuracy, it can be then used to characterize the transport properties of the media. This in order paves the way for structure manipulation and transport optimization by changing the correlation functions.

For understanding mass transport in porous media, three phenomena: molecular diffusion, Knudsen diffusion and convection are most important [155]. Molecular diffusion

accounts for the transport of chemical species under chemical potential gradients [156], convection accounts for transport under pressure gradients [10], and Knudsen diffusion accounts for slip flow at small length scales or in rarefied gases [157]. These phenomena can be studied either at pore level, or at macro scale; however, to account for the structural details of the porous media, pore scale models must be used. For this work, pore scale simulations of molecular diffusion, and Knudsen diffusion are performed. The convective flow was not simulated, as the current model in use can only solve Navier-Stokes equations for small geometries.

5.1.1 Molecular Diffusion

Molecular diffusion of chemical species in a mixture is governed by Maxwell-Stefan equation. For isothermal diffusion, the equation is given as follows [10]:

$$\nabla x_i = \sum_{\substack{j=1 \\ j \neq i}}^n \frac{x_i \mathbf{N}_j^D - x_j \mathbf{N}_i^D}{c_t \mathcal{D}_{ij}}, \quad (5.1)$$

where x_i and x_j are molar fractions of species i and j respectively, \mathbf{N}_i^D and \mathbf{N}_j^D are molar fluxes of species i and j respectively, c_t is the total mixture concentration, \mathcal{D}_{ij} is the binary diffusion coefficient. For a binary mixture with species 1, and 2, Eq. (5.1) can be written as:

$$\begin{aligned} \nabla x_1 &= \frac{x_1 \mathbf{N}_2^D - x_2 \mathbf{N}_1^D}{c_t \mathcal{D}_{12}}, \\ \nabla x_2 &= \frac{x_2 \mathbf{N}_1^D - x_1 \mathbf{N}_2^D}{c_t \mathcal{D}_{12}}, \end{aligned} \quad (5.2)$$

where $x_1 + x_2 = 1$. For pure diffusion, i.e., in absence of convection, no net flow of mixture occurs.

$$\mathbf{N}_t^D \equiv \mathbf{N}_1^D + \mathbf{N}_2^D = 0, \quad (5.3)$$

where \mathbf{N}_t^D is the net molecular flux of the mixture. By using Eq. (5.3) in Eq. (5.2) and rearranging, the following equation can be obtained for the species flux:

$$\mathbf{N}_1^D \equiv -\mathbf{N}_2^D = -\mathcal{D}_{12} c_t \nabla x_1 = -\mathcal{D}_{12} \nabla c_1. \quad (5.4)$$

Equation (5.4) is the well known Fick's equation for binary diffusion [158].

The diffusion coefficient \mathcal{D}_{12} is dependent on the species, temperature and pressure. The following empirical relation is most commonly used to obtain the diffusivity of a mixture in

Bar·cm²/s [159]:

$$pD_{12} = \frac{0.00266T^{1.5}}{\sqrt{M_{12}\sigma_{12}^2}\Omega_D}, \quad (5.5)$$

where p is the pressure in Bar, T is the temperature in K, M_{12} is the harmonic mean of molecular weights of species 1 and 2 (in gram/mol), and σ_{12} is the arithmetic mean of the Lennard-Jones parameter σ (in Å) for species 1 and 2. The collision integral Ω_D is given as follows [159]:

$$\Omega_D = \frac{1.06036}{T_1^{0.1561}} + \frac{0.193}{\exp(0.47635T_1)} + \frac{1.03587}{\exp(1.52996T_1)} + \frac{1.76474}{\exp(3.89411T_1)}, \quad (5.6)$$

where $T_1 = T/\epsilon_{12}$, and ϵ_{12} is the geometric mean of Lennard-Jones parameter ϵ (in K) for species 1 and 2.

5.1.2 Knudsen Diffusion

For very small pore sizes or in rarefied gases, the mean free path of the gases is much higher than the length scale of the system. In this case, the molecule wall-collisions will be much higher compared to molecule-molecule interactions. Maxwell [160] showed that in rarefied gases the imbalance in stresses results in a slip flow parallel to the wall. The same phenomenon was observed by Knudsen during his experimentation of flow of rarefied gases in capillaries. An empirical relationship was derived for the average molar flux in capillaries as follows [10, 161]:

$$N = - \left(\frac{r_0^2}{8\mu} \langle P \rangle + D_{K,0} \frac{1 + c_1^k}{1 + c_2^k} \right) \frac{1}{RT} \frac{\Delta P}{L}, \quad (5.7)$$

where $\langle P \rangle$ is the average pressure over capillary, D_K is the Knudsen diffusivity and c_1^k , and c_2^k are empirical parameters. Comparing these equations and matching the observations of Knudsen to the Maxwell slip, the following equation is derived for Knudsen diffusion in the capillaries [10, 162]:

$$\mathbf{N}_i^D = -D_{K,i} \nabla c_i, \quad (5.8)$$

where \mathbf{N}_i^D is the molar Knudsen flux of species i , and $D_{K,i}$ is the Knudsen diffusion coefficient. The Knudsen diffusion coefficient can be obtained using the following equation [10, 162]:

$$D_{K,i} = \frac{2}{3} r_0 \sqrt{\frac{8RT}{\pi M_i}}, \quad (5.9)$$

where r_0 is the pore radius, and M_i is the molecular weight of species i .

Table 5.1 – Applicability of different flow models in different flow regimes based on Knudsen number [157]

| Knudsen number | Flow model |
|--------------------|--|
| $Kn < 0.001$ | Continuum region; Fick's, Navier-Stokes valid with no-slip boundary condition |
| $0.001 < Kn < 0.1$ | Continuum-transition region; Continuum models valid only with slip boundary condition |
| $0.1 < Kn < 10$ | Transition region; Continuum models not valid, moment equations or Burnett equation with slip boundary condition |
| $Kn > 10$ | Free molecule flow; No continuum model valid |

5.1.3 Transport in Transition Region

The extent of molecule-wall interactions over molecule-molecule interactions is given by Knudsen number, which is given as follows [157]:

$$Kn = \frac{\lambda}{L}, \quad (5.10)$$

where λ is the molecular mean free path (not to be confused with the annealing parameter λ is chapter 4), and L is the characteristic length scale of the media. For large pore sizes (large L), or for high pressures (small λ), the Knudsen number is low, which signifies that the molecule-wall interactions are negligible. For small pore sizes, or for rarefied gases however, the Knudsen number is high, signifying the increased importance of molecule-wall interactions. Based on the Knudsen number, the transport can be characterized in different domains. Table 5.1 shows the characterization of transport in different Knudsen regions.

In this work, the transport of an oxygen nitrogen mixture in Ti foam is studied. The mean free paths at STP for oxygen and nitrogen are 63.3nm and 58.8nm, respectively [163]. The characteristic length for the Ti foam is around $10\mu m$, resulting in a Knudsen number of around 0.006. The Knudsen number suggests that, the transport may have some Knudsen effects, which may need to be accounted for.

To combine the continuum model (Fick's diffusion) with the slip flow (Knudsen diffusion), a series network resistance model known as Bosanquet approximation is conventionally used [164]. The molecular diffusion and Knudsen diffusion are assumed to be in series. Combining

Eqns. (5.4), and (5.8), the following equation can be obtained for total diffusion:

$$\mathbf{N}_i^{tot} = -D_{ij}^{tot} \nabla c_i, \quad (5.11)$$

where \mathbf{N}_i^{tot} is the total molar flux of species i , and D_{ij}^{tot} is the net binary diffusion coefficient of species i in j , which is given as:

$$\frac{1}{D_{ij}^{tot}} = \frac{1}{\mathcal{D}_{ij}} + \frac{1}{D_{K,i}} \quad (5.12)$$

5.2 Simulation Methodology

5.2.1 Governing Equation

For simulating mass transport in the porous media, the mass conservation equation is solved for each species. In the absence of chemical reactions, the mass conservation for species i can be given as:

$$\nabla \cdot \mathbf{N}_i^{tot} \equiv \nabla \cdot (-D_i^{tot} \nabla c_i) = 0, \quad (5.13)$$

To simulate net diffusion with both: molecular, and Knudsen diffusion, Eq. (5.11) is used for flux estimation. In this study, pure molecular diffusion is also studied in order to be able to decouple the effective Knudsen parameter from the net parameters. For pure molecular diffusion simulation, Eq. (5.4) is used for flux estimation.

The simulations are performed for a constant temperature of $353K$, and a constant total pressure of 1atm (101325 Pa). The molecular diffusion coefficient is calculated using Eq. (5.5). The Knudsen diffusion coefficient is calculated using Eq. (5.9). The pore sizes at each location of the porous media are obtained by a sphere fitting method based on the distance transform method [38, 39].

5.2.2 Domain Generation

Once a stack of reference images or the reconstructed images have been obtained, the percolating void phase is identified in the 3D image. The cluster identification method developed for computing two-point cluster functions is used for this purpose. The entire percolating void volume is extracted using the cluster labels. An in-house Python based code (developed by Mayank Sabharwal [165]) is used to generate a 3D discretization (mesh) of the extracted

void phase. First order Lagrange elements are used for meshing. Each voxel of the 3D image essentially become an element in the mesh. Since the governing equation is linear, further grid refinements will not improve the results significantly. The net flow rate across one of the meshed domains was estimated as 1.254×10^{-8} mol/s for a mesh using $100 \times 100 \times 100$ elements. The net flow rate across the same domain was found to be 1.239×10^{-8} mol/s for a mesh using $200 \times 200 \times 200$ elements, showing only a 1% change in estimations. The meshing code also identifies the local pore radius for each element using a sphere fitting method, which is based on the distance transform method [38, 39]. The pore radius is stored for simulation purposes.

5.2.3 Simulation

The transport in the discretized domain is solved using a finite element based open source software openFCST [166, 167]. Gaussian numerical integration is used to evaluate the weak form of the governing equation. A direct solver MUMPS is used for solving the resulting system of equations. Transport in each direction is simulated separately to estimate effective properties in each direction. For example, to estimate x -direction effective properties, concentration is specified at inlet and outlet yz planes. The boundary conditions for each case were specified as follows:

$$\begin{aligned} x_{O_2} &= x_{O_2}^{in} \text{ on } \Gamma_1, \\ x_{O_2} &= x_{O_2}^{out} \text{ on } \Gamma_2, \text{ and} \\ \mathbf{N} \cdot \mathbf{n} &= 0 \text{ everywhere else,} \end{aligned} \tag{5.14}$$

where Γ_1 is the inlet plane and Γ_2 is the outlet plane opposite to the inlet plane. The governing equations are solved with the boundary conditions, and the fluxes of the species are calculated at each element. By integrating the fluxes over the outlet cross-section area, the net flow rate of species (mol/s) can be obtained. From the net flow rate, the effective diffusion coefficient in direction x can be obtained as follows:

$$D_{i,x}^{eff} = \frac{\dot{N}_x L_x}{A_{yz}(c_{i,in} - c_{i,out})}, \tag{5.15}$$

where \dot{N}_x is the net flow rate (mol/s) in x direction, L_x is the length of the media in x direction, A_{yz} is the total cross section area of the yz plane, $c_{i,in}$ is the concentration of species i at the inlet ($x = 0$), and $c_{i,out}$ is the concentration of species i at the outlet ($x = L_x$). The

effective diffusion coefficients for other directions can be obtained in a similar way.

Using the pure molecular diffusion simulations, effective molecular diffusivity in all three directions is obtained. Similarly, using the combined molecular and Knudsen diffusion simulations, effective total diffusivity in all three directions is obtained. Finally, the Bosanquet equation is used for estimating the effective Knudsen diffusion coefficient as follows:

$$\frac{1}{D_{ij}^{tot,eff}} = \frac{1}{D_{ij}^{D,eff}} + \frac{1}{D_i^{K,eff}} \quad (5.16)$$

Using this methodology, both effective diffusion coefficients: molecular, and Knudsen can be obtained.

5.3 Representative Size Estimation

For simulation of discretized domains, the size of the domain can affect its properties [68]. For the simulations results to be representative of the actual porous media, the domain size must be sufficient for capturing the complete physical behavior. This is critical for performing macro scale analysis and comparison on porous media, e.g., the simulations must be performed on a representative size for the estimated properties to be comparable to macro-scale properties measured by experiments. There are several ways of estimating the representative size of a media. The characteristic lengths obtained for different porous media in Chapter 4 provide one way of approximating representative size. The lengths estimated using stochastic analysis of two-point correlation function are however small, and may not results in correct transport estimations. Statistically, the size of an image should be larger than the representative size of porous media features. The chord length function, and lineal path function provide a good estimate of the largest features present in porous media. It can be hypothesized that, for an image to be representative, its size must be sufficiently higher than the maximum chord size in the porous media.

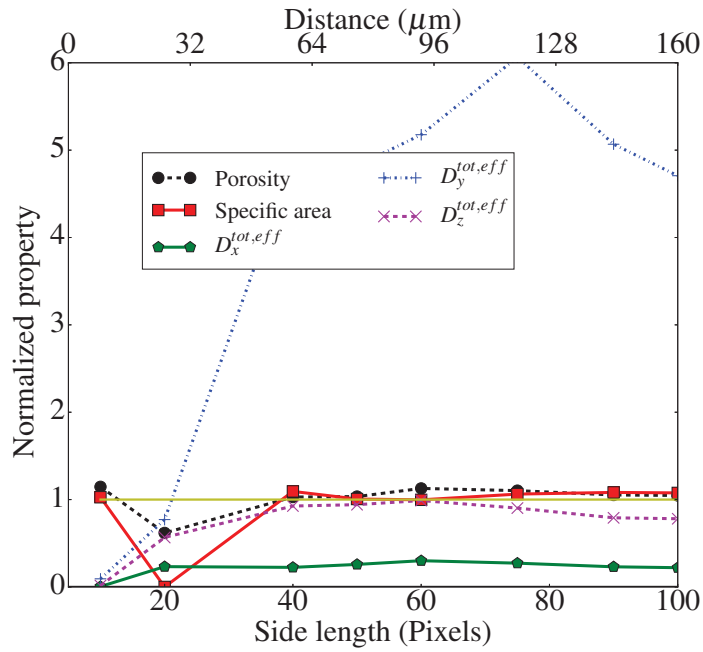
To ensure that a best possible size is chosen for reconstruction and simulation, several parameters are used for estimating the representative size of the porous media used for transport studies. Since 3D reference images are needed for comparison, the 3D micro-CT image of a Ti foam is used in this study. Samples of different sizes are extracted from the reference images, and their porosity, specific surface area, and effective total diffusion coefficient

($D^{tot,eff}$) in each direction are analyzed. The representative size is defined as the size after which any increase in sample dimension does not affect its effective statistical and transport properties. Since the thickness of Ti foam is small, the maximum size along the thickness (y direction) is limited to 100 pixels; however, larger images can be extracted in x direction. To ensure that representative size analysis was performed accurately, the properties were evaluated for larger image sizes in the direction where more pixels are available.

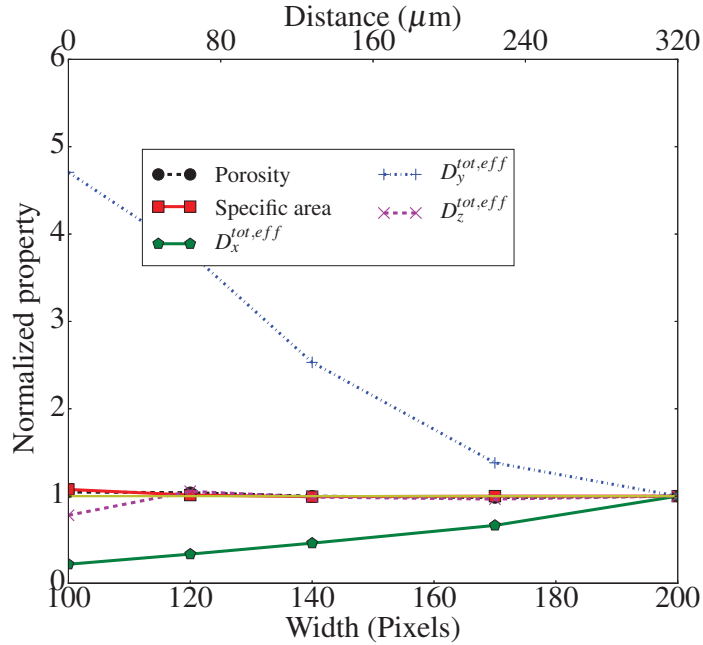
Figure 5.1 shows the effect of image size on the properties for the Ti foam micro-CT images. For image sizes up-to 100 pixels, the image is cubic. For larger sizes, since the thickness is limited, the size is only increased in x direction, and is kept fixed at 100 pixels in y and z directions. It can be seen that the statistical properties (porosity, and surface area) are the same for all sizes above 100 pixels. Among the transport properties, it is observed that the diffusion coefficient for z direction shows asymptotic behavior after a size of 100 pixels, and therefore should be representative. The diffusion coefficients in other two directions however, do not display any asymptotic behavior even at a size of 200 pixels. Therefore, the transport properties in x and y directions from these samples can not be used for macro scale analysis. Due to the limitation of reference image size, the reconstructions can only be performed upto a size of 100 pixels. Even though the reconstructions of size 100^3 pixels will not be representative of macro scale, the properties in z direction may be useful for comparison against reference structure properties. Only z direction properties are therefore used for further analysis. Since reconstruction size is limited to 100 pixels, representative analysis for sizes larger than 200 pixels was not performed, as it does not serve any purpose for current analysis.

5.4 Transport Studies in Ti Foam

To assess the sensitivity of transport properties towards correlation functions, multiple reconstructions of Ti foam were performed with multiple correlation function combinations, and different tolerances. Five samples of each porous media were reconstructed with different correlation functions. A 3D reference image of size 100^3 pixels was chosen. The resolution of the image is $1.6\mu m/\text{pixel}$ in all the three directions. For comparison purposes, all the reconstructions were also performed at a size of 100^3 pixels. The average transport properties



(a) Representative size analysis for a cubic image. The size for all the sides is same corresponding to each data point in the plot



(b) Representative size analysis for a non-cubic image. y and z dimensions are 100 pixels each. x dimension is varied and indicated by data points on the plot

Figure 5.1 – Effect of image size on normalized structural and transport properties of Ti foam micro-CT image. All the properties are normalized by their value at size 200 pixels

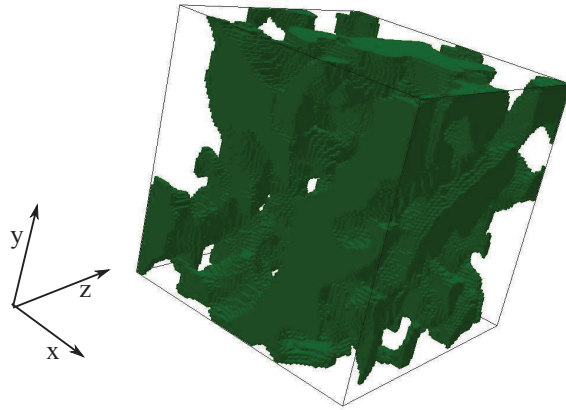
of each combination are then compared to the reference structure properties. The following sections describe the transport studies in reference and reconstructed images in details.

5.4.1 Transport Analysis in Reference Images

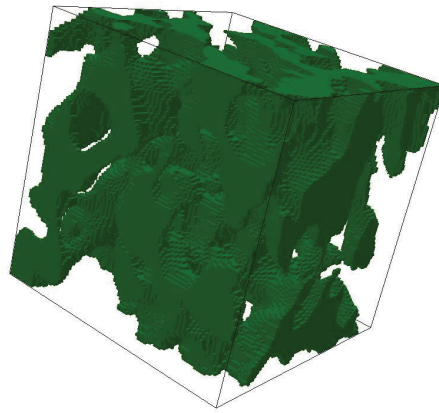
Mass transport was analyzed in all the thirteen sub-sample of the reference image, in order to see the variability within the media. As described in Section 5.2, first, the percolating void phase from each of the reference images is extracted. The void phase is then meshed using a first order Lagrange element. Figure 5.2 shows the discretized images of the void phase for two sub-samples. Figure 5.2(a) shows the mesh for the sub-sample which was used as a reference image for further reconstructions. The directions in all the meshes, and in all upcoming solutions are the same as depicted in Fig. 5.2(a).

Once the images are discretized to generate a mesh, bulk diffusion and combined bulk and Knudsen diffusion is simulated in the mesh. The simulation details and boundary conditions are described in Section 5.2. To validate the accuracy of the implementation and the solution, oxygen molar fraction over the domain is analyzed. Figure 5.3 shows the oxygen distribution across the discretized domain shown in Fig. 5.2(a). The direction is as depicted in Fig. 5.2(a). It can be seen that the boundary conditions are correctly implemented. The concentration front propagates in almost a linear manner, which is expected in a pure diffusion problem.

The simulation also yields the net flux of oxygen across the domain, which can be used to estimate effective diffusion coefficients. Due to large pore sizes in Ti foam, Knudsen effect is negligible, and does not affect the overall transport. For example, the bulk effective diffusion coefficient for the reference image in z direction is $5.82 \times 10^{-6} m^2/s$, while the effective Knudsen diffusion coefficient is $6.07 \times 10^{-4} m^2/s$. Due to almost two-orders of magnitude difference, Knudsen diffusion is neglected in subsequent Ti foam analysis. The average effective bulk diffusion coefficients in z direction for the thirteen Ti foam reference images was obtained as $(4.56 \pm 0.40) \times 10^{-6} m^2/s$. For the reference image used for further reconstructions, it was obtained as $5.82 \times 10^{-6} m^2/s$.



(a) A mesh obtained from a 3D image of Ti foam sub-sample. This sub-sample was used as reference structure for reconstructions



(b) A mesh obtained from another sub-sample of 3D image of Ti foam

Figure 5.2 – The discretized void phase of different sub-samples of Ti foam 3D image

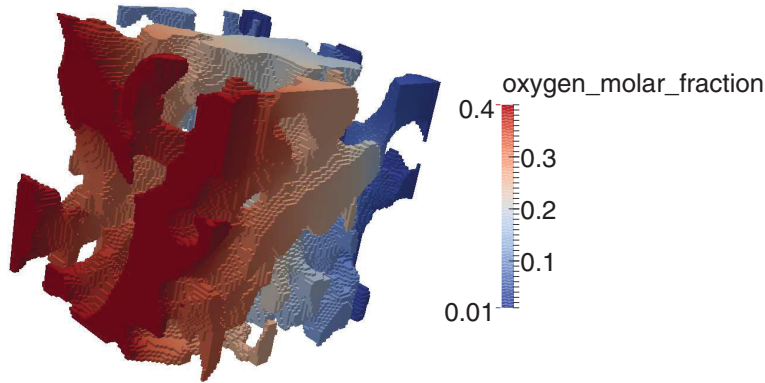


Figure 5.3 – Oxygen profile for diffusion along z direction in the discretized domain

5.4.2 Transport Analysis in Reconstructed Images

To see the effect of correlation functions on Ti foam reconstruction transport properties, one of the thirteen sub-samples was taken as a reference image. Reconstructions were performed using different correlation functions and combinations. The new DPN swapping method with $a = 0$, and $b = 0.5$ is used in conjunction with two grid levels, and threshold based energy minimization. Five reconstructions were performed using each correlation function or combination. The rest of the parameters are the same as described in Table 4.3, unless otherwise specified.

Sensitivity Analysis

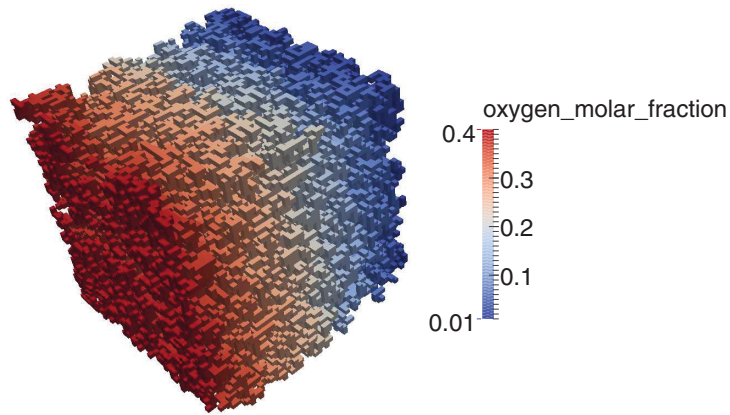
First, the sensitivity of molecular diffusion to different correlation functions was studied. Reconstructions were performed using only $S_2^{(v)}(r)$, only $L^{(v)}(r)$, and only $C^{(v)}(r)$. The final tolerance indicates the level of optimization and accuracy of the reconstruction. For each correlation function, effect of tolerance on diffusion coefficient was studied. Figure 5.4 shows the concentration profile on the reconstructions using two-point correlation functions for different energy tolerances. It can be seen that the quality of reconstructed images improves with decreasing tolerance. Table 5.2 shows the effective diffusivities in z direction for the reference and reconstructed images using different tolerances. For easier comparison, the percentage difference between reference and reconstructed diffusivity (deviation) was plotted against the energy tolerance. Figure 5.5 shows the deviation in diffusivity estimation compared to reference image at different energy tolerances. It is observed that all the reconstructed im-

Table 5.2 – Effect of tolerance on z direction effective bulk diffusivity for two-point correlation function based reconstructions. The margins of error are estimated based on 5 samples and reflect a 95% confidence interval

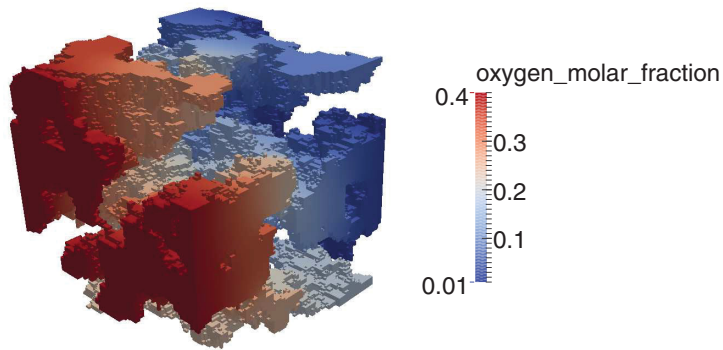
| Tolerance | $D_{O_2N_2,z}^{eff} \times 10^{-6} m^2/s$ | Average % deviation from reference |
|-----------------|---|------------------------------------|
| Reference image | 5.82 | 0.00 |
| 10^0 | 3.54 ± 0.00 | -39.18 |
| 10^{-1} | 5.10 ± 0.02 | -13.76 |
| 10^{-2} | 5.69 ± 0.04 | -12.42 |
| 10^{-3} | 5.44 ± 0.05 | -2.26 |
| 10^{-4} | 5.44 ± 0.05 | -6.60 |
| 10^{-5} | 5.08 ± 0.24 | -12.65 |
| 10^{-6} | 4.79 ± 0.39 | -17.69 |
| 10^{-7} | 5.20 ± 0.24 | -10.67 |
| 10^{-8} | 5.22 ± 0.08 | -10.29 |

ages underpredict diffusivity. For very coarse reconstructions (high tolerance), the diffusivity is significantly underpredicted, as significant noise remains in the reconstructions, resulting in low connectivity. Decreasing the tolerance improves the transport estimation in the beginning; however, for tolerances lower than 10^{-3} , the effective diffusivity does not change significantly. Even though the porosity of the image is always the same, the diffusivity varies with two-point correlation function. This shows that porosity alone is not sufficient for diffusion characterization. For all the tolerances lower than 10^{-3} , the diffusivity estimates are within 17% of the reference value. This suggests that two-point correlation function is able to characterize molecular diffusion closely, but not completely. Overall, the analysis suggests that the molecular diffusivity has a relationship with two-point correlation function; however, it alone is not sufficient to characterize molecular diffusion.

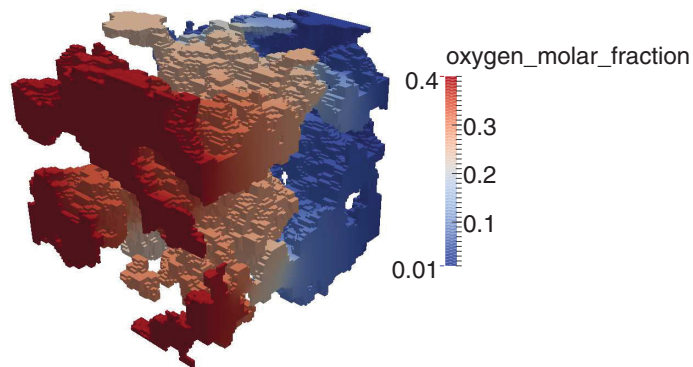
To see whether molecular diffusion has dependence on other void phase correlation functions, a similar tolerance sensitivity study was performed using void phase lineal path function. Figure 5.6 shows the concentration profile on the discretized geometries at different tolerances using void phase lineal path function for reconstruction. The images are not similar to the reference structure, as they show more jagged interfaces, and have less contours. A decreasing tolerance seems to make the structure more unrealistic. Table 5.3 shows the effective diffusivity in z direction for different tolerances of lineal path function. Unlike the two-point correlation function, the void lineal path function could not be optimized below a



(a) Concentration profile on a reconstruction using tolerance of 1.0



(b) Concentration profile on a reconstruction using tolerance of 10^{-4}



(c) Concentration profile on a reconstruction using tolerance of 10^{-8}

Figure 5.4 – Concentration profile on the discretized geometries of two-point correlation function based reconstructions with different tolerances

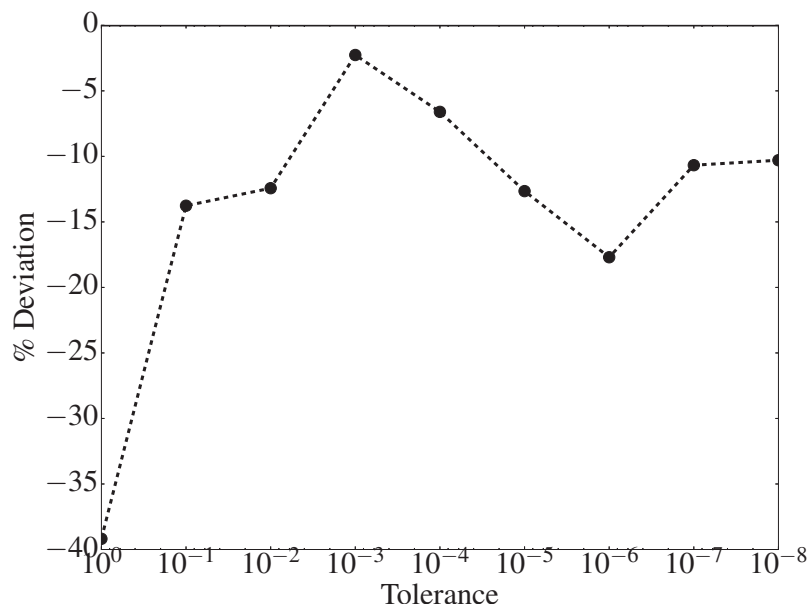
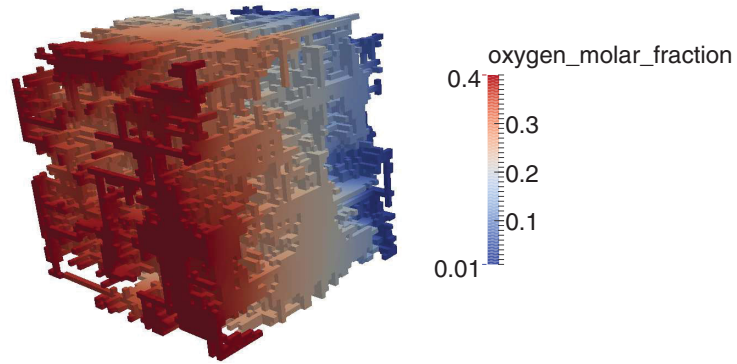


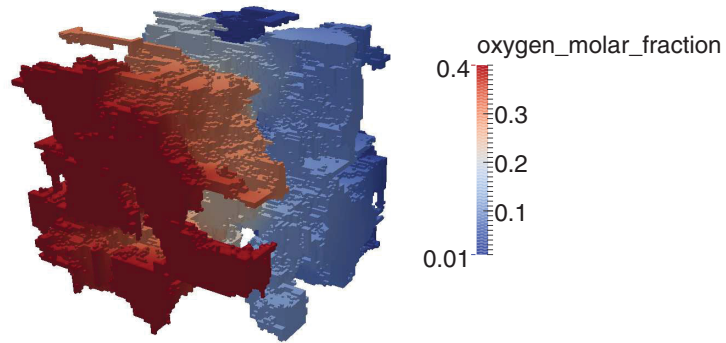
Figure 5.5 – Variation of error in effective diffusivity with change in energy tolerance for two-point correlation function based reconstructions

tolerance of approximately 2.45×10^{-5} . This indicates that the lineal path function produces a more complex energy landscape than two-point correlation function, which is difficult to optimize. The table also shows the deviation in diffusivity of each reconstruction from reference image, and the L_2 norm of error associated with the two-point correlation function. The deviation of diffusivity from reference image is shown in Fig. 5.7.

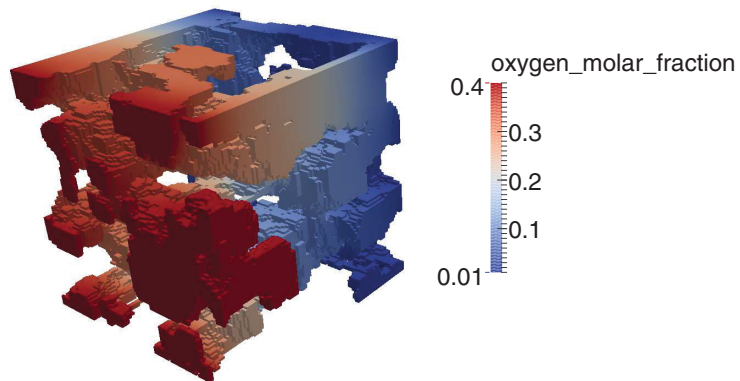
It is observed that most of the lineal path function based reconstructions have the z direction diffusivity within 20% of the reference image. The estimates are similar to two-point correlation function based reconstructions in accuracy. This is likely due to the fact that, optimizing lineal path function also results in partial optimization of two-point correlation function, as can be seen in Table 5.3. Since the two-point correlation function is able to characterize molecular diffusion, an indirect optimization of it should result in close estimations. An independent verification of this fact is however difficult, as it will require optimization of lineal path function without affecting the two-point correlation function. Overall, it is likely that the lineal path function has an indirect relationship with molecular diffusion through the two-point correlation function.



(a) Concentration profile on a reconstruction using tolerance of 10^{-1}



(b) Concentration profile on a reconstruction using tolerance of 10^{-3}



(c) Concentration profile on a reconstruction using tolerance of 2.45×10^{-5}

Figure 5.6 – Concentration profiles on the discretized geometries of void phase lineal path function based reconstructions with different tolerances

Table 5.3 – Effect of tolerance on effective bulk diffusivity for void phase lineal path function based reconstructions. The margins of error are estimated based on 5 samples and reflect a 95% confidence interval

| Tolerance | $D_{O_2N_2,z}^{eff} \times 10^{-6} m^2/s$ | Average % deviation from reference | L_2 norm of $S_2^{(v)}(r)$ |
|-----------------------|---|------------------------------------|------------------------------|
| Reference image | 5.82 | 0.00 | |
| 10^0 | 4.78 ± 0.00 | -17.83 | 0.31 ± 0.00 |
| 10^{-1} | 5.50 ± 0.00 | -5.42 | 0.09 ± 0.00 |
| 10^{-2} | 5.28 ± 0.01 | -9.32 | 0.06 ± 0.00 |
| 10^{-3} | 4.64 ± 0.18 | -20.25 | 0.05 ± 0.01 |
| 10^{-4} | 4.64 ± 0.62 | -20.28 | 0.06 ± 0.04 |
| 2.45×10^{-5} | 4.99 ± 0.07 | -14.23 | 0.02 ± 0.00 |

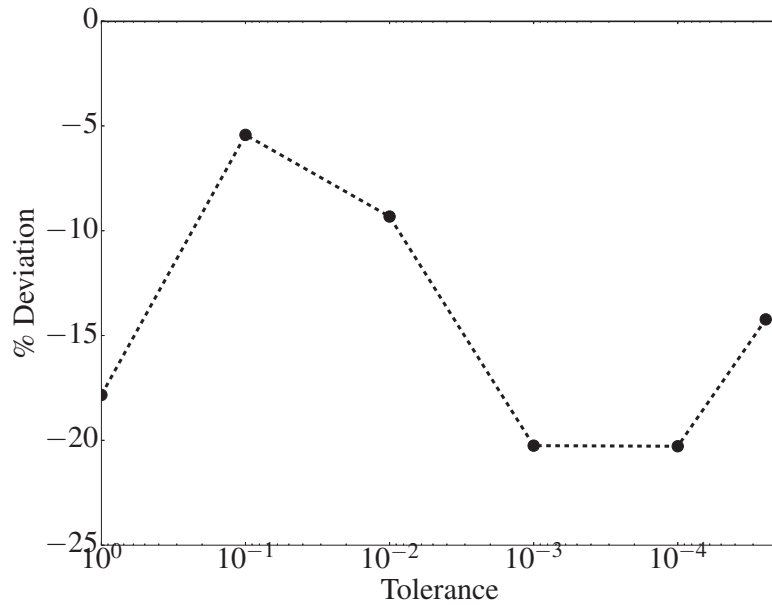


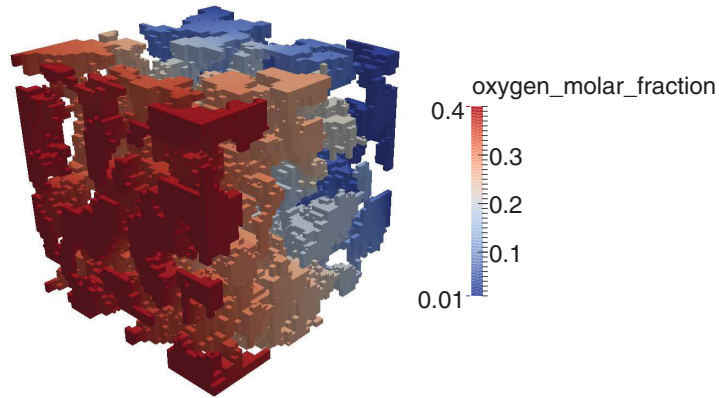
Figure 5.7 – Variation of error in effective diffusivity with change in energy tolerance for void phase lineal path function based reconstructions

Another tolerance sensitivity study was performed using void phase chord length function. Figure 5.8 shows the concentration profile on the discretized geometries at different tolerances using void phase chord length function for reconstruction. The reconstructions bear better resemblance to reference structure than the lineal path function based reconstructions; however, they are worse than two-point correlation function based reconstructions. Table 5.4 shows the effective diffusivity in z direction for different tolerances of chord length function, their deviation from reference, and the L_2 norm of error associated with two-point correlation function. The void phase chord length function could not be optimized below a tolerance of approximately 5.12×10^{-5} . This is likely due to the noisy nature of chord length function, resulting in a complex energy landscape, where reaching a global optimum is difficult. The deviation of diffusivity from reference image is shown in Fig. 5.9.

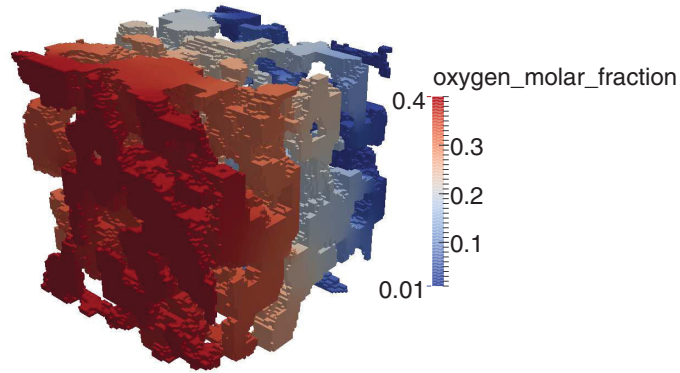
It is seen that all the void phase chord length function based reconstructions significantly underpredict effective diffusivity, and improving the tolerance has no significant impact on the diffusivity estimations. The overall predictions are significantly worse than two-point correlation function based, or lineal path function based reconstructions. This suggests that chord-length function may not have a direct relationship with molecular diffusion in porous media. One of the reasons for consistent low estimation of diffusivity in chord length function based reconstructions may be the non-optimization of two-point correlation function. The L_2 norms of two-point correlation function for current reconstructions are almost twice as high as the L_2 norms in lineal path function based reconstructions. This however, does not account fully for the extent of diffusivity underprediction by chord length function based reconstructions. Another possible reason is that, optimization of the chord length function alone may be resulting in creating porous media structures with higher tortuosity.

Effect of Multiple Correlation Functions

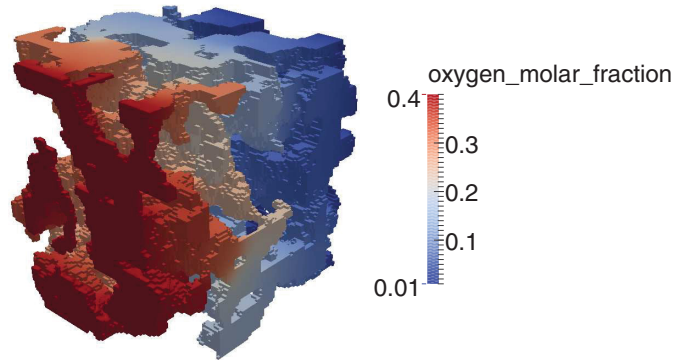
The sensitivity analysis shows that the two-point correlation function is able to closely characterize molecular diffusion in porous media; however, it is not sufficient for complete characterization. A combination of other void phase correlation functions with two-point correlation may improve estimate of molecular diffusivity. The two-point correlation function was combined with void phase lineal path function, and chord length function to estimate the effect on effective diffusivity estimations. Five reconstructions of size 100^3 pixels were made



(a) Concentration profile on a reconstruction using tolerance of 10^{-1}



(b) Concentration profile on a reconstruction using tolerance of 10^{-3}



(c) Concentration profile on a reconstruction using tolerance of 5.12×10^{-5}

Figure 5.8 – Concentration profiles on the discretized geometries of void phase chord length function based reconstructions with different tolerances

Table 5.4 – Effect of tolerance on effective bulk diffusivity for void phase chord length function based reconstructions. The margins of error are estimated based on 5 samples and reflect a 95% confidence interval

| Tolerance | $D_{O_2N_2,z}^{eff} \times 10^{-6} m^2/s$ | Average % deviation from reference | L_2 norm of $S_2^{(v)}(r)$ |
|-----------------------|---|------------------------------------|------------------------------|
| Reference image | 5.82 | 0.00 | |
| 10^0 | 3.95 ± 0.00 | -32.05 | 0.60 ± 0.00 |
| 10^{-1} | 3.38 ± 0.00 | -41.98 | 0.20 ± 0.00 |
| 10^{-2} | 3.53 ± 0.02 | -39.38 | 0.20 ± 0.00 |
| 10^{-3} | 2.85 ± 0.02 | -51.04 | 0.15 ± 0.00 |
| 10^{-4} | 2.90 ± 0.23 | -50.09 | 0.13 ± 0.01 |
| 5.12×10^{-5} | 3.37 ± 0.08 | -42.04 | 0.10 ± 0.00 |

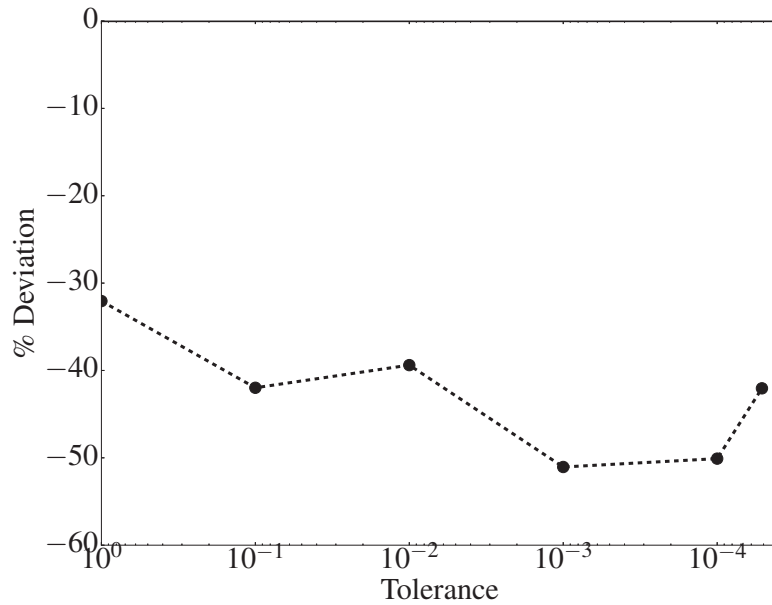


Figure 5.9 – Variation of error in effective diffusivity with change in energy tolerance for void phase chord length function based reconstructions

Table 5.5 – Comparison of discrepancy in different correlation functions for 3D Ti foam reconstructions with different correlation functions. Blue color indicates the function which is being optimized. Green color indicates a function which is not included in optimization but still gets optimized. The margins of error are estimated based on 5 samples and reflect a 95% confidence interval

| Functions used | L2 norms of error for the function | | | |
|-----------------------------|------------------------------------|----------------------------------|----------------------------------|----------------------------------|
| | $S_2^{(v)}(r)$ | $C_2^{(v)}(r)$ | $L^{(v)}(z)$ | $C^{(v)}(z)$ |
| $S_2^{(v)}(r)$ | $(1.00 \pm 0.00) \times 10^{-6}$ | $(1.32 \pm 0.44) \times 10^{-4}$ | $(2.52 \pm 1.74) \times 10^{-3}$ | $(1.03 \pm 0.02) \times 10^{-2}$ |
| $S_2^{(v)}(r) + L^{(v)}(r)$ | $(3.03 \pm 0.12) \times 10^{-8}$ | $(2.77 \pm 2.57) \times 10^{-5}$ | $(2.42 \pm 0.00) \times 10^{-5}$ | $(3.33 \pm 0.02) \times 10^{-3}$ |
| $S_2^{(v)}(r) + C^{(v)}(r)$ | $(5.18 \pm 0.04) \times 10^{-5}$ | $(1.58 \pm 0.11) \times 10^{-3}$ | $(3.66 \pm 0.08) \times 10^{-2}$ | $(4.31 \pm 0.14) \times 10^{-6}$ |

using each correlation function combination, and their transport properties were analyzed. The energy tolerance for each correlation function was specified as 10^{-6} .

Table 5.5 shows the L_2 norms of different correlation functions for different combinations. It can be seen that when using void phase lineal path function, the two-point correlation function gets minimized to a low tolerance; however, when using void phase chord length function, the final convergence is higher. This is due to the noisy nature of chord length function, which makes a complex energy landscape, making it difficult to optimize. Using lineal path function also results in partial improvement of chord length function, even when it is not included in minimization.

Table 5.6 shows the effective molecular diffusion coefficient in z direction for the reference and reconstructed Ti foam images. It is observed that, adding either void phase lineal path function, or chord length function to two-point correlation function improves the diffusivity by a small margin. Using the lineal path function results in a better estimate, as it also indirectly improves chord length function as seen in Table 5.5. The chord length function and lineal path function may be weakly related to molecular diffusion, thereby improving its estimation; however, by themselves, they can not estimate diffusivity, as two-point correlation function appears to be the key statistical function for characterizing molecular diffusion.

Table 5.6 – Comparison of transport properties of reference and reconstructed Ti foam structure. The margins of error are estimated based on 5 samples and reflect a 95% confidence interval

| Type | $D_{O_2N_2,z}^{eff} \times 10^{-6} m^2/s$ | Average % deviation from reference |
|-----------------------------|---|------------------------------------|
| Reference image | 5.82 | 0 |
| $S_2^{(v)}(r)$ | 4.79 ± 0.39 | -17.69 |
| $S_2^{(v)}(r) + L^{(v)}(r)$ | 5.08 ± 0.08 | -12.71 |
| $S_2^{(v)}(r) + C^{(v)}(r)$ | 4.90 ± 0.08 | -15.8 |

Discussion

For all the reconstructions, it is observed that the effective molecular diffusivity estimations are always lower than the reference value. The effective diffusivity of a porous media is given as follows [10]:

$$D_{ij}^{eff} = \frac{\epsilon}{\tau} D_{ij}, \quad (5.17)$$

where ϵ is the porosity, τ is the tortuosity, and D_{ij} is the bulk diffusivity. For all the optimized reconstructions, the porosity is the same as the reference image. Since the bulk diffusivity is specified as same in all the simulations, the underprediction in the reconstructions must be due to difference in tortuosity between reference and reconstructed images. Conventionally, the tortuosity is estimated from effective media approximations such as Bruggeman equation [51]:

$$\tau = \epsilon^{-0.5}. \quad (5.18)$$

Since the effective diffusivity for the images is known from pore scale simulations, tortuosity of each image can be estimated by adjusting Eq. (5.17) as follows:

$$\tau = \epsilon \frac{D_{ij}}{D_{ij}^{eff}}. \quad (5.19)$$

Table 5.7 shows the tortuosity estimations for the reference and reconstructed images discussed in Table 5.6. As expected, it can be seen that the tortuosity of the reconstructed images is higher than the reference image, resulting in underprediction of effective diffusivity. The reason for consistently higher tortuosity may be due to exclusion of some critical correlation function, or some phenomenon inherent to reconstruction process. It is usually observed that the interfaces in reconstructions are less smooth than the reference image, which may contribute in increasing tortuosity. Since the reconstructions are performed by

Table 5.7 – Tortuosity estimations for reference and reconstructed images from pore scale simulations, and their comparison with Bruggeman estimation

| Type | Tortuosity estimation from pore scale simulation | Tortuosity estimation from Bruggeman equation |
|-----------------------------|--|---|
| Reference image | 1.814 | 1.61 |
| $S_2^{(v)}(r)$ | 2.2 ± 0.15 | 1.61 |
| $S_2^{(v)}(r) + L^{(v)}(r)$ | 2.07 ± 0.03 | 1.61 |
| $S_2^{(v)}(r) + C^{(v)}(r)$ | 2.15 ± 0.03 | 1.61 |

pixel swapping from a random initial image, the surfaces do not possess the same degree of smoothness as the reference image. This phenomenon is inherent to pixel based reconstruction methods, and may be a contributing factor in underprediction of effective diffusivity. It is also observed that Bruggeman correlation underpredicts tortuosity, which has also been observed for other porous media in literature [168].

5.5 Summary

A preliminary analysis of molecular diffusion was performed in Ti foam. The analysis shows that two-point correlation function is able to characterize effective molecular diffusivity of a porous media. For accurate characterization of molecular diffusivity of reference structures, the two-point correlation function should be optimized. The lineal path function also seems to characterize the molecular diffusion to some extent, which is most likely due to its indirect relationship with two-point correlation function; however, reconstruction using only lineal path function results in unrealistic structure of porous media. Addition of void phase lineal path function or chord length function to two-point correlation function improves the estimations by a marginal amount. Overall, the two-point correlation function appears to be the key parameter for characterizing molecular diffusion. The two-point correlation function based reconstructions are able to reproduce the reference structure diffusivity within 17% error.

It must be noted that all these conclusions are based on a preliminary study of mass transport in a single porous media; therefore, this study provides only limited information on mass transport characterization. Since a single porous media was used, the obtained re-

sults could be very specific to this case. A detailed study is therefore required, using multiple porous media with different porosity, domain size, and pore features. The characterization of molecular diffusivity also needs to be improved. There can be two reasons for the small but consistent underestimation of diffusion: 1) some phenomena inherent to stochastic reconstructions, which results in higher tortuosity, and lower diffusivity, or 2) some other statistical information is required for complete characterization. Further detailed analysis of molecular diffusion in different porous media structures is required to confirm this hypothesis. Also, larger reconstructions need to be used for better representative estimation, and more accurate contour reproduction.

Chapter 6

Conclusions and Future Work

Advances in imaging techniques are providing new and interesting insights on the morphology of porous materials; however, current understanding of key parameters affecting transport processes in porous media remains limited. A mathematical representation of the porous media parameters is required for parametric characterization. Mathematical characterization of the morphology provides a way to relate transport properties of a porous media to its structural properties. A methodology to generate microstructures with desired parametrization functions is also necessary for transport simulations. By performing transport simulations on the generated microstructures, the structural parameters can be correlated to the effective transport properties, which provides a way for designing porous media with desired transport performance.

6.1 Conclusions

The primary aim of this work was to develop a methodology to understand transport in realistic geometries of porous media. Statistical analysis tools and stochastic reconstruction methodology were required, which could generate high accuracy reconstructions with multiple correlation functions at minimal computational cost. In order to achieve these goals, a simulated annealing based reconstruction method was implemented using an in-house C++ based program. For improving the conventional simulated annealing based reconstruction methodology, a detailed literature review was performed in order to identify potential new techniques. Based on the shortcomings of the conventional method, new pixel swapping methods, energy minimization methods, and annealing methods were identified. The program enables the comparison of different techniques against each other in terms of recon-

struction accuracy and computational speed.

A new threshold energy based acceptance criteria was implemented, which used threshold energy instead of conventional probability based acceptance. The threshold based method fractionally improves the speed of the reconstruction process compared to the conventional probability based method. A dynamic annealing schedule was also implemented, resulting in around 15% time saving compared to conventional static annealing for a 200^2 pixels size image. The time savings are dependent on image sizes, and can be even higher for larger images.

A unified pixel swapping algorithm was presented, which can implement random, surface or biased pixel swapping by parameter modification. The conventional DPN based method presented by Tang et al. [98] was found to result in unrealistic and flattened structures due to the high amount of bias towards DPN values, a phenomenon, which so far has not been noticed due to the small image sizes used in reconstructions. A detailed parameter optimization of the DPN method resulted in an optimum set of parameters, which minimize the reconstruction time while keeping the reconstructions realistic. The optimized method does not impose maximum probability on highest DPN sets, and asserts a minor bias on DPN value ($b = 0.5$). Overall, the new DPN method was found to reduce the reconstruction time by approximately a factor of 3 compared to random swapping for 200^2 pixels size image. Higher time reductions are expected for larger images.

A multigrid hierarchical method was presented which uses the DPN information for hierarchy implementation. The method performs reconstructions at small scales and consecutively refines them. The new method does not use gray pixels values for freezing. Instead, DPN information is used to freeze pixels during refinement, which makes its implementation easy, as DPN information is readily available. For a 600^2 pixels size image, the new multigrid method was found to reduce the reconstruction time by a factor of 15 compared to a single grid method. For 3D reconstructions, the new DPN based multigrid method provides around 100 times speed reduction compared to conventional single grid and random swapping based method. Reconstructions of medium 3D images (300^3 - 600^3) can now be performed in practical amount of time, enabling detailed study of physical process in the reconstructed 3D structures.

Due to the accuracy and high speed of the developed reconstruction method, using multiple correlation functions is now possible for reconstructions. A preliminary transport study was performed on reference and reconstructed structures of Ti foam. The ability of different correlation functions to characterize molecular diffusivity was studied. A sensitivity analysis showed that the two-point correlation function is a key parameter for characterizing molecular diffusion in porous media. The effective diffusivity of the reconstructions shows a small (approximately 15%), but consistent underprediction compared to reference structure diffusivity. Combining two-point correlation function with either void phase lineal path function, or chord length function marginally improves the estimation, suggesting a possible weak relation between molecular diffusion and these functions.

In summary, this thesis presents:

- Development of a stochastic reconstruction method based on biased pixel swapping method
- Development of a multigrid hierarchical annealing method based on DPN information
- Implementations of new energy minimization and annealing methods
- A detailed study of effect of pixel bias on reconstructed structures
- Development of a unified pixel swapping algorithm
- Study of effect of correlation functions on structural and physical accuracy of reconstructions

6.2 Future Work

This thesis has primarily focused on developing a reconstruction framework for porous media studies. Due to time restrictions and implementation complexities, two important correlation functions, two-point cluster function and pore size distribution function are not implemented in the reconstruction methodology. It is observed from literature analysis, and current studies that these correlation functions may play an important role in improving the physical accuracy of the reconstructed structures. Future work will therefore focus on implementing

these correlation functions in the reconstruction program.

This work only performed a preliminary analysis on transport properties of the reconstructed structures. Since the primary aim of the reconstruction method is to generate domains for physical studies, future work will focus on use of the program for studying different porous media and their physical properties. The focus will specially be on studying porous media with different porosity and structural features. The future studies will also use larger images in order to be representative in all the directions.

References

- [1] Y. Jiao, F.H. Stillinger, and S. Torquato. Modeling heterogeneous materials via two-point correlation functions: Basic principles. *Physical Review E*, 76(3):031110, 2007.
- [2] J.D. Wishart, Z. Dong, and M. Secanell. Optimization of a PEM fuel cell system for low-speed hybrid electric vehicles. In *ASME 2006 International Design Engineering Technical Conferences & Computers and Information in Engineering Conference*, Philadelphia, Pennsylvania, USA, September 10-13, 2006.
- [3] Dimitrios Papageorgopoulos. U.S. Department of Energy Hydrogen and Fuel Cells Overview. In *H2FC-FAIR*, Hannover, Germany, April 2013. U.S. Department of Energy.
- [4] James Larminie and Andrew Dicks. *Fuel Cell Systems Explained*. Wiley, West Sussex, England, 2 edition, 2003.
- [5] R. O' Hayre, S. W. Cha, W. Colella, and F. B. Prinz. *Fuel Cell Fundamentals*. Wiley, New York, USA, 2 edition, 2008.
- [6] Prafful Mangal, Lalit M Pant, Nicholas Carrigy, Mark Dumontier, Valentin Zingan, Sushanta Mitra, and Marc Secanell. Experimental study of mass transport in PEMFCs: Through plane permeability and molecular diffusivity in GDLs. *Electrochimica Acta*, 167:160–171, 2015.
- [7] M. Eikerling. Water management in cathode catalyst layers of PEM fuel cells. *Journal of the Electrochemical Society*, 153(3):E58–E70, 2006.
- [8] A.Z. Weber, R.L. Borup, R.M. Darling, P.K. Das, T.J. Dursch, W. Gu, D. Harvey, A. Kusoglu, S. Litster, M.M. Mench, R. Mukundan, J.P. Owejan, J.G. Pharoah, M. Secanell, and I.V. Zenyuk. A critical review of modeling transport phenomena in polymer-

- electrolyte fuel cells. *Journal of the Electrochemical Society*, 161(12):F1254–F1299, 2014.
- [9] L. M. Pant, S. K. Mitra, and M. Secanell. Absolute permeability and Knudsen diffusivity measurements in PEMFC gas diffusion layers and micro porous layers. *Journal of Power Sources*, 206:153–160, 2012.
- [10] P.J.A.M. Kerkhof. A modified Maxwell-Stefan model for transport through inert membranes: The binary friction model. *The Chemical Engineering Journal and the Biochemical Engineering Journal*, 64(3):319–343, 1996.
- [11] M. Quintard, L. Bletzacker, D. Chenu, and S. Whitaker. Nonlinear, multicomponent, mass transport in porous media. *Chemical Engineering Science*, 61(8):2643–2669, 2006.
- [12] L. Shen and Z. Chen. Critical review of the impact of tortuosity on diffusion. *Chemical Engineering Science*, 62(14):3748–3755, 2007.
- [13] N.B. Carrigy, L.M. Pant, S. Mitra, and M. Secanell. Knudsen diffusivity and permeability of pemfc microporous coated gas diffusion layers for different polytetrafluoroethylene loadings. *Journal of the Electrochemical Society*, 160(2):F81–F89, 2013.
- [14] J.M. Lamanna and S.G. Kandlikar. Determination of effective water vapor diffusion coefficient in PEMFC gas diffusion layers. *International Journal of Hydrogen Energy*, 36(8):5021–5029, 2011.
- [15] D. Kramer, S.A. Freunberger, R. Fluckiger, I.A. Schneider, A. Wokaun, F.N. Buchi, and G.G. Scherer. Electrochemical diffusimetry of fuel cell gas diffusion layers. *Journal of Electroanalytical Chemistry*, 612(1):63–77, 2008.
- [16] D. Baker, C. Wieser, K.C. Neyerlin, and M.W. Murphy. The use of limiting current to determine transport resistance in PEM fuel cells. volume 3, pages 989–999, 2006.
- [17] X. Ye and C.-Y. Wang. Measurement of water transport properties through membrane electrode assemblies: Part II. Cathode diffusion media. *Journal of the Electrochemical Society*, 154(7):B683–B686, 2007.
- [18] X. Cui, A.M.M. Bustin, and R.M. Bustin. Measurements of gas permeability and diffusivity of tight reservoir rocks: Different approaches and their applications. *Geofluids*, 9(3):208–223, 2009.

- [19] M.K. Dabbous, A.A. Reznik, J.J. Taber, and P.F. Fulton. The Permeability of Coal to Gas and Water. *SPE Journal*, 14(6):563–572, 1974.
- [20] P.D. Gamson, B.B. Beamish, and D.P. Johnson. Coal microstructure and micropermeability and their effects on natural gas recovery. *Fuel*, 72(1):87–99, 1993.
- [21] Z. Pan and L.D. Connell. Modelling permeability for coal reservoirs: A review of analytical models and testing data. *International Journal of Coal Geology*, 92:1–44, 2012.
- [22] R. B. Evans III, G.M. Watson, and J. Truitt. Interdiffusion of gases in a low permeability graphite at uniform pressure. *Journal of Applied Physics*, 33(9):2682–2688, 1962.
- [23] R. B. Evans III, G.M. Watson, and J. Truitt. Interdiffusion of gases in a low-permeability graphite. II. Influence of pressure gradients. *Journal of Applied Physics*, 34(7):2020–2026, 1963.
- [24] J.H. Dunsmuir, S.R. Ferguson, K.L. D’Amico, and J.P. Stokes. X-ray microtomography. A new tool for the characterization of porous media. volume Pi, pages 423–430, 1991.
- [25] M.E. Coles, R.D. Hazlett, E.L. Muegge, K.W. Jones, B. Andrews, B. Dowd, P. Siddons, A. Peskin, P. Spanne, and W.E. Soll. Developments in synchrotron X-ray microtomography with applications to flow in porous media. volume Omega, pages 413–424, 1996.
- [26] C.H. Arns, F. Bauget, A. Limaye, A. Sakellariou, T.J. Senden, A.P. Sheppard, R.M. Sok, W.V. Pinczewski, S. Bakke, L.I. Berge, P.-E. Oren, and M.A. Knackstedt. Pore-scale characterization of carbonates using x-ray microtomography. *SPE Journal*, 10(4):475–484, 2005.
- [27] H. Ostadi, P. Rama, Y. Liu, R. Chen, X.X. Zhang, and K. Jiang. 3D reconstruction of a gas diffusion layer and a microporous layer. *Journal of Membrane Science*, 351(1-2): 69–74, 2010.
- [28] P.R. Shearing, J. Gelb, and N.P. Brandon. X-ray nano computerised tomography of SOFC electrodes using a focused ion beam sample-preparation technique. *Journal of the European Ceramic Society*, 30(8):1809–1814, 2010.

- [29] W.K. Epting, J. Gelb, and S. Litster. Resolving the three-dimensional microstructure of polymer electrolyte fuel cell electrodes using nanometer-scale X-ray computed tomography. *Advanced Functional Materials*, 22(3):555–560, 2012.
- [30] S. Litster, W. K. Epting, E. A. Wargo, S. R. Kalidindi, and E. C. Kumbur. Morphological Analyses of Polymer Electrolyte Fuel Cell Electrodes with Nano-Scale Computed Tomography Imaging. *Fuel Cells*, 13(5):935–945, 2013. ISSN 1615-6854.
- [31] N. Khajeh-Hosseini-Dalasm, T. Sasabe, T. Tokumasu, and U. Pasaogullari. Effects of polytetrafluoroethylene treatment and compression on gas diffusion layer microstructure using high-resolution X-ray computed tomography. *Journal of Power Sources*, 266:213–221, 2014.
- [32] B. Bera, S.K. Mitra, and D. Vick. Understanding the micro structure of Berea Sandstone by the simultaneous use of micro-computed tomography (micro-CT) and focused ion beam-scanning electron microscopy (FIB-SEM). *Micron*, 42(5):412–418, 2011.
- [33] S. Thiele, R. Zengerle, and C. Ziegler. Nano-morphology of a polymer electrolyte fuel cell catalyst layer-imaging, reconstruction and analysis. *Nano Research*, pages 1–12, 2011.
- [34] C. Ziegler, S. Thiele, and R. Zengerle. Direct three-dimensional reconstruction of a nanoporous catalyst layer for a polymer electrolyte fuel cell. *Journal of Power Sources*, 196(4):2094–2097, 2011.
- [35] N.S.K. Gunda, H.-W. Choi, A. Berson, B. Kenney, K. Karan, J.G. Pharoah, and S.K. Mitra. Focused ion beam-scanning electron microscopy on solid-oxide fuel-cell electrode: Image analysis and computing effective transport properties. *Journal of Power Sources*, 196(7):3592–3603, 2011.
- [36] A. Cecen, E.A. Wargo, A.C. Hanna, D.M. Turner, S.R. Kalidindi, and E.C. Kumbur. 3-D microstructure analysis of fuel cell materials: Spatial distributions of tortuosity, void size and diffusivity. *Journal of the Electrochemical Society*, 159(3):B299–B307, 2012.
- [37] K.J. Lange, H. Carlsson, I. Stewart, P.-C. Sui, R. Herring, and N. Djilali. PEM fuel cell CL characterization using a standalone FIB and SEM: Experiments and simulation. *Electrochimica Acta*, 85:322–331, 2012.

- [38] T. Hutzenlaub, J. Becker, R. Zengerle, and S. Thiele. Modelling the water distribution within a hydrophilic and hydrophobic 3D reconstructed cathode catalyst layer of a proton exchange membrane fuel cell. *Journal of Power Sources*, 227:260–266, 2013.
- [39] X. Zhang, Y. Gao, H. Ostadi, K. Jiang, and R. Chen. Modelling water intrusion and oxygen diffusion in a reconstructed microporous layer of PEM fuel cells. *International Journal of Hydrogen Energy*, 39(30):17222–17230, 2014.
- [40] F. Verhelst, P. David, W. Fermont, L. Jegers, and A. Vervoort. Correlation of 3D-computerized tomographic scans and 2D-colour image analysis of Westphalian coal by means of multivariate statistics. *International Journal of Coal Geology*, 29(1-3):1–21, 1996.
- [41] F.J. Simons, F. Verhelst, and R. Swennen. Quantitative characterization of coal by means of microfocal X-ray computed microtomography (CMT) and color image analysis (CIA). *International Journal of Coal Geology*, 34(1-2):69–88, 1997.
- [42] M. Van Geet, R. Swennen, and M. Wevers. Quantitative analysis of reservoir rocks by microfocus X-ray computerised tomography. *Sediment Geol*, 132(1-2):25–36, 2000.
- [43] M. Van Geet, R. Swennen, and M. Wevers. Towards 3-D petrography: Application of microfocus computer tomography in geological science. *Computers & Geosciences*, 27(9):1091–1099, 2001.
- [44] C.H. Arns, F. Bauget, A. Ghous, A. Sakellariou, T.J. Senden, A.P. Sheppard, R.M. Sok, W.V. Pinczewski, J.C. Kelly, and M.A. Knackstedt. Digital core laboratory: Petrophysical analysis from 3D imaging of reservoir core fragments. *Petrophysics*, 46(4):260–277, 2005.
- [45] V. Cnudde and M.N. Boone. High-resolution X-ray computed tomography in geosciences: A review of the current technology and applications. *Earth-Science Reviews*, 123:1–17, 2013.
- [46] Lalit M Pant, Haiping Huang, Marc Secanell, Steve Larter, and Sushanta K Mitra. Multi scale characterization of coal structure for mass transport. *Fuel*, 159:315–323, Jan 2015.

- [47] J.R. Wilson, W. Kobsiriphat, R. Mendoza, H.-Y. Chen, J.M. Hiller, D.J. Miller, K. Thornton, P.W. Voorhees, S.B. Adler, and S.A. Barnett. Three-dimensional reconstruction of a solid-oxide fuel-cell anode. *Nature Materials*, 5(7):541–544, 2006.
- [48] Richard Wirth. Focused Ion Beam (FIB) combined with SEM and TEM: Advanced analytical tools for studies of chemical composition, microstructure and crystal structure in geomaterials on a nanometre scale. *Chemical Geology*, 261(3-4):217–229, 2009.
- [49] W.R. Campaigne and P.W. Fieguth. Frozen-state hierarchical annealing. *IEEE Transactions on Image Processing*, 22(4):1486–1497, 2013.
- [50] S. Torquato and G. Stell. Microstructure of two-phase random media. I. The n-point probability functions. *The Journal of Chemical Physics*, 77(4):2071–2077, 1982.
- [51] D. A. G. Bruggeman. Berechnung Verschiedener Physikalischer Konstanten von Heterogenen Substanzen. I. Dielektrizitätskonstanten und Leitfähigkeiten der Mischkörper aus Isotropen Substanzen. *Annalen der Physik-leipzig*, 24:636–679, 1935.
- [52] J.C. Maxwell-Garnett. Colours in metal glasses and in metallic films. *Philosophical Transactions of the Royal Society London*, 203:385–420, 1904.
- [53] O. Levy and D. Stroud. Maxwell Garnett theory for mixtures of anisotropic inclusions: Application to conducting polymers. *Physical Review B*, 56(13):8035–8046, 1997.
- [54] Robert E. De La Rue and Charles W. Tobias. On the Conductivity of Dispersions. *Journal of the Electrochemical Society*, 106(9):827–833, 1959.
- [55] W.F. Brown Jr. Solid mixture permittivities. *The Journal of Chemical Physics*, 23(8):1514–1517, 1955.
- [56] H. L. Frisch. Statistics of Random Media. *Transactions of The Society of Rheology*, 9(1):293–312, 1965.
- [57] S. Torquato and G. Stell. Microstructure of two-phase random media. III. The n-point matrix probability functions for fully penetrable spheres. *The Journal of Chemical Physics*, 79(3):1505–1510, 1983.
- [58] P Smith and S Torquato. Computer simulation results for the two-point probability

- function of composite media. *Journal of Computational Physics*, 76(1):176 – 191, 1988. ISSN 0021-9991.
- [59] J.G. Berryman. Measurement of spatial correlation functions using image processing techniques. *Journal of Applied Physics*, 57(7):2374–2384, 1985.
- [60] D.A. Coker and S. Torquato. Extraction of morphological quantities from a digitized medium. *Journal of Applied Physics*, 77(12):6087–6099, 1995.
- [61] J.A. Quiblier. A new three-dimensional modeling technique for studying porous media. *Journal of Colloid and Interface Science*, 98(1):84–102, 1984.
- [62] P.M. Adler, C.G. Jacquin, and J.A. Quiblier. Flow in simulated porous media. *International Journal of Multiphase Flow*, 16(4):691–712, 1990.
- [63] C. L. Y. Yeong and S. Torquato. Reconstructing random media. *Physical Review E*, 57(1):495–506, 1998.
- [64] M.S. Talukdar, O. Torsaeter, M.A. Ioannidis, and J.J. Howard. Stochastic reconstruction of chalk from 2D images. *Transport in Porous Media*, 48(1):101–123, 2002.
- [65] K.M. Gerke, M.V. Karsanina, and E.B. Skvortsova. Description and reconstruction of the soil pore space using correlation functions. *Eurasian Soil Science*, 45(9):962–973, 2012.
- [66] Lalit M. Pant, Sushanta K. Mitra, and Marc Secanell. Stochastic reconstruction using multiple correlation functions with different-phase-neighbor-based pixel selection. *Physical Review E*, 90:023306, Aug 2014.
- [67] A. Cecen, T. Fast, E.C. Kumbur, and S.R. Kalidindi. A data-driven approach to establishing microstructure-property relationships in porous transport layers of polymer electrolyte fuel cells. *Journal of Power Sources*, 245:144–153, 2014.
- [68] E.A. Wargo, A.C. Hanna, A. Een, S.R. Kalidindi, and E.C. Kumbur. Selection of representative volume elements for pore-scale analysis of transport in fuel cell materials. *Journal of Power Sources*, 197:168–179, 2012.
- [69] S.R. Kalidindi, S.R. Niezgodna, and A.A. Salem. Microstructure informatics using higher-order statistics and efficient data-mining protocols. *JOM*, 63(4):34–41, 2011.

- [70] S.R. Niezgoda, Y.C. Yabansu, and S.R. Kalidindi. Understanding and visualizing microstructure and microstructure variance as a stochastic process. *Acta Materialia*, 59(16):6387–6400, 2011.
- [71] P. Capek, V. Hejtmanek, L. Brabec, A. Zikanova, and M. Kocirik. Stochastic reconstruction of particulate media using simulated annealing: Improving pore connectivity. *Transport in Porous Media*, 76(2):179–198, 2009.
- [72] Y. Jiao, F.H. Stillinger, and S. Torquato. A superior descriptor of random textures and its predictive capacity. *Proceedings of the National Academy of Sciences of the United States of America*, 106(42):17634–17639, 2009.
- [73] B. Lu and S. Torquato. Lineal-path function for random heterogeneous materials. *Physical Review A*, 45(2):922–929, 1992.
- [74] S. Torquato and B. Lu. Chord-length distribution function for two-phase random media. *Physical Review E*, 47(4):2950–2953, 1993.
- [75] C. Manwart, S. Torquato, and R. Hilfer. Stochastic reconstruction of sandstones. *Physical Review E*, 62(1 B):893–899, 2000.
- [76] M.S. Talukdar, O. Torsaeter, and M.A. Ioannidis. Stochastic reconstruction of particulate media from two-dimensional images. *Journal of Colloid and Interface Science*, 248(2):419–428, 2002.
- [77] M.S. Talukdar and O. Torsaeter. Reconstruction of chalk pore networks from 2D backscatter electron micrographs using a simulated annealing technique. *Journal of Petroleum Science and Engineering*, 33(4):265–282, 2002.
- [78] X. Zhao, J. Yao, and Y. Yi. A new stochastic method of reconstructing porous media. *Transport in Porous Media*, 69(1):1–11, 2007.
- [79] S. Torquato, J.D. Beasley, and Y.C. Chiew. Two-point cluster function for continuum percolation. *The Journal of Chemical Physics*, 88(10):6540–6547, 1988.
- [80] S. Torquato. Statistical description of microstructures. *Annual Reviews of Materials Science*, 32:77–111, 2002.

- [81] J. Caers. Geostatistical reservoir modelling using statistical pattern recognition. *Journal of Petroleum Science and Engineering*, 29(3-4):177–188, 2001.
- [82] H. Okabe and M. J. Blunt. Prediction of permeability for porous media reconstructed using multiple-point statistics. *Physical Review E*, 70(6 2):066135, 2004.
- [83] H. Okabe and M. J. Blunt. Pore space reconstruction using multiple-point statistics. *Journal of Petroleum Science and Engineering*, 46(1-2):121–137, 2005.
- [84] P. Tahmasebi and M. Sahimi. Reconstruction of three-dimensional porous media using a single thin section. *Physical Review E*, 85(6), 2012.
- [85] P. Tahmasebi and M. Sahimi. Cross-correlation function for accurate reconstruction of heterogeneous media. *Physical Review Letters*, 110(7):078002, 2013.
- [86] M. Joshi. *A class of stochastic models for porous materials*. PhD thesis, University of Kansas, 1974.
- [87] M. Giona and A. Adrover. Closed-Form Solution for the Reconstruction Problem in Porous Media. *AIChE Journal*, 42(5):1407–1415, 1996.
- [88] Ahmed Ouenes, Srinivasa Bhagavan, P.H. Bunge, and B.J. Travis. Application of simulated annealing and other global optimization methods to reservoir description: myths and realities. In *Proceedings of Society of Petroleum Engineers*, pages 547–560, 1994.
- [89] A. P. Roberts and M. A. Knackstedt. Structure-property correlations in model composite materials. *Physical Review E*, 54(3):2313–2328, 1996.
- [90] M.D. Rintoul and S. Torquato. Reconstruction of the structure of dispersions. *Journal of Colloid and Interface Science*, 186(2):467–476, 1997.
- [91] M. G. Rozman and M. Utz. Efficient reconstruction of multiphase morphologies from correlation functions. *Physical Review E*, 63(6 II):066701/1–066701/8, 2001.
- [92] A. Hajizadeh and Z. Farhadpour. An Algorithm for 3D Pore Space Reconstruction from a 2D Image Using Sequential Simulation and Gradual Deformation with the Probability Perturbation Sampler. *Transport in Porous Media*, 94(3):859–881, 2012.

- [93] J. Poutet, D. Manzoni, F. Hage-Chehade, C.G. Jacquin, M.J. Bouteca, J.-F. Thovert, and P.M. Adler. The effective mechanical properties of reconstructed porous media. *International Journal of Rock Mechanics and Mining Sciences and Geomechanics*, 33(4):409–415, 1996.
- [94] R.D. Hazlett. Statistical characterization and stochastic modeling of pore networks in relation to fluid flow. *Mathematical Geology*, 29(6):801–822, 1997.
- [95] C. L. Y. Yeong and S. Torquato. Reconstructing random media. II. Three-dimensional media from two-dimensional cuts. *Physical Review E*, 58(1):224–233, 1998.
- [96] M.S Talukdar, O. Torsaeter, M.A. Ioannidis, and J.J. Howard. Stochastic reconstruction, 3D characterization and network modeling of chalk. *Journal of Petroleum Science and Engineering*, 35(1-2):1–21, 2002.
- [97] M.G. Politis, E.S. Kikkinides, M.E. Kainourgiakis, and A.K. Stubos. A hybrid process-based and stochastic reconstruction method of porous media. *Microporous and Mesoporous Materials*, 110(1):92–99, 2008.
- [98] T. Tang, Q. Teng, X. He, and D. Luo. A pixel selection rule based on the number of different-phase neighbours for the simulated annealing reconstruction of sandstone microstructure. *Journal of Microscopy*, 234(3):262–268, 2009.
- [99] P. Capek, V. Hejtmanek, J. Kolafa, and L. Brabec. Transport Properties of Stochastically Reconstructed Porous Media with Improved Pore Connectivity. *Transport in Porous Media*, 88(1):87–106, 2011.
- [100] P. Capek, M. Vesel, B. Bernauer, P. Sysel, V. Hejtmek, M. Koik, L. Brabec, and O. Prokopov. Stochastic reconstruction of mixed-matrix membranes and evaluation of effective permeability. *Computational Materials Science*, 89:142–156, 2014.
- [101] N.A. Siddique and F. Liu. Process based reconstruction and simulation of a three-dimensional fuel cell catalyst layer. *Electrochimica Acta*, 55(19):5357–5366, 2010.
- [102] R. Barbosa, J. Andaverde, B. Escobar, and U. Cano. Stochastic reconstruction and a scaling method to determine effective transport coefficients of a proton exchange membrane fuel cell catalyst layer. *Journal of Power Sources*, 196(3):1248–1257, 2011.

- [103] M. El Hannach, R. Singh, N. Djilali, and E. Kjeang. Micro-porous layer stochastic reconstruction and transport parameter determination. *Journal of Power Sources*, 282:58–64, 2015.
- [104] D. Banham, F. Feng, T. Frstenhaupt, K. Pei, S. Ye, and V. Birss. Effect of Pt-loaded carbon support nanostructure on oxygen reduction catalysis. *Journal of Power Sources*, 196(13):5438–5445, 2011.
- [105] K.J. Lange, P.-C. Sui, and N. Djilali. Pore scale simulation of transport and electrochemical reactions in reconstructed PEMFC catalyst layers. *Journal of the Electrochemical Society*, 157(10):B1434–B1442, 2010.
- [106] S.H. Kim and H. Pitsch. Reconstruction and effective transport properties of the catalyst layer in pem fuel cells. *Journal of the Electrochemical Society*, 156(6):B673–B681, 2009.
- [107] J. Becker, C. Wieser, S. Fell, and K. Steiner. A multi-scale approach to material modeling of fuel cell diffusion media. *International Journal of Heat and Mass Transfer*, 54(7-8):1360–1368, 2011.
- [108] P. Rama, Y. Liu, R. Chen, H. Ostadi, K. Jiang, Y. Gao, X. Zhang, R. Fisher, and M. Jeschke. Multiscale modeling of single-phase multicomponent transport in the cathode gas diffusion layer of a polymer electrolyte fuel cell. *Energy and Fuels*, 24(5):3130–3143, 2010.
- [109] J.T. Gostick. Random pore network modeling of fibrous pemfc gas diffusion media using voronoi and delaunay tessellations. *Journal of the Electrochemical Society*, 160(8):F731–F743, 2013.
- [110] J. Hinebaugh, Z. Fishman, and A. Bazylak. Unstructured pore network modeling with heterogeneous PEMFC GDL porosity distributions. *Journal of the Electrochemical Society*, 157(11):B1651–B1657, 2010.
- [111] S. Shukla, K. Domican, K. Karan, S. Bhattacharjee, and M. Secanell. Analysis of low platinum loading thin polymer electrolyte fuel cell electrodes prepared by inkjet printing. *Electrochimica Acta*, 156:289–300, 2014.

- [112] Shantanu Shukla, Subir Bhattacharjee, and Marc Secanell. Rationalizing Catalyst Inks for PEMFC Electrodes Based On Colloidal Interactions. *ECS Transactions*, 58(1):1409–1428, 2013.
- [113] J.W. Cahn. Phase separation by spinodal decomposition in isotropic systems. *The Journal of Chemical Physics*, 42(1):93–99, 1965.
- [114] A.P. Roberts and M. Teubner. Transport properties of heterogeneous materials derived from Gaussian random fields: Bounds and simulation. *Physical Review E*, 51(5):4141–4154, 1995.
- [115] P. Levitz. Off-lattice reconstruction of porous media: Critical evaluation, geometrical confinement and molecular transport. *Advances in Colloid and Interface Science*, 76-77:71–106, 1998.
- [116] M. Ioannidis, M. Kwiecien, and I. Chatzis. Computer generation and application of 3-D model porous media: from pore-level geostatistics to the estimation of formation factor. pages 185–194, 1995.
- [117] M.A. Ioannidis, M.J. Kwiecien, and I. Chatzis. Electrical Conductivity and Percolation Aspects of Statistically Homogeneous Porous Media. *Transport in Porous Media*, 29(1):61–83, 1997.
- [118] D.T. Fullwood, S.R. Niezgodna, and S.R. Kalidindi. Microstructure reconstructions from 2-point statistics using phase-recovery algorithms. *Acta Materialia*, 56(5):942–948, 2008.
- [119] D. Cule and S. Torquato. Generating random media from limited microstructural information via stochastic optimization. *Journal of Applied Physics*, 86(6):3428–3437, 1999.
- [120] A. N. Diogenes, L. O. E. dos Santos, C. P. Fernandes, A. C. Moreira, and C. R. Apoloni. Porous media microstructure reconstruction using pixel based and object based simulated annealing comparison with other reconstruction methods. In *Fifth International Conference Multiscale Materials Modeling MMM2010*, Freiburg, Germany, October 48 2010. Fraunhofer Institute for Mechanics of Materials IWM.

- [121] M.S. Talukdar, O. Torsaeter, and J.J. Howard. Stochastic reconstruction of chalk samples containing vuggy porosity using a conditional simulated annealing technique. *Transport in Porous Media*, 57(1):1–15, 2004.
- [122] R. Barbosa, B. Escobar, U. Cano, R. Pedicini, R. Ornelas, and E. Passalacqua. Stochastic reconstruction at two scales and experimental validation to determine the effective electrical resistivity of a PEMFC catalyst layer. *ECS Transactions*, 41(1):2061–2071, 2011.
- [123] C.E. Zachary and S. Torquato. Improved reconstructions of random media using dilation and erosion processes. *Physical Review E*, 84(5), 2011.
- [124] D. Chen, X. He, Q. Teng, Z. Xu, and Z. Li. Reconstruction of multiphase microstructure based on statistical descriptors. *Physica A*, 415:240–250, 2014.
- [125] E.-Y. Guo, N. Chawla, T. Jing, S. Torquato, and Y. Jiao. Accurate modeling and reconstruction of three-dimensional percolating filamentary microstructures from two-dimensional micrographs via dilation-erosion method. *Materials Characterization*, 89:33–42, 2014.
- [126] Y. Jiao and N. Chawla. Modeling and characterizing anisotropic inclusion orientation in heterogeneous material via directional cluster functions and stochastic microstructure reconstruction. *Journal of Applied Physics*, 115(9), 2014.
- [127] S.K. Alexander, P. Fieguth, M.A. Ioannidis, and E.R. Vrscay. Hierarchical annealing for synthesis of binary images. *Mathematical Geosciences*, 41(4):357–378, 2009.
- [128] W.R. Campaigne, P. Fieguth, and S.K. Alexander. Frozen-state hierarchical annealing. *Lecture Notes in Computer Science (including subseries Lecture Notes in Artificial Intelligence and Lecture Notes in Bioinformatics)*, 4141 LNCS:41–52, 2006.
- [129] D. D. Chen, Q. Teng, X. He, Z. Xu, and Z. Li. Stable-phase method for hierarchical annealing in the reconstruction of porous media images. *Physical Review E*, 89(1):013305, 2014.
- [130] S. Torquato. *Random Heterogeneous Materials: Microstructure and Macroscopic Properties*. Springer, New York, USA, 2000.

- [131] J.G. Berryman and S.C. Blair. Use of digital image analysis to estimate fluid permeability of porous materials: Application of two-point correlation functions. *Journal of Applied Physics*, 60(6):1930–1938, 1986.
- [132] M.A. Ioannidis, M.J. Kwiecien, and I. Chatzis. Statistical analysis of the porous microstructure as a method for estimating reservoir permeability. *Journal of Petroleum Science and Engineering*, 16(4):251–261, 1996.
- [133] N. F. Berk. Scattering properties of a model bicontinuous structure with a well defined length scale. *Physical Review Letters*, 58(25):2718–2721, 1987.
- [134] A.P. Radlinski, M.A. Ioannidis, A.L. Hinde, M. Hainbuchner, M. Baron, H. Rauch, and S.R. Kline. Angstrom-to-millimeter characterization of sedimentary rock microstructure. *Journal of Colloid and Interface Science*, 274(2):607–612, 2004.
- [135] A.P. Radlinski, M. Mastalerz, A.L. Hinde, M. Hainbuchner, H. Rauch, M. Baron, J.S. Lin, L. Fan, and P. Thiyagarajan. Application of SAXS and SANS in evaluation of porosity, pore size distribution and surface area of coal. *International Journal of Coal Geology*, 59(3-4):245–271, 2004.
- [136] J.G. Berryman and G.W. Milton. Normalization constraint for variational bounds on fluid permeability. *The Journal of Chemical Physics*, 83(2):754–760, 1985.
- [137] D.A. Coker, S. Torquato, and J.H. Dunsmuir. Morphology and physical properties of Fontainebleau sandstone via a tomographic analysis. *Journal of Geophysical Research B: Solid Earth*, 101(8):17497–17506, 1996.
- [138] J.M. Zalc, S.C. Reyes, and E. Iglesia. The effects of diffusion mechanism and void structure on transport rates and tortuosity factors in complex porous structures. *Chemical Engineering Science*, 59(14):2947–2960, 2004.
- [139] A. Berson, H.-W. Choi, and J.G. Pharoah. Determination of the effective gas diffusivity of a porous composite medium from the three-dimensional reconstruction of its microstructure. *Physical Review E*, 83(2):026310, 2011.
- [140] Walter Kauzman. *Kinetic Theory of Gases*. Dover Publications Inc., New York, 2012.

- [141] Azriel Rosenfeld and John L. Pfaltz. Sequential Operations in Digital Picture Processing. *Journal of the Association for Computing Machinery*, 13(4):471–494, oct 1966. ISSN 0004-5411.
- [142] Robert Endre Tarjan. Efficiency of a Good But Not Linear Set Union Algorithm. *Journal of the Association for Computing Machinery*, 22(2):215–225, April 1975. ISSN 0004-5411.
- [143] J. Hoshen and R. Kopelman. Percolation and cluster distribution. I. Cluster multiple labeling technique and critical concentration algorithm. *Physical Review B*, 14(8):3438–3445, 1976.
- [144] U. Wolff. Collective Monte Carlo Updating for Spin Systems. *Physical Review Letters*, 62(4):361–364, 1989.
- [145] J. Martin-Herrero. Hybrid cluster identification. *Journal of Physics A: Mathematical and General*, 37(40):9377–9386, 2004.
- [146] G. Dueck. New optimization heuristics; The great deluge algorithm and the record-to-record travel. *Journal of Computational Physics*, 104(1):86–92, 1993.
- [147] N. Metropolis, A.W. Rosenbluth, M.N. Rosenbluth, A.H. Teller, and E. Teller. Equation of state calculations by fast computing machines. *The Journal of Chemical Physics*, 21(6):1087–1092, 1953.
- [148] G. Dueck. Threshold accepting: A general purpose optimization algorithm appearing superior to simulated annealing. *Journal of Computational Physics*, 90(1):161–175, 1990.
- [149] Stuart Geman and Donald Geman. Stochastic relaxation, Gibbs distributions, and the Bayesian restoration of images. *IEEE Transactions on Pattern Analysis and Machine Intelligence*, PAMI-6(6):721–741, 1984.
- [150] L. Ingber. Simulated annealing: Practice versus theory. *Mathematical and Computer Modelling*, 18(11):29–57, 1993.
- [151] P. Siarry, G. Berthiau, F. Durbin, and J. Haussy. Enhanced Simulated Annealing for Globally Minimizing Functions of Many-Continuous Variables. *ACM Transactions on Mathematical Software*, 23(2):209–228, 1997.

- [152] Y. Jiao, F. H. Stillinger, and S. Torquato. Modeling heterogeneous materials via two-point correlation functions. II. Algorithmic details and applications. *Physical Review E*, 77(3):031135, 2008.
- [153] J. Sauvola and M. Pietikainen. Adaptive document image binarization. *Pattern Recognition*, 33(2):225–236, 2000.
- [154] G.M. Baniak, A.D. La Croix, C.A. Polo, T.L. Playter, S.G. Pemberton, and M.K. Gingras. Associating X-Ray Microtomography with Permeability Contrasts in Bioturbated Media. *Ichnos:an International Journal of Plant and Animal*, 21(4):234–250, 2014.
- [155] L.M. Pant, S.K. Mitra, and M. Secanell. A generalized mathematical model to study gas transport in PEMFC porous media. *International Journal of Heat and Mass Transfer*, 58(1-2):70–79, 2013.
- [156] R. Krishna and J. A. Wesselingh. The Maxwell-Stefan approach to mass transfer. *Chemical Engineering Science*, 52(6):861–911, 1997. ISSN 0009-2509.
- [157] R.K. Agarwal, K.-Y. Yun, and R. Balakrishnan. Beyond Navier-Stokes: Burnett equations for flows in the continuum-transition regime. *Physics of Fluids*, 13(10):3061–3085, 2001.
- [158] Adolf Fick. Ueber Diffusion. *Annalen der Physik-leipzig*, 170(1):59–86, 1855. ISSN 1521-3889.
- [159] Robert C. Reid, John M. Prausnitz, and Bruce E. Poling. *The Properties of Gases and Liquids*. McGraw-Hill, 1987.
- [160] James Clark Maxwell. The scientific papers of James Clark Maxwell. volume 2. Dover Publications, 1965.
- [161] R. E. Cunningham and R. J. J. Williams. *Diffusion in Gases and Porous Media*. Pelnum Press, New York, 1980.
- [162] E. A. Mason and A. P. Malinauskas. *Gas Transport in Porous Media: The Dusty Gas Model*. Elsevier, Amsterdam, 1983.

- [163] J.O. Hirschfelder, C.F. Curtiss, and R.B. Bird. *Molecular Theory of Gases and Liquids*. Wiley, 1954.
- [164] P.J.A.M. Kerkhof. New Light on Some Old Problems: Revisiting the Stefan Tube, Graham’s Law, and the Bosanquet Equation. *Industrial and Engineering Chemistry Research*, 36(3):915–922, 1997.
- [165] Lalit M Pant, Mayank Sabharwal, Sushanta Mitra, and Marc Secanell. Stochastic Reconstruction and Transport Simulation of PEFC Catalyst Layers. *ECS Transactions*, 69(17):105–120, 2015.
- [166] openFCST: An open source fuel cell simulation toolbox. URL <http://www.openfcst.org>.
- [167] M. Secanell, A. Putz, P. Wardlaw, V. Zingan, M. Bhaiya, M. Moore, J. Zhou, C. Balen, and K. Domican. OpenFCST: An open-source mathematical modelling software for polymer electrolyte fuel cells. In *ECS Transactions*, volume 64, pages 655–680, 2014.
- [168] N. Zamel, N.G.C. Astrath, X. Li, J. Shen, J. Zhou, F.B.G. Astrath, H. Wang, and Z.-S. Liu. Experimental measurements of effective diffusion coefficient of oxygen-nitrogen mixture in PEM fuel cell diffusion media. *Chemical Engineering Science*, 65(2):931–937, 2010.

Appendix A

Computational Algorithms for Correlation Function Estimation

This chapter presents computational algorithms for estimating different correlation functions from digital images of random media. The algorithms follow C++ style of nomenclature and indexing. For example, all the indices start at 0 instead of 1, and a variable followed by ++ represents an increment by 1. All the algorithms, except the one-point correlation function, and cluster identification are presented for computing correlation functions for a pixel row in x direction, and can be adjusted as per need for other directions. Once the correlation functions for all the rows and columns are obtained, they can be averaged separately in each direction. The y and z indices for the row of interest in the following sections are defined B and C respectively.

A.1 Algorithm for Computing Volume Fraction

Algorithm A.1 presents the computational method for obtaining volume fraction of phase i in a digital image.

A.2 Algorithm for Computing Two-point Correlation Function

Algorithm A.2 is presented to compute two-point correlation function of a pixel row for phase i in a digital image. Once the correlation function for a row is obtained, the average x -direction two-point correlation function for entire image is obtained by summing the two-point correlation function of all rows and dividing by the number of rows.

Algorithm A.1 Algorithm for computing volume fraction for phase i

```
Read the image; ▷ Let's define the image as  $\Omega$ 
Read the  $x$ ,  $y$  and  $z$  dimensions; ▷ Let's say  $W$ ,  $H$ , and  $D$ 
 $N_{\text{pixels},i} = 0$ ;
for  $0 \leq a < W$  do
  for  $0 \leq b < H$  do
    for  $0 \leq c < D$  do
      if  $\Omega(a, b, c) == i$  then
         $N_{\text{pixels},i}++$ ;
      end if
    end for
  end for
end for
 $\phi_i = N_{\text{pixels},i}/(WHD)$ ;
```

Algorithm A.2 Algorithm for computing two-point correlation function for phase i

```
Read the image; ▷ Let's define the image as  $\Omega$ 
Read the  $x$ ,  $y$  and  $z$  dimensions; ▷ Let's say  $W$ ,  $H$ , and  $D$ 
Define  $r_{\text{max}}$  as the maximum  $r$  for which you want to compute the function;
Define an array  $E_+[r_{\text{max}}]$  (size  $r_{\text{max}}$ ), which keeps track of positive encounters at each  $r$ ;
for  $0 \leq r \leq r_{\text{max}}$  do
   $L_{\text{max}} = W - r$ ;
  for  $0 \leq a < L_{\text{max}}$  do
    Pixel1 =  $\Omega(a, B, C)$ ;
    Pixel2 =  $\Omega(a + r, B, C)$ ;
    if Pixel1 ==  $i$  and Pixel2 ==  $i$  then
       $E_+[r]++$ ;
    end if
  end for
   $S_2^{(i)}(r) = E_+[r]/L_{\text{max}}$ ;
end for
```

Algorithm A.3 Algorithm for computing lineal path function for phase i

```
Read the image;                                ▷ Let's define the image as  $\Omega$ 
Read the  $x$ ,  $y$  and  $z$  dimensions;                ▷ Let's say  $W$ ,  $H$ , and  $D$ 
Define  $r_{\max}$  as the maximum  $r$  for which you want to compute the function;
Define  $L[r_{\max}]$  as the array of lineal path function;
Define  $L_{\text{chord}} = 0$ ;                            ▷ Keeps track of the length of each encountered chord
Define  $\text{pix} = 0$ ;                                ▷ Keeps counter of the pixel index. Started at beginning of image
while  $\text{pix} \leq W$  do                                ▷ While image end not reached
    if  $(\text{pix} < W)$  and  $(\Omega(\text{pix}, B, C) == i)$  then    ▷ While within image and in phase  $i$ 
         $L_{\text{chord}}++$ ;
    else                                            ▷ Once a complete chord is encountered
        for  $0 \leq r < L_{\text{chord}}$  do
            if  $r < r_{\max}$  then
                 $L[r] = L[r] + (L_{\text{chord}} - r)/(W - r)$ ;
            end if
        end for
         $L_{\text{chord}} = 0$ ;                            ▷ Reset  $L_{\text{chord}}$  to 0 for next chord calculation
    end if
     $\text{pix}++$ ;                                        ▷ Increment pixel counter
end while
```

A.3 Algorithm for Computing Lineal Path Function

Algorithm A.3 is presented to compute lineal-path function of a pixel row for phase i in a digital image. Once the correlation function for a row is obtained, the average x -direction lineal path function for entire image is obtained by summing the lineal path function of all rows and dividing by the number of rows.

A.4 Algorithm of computing Chord Length Function

Algorithm A.4 presents a method to compute chord length function of a pixel row for phase i in a digital image. The average x -direction chord length function for entire image is obtained by summing the chord encounters over all rows and normalizing them by total number of chords. It must be noted that simply summing up chord length functions for each row, and averaging by number of rows will result in incorrect estimation.

Algorithm A.4 Algorithm for computing chord length function for phase i

```
Read the image;                                ▷ Let's define the image as  $\Omega$ 
Read the  $x$ ,  $y$  and  $z$  dimensions;                ▷ Let's say  $W$ ,  $H$ , and  $D$ 
Define  $r_{\max}$  as the maximum  $r$  for which you want to compute the function;
Define  $C[r_{\max}]$  as the array of chord length function;
Define  $n_{\text{chords}} = 0$ ;                        ▷ Keeps track of number of chord encountered
Define  $L_{\text{chord}} = 0$ ;                        ▷ Keeps track of the length of each encountered chord
Define  $\text{pix} = 0$ ;                             ▷ Keeps counter of the pixel index. Started at beginning of image
while  $\text{pix} \leq W$  do                          ▷ While image end not reached
  if  $(\text{pix} < W)$  and  $(\Omega(\text{pix}, B, C) == i)$  then    ▷ While within image and in phase  $i$ 
     $L_{\text{chord}}++$ ;
  else                                            ▷ Once a complete chord is encountered
    if  $r < r_{\max}$  then
       $C[L_{\text{chord}}]++$ ;    ▷ Increment the number of chords encountered of length  $L_{\text{chord}}$ 
       $n_{\text{chords}}++$ ;    ▷ Increment the number of chords encountered
    end if
     $L_{\text{chord}} = 0$ ;    ▷ Reset  $L_{\text{chord}}$  to 0 for next chord calculation
  end if
   $\text{pix}++$ ;    ▷ Increment pixel counter
end while
Normalize  $C[r]$  by  $n_{\text{chords}}$  to obtain chord length function;
```

A.5 Algorithm for Computing Two-point Cluster Function

This section presents the algorithm to compute the two-point cluster function for a random media. Before computing the cluster function however, the cluster labels must be identified. The following subsections present the algorithms for cluster identification and then cluster function computing.

A.5.1 Cluster Identification

The overall algorithm for the cluster identification for phase i is given by Algorithm A.5 followed by Algorithm A.6 for final cluster number assignment. Six neighbor connectivity is used to identify connected components in a 3D image. The neighbors reduce to four for a 2D image. A cluster equivalence array, EQ, is used for storing cluster label equivalence information. EQ[i] denotes the equivalent of label i , i.e., when two connected pixels with different cluster numbers are found (and one of them is i), the other label and i are equivalent, since they represent pixels belonging to same cluster. EQ[0] stores the maximum cluster label

| | | | | | | |
|-------|----|---|---|---|---|---|
| Index | 0 | 1 | 2 | 3 | 4 | 5 |
| Value | 21 | 1 | 3 | 5 | 4 | 5 |

Figure A.1 – An illustration of the cluster equivalence array

assigned in the image. Figure A.1 shows an illustration of the cluster equivalence array. At the indicated stage in the figure, 21 pixels have been identified as indicated by EQ[0]. If more than a single labeled neighbor is found for the next pixel, a union find algorithm is used to find a unique cluster label among connected clusters. The root equivalence label is defined as the equivalent label whose equivalent is the same as the itself, i.e., when EQ[label] = label. For example, in Fig. A.1, the equivalent of label 2 is 3; however, 3 is not the root, as its equivalent is 5. Label 5 is its own equivalent, thereby making it the root equivalent of labels 2, 3 and 5. If a consecutive pixel is found with neighbor labels 2 and 3, it will be assigned a label of 5. Once all the pixels of the image are labeled, and all the equivalent labels identified, a second pass is performed to merge all clusters with equivalent labels and assign single unique labels. Algorithm A.6 describe the algorithm of the second pass.

A.5.2 Cluster Function Computation

Algorithm A.7 presents a method to compute two-point cluster function for phase i in a digital image. The average x -direction two-point correlation function is obtained by summing the two-point cluster function of all rows and dividing by the number of rows.

Algorithm A.5 Algorithm for cluster identification

```
Read the image;                                ▷ Let's define the image as  $\Omega$ 
Read the  $x$ ,  $y$  and  $z$  dimensions;                ▷ Let's say  $W$ ,  $H$ , and  $D$ 
Initiate a label array (Label) to 0;           ▷ Contains the cluster label of each pixel
Define a cluster equivalence array EQ with just one element EQ[0];
for  $0 \leq a < W$  do
  for  $0 \leq b < H$  do
    for  $0 \leq c < D$  do
      if  $\Omega(a, b, c) == i$  then                ▷ If the pixel belongs to phase  $i$ 
        Find Label(a-1,b,c), Label(a,b-1,c), Label (a,b,c-1)1;
        if Label(a-1,b,c)==0 and Label(a,b-1,c)==0 and Label (a,b,c-1)==0 then2
          EQ[0]++;                                ▷ Make new label
          Generate a new element of array EQ;
          EQ[EQ[0]] = EQ[0];                    ▷ Label and equivalent label are same
        else                                     ▷ If labeled neighbors exist
          if Only one of the labels is non-zero, or if all labels are same then
            Label(a,b,c)=non zero label;
          else                                   ▷ If multiple labels exist in neighborhood
            Find all the non-zero neighbor labels;
            Find root label for all these labels;
            Assign the maximum label to current pixel;
            Update the equivalence labels of the neighbors with maximum label;
          end if
        end if
      end if
    end for
  end for
end for
end for
```

¹Labels of the pixel above, to the left and on the front of current pixel. Since the image is being scanned in one direction, it is assured that the label of pixels down, right and behind are not yet assigned, and are at the default value of zero

²If none of the pixels in the neighborhood haven been assigned any label, i.e., none of them belong to phase i

Algorithm A.6 Algorithm for assigning final labels to clusters

```
for  $0 \leq a < W$  do
  for  $0 \leq b < H$  do
    for  $0 \leq c < D$  do
      if  $\Omega(a, b, c) == i$  then
        tmp = Label(a, b, c);
        root = Root label of tmp from EQ;
        if No new label assigned for the root then
          Assign a new label for the root;
          Label(a, b, c) = new label;
        else
          Label(a, b, c) = new label for root label;
        end if
      end if
    end for
  end for
end for
```

Algorithm A.7 Algorithm for computing two-point cluster function for phase i

```
Read the image; ▷ Let's define the image as  $\Omega$ 
Read the image cluster labels; ▷ Let's define the label array as L
Read the  $x$ ,  $y$  and  $z$  dimensions; ▷ Let's say  $W$ ,  $H$ , and  $D$ 
Define  $r_{\max}$  as the maximum  $r$  for which you want to compute the function;
Define an array  $E_+[r_{\max}]$  (size  $r_{\max}$ ), which keeps track of positive encounters at each  $r$ ;
for  $0 \leq r \leq r_{\max}$  do
   $L_{\max} = W - r$ ;
  for  $0 \leq a < L_{\max}$  do
    Pixel1 =  $\Omega(a, B, C)$ ;
    Pixel2 =  $\Omega(a + r, B, C)$ ;
    Label1 = Label(a, B, C);
    Label2 = Label(a+r, B, C);
    if Pixel1 ==  $i$  and Pixel2 ==  $i$  and (Label1 == Label2) then
      |  $E_+[r]++$ ;
    end if
  end for
   $C_2^{(i)}(r) = E_+[r]/L_{\max}$ ;
end for
```

Appendix B

Computational Algorithms for Stochastic Reconstruction

B.1 Reference Image Synthesis

This section describes the reference image synthesis for a refinement scale s , from an image of refinement scale $s - 1$. Algorithm B.1 presents the details of the computational program for generating the image. The algorithm is designed to half the dimension of the image by using a $2 \times 2 \times 2$ pixels (2×2 for 2D) averaging region for generating a new pixel.

B.2 Image Resizing Method

Algorithm B.2 presents the algorithm for resizing a 2D binary image. The algorithm can be simply expanded to resize 3D images as well.

B.3 DPN Computation Methods

B.3.1 DPN Value Computation Algorithm

Algorithm B.3 shows the method for computing DPN values of the image. Two arrays, DPN_w and DPN_b , of the same dimensions as the image are created. DPN_w contains the DPN information for white pixels, while DPN_b contains the DPN information about the black pixels. The Complete DPN information is computed at the beginning of the reconstruction, and thereafter updated as per pixel swap. Once the DPNs of each pixel are known, the DPN sets can be assembled for probability calculations. As the DPN values for each pixel are known and stored, only the swapped pixels and their neighborhoods need to be

Algorithm B.1 Algorithm for generating coarse reference image at scale s

Read the image at scale $s - 1$, Ω^{s-1} ;
Compute the void volume fraction ϕ_v^{s-1} of Ω^{s-1} using Algorithm A.1;
Read the x , y and z dimensions; ▷ Let's say W , H , and D
Initialize a new black image (pixel=0) of dimension $W/2$, $H/2$, and $D/2$ at scale s , Ω^s ;
procedure ASSIGN PIXEL VALUES
 Initialize void pixels $\text{Pix}_v = 0$;
 Initialize undecided pixel collection;
 for $0 \leq a < W/2$ **do**
 for $0 \leq b < H/2$ **do**
 for $0 \leq c < D/2$ **do**
 procedure FIND AVERAGE PIXEL VALUE FROM PARENT SCALE
 Initialize total pixel value $\text{Pix}_t = 0$;
 for $0 \leq i < 2$ **do**
 for $0 \leq j < 2$ **do**
 for $0 \leq k < 2$ **do**
 $\text{Pix}_t = \text{Pix}_t + \Omega^{s-1}(2a + i, 2b + j, 2c + k)$;
 end for
 end for
 end for
 end procedure
 Pixel average, $\overline{\text{Pix}_t} = \text{Pix}_t/8$;
 if ($\overline{\text{Pix}_t} < 126.5$) **then**
 $\Omega^s(a, b, c) = 0$;
 else if ($\overline{\text{Pix}_t} > 126.5$) **then**
 $\Omega^s(a, b, c) = 255$;
 Pix_v++ ;
 else
 Add $\Omega^s(a, b, c)$ to undecided collection;
 end if
 end for
 end for
 end for
 Compute void fraction $\phi_v^s = \text{Pix}_v/(WHD/8)$;
 procedure ASSIGN PHASES TO UNDECIDED PIXELS
 while ($\phi_v^s < \phi_v^{s-1}$) **do**
 Pick a random pixel from the undecided list;
 Assign it the void phase, i.e., color 255;
 Remove from list;
 Pix_v++ ;
 Re-compute void fraction $\phi_v^s = \text{Pix}_v/(WHD/8)$;
 end while
 end procedure
end procedure

Algorithm B.2 Algorithm for resizing a binary image using nearest neighbor interpolation

```
Read the original image,  $\Omega$ ;  
Read the  $x$  and  $y$  dimensions of original image; ▷ Let's say  $W$  and  $H$   
Read the  $x$  and  $y$  reconstruction dimensions; ▷ Let's say  $W_r$  and  $H_r$   
Define the resized image as  $\Omega_r$ ;  
 $scale_x = W/W_r$ ;  
 $scale_y = H/H_r$ ;  
for  $0 \leq i < W_r$  do  
    for  $0 \leq j < H_r$  do  
         $nearest_x = \text{round}(scale_x \times i)$ ;  
         $nearest_y = \text{round}(scale_y \times j)$ ;  
         $\Omega_r(i, j) = \Omega(nearest_x, nearest_y)$ ;  
    end for  
end for
```

updated after a pixel swap. This saves considerable amount of computation time compared to the method where the DPN information has to be completely recomputed after each swap.

B.4 DPN Set Assembling Algorithm

Algorithm B.4 presents the method for assembling the initial DPN sets for both phases. The sets are assembled at the beginning of the reconstruction after the DPN values for each pixel have been computed, and the arrays DPN_w , and DPN_b are obtained. The array is assembled by scanning through the image, and assigning each pixel to its corresponding DPN set based on its phase and DPN value.

B.5 DPN Set Updating

Algorithm B.5 presents the computational method for updating DPN sets after a pixel swap. First, the old swapped pixels and their neighbors are removed from their corresponding sets. Then the new DPN values for the pixels are calculated. Finally, the pixels are inserted in the sets corresponding to their new DPN values. In this algorithm $Set_x[i]$ refers to the array of pixels which are of phase x and have i number of DPNs.

Algorithm B.3 Algorithm for calculating DPN values for the image

```
Read the image,  $\Omega$ ;  
Read the  $x$ ,  $y$  and  $z$  dimensions; ▷ Let's say  $W$ ,  $H$ , and  $D$   
Define two arrays,  $DPN_b$  (for black pixels), and  $DPN_w$  (for white pixels);  
Initialize  $DPN_b$  and  $DPN_w$  to zeros;  
for  $0 \leq a < W$  do  
  for  $0 \leq b < H$  do  
    for  $0 \leq c < D$  do  
      procedure COMPUTE NUMBER OF DIFFERENT PHASE NEIGHBORS  
        Initialize  $dpn=0$ ;  
        for  $(a-1) \leq i \leq (a+1)$  do  
          for  $(b-1) \leq j \leq (b+1)$  do  
            for  $(c-1) \leq k \leq (c+1)$  do  
              if  $(\Omega(i, j, k) \neq \Omega(a, b, c))$  then  
                 $dpn++$ ;  
              end if  
            end for  
          end for  
        end for  
      end procedure  
      procedure ASSIGN DPN VALUE  
        if  $(\Omega(a, b, c) == 0)$  then ▷ If black pixel  
           $DPN_b(a, b, c) = dpn$ ;  
        else ▷ If white pixel  
           $DPN_w(a, b, c) = dpn$ ;  
        end if  
      end procedure  
      Reset  $dpn = 0$  for next pixel;  
    end for  
  end for  
end for
```

Algorithm B.4 Algorithm for assembling initial DPN sets

```
Read the image,  $\Omega$ ;  
Read the  $x$ ,  $y$  and  $z$  dimensions; ▷ Let's say  $W$ ,  $H$ , and  $D$   
Read the DPN arrays  $DPN_b$  and  $DPN_w$ ;  
Define two maps  $Set_b$ , and  $Set_w$ ;  
for  $0 \leq a < W$  do  
  for  $0 \leq b < H$  do  
    for  $0 \leq c < D$  do  
      if ( $\Omega(a, b, c) == 0$ ) then ▷ If black pixel  
         $dpn = DPN_b(a, b, c)$ ;  
        Insert the coordinate pair  $(a, b, c)$  in  $Set_b[dpn]$ ;  
      else ▷ If white pixel  
         $dpn = DPN_w(a, b, c)$ ;  
        Insert the coordinate pair  $(a, b, c)$  in  $Set_w[dpn]$ ;  
      end if  
    end for  
  end for  
end for  
end for
```

Algorithm B.5 Algorithm for updating the DPN sets for a swapped pixel and its neighbors

Read the image before swapping, Ω_{old} ;

Read the old DPN arrays $DPN_{b,old}$ and $DPN_{w,old}$;

Define the swapped pixel locations as (x_1, y_1, z_1) , and (x_2, y_2, z_2) ;

Remove the pixel and neighbors from $set(x_1, y_1, z_1)$;

Remove the pixel and neighbors from $set(x_2, y_2, z_2)$;

procedure REMOVE THE PIXEL AND NEIGHBORS FROM SET(x,y,z)

for $(x - 1) \leq i \leq (x + 1)$ **do**

for $(y - 1) \leq j \leq (y + 1)$ **do**

for $(z - 1) \leq k \leq (z + 1)$ **do**

if $(\Omega_{old}(i, j, k) == 0)$ **then**

$dpn_{old} = DPN_{b,old}(i, j, k)$;

 Remove (i, j, k) from $Set_b[dpn_{old}]$;

else

$dpn_{old} = DPN_{w,old}(i, j, k)$;

 Remove (i, j, k) from $Set_w[dpn_{old}]$;

end if

end for

end for

end for

end procedure

Read the updated image after swapping, Ω_{new} ;

Read the updated DPN arrays $DPN_{b,new}$ and $DPN_{w,new}$;

Add the pixel and neighbors to $set(x_1, y_1, z_1)$;

Add the pixel and neighbors to $set(x_2, y_2, z_2)$;

procedure ADD THE PIXEL AND NEIGHBORS TO SET(x,y,z)

for $(x - 1) \leq i \leq (x + 1)$ **do**

for $(y - 1) \leq j \leq (y + 1)$ **do**

for $(z - 1) \leq k \leq (z + 1)$ **do**

if $(\Omega_{new}(i, j, k) == 0)$ **then**

$dpn_{new} = DPN_{b,new}(i, j, k)$;

 Add (i, j, k) to $Set_b[dpn_{new}]$;

else

$dpn_{new} = DPN_{w,new}(i, j, k)$;

 Add (i, j, k) to $Set_w[dpn_{new}]$;

end if

end for

end for

end for

end procedure

▷ Pixel is black

▷ Pixel is white

▷ Pixel is black

▷ Pixel is white